



University of Kentucky
UKnowledge

University of Kentucky Doctoral Dissertations

Graduate School

2007

SPECTROSCOPY AND STRUCTURES OF Cu-ORGANONITROGEN COMPLEXES

Xu Wang

University of Kentucky, xwang6@uky.edu

[Right click to open a feedback form in a new tab to let us know how this document benefits you.](#)

Recommended Citation

Wang, Xu, "SPECTROSCOPY AND STRUCTURES OF Cu-ORGANONITROGEN COMPLEXES" (2007).
University of Kentucky Doctoral Dissertations. 504.
https://uknowledge.uky.edu/gradschool_diss/504

This Dissertation is brought to you for free and open access by the Graduate School at UKnowledge. It has been accepted for inclusion in University of Kentucky Doctoral Dissertations by an authorized administrator of UKnowledge. For more information, please contact UKnowledge@lsv.uky.edu.

ABSTRACT OF DISSERTATION

Xu Wang

The Graduate School
University of Kentucky

2007

SPECTROSCOPY AND STRUCTURES OF Cu-ORGANONITROGEN COMPLEXES

ABSTRACT OF DISSERTATION

A dissertation submitted in partial fulfillment of the
requirements for the degree of Doctor of Philosophy in the
College of Arts and Sciences
at the University of Kentucky

By

Xu Wang

Lexington, Kentucky

Director: Dr. Dong-Sheng Yang, Professor of Chemistry

Lexington, Kentucky

2007

Copyright © Xu Wang 2007

ABSTRACT OF DISSERTATION

SPECTROSCOPY AND STRUCTURES OF Cu-ORGANONITROGEN COMPLEXES

Copper-organonitrogen complexes are studied by threshold photoionization and zero electron kinetic energy photoelectron spectroscopy. These complexes are prepared in pulsed laser vaporization supersonic molecular beams. Adiabatic ionization energies of the neutral species and vibrational frequencies of the neutral and ionic complexes were measured. Metal-ligand bond dissociation energies were obtained from the theoretical calculations or the experiments. More importantly, by combining the spectroscopic measurements, quantum chemical calculations, and spectral simulations, metal-ligand bonding structures are determined for copper complexes of diamines, pyridine, diazines, aminopyridines, polypyridines, and imidazole.

The Cu-ethylenediamine, -(1,3-propanediamine), and -(1,4-butanediamine) complexes have been determined to be in a hydrogen-bond stabilized monodentate configuration. However, Cu atom binds to both two nitrogens in the methyl-substituted ethylenediamines. The change of the Cu binding from the monodentate to the bidentate mode arises from the competition between copper coordination and hydrogen bonding. Although pyridine, diazines, and imidazole molecules can function as a σ -donor through the nitrogen atom, a π -acceptor or π -donor through six-membered or five-membered aromatic ring, only the σ bonding mode is predicted by the theory and identified by the ZEKE spectroscopy. For aminopyridine molecules, σ bonding through the sp^2 or sp^3 hybrid electron lone pair and π bonding through the pyridine ring are possible. Yet, the σ bonding through the sp^2 electron donation is calculated to be the strongest, and the Cu-

aminopyridine complexes formed by such bonding mechanism are identified by the experiments. Moreover, monodentate Cu-(4,4'-bipyridine), bidentate Cu-(2,2'-bipyridine) and Cu-(1,10-phenanthroline), and tridentate Cu-(2,2':6',2''-terpyridine) are established to be the most stable structure and are observed by experiments. It is surprising to find that the tridentate planar structure of Cu-(2,2':6',2''-terpyridine) changes to a twisted C_s structure upon ionization.

KEYWORDS: ZEKE Spectroscopy, Cu-Organonitrogen, Quantum Chemical Calculations, Spectral Simulation, Metal-Ligand Bonding

Xu Wang

1/14/2007

SPECTROSCOPY AND STRUCTURES OF Cu-ORGANONITROGEN COMPLEXES

By
Xu Wang

Dong-Sheng Yang
Director of Dissertation
Robert B. Grossman
Director of Graduate Studies
1/14/2007

RULES FOR THE USE OF DISSERTATIONS

Unpublished dissertations submitted for the Doctor's degree and deposited in the University of Kentucky Library are as a rule open for inspection, but are to be used only with due regard to the rights of the authors. Bibliographical references may be noted, but quotations or summaries of parts may be published only with the permission of the author, and with the usual scholarly acknowledgements.

Extensive copying or publication of the dissertation in whole or in part also requires the consent of the Dean of the Graduate School of the University of Kentucky.

A library that borrows this dissertation for use by its patrons is expected to secure the signature of each user.

Name

Date

DISSERTATION

Xu Wang

The Graduate School
University of Kentucky
2007

SPECTROSCOPY AND STRUCTURES OF Cu-ORGANONITROGEN COMPLEXES

DISSERTATION

A dissertation submitted in partial fulfillment of the
requirements for the degree of Doctor of Philosophy in the
College of Arts and Sciences
at the University of Kentucky

By

Xu Wang

Lexington, Kentucky

Director: Dr. Dong-Sheng Yang, Professor of Chemistry

Lexington, Kentucky

2007

Copyright © Xu Wang 2007

Dedicated to my wife, Ling, my son, Shawn, my brother and mother, and in memory of my father.

ACKNOWLEDGMENTS

There are many wonderful people to thank for their help in producing this work. My advisor, Dr. Dong-Sheng Yang, has been a mentor and role model in my life. He encouraged me not only to grow as an experimentalist but also as a scientist and an independent thinker. His enthusiasm and earnestness has inspired my long-term career goals. Moreover, his understanding, patience, and most importantly, his friendship have allowed me to accomplish this degree while separated from my family. Thank you, Dr. Yang.

Carrying out this research would not have been possible without the help of Dr. Shenggang Li and Dr. Jason F. Fuller. I thank Shenggang for generously sharing his knowledge in computational chemistry and experimental reasoning. He has cheerfully answered many questions without hesitation. More importantly, he has spent a great deal of time and effort to develop a program package, which has significantly reduced the amount of time required for spectral simulations. In addition to Shenggang, I thank Jason for teaching me how to perform experiments. His willingness and creativity in hardware design and experimental operation has benefited our research efforts very much.

I am also very grateful to one of my best friends, Brad R. Sohnlein. Brad and I entered the chemistry graduate program at the same time, nearly five years ago. During these five years, we endured, together, the oral qualifying exam, the success and failure of many experiments, and the excitement and turmoil of writing a dissertation. We were puzzled over many of the same problems, but worked together to resolve those issues. In addition, Brad has taken every opportunity to improve my English, whether in daily conversation or in my writing. His great friendship and kindness are deeply appreciated. I am also very thankful to other coworkers, including Dr. Yuxiu Lei, Dr. Sergiy Krasnokutski, and Mr. Jung Sup Lee for their help, cooperation, and friendship during the course of my time at UK. Their friendliness has made my academic journey very enjoyable.

I would like to thank Dr. Dennis Clouthier for teaching me the fundamental knowledge through his teachings in class and discussions as one of the members of my dissertation committee. He also collaborated with Shenggang to improve the simulation program package. I would also like to thank the other members of my dissertation committee for their guidance: Dr. John P. Selegue, Dr. Gang Cao, and Dr. Changguo Zhan.

There are no words that can express my gratitude towards my brother and mother. Their love and support at many times helped me to stay on track and keep moving forward. Dad, you always believed in me, even when I sometimes had doubts in myself. You never died in my heart, and I know you will watch over me and always take care of me and my family.

Finally, I am most thankful to my wonderful wife, Ling, and my newborn son, Shawn. I wish I could express in words how much I appreciate their support, understanding, and patience. Being 3000 miles away from my wife and son was extremely difficult, but a motivation that kept pushing me towards the finishing line. My son has shown his patience even though he is only two months old. He often laughs out loud, and that sound through the telephone immediately cheered me up when I was exhausted during this dissertation writing process. This dissertation is primarily dedicated to them.

TABLE OF CONTENTS

ACKNOWLEDGMENTS	iii
TABLE OF CONTENTS	v
LIST OF TABLES	ix
LIST OF FIGURES	xiii
Chapter 1 Introduction	1
1.1 PFI-ZEKE photoelectron spectroscopy	3
1.1.1 Mechanism and history	3
1.1.2 Advantages and applications.....	5
1.2 Experimental methodology	6
1.2.1 Apparatus	6
1.2.2 Preparation of metal complexes in the gas phase	6
1.2.3 Generation and detection of ions and electrons	9
1.2.4 Timing control and data acquisition.....	12
1.3 Computational methodology.....	13
1.3.1 Quantum chemical calculations	13
1.3.1.1 Computational methods	13
1.3.1.2 Computational strategy and procedure	15
1.3.2 Franck-Condon spectral simulations.....	17
1.4 The scope of this dissertation.....	19
Chapter 2 Spectroscopy and structures of copper-diamine complexes.....	26
2.1 Experimental and computational methods.....	27
2.2 Results and discussion	28
2.2.1 Computation.....	28
2.2.1.1 Isomers of free ligands.....	28
2.2.1.2 Isomers of Cu-en.....	31
2.2.1.3 Isomers of Cu-meen, -dmen, -tren, and -tmen	33

2.2.1.4	Isomers of Cu-pn and -bn	34
2.2.2	Spectroscopy	35
2.2.2.1	ZEKE spectra of Cu-en	35
2.2.2.2	ZEKE spectra of Cu-meen	37
2.2.2.3	ZEKE spectra of Cu-dmen	38
2.2.2.4	Photoionization efficiency spectra of Cu-tren and -tmen	39
2.2.2.5	ZEKE spectra of Cu-pn	40
2.2.2.6	ZEKE spectra of Cu-bn	42
2.2.2.7	Comparison of experimental measurements and ab initio calculations	44
2.3	Conclusion	44
Chapter 3	Spectroscopy and structures of copper-(pyridine) _n (n=1,2) complexes	68
3.1	Experimental and computational methods	69
3.2	Results and discussion	70
3.2.1	Cu-pyridine	70
3.2.2	Cu-(pyridine) ₂	73
3.3	Summary of the ZEKE spectroscopic measurements	76
3.4	Conclusion	78
Chapter 4	Spectroscopy and structures of copper-diazine complexes	91
4.1	Experimental and computational methods	92
4.2	Results and discussion	93
4.2.1	Equilibrium structures and vibrational frequencies	93
4.2.1.1	Cu-pyrazine	94
4.2.1.2	Cu-pyrimidine	95
4.2.1.3	Cu-pyridazine	96
4.2.2	ZEKE spectra	97
4.2.2.1	Cu-pyrazine	97
4.2.2.2	Cu-pyrimidine	98

4.2.2.3	Cu-pyridazine.....	100
4.2.3	Ionization and bond dissociation energies	101
4.3	Conclusion	102
Chapter 5	Spectroscopy and structures of copper-aminopyridine complexes	114
5.1	Experimental and computational methods.....	115
5.2	Results and discussion	116
5.2.1	Equilibrium structures and vibrational frequencies	116
5.2.1.1	Cu-4AP	117
5.2.1.2	Cu-3AP	118
5.2.1.3	Cu-2AP	119
5.2	ZEKE spectra and vibrational analysis.....	121
5.2.1	Cu-4AP	121
5.2.2	Cu-3AP	124
5.2.3	Cu-2AP	125
5.3	Ionization energies and vibrational frequencies.....	127
5.4	Conclusion	128
Chapter 6	Spectroscopy and structures of Copper-polypyridine complexes.	140
6.1	Experimental and computational methods.....	143
6.2	Results and discussion	144
6.2.1	Cu-22BIPY	144
6.2.1.1	Theoretical geometries, electronic states and energies	144
6.2.1.2	ZEKE spectroscopy	147
6.2.2	Cu-44BIPY	149
6.2.2.1	Theoretical geometries, electronic states, and energies	149
6.2.2.2	ZEKE spectroscopy	150
6.2.3	Cu-TERPY	151
6.2.3.1	Theoretical geometries, electronic states, and energies	151

6.2.3.2	ZEKE spectroscopy	154
6.2.4	Cu-PHEN	155
6.2.4.1	Theoretical geometries, electronic states, and energies	155
6.2.4.2	ZEKE spectroscopy	156
6.3.	Summary of the ZEKE measurements and theoretical calculations	157
6.4	Conclusion	158
Chapter 7	Spectroscopy and structures of Cu- and Al-imidazole complexes	180
7.1.	Experimental and computational methods	181
7.2.	Ab Initio Calculations	183
7.2.1	Cu-Imidazole	183
7.2.2	Al-Imidazole	184
7.3	ZEKE Spectra	186
7.3.1	Cu-Imidazole	187
7.3.2	Al-Imidazole	188
7.4.	Metal-Ligand Binding in Cu- and Al-Imidazole	191
7.5.	Conclusions	193
Chapter 8	Summary	202
References:	205
VITA	223

LIST OF TABLES

Table 2.1. Relative electronic energies (E_e , kJ mol ⁻¹) and geometries (R, Å; \angle , degrees) of ethylenediamine and methyl-substituted derivatives from MP2/6-311+G(<i>d,p</i>) calculations.	46
Table 2.2. Relative electronic energies (E_e , kJ mol ⁻¹), adiabatic ionization energies (AIE, eV), bond dissociation energies (D_0 , kJ mol ⁻¹), and geometries (R, Å; \angle , degrees) of copper-diamine complexes from MP2/6-311+G(<i>d,p</i>) calculations.....	47
Table 2.3. Adiabatic ionization energies (AIE) of copper-amine complexes from ZEKE spectra.	50
Table 2.4. ZEKE peak positions and assignments of the Cu-en, -meen, and -dimeen complexes.	51
Table 2.5. ZEKE peak positions (cm ⁻¹) and assignments of the Cu-pn complexes.....	52
Table 2.6. ZEKE peak positions (cm ⁻¹) and assignments of the Cu-bn complexes.	53
Table 2.7. Adiabatic ionization energies (AIE, eV) and vibrational frequencies (cm ⁻¹) of Cu-diamine complexes from ZEKE measurements and MP2/6-311+G(<i>d,p</i>) calculations.	54
Table 2.8. Vibrational frequencies (cm ⁻¹) of the observed isomers of Cu-en, -meen, -dmen, -pn, and -bn from MP2/6-311+G(<i>d,p</i>) calculations.	56
Table 3.1. Point groups, electronic states, equilibrium energies (E_e , a.u.), geometries (R, Å; \angle , °), and vibrational frequencies (cm ⁻¹) of the Cu-pyridine σ complexes from the B3P86 and MP2 calculations using 6-311+G(<i>d,p</i>) basis set.....	80
Table 3.2. ZEKE peak positions (cm ⁻¹) and assignments of the Cu-pyridine and -(pyridine) ₂ complexes.....	81
Table 3.3. Point groups, electronic states, energies (a.u.), equilibrium geometries (R, Å; \angle , °), and vibrational frequencies of the eclipsed and staggered isomers of the Cu(pyridine) ₂ complexes from the B3P86 and MP2 calculations using 6-311+G(<i>d,p</i>)	

basis set.....	82
Table 3.4. Adiabatic ionization energies (AIE, cm^{-1}), bond dissociation energies (D_0^+/D_0 , kJ mol^{-1}) and vibrational frequencies (cm^{-1}) of Cu-pyridine and -(pyridine) ₂ from ZEKE measurements and the B3P86 and MP2 calculations using 6-311+G(<i>d,p</i>) basis set.....	85
Table 4.1. Electronic states, equilibrium geometries (\AA , degree), and vibrational frequencies (cm^{-1}) of the Cu-diazine σ -complexes from MP2/6-311+G(<i>d,p</i>) calculations. The N and C atom labeling scheme is depicted in Figure 4.1.	104
Table 4.2. ZEKE peak position (cm^{-1}) and assignment of the Cu-diazine σ -complexes.	106
Table 4.3. Adiabatic ionization energies (AIE, cm^{-1}), metal-ligand bond energies (D_0 , D_0^+ , kJ mol^{-1}), and vibrational frequencies (cm^{-1}) of the Cu-diazine σ -complexes from ZEKE measurements and MP2/6-311+G(<i>d,p</i>) calculations. D_0 and D_0^+ are metal-ligand bond dissociation energies for the neutral and ionic complexes, respectively.	107
Table 5.1. Molecular symmetries, equilibrium geometries (\AA , degree), and vibrational frequencies (cm^{-1}) of the Cu-aminopyridine $\sigma\alpha$ -complexes from MP2/6-311+G(<i>d,p</i>) calculations. The N and C atom labeling scheme is depicted in Figure 5.1.	129
Table 5.2. ZEKE peak positions (cm^{-1}) and assignments of the Cu-aminopyridine complexes.	131
Table 5.3. Adiabatic ionization energies (AIE, cm^{-1}), metal-ligand bond energies (D_0 , D_0^+ , kJ mol^{-1}), and vibrational frequencies (cm^{-1}) of the Cu-aminopyridine σ -complexes from ZEKE measurements and MP2/6-311+G(<i>d,p</i>) calculations.	132
Table 6.1. Point groups, relative energies (E_e , cm^{-1}), geometric structures (R, \AA ; \angle , degree) of 2,2'-bipyridine isomers from B3LYP/6-311+G(<i>d,p</i>) and MP2/6-311+G(<i>d,p</i>) calculations.	160
Table 6.2. Electronic states, point groups, relative energies (E_e and E_0 , cm^{-1}) ^a , bond	

dissociation energies (D_0 , kJ mol^{-1}), and geometric structures (R , \AA ; \angle , degree) of Cu-(2,2-bipyridine) complexes from B3LYP/6-311+G(d,p) and MP2/6-311+G(d,p) calculations.	161
Table 6.3. Peak positions (cm^{-1}) and assignments of the Cu-(2,2'-bipyridine) ZEKE spectrum.....	162
Table 6.4. Electronic states, adiabatic ionization energies (AIE, cm^{-1}), dissociation energies (D_0 , kJ mol^{-1}) and geometric structures (R , \AA ; \angle , degree), of Cu-(4,4'-bipyridine) complexes and free ligand from B3LYP/6-311+G(d,p) and MP2/6-311+G(d,p) calculations.....	163
Table 6.5. Peak positions (cm^{-1}) and assignments of the Cu-(4,4'-bipyridine) ZEKE spectrum.....	164
Table 6.6. Relative energies (kJ mol^{-1}), symmetries, dipole moments, and geometric structures (R , \AA ; \angle , degree) of 2,2':6',2''-terpyridine from B3LYP/6-311+G(d,p) calculations	165
Table 6.7. Relative energies (cm^{-1}), bond dissociation energies (kJ mol^{-1}) and geometries (R , \AA ; \angle , degree) of different binding isomers of Cu-(2,2':6':2''-terpyridine) from B3LYP/6-311+G(d,p) calculations.....	166
Table 6.8. Electronic states and geometries (R , \AA ; \angle , degree) of the tridentate Cu-(2,2':6':2''-terpyridine) from B3LYP/6-311+G(d,p) calculations.....	167
Table 6.9. Peak positions (cm^{-1}) and assignments of the Cu-(2,2':6':2''-terpyridine) ZEKE spectrum.....	168
Table 6.10. Peak positions (cm^{-1}) and assignments of the Cu-(1,10-phenanthroline) ZEKE spectrum.....	169
Table 6.11. Adiabatic ionization energies (AIE, cm^{-1}), metal-ligand bond dissociation energies (D_0 and D_0^+ , kJ mol^{-1}), and vibrational frequencies (cm^{-1}) of the Cu-polypyridine complexes from the ZEKE spectra and calculations.....	170
Table 7.1. Peak positions (cm^{-1}) and assignments for the ZEKE spectra of Cu- and	

Al-imidazole σ complexes.....	194
Table 7.2. Adiabatic ionization energies (AIE, cm^{-1}), metal-ligand bond dissociation energies (D_0 and D_0^+ , kJ mol^{-1}), and vibrational frequencies (cm^{-1}) of Cu- and Al-imidazole σ complexes from the ZEKE spectra and MP2/6-311+G(<i>d,p</i>) calculations. D_0 and D_0^+ are metal-ligand bond dissociation energies of the neutral and ionic complexes, respectively.....	195
Table 8.1. Adiabatic ionization energies (AIE, cm^{-1}) and Cu^+ -ligand stretching frequencies of the Cu-complexes from ZEKE measurements. The experimental AIEs have an uncertainty of $\sim 5 \text{ cm}^{-1}$. The Cu^+ -ligand stretching vibrations are largely characterized by Cu displacements.....	204

LIST OF FIGURES

Figure 1.1. Schematic for generating ZEKE electrons.	21
Figure 1.2. Schematic of the copper oven used to vaporize solid ligands.	22
Figure 1.3. Schematic diagram of the PFI-ZEKE spectrometer. DP: oil diffusion pump; TP: turbo molecular pump; VL: vaporization laser; FDDL: frequency-doubled dye laser; MCP: microchannel plate detector.	23
Figure 1.4. Schematic diagrams of the voltage divider circuits for ion (a) and electron (b) detection.	24
Figure 1.5. Schematic of the trigger sequence. GA: gated integrator; ADC: analog-to-digital adapter. The timing sequence in the dashed square box is applied when a Nd:YAG laser is used for pumping the dye laser.	25
Figure 2.1. Low-energy rotational isomers of ethylenediamine.	58
Figure 2.2. CH \cdots N hydrogen-bonded isomers of N,N,N' -trimethylethylenediamine (a) and N,N,N' ,N' -tetramethylethylenediamine (b).	59
Figure 2.3. Low-energy rotational isomers of 1,3-propanediamine (a) and 1,4-butanediamine (b).	60
Figure 2.4. Rotational isomers of Cu-ethylenediamine.	61
Figure 2.5. Experimental ZEKE spectrum of Cu-ethylenediamine and simulations of four Cu-ethylenediamine isomers (b) - (e).	62
Figure 2.6. Experimental ZEKE spectrum of Cu-(N-methylethylenediamine) (a) and simulations of five Cu-(N-methylethylenediamine) isomers (b) - (f).	63
Figure 2.7. Experimental ZEKE spectrum of Cu-(N,N-dimethylethylenediamine) (a) and simulations of five Cu-(N,N-dimethylethylenediamine) isomers (b) - (f).	64
Figure 2.8. Photoionization efficiency spectra of Cu-(N,N,N'-trimethylethylenediamine) (a) and -(N,N,N',N'-tetramethylethylenediamine) (b).	65
Figure 2.9. Experimental ZEKE spectrum and simulations from H-bond I (b), H-bond II	

(c), Ring (d), Trans (e), and a mixture of H-bond I and II (f) isomers of Cu-(1,3-propanediamine).....	66
Figure 2.10. Experimental ZEKE spectrum (a) and simulations (20 K) from H-bond I (b), H-bond II (c), Ring (d), Trans (e), and a mixture of H-bond I and II (f) isomers of Cu-(1,4-butanediamine).....	67
Figure 3.1. Structure of pyridine from B3P86/6-311+G(<i>d,p</i>) and MP2/6-311+G(<i>d,p</i>) (in parenthesis) calculations: bond lengths, Å, bond angles, °.....	86
Figure 3.2. ZEKE spectrum of Cu-pyridine seeded in helium (a) and simulations from B3P86 (b) and MP2 (c) calculations at 60 K. The peak with asterisk is a Cu atomic transition.	87
Figure 3.3. ZEKE spectrum of Cu-pyridine seeded in argon (a) and MP2 simulation at 5 K (b). The peak with an asterisk is a Cu atomic transition.	88
Figure 3.4. Experimental ZEKE spectrum of Cu-(pyridine) ₂ and simulations (80 K) of the D _{2h} structures from B3P86 (b) and MP2 calculations (c) and the D _{2d} structure from MP2 calculations (d).	89
Figure 3.5. Eclipsed and staggered structures of Cu-(pyridine) ₂	90
Figure 4.1. Structures and permanent electric dipole moments of diazine molecules from MP2/6-311+G(<i>d,p</i>) calculations. Bond distances are in Angstrom, and bond angles are in degrees. The dipole moments in parentheses are experimental values from reference [207].	108
Figure 4.2. Structural isomers and relative electronic energies of Cu-pyrazine (a), -pyrimidine (b), and -pyridazine (c) from MP2/6-311+G(<i>d,p</i>) calculations. Bond distances are in Angstrom. The atomic labeling of the diazine molecules is the same as that in Figure 4.1.	109
Figure 4.3. ZEKE spectrum of Cu-pyrazine seeded in helium (a) and simulation (b) of the σ-complex at 80 K. Peaks with asterisks are Cu atomic transitions.	110
Figure 4.4. ZEKE spectrum of Cu-pyrimidine seeded in helium (a) and simulations of	

the σ - (b) and π - (c) complexes at 80 K. Peaks with asterisks are Cu atomic transitions.....	111
Figure 4.5. ZEKE spectrum of Cu-pyrimidine seeded in a 1:2 Ar/He mixture (a) and simulation (b) of the σ -complex at 20 K.	112
Figure 4.6. ZEKE spectrum of Cu-pyridazine seeded in helium (a) and simulation (b) of the σ -complex at 80 K.	113
Figure 5.1. Structures of 4- (a), 3- (b), and 2- (c) aminopyridine from MP2/6-311+G(<i>d,p</i>) calculations. The bond distances are in angstroms and the bond angles are in degrees.	133
Figure 5.2. Structural isomers and relative electronic energies, adiabatic ionization energies (AIE) and bond dissociation energies (D_0) of Cu-(4-aminopyridine) (a), -(3-aminopyridine) (b), and -(2-aminopyridine) (c) from MP2/6-311+G(<i>d,p</i>) calculations. The bond distances are in angstroms; for σ -complexes the Cu-N distance is given, while for π -complexes the vertical Cu-ring distance is given.....	134
Figure 5.3. Experimental ZEKE spectrum of Cu-(4-aminopyridine) seeded in helium (a) and simulations of the σ_α (b) and σ_β (c) complexes at 50 K, except for the neutral Cu-4AP stretching mode where 150 K was specified.....	135
Figure 5.4. Experimental ZEKE spectrum of Cu-(4-aminopyridine) seeded in argon (a) and simulations of the σ_α (b) and σ_β (c) complexes at 10 K.	136
Figure 5.5. Experimental ZEKE spectrum of Cu-(3-aminopyridine) seeded in helium (a) and simulations of the σ_α (b), σ_β (c) and π (d) complexes at 60 K, except for the neutral Cu-3AP stretching mode where 150 K was specified.	137
Figure 5.6. Experimental ZEKE spectrum of Cu-(3-aminopyridine) seeded in argon (a) and simulations of the σ_α (b), σ_β (c) and π complexes at 10 K.	138
Figure 5.7. Experimental ZEKE spectrum of Cu-(2-aminopyridine) seeded in the 1:1 mixture of helium and argon.....	139
Figure 6.1. Structures of 2,2'-bipyridine (a), 4,4'-bipyridine (b), 2,2':6',2''-terpyridine	

(c), and 1,10-phenanthroline (d).	171
Figure 6.2. Stable rotational isomers of the trans (a) and cis (b) 2,2'-bipyridine.....	172
Figure 6.3. Isomers of Cu-(2,2'-bipyridine).	173
Figure 6.4. ZEKE spectrum of Cu-22BIPY seeded in Ar (a) and simulations of the cis (b) and trans (c) structures obtained by B3LYP calculations and the simulation (d) of the cis structure at 20 K obtained by MP2 calculations.	174
Figure 6.5. ZEKE spectrum of Cu-44BIPY seeded in 1:1 Ar/He mixture gas (a) and simulations from the B3LYP (b) and MP2 (c) at 20 K calculations.	175
Figure 6.6. Potential energy surface for TERPY with respect to the rotation angles (ϕ' and ϕ'') among three pyridine rings calculated at the B3LYP/6-311+G(<i>d,p</i>) level of theory. Energies are relative to the global minimum.	176
Figure 6.7. ZEKE spectrum of Cu-(2,2':6'',2-terpyridine) seeded in He (a) and spectral simulations of the T (b), M _I (c), M _{II} (d), M _{III} (e), and B (f) complexes at 50K (b) from the B3LYP/6-311+G(<i>d,p</i>) calculations.....	177
Figure 6.8. Bidentate and π bonding structures of Cu-(1,10-phenanthroline) from B3LYP/6-311+G(<i>d,p</i>) calculations. Bond distances are in angstrom. AIE, adiabatic ionization energy; D ₀ , metal-ligand bond dissociation energy.	178
Figure 6.9. ZEKE spectrum of Cu-1,10-phenanthroline seeded in Ar (a) and spectral simulation at 20 K (b) from the B3LYP/6-311+G(<i>d,p</i>) calculations.....	179
Figure 7.1. Structure of imidazole from MP2/6-311+G(<i>d,p</i>) calculations. Bond distances are in angstrom, and bond angles are in degrees. This molecule has a permanent electric dipole moment of 3.8 D (Ref. ²⁰⁷).	196
Figure 7.2. σ and π structures of Cu-imidazole (a) and Al-imidazole (b) from MP2/6-311+G(<i>d,p</i>) calculations. Bond distances are in angstrom. AIE, adiabatic ionization energy; D ₀ , metal-ligand bond dissociation energy.....	197
Figure 7.3. ZEKE spectrum of Cu-imidazole seeded in helium (a) and simulations of the ¹ A' ← ² A' transition of the σ structure (b) and the ¹ A ← ² A transition of the π	

structure (c) at 80 K.	198
Figure 7.4. ZEKE spectrum of Cu-imidazole seeded in argon (a) and simulations of the $^1A' \leftarrow ^2A'$ transition of the σ structure (b) and the $^1A \leftarrow ^2A$ transition of the π structure (c) at 10 K.	199
Figure 7.5. ZEKE spectrum of Al-imidazole seeded in helium (a) and simulations of the $^1A' \leftarrow ^2A'$ (b) and $^1A' \leftarrow ^2A''$ (c) transitions of the σ structure at 80 K.	200
Figure 7.6. ZEKE spectrum of Al-imidazole seeded in argon (a) and simulations of the $^1A' \leftarrow ^2A'$ (b) and $^1A' \leftarrow ^2A''$ (c) transitions of the σ structure at 10 K.	201

Chapter 1 Introduction

Metal-ligand weak interactions are known to play a profound role in supramolecular chemistry,¹⁻⁸ biochemistry,⁹⁻¹⁶ catalysis,^{8,17-25} and environmental science.^{9,11,14,15,26} In the last 20 years, supramolecular chemistry has been considered to be a rapid growing branch for developing new materials by assembling various molecular blocks and metal ions.³ Detailed investigation of the structures and formations of supramolecular systems becomes crucial to make these assemblies suitable for applications as functional materials. Metal ions play essential roles in about 30% of enzymes.²⁷ Protein-bound metal sites can be classified into five types: structural, storage, electron transfer, di-oxygen binding and catalytic functions.^{16,28} Insights into the electronic and geometric structures are important for understanding reaction mechanisms of these metal containing active sites in biology. Metal compounds are widely used as catalysts in numerous industrial processes, such as hydrogenation, carbonylation, and the low-pressure polymerization of ethylene and propene.²⁹ Those catalytic dynamics and regio- and stereoselectivity are controlled by the reactivities of metal centers with different organic molecules through metal-ligand bonding interactions.^{1,17,22,25} In addition, several metal ions are present in the atmosphere, water, and soil environments.³⁰ Therefore, it can be imagined that metal-ligand interactions are present everywhere in our world, and it is valuable to explore how such interactions affect the environment from a chemistry viewpoint.

Nitrogen is the fourth most abundant element in living systems next to carbon, hydrogen, and oxygen.²⁷ Nitrogen-containing organic compounds are found in the cells of all living plants and animals. Nitrogen is present in many vitamins and hormones, amino acids, proteins, and nucleotides. In addition, many nitrogen-containing

compounds are used as industrial products such as nylon, dyes, explosives, and pharmaceutical agents.

Copper is a transition metal belonging to group 11 in the periodic table and has a $3d^{10}4s^1$ valence electron configuration. Copper plays an important role in organisms as one of the so-called “essential” metals.^{11,27} In these systems, copper acts as part of the active site of proteins or enzymes. Copper complexes are important as catalysts in organic synthesis. In transition metal-promoted reactions of carbon-centered radicals, Cu (I) follows a reductive process to produce carbon-centered radicals.³¹ Cu (I) halide complexes with bidentate and polydentate amines are very useful catalysts for atom transfer radical polymerization.³² The ubiquitous Cu-organonitrogen complexes and their extensive applications have inspired much interest in the bonding, structures, and properties of Cu and nitrogen containing molecules. This dissertation presents a systematic study of the metal-ligand binding interaction in Cu-organonitrogen complexes.

There have been numerous experimental investigations of the bonding interactions, energies, and structures of Cu complexes and clusters. Some of these studies include photodissociation,³³⁻⁴¹ laser induced fluorescence (LIF) spectroscopy,⁴²⁻⁴⁵ threshold collision-induced dissociation (CID),^{37,38,46-48} neutralization-reionization mass spectrometry,⁴⁹⁻⁵³ matrix-isolation electron spin resonance (ESR)⁵⁴⁻⁶³ spectroscopy, photoelectron (PES) spectroscopy,⁶⁴⁻⁷¹ resonant two-photon ionization (R2PI) spectroscopy, and infrared (IR) spectroscopy.^{72,73} Although much information about Cu complexes have been obtained by these measurements, these techniques have limitations from a spectroscopy point of view. Conventional PES measurements provide poor spectral resolution for studying vibrations and structures of metal complexes. LIF spectroscopy has higher resolution, but lacks mass-selectivity. Although photodissociation spectroscopy has the advantage of mass-selectivity, the spectral resolution is typically inferior to the LIF and R2PI spectroscopies. The bonding modes of some metal complexes have been predicted by combining theoretical calculations with

equilibrium mass spectrometry, radiative association, CID, or LIF experiments, but no spectroscopic evidence has been reported for these Cu systems. In addition, very little is known about the thermodynamics of neutral species. In the last 20 years, pulsed-field ionization-zero electron kinetic energy spectroscopy (PFI-ZEKE) has been employed as a powerful technique to study weakly-bond metal-ligand complexes.⁷⁴ In our lab, we have successfully used this technique to investigate the electronic states, molecular structures, metal-ligand bond strengths, and metal-ligand vibrations of many transition metal complexes in the gas phase.⁷⁵⁻⁹⁴

1.1 PFI-ZEKE photoelectron spectroscopy

1.1.1 Mechanism and history

About 40 years ago, Turner et al, for the first time, measured the electronic energy levels of molecular systems by ultraviolet (UV) PES spectroscopy.⁹⁵ In this technique, the energy of a photon is used to photoionize a molecule from the initial neutral state to a final ionic state with an electron ejected: $M + h\nu \rightarrow M^+ + e^-$. The excess energy is transformed into the kinetic energy (KE) of the emitted electron. Hence, the energy difference between the initial neutral state and the final ionic state can be expressed as the energy of the incident photon minus the kinetic energy of the emitted electron. The first ionization energy of a molecule is thus the minimum energy required to ionize its neutral ground state to its ion ground state. Furthermore, according to Koopman's theorem, the ionization energy of a one-electron molecular orbital of the neutral molecule equals the negative of the orbital energy of that orbital. Therefore, the molecular orbital energy levels can be obtained from a photoelectron spectrum.⁹⁶ In conventional PES, photoelectrons are ejected using fixed-wavelength radiation. This technique has been widely used, as it is relatively easy to implement experimentally. However, the spectral

resolution of conventional PES is limited due to the difficulties in separating kinetic electrons with small energy differences and the electronic disturbance from surface potentials of the metal spectrometer. Consequently, vibrational levels are scarcely resolved in the conventional photoelectron spectra of metal complexes.

In order to improve the spectral resolution, a different approach called ZEKE photoelectron spectroscopy was developed using a tunable photon source.⁹⁷ In ZEKE spectroscopy, the photon energy is tuned across various ionization thresholds, and only photoelectrons emitted with zero electron kinetic energy are detected. Hence, energies of ionization thresholds equal incident photon energies. In principle, the resolution of ZEKE measurement is only limited by the bandwidth of the photon source. In practice, the ZEKE spectra of metal complexes have a resolution better than a few wavenumbers.⁹⁸

There are two ways to implement the ZEKE technique. One method is to generate ZEKE electrons directly via threshold photoionization of the molecule, and the other method is to generate the ZEKE electrons by delayed PFI of Rydberg states. In this dissertation, the time-delayed PFI approach is employed. The time delay is used to discriminate against the electrons produced from direct ionization.^{99,100} In this method high-lying ($n > 150$) Rydberg states are produced, which have unexpected long lifetimes.^{97,101,102} Neutral molecules are first photoexcited to high-lying Rydberg states that converge to various eigenstates of the ions. After a few micro-seconds delay, a small electric pulse is applied to remove the Rydberg electrons from the ionic cores. Stray fields inside the apparatus cause the free ZEKE electrons produced by direct photoionization to move during the time delay, but they have no effects on the ZEKE Rydberg states. Therefore, the delayed field ionization has high efficiency for collecting ZEKE electrons. ZEKE electrons from PFI of these Rydberg states converging to various thresholds carry, in principle, the same information as that from direct photoionization. A slight energy correction induced by the delayed field may need to be considered for calibrating a ZEKE spectrum. This energy shift is calculated by $\delta = CE_p^{1/2}$, where δ is

in cm^{-1} and E_p is in V cm^{-1} . The constant C can be determined by measuring the ZEKE signals at various electric fields. PFI-ZEKE has been used as the most powerful variant of ZEKE spectroscopy.⁹⁸

1.1.2 Advantages and applications

Over the last two decades, ZEKE spectroscopy has been widely used to obtain ionization energies (IEs), vibrational and rotational levels, molecular conformations, and electronic states of numerous molecules and complexes. No doubt, the most significant advantage of PFI-ZEKE is its superior spectral resolution compared to conventional PES methods. PFI-ZEKE PES probes fully-resolved vibrational structures of metal complexes with line widths less than 1 meV ⁹⁸ and rotationally resolved structures of small molecules.⁷⁴ Since the IEs of many metal compounds are in the spectral region easily accessible by frequency-doubled tunable dye lasers, ZEKE spectroscopy has extensive applications for a wide range of metal complexes. The harmonic vibrational frequencies, anharmonicities, and coupling constants of low frequency metal-ligand vibrations can be determined from the vibrational levels of the cation. In addition, binding information about the neutral metal complexes may be determined using ZEKE spectroscopy. For example, some neutral vibrational modes are sufficiently small and may be thermally populated at room temperature and measured by the ZEKE experiment. Given the bond dissociation energy (BDE) of the ionic complex (D_0^+), that of the neutral complex (D_0) can be calculated through a thermodynamic cycle: $AIE(M) - AIE(M-L) = D_0^+(M-L) - D_0(M-L)$, where $D_0^+(M-L)$ and $D_0(M-L)$ are the bond energies of the ionic and neutral complexes, and AIE (M) and AIE (M-L) are the adiabatic ionization energies of the metal and complex. Furthermore, the molecular conformations and electronic states of both ionic and neutral metal complexes can be determined by combining ZEKE measurements with quantum chemical calculations and

spectral simulations.

1.2 Experimental methodology

1.2.1 Apparatus

The experiments were performed with a home-built metal cluster beam ZEKE spectrometer. The schematic of the apparatus is shown in Fig. 1.1. It consists of two vacuum chambers, several vacuum pumps, and various electronic devices. The first chamber houses the metal cluster source and, thus, is termed the source chamber hereafter. The second chamber houses the ZEKE spectrometer and is called the detector chamber. A gate valve is used to separate the two chambers and protect the detector from an unexpected high pressure in the source chamber. The ZEKE spectrometer is a two-field, space-focused, Wiley-McLaren time-of-flight (TOF) mass spectrometer.¹⁰³ It consists of a two-stage extraction assembly, a 34 cm long flight tube, and a dual microchannel plate (MCP) detector (Galileo). The entire spectrometer is housed in a cylindrical, double-walled, μ -metal shield to isolate it from the earth's magnetic field.

1.2.2 Preparation of metal complexes in the gas phase

Metal complexes are prepared by reactions of laser vaporized metal atoms and organic ligands in the source chamber. Metal atoms are produced by pulsed laser vaporization of a metal rod in the presence of a carrier gas. Gas phase ligands are pre-mixed with the carrier gas and supersonically expand into the vacuum. However, for ligands in the liquid or solid state, an outside-pickup source (shown in Figure 1.1) or an oven design (Figure 1.2) is used to obtain enough vapor of the ligand. This ligand vapor is introduced downstream of the ablation and interacts with the metal atoms entrained in the carrier gas.

The cluster source is housed in the 11-inch cubic chamber (Figure 1.1). The source chamber is pumped by a 2200 L/s oil diffusion pump (DP, Edwards, Diffstak 250/2000M) backed by a 40 L/s mechanical rotary pump (Edwards, E2M40). A butterfly valve is used to separate and protect the source chamber from the oil diffusion pump. The pressure inside the source chamber is measured by an active inverted magnetron gauge (SG-II; Edwards, AIM-S-NW25), and the foreline pressure is measured by a linear active pirani gauge (SG-I; Edwards, AGP-M-NW16). In order to protect the spectroscopy chamber, the source chamber is isolated from the spectroscopy chamber by a gate valve (MDC, GV-1500V-P) except when experimental measurements are in progress. The gate valve can be opened and closed manually by an electric switch or controlled by a pressure set point via the SG-II gauge. A nitrogen gas line is connected to both vacuum chambers to facilitate their occasional opening by increasing the internal pressure to that of the atmosphere. To open the source chamber, all the gas lines and pumps need to be isolated; the power of the gate valve should be unplugged. To evacuate the source chamber, first use the rotary pump to evacuate the chamber till the SG-I gauge reaches 7.5×10^{-3} torr. Then turn off the vacuum failure protection, isolate the rotary pump from the chamber, and switch it back to the foreline. Finally, open the butterfly valve to pump the chamber with the diffusion pump. After ~ 15 minutes of pumping, the source chamber should have a base pressure on the order of 10^{-6} Torr. The operating pressure is in the range of $\sim 10^{-4}$ to 10^{-6} Torr, which varies according to the gas pulse width, backing pressure of the carrier gas, and vapor pressure of the ligand.

The second harmonic output (532 nm) of a neodymium-doped yttrium aluminum garnet (Nd:YAG) laser (Quanta-Ray, GCR3) with a laser pulse energy of 4 mJ is used as the vaporization laser to produce metal atoms. In principle, the vaporization laser power should be kept as low as possible to minimize the plasma formation. However, in practice, the laser may need to be focused on the surface of the metal rod by a 30 cm focal length lens. The focus of the laser is easily adjusted by moving the lens back and

forth to optimize the production of metal complexes. Moreover, the laser beam needs to be aligned. The criterion of a good alignment is that while translating the lens back and forth the laser beam should always penetrate the pin hole of the faceplate without any blockage. The metal rod is held by a micromotor (Micro Mo Electronics, 1516E012S), which allows for simultaneous rotation and translation of the rod to ensure that each laser pulse ablates a fresh metal surface. It is not necessary to clean the metal rod with sandpaper or steel wool. Using soap or a small amount methanol will do the job. Metal oxides on the surface may be removed by laser ablation.

The carrier gas is delivered to the source chamber by a home-built piezoelectric pulsed valve. This valve assembly is mounted on the wall of the source chamber and isolated from the vacuum when it is not in use. The carrier gas can be helium or argon (Scott-Gross, ultrahigh purity), or a mixture of the two at 40 ~ 60 psi backing pressure. The backing pressure needs to be optimized to maximize the signal of the desired complex. In this work, no gas phase ligand was involved. For the pick-up source used for liquid ligands, the compound was stored in a glass bottle, and the flow of ligand vapor was controlled manually by a needle valve. The ligand vapor is introduced to a small reaction chamber (~ 1.5 mL) by a stainless steel capillary down stream from the ablation. In this collision cell, the organic molecules interact with the metal atoms entrained in the carrier gas. For a liquid ligand with low vapor pressure at room temperature, the pick-up source and the faceplate were heated to an appropriate temperature in order to obtain enough vapor. The oven used for vaporizing solid ligands is made of copper, a good thermo-conductor. During the experiment, the ligand is stored in the lower-end compartment of the oven. The oven is heated by a heating cartridge (Figure 1.2) and controlled by a thermo-controller (Omega CN2110). Along with this oven design, a copper water cooling tube is bound to the shell of the pulsed valve to protect the valve from over heating. The mixture of metal atoms, ligand vapor, and carrier gas passes through a clustering tube (2 mm inner diameter, 3 cm length) to facilitate the formation of

complexes. The resultant complexes are supersonically expanded into high vacuum. During this process, the rotational and vibrational internal energies of the complexes are converted into translational energies. Consequently, the metal complexes will have much lower internal temperatures. Thus, the supersonic expansion technique reduces the spectral congestion and improves the spectral resolution. A few centimeters downstream from the clustering tube, the molecular beam is collimated by a 4 mm diameter homemade skimmer. The signal size may be increased by reducing the distance between the clustering tube and the skimmer. A pair of charged deflection plates, with 300 ~ 500 V from a DC high voltage power supplier (Stanford, PS325), is placed right after the skimmer to remove residual ionic species from the molecular beam. Thus, only neutral molecules enter the spectroscopy chamber.

1.2.3 Generation and detection of ions and electrons

TOF mass spectrometry is employed to identify the desired metal complex. The ionization threshold of the metal complex is located by recording the ion signal as a function of the laser wavelength. The 0-0 band of ZEKE signal is searched around the ionization threshold, and the ZEKE spectrum is recorded as a function of the laser wavelength.

The spectroscopy chamber is a six-way cross of 6-inch diameter tubes and houses a 13-inch long TOF mass spectrometer (Figure 1.1). This chamber is pumped by two 400 L/s turbomolecular pumps (Seiko Seiki, STP-400), and these turbomolecular pumps share a foreline mechanical rotary pump (Edwards, E2M40). To protect the vacuum system, gate valves are located at each of the turbo pump inlets. An ionization gauge (SG-III; Varian, 571) is used to measure the pressure inside the chamber, and a liner active pirani gauge (SG-IV; Edwards, APG-L-NW16) is used to measure the pressure in the foreline. To start the turbo pumps from atmospheric pressure, the protection switch must be turned

off, and the gate valves must be opened. Then, the backing pump is used to evacuate the chamber directly. As the pressure drops, the turbo pumps are started. After the turbomolecular pumps reach full speed, the protection switch is turned back on. If the pressure in the foreline reaches 7.5×10^{-3} Torr, the two gate valves will be shut off automatically to prevent backstreaming. A high-purity nitrogen gas line is connected to the chamber for venting. It should be emphasized that the vacuum must be vented through the nitrogen gas line.

In the ZEKE spectrometer, a DC voltage is applied on two cylindrical metal cans for ion extraction, while a pulsed electric field is used for electron generation and extraction. A MCP detector is housed in another cylindrical metal can to detect both ions and electrons. In order to generate more homogeneous electric field, fine grids of gold wires are attached on the extraction cans, flight tube, and detector housing. The entire spectrometer is encased by a cylindrical, double-walled, μ -metal shield to isolate it from the earth's magnetic field. All electronic connections are made through BNC (Bayonet Neill Concelman) or SHV (safety high voltage) coaxial connectors welded on the flange at the top of the TOF spectrometer. Two 1-inch diameter quartz windows are located at two sides of the chamber along the axis perpendicular to the flight tube and the molecular beam in order to allow the photoionization laser beam to pass through the chamber.

The supersonic molecular beam crosses with the pulsed UV laser beam at the center of the spectroscopy chamber. The output of a tunable dye laser (Lumonics, HD500) is frequency-doubled by a beta-barium borate (BBO) crystal and used as the photoionization laser. A XeCl excimer laser (308 nm, ~ 400 mJ, Lumonics, PM884) is employed to pump the dye laser to generate a tunable wavelength range of 220-355 nm with pulsed energies of 0.5 \sim 2.0 mJ. To generate laser wavelengths shorter than 220 nm with higher pulsed energy (0.4 \sim 1.5 mJ), the third harmonic output (355 nm) of a Nd:YAG laser (~ 180 mJ, Continuum, surelite-III) is used as the pump laser. The beam size of the ionization laser is adjustable through a telescope. Ions produced by

photoionization are extracted and accelerated to the detector by the electric field formed between the inner and outer extraction cans. +2500 and +1700 V potentials are applied on the outer and inner cans, respectively. These voltages are provided by two DC power suppliers (Stanford Research Systems, PS350) to generate a 320 V cm^{-1} electric field in the ionization region. The MCP detector consists of two microchannel plates with angled channels rotated 180° from each other producing a chevron (v-like) shape. Once an accelerated electron enters and hits the wall of one microchannel plate, a large number of secondary electrons are generated and accelerated by the electric field applied across both ends of the MCP. This process is repeated many times along the channel; consequently, this cascade process yields more and more secondary electrons (up to several orders) emerging from the rear of the plate. This electron amplification process repeats in the second plate. Voltages applied on the MCPs are supplied by a voltage divider circuit shown in Figure 1.4 and a DC power supplier (Stanford Research Systems, PS350). A higher voltage has a larger production of secondary electron and a stronger amplification. However, due to a 1 kV threshold, a typical negative voltage of $\sim -900 \text{ V}$ is applied on the each MCP for a strong amplification.

According to the fundamentals of TOF mass spectrometry, ionic species with different masses can be distinguished by their flight times. Referring to the flight time of a known ion, the masses of those ionic species can be easily calculated. A mass spectrum is recorded with a laboratory computer and monitored by an oscilloscope. A photoionization efficiency (PIE) spectrum is recorded by measuring the mass-selected ion signal with the UV laser scanned across the ionization threshold. The onset in a PIE spectrum corresponds to the ionization energy of the neutral molecule. The ionization threshold measured by PIE spectroscopy may have a large error due to a slowly rising onset. Vibrational levels are hardly resolved by the PIE measurements due to the poor spectral resolution and interference from auto-ionization. Moreover, the electric field applied on the photoionization region induces a reduction of the ionization threshold,

which is given by $6.1 \cdot \sqrt{E}$, where E is the electric field strength in V cm^{-1} . A $\sim 110 \text{ cm}^{-1}$ correction is calculated from the 320 V cm^{-1} field used in our measurements.

Figure 1.3 shows a schematic of the ZEKE electron generation. In the intersection region of the molecular beam and the UV laser beam, metal complexes are first photoexcited to high-lying Rydberg states ($n > \sim 150$). This region is a few mm before the spectrometer center. After a time delay of $\sim 3.0 \mu\text{s}$, a -1.2 V cm^{-1} pulsed electric field is applied to the outer can for 100 ns to ionize those high-lying Rydberg states. During the time delay, a small DC field of -0.08 V cm^{-1} is applied to the outer can to help remove electrons produced from direct photoionization. Both the ionization field and the small DC field are provided by a pulsed digital delay generator (Stanford, DG535). The ZEKE electrons are also extracted and accelerated by the same ionization field by a voltage of +5 V applied to the TOF tube. In order to detect electrons, a different voltage divider circuit is used for the MCP detector (Figure 1.4), and a typical positive voltage of +2050 V is used for an optimized signal-noise ratio. A ZEKE spectrum is recorded by scanning the laser wavelength from a few hundred cm^{-1} below the ionization threshold to a shorter wavelength where no further ZEKE signal may be observed.

1.2.4 Timing control and data acquisition

In a pulsed experiment, the timing sequence is critical. In our experiments, gas, laser, and electronic pulses all must be synchronized. Figure 1.5 shows the typical trigger sequence for the spectroscopy measurement obtained by experimental testing. This sequence is controlled by two pulsed digital delay generators (Stanford Research Systems DG535). Due to a longer operation time of the piezoelectric pulsed valve, the flash lamp of the vaporization Nd:YAG laser is triggered $\sim 200 \mu\text{s}$ after the pulsed valve is triggered. Since the outputs of the excimer and dye lasers have almost no delay, they are triggered simultaneously with the oscilloscope, gated integrator (Stanford, SR250),

and analog-to-digital converter (ADC), $\sim 550 \mu\text{s}$ ($\sim 900 \mu\text{s}$ with argon carrier gas) after the flash lamp of the vaporization laser is triggered. The timing sequence is repeated at a frequency of 10 Hz. If a Nd:YAG laser is used to pump the dye laser, it should be triggered $\sim 200 \mu\text{s}$ before the data acquisition devices because of the delay between the laser output and the trigger. In ZEKE experiments, a $\sim 3 \mu\text{s}$ time delay is used prior to the application of the pulsed electric field. A preamplifier (Stanford Research Systems, SR445) is used to amplify the signal from the MCP detector up to 5^4 times. The amplified signal is averaged over 30 shots per data point by the gated integrator. The averaged signal is fed to the oscilloscope for monitoring and collected by a computer. As the computer can only process digital signals, the analog signal is digitized by a data acquisition (DAQ) board (National Instruments, Lab-PC+) plugged into the computer. A home-made adapter is connected between the boxcar integrator and the DAQ device, and triggered by the pulsed delay generator. The program used to record spectra is named HDZEKECM and runs on the DOS (Microsoft) operating system. The computer also controls the scan of the dye laser through a home-made 9-pin to 25 pin RS-232 adapter. The oscilloscope is also connected to the computer by a general purpose interface board (National Instruments, AT-GPIB) and a GPIB cable, using a program called TEK320 to record mass spectra.

1.3 Computational methodology

1.3.1 Quantum chemical calculations

1.3.1.1 Computational methods

With a rapid growth in CPU speed, quantum chemical calculations using available program packages have become increasingly more sophisticated and valuable for predicting, modeling, and understanding experimental measurements. Quantum

chemical calculations can provide quite reliable results about molecular geometries, energies, electronic states, vibrational frequencies, and reaction dynamics. In our work, theoretical calculations are employed to predict the molecular structures, electronic states, bond strengths, and vibrational frequencies of the neutral and ionic metal complexes as well as the AIEs of the neutral metal complexes.

The Hartree-Fock (HF) method has been widely used to solve problems from small- to medium-sized molecules.¹⁰⁴ However, as HF theory neglects electron correlation, it has been recognized that the HF method is not always reliable for describing many molecular systems. A number of so-called post-Hartree-Fock methods have been devised to improve theoretical results by including electron correlation to the multi-electron wave function. One of these approaches, Møller-Plesset (MP) perturbation theory, treats electron correlation as a perturbation of the HF function.¹⁰⁵ In this theory, the energy of the system is expanded as:

$$E = E_0 + \lambda E_1 + \lambda^2 E_2 + \dots + \lambda^n E_n \quad (1.1)$$

where E_n are the n th order corrections to the energy. In this work, the second order MP method (MP2) is used in the theoretical calculations, as it yields good predictions for the Cu complexes. In addition to the MP2 method, the MP3 and MP4 methods include higher order energy corrections. However, the MP3 method yields little improvement, and both MP3 and MP4 methods are much more expensive. Therefore, we mainly used the MP2 method for the theoretical calculations in this work.

Although the MP2 method is successful in studying Cu organonitrogen complexes and has an acceptable computational efficiency for these relatively large molecules, MP2 calculations with small basis sets are of little practical value, and a large basis set is needed to yield meaningful results. In our work, all the calculations are carried out with 6-311+G(d,p) or larger basis sets. The geometry optimization by the MP2 method is usually started from an optimized structure obtained from faster density functional theory (DFT) calculations.

In addition to MP2 calculations, some complexes were investigated by DFT. DFT methods are different from the wavefunction-based ab initio methods where the energy of an electronic system is expressed in terms of its electron density. DFT methods have a lower computational cost and a wider range of applications. Although there have been some concerns about the accuracy and reliability of DFT, these calculations have become very popular in modeling various types of molecular systems¹⁰⁶⁻¹¹² and have yielded reasonable agreement with the experimental results.

1.3.1.2 Computational strategy and procedure

In this work, both MP2 and DFT calculations were performed with the GAUSSIAN 2003 program package¹¹³ installed on the supercomputer in the Computational Center at the University of Kentucky. In the DFT calculations, Becke's three parameter hybrid exchange functional (B3)¹¹⁴ was combined with the gradient-corrected correlation functional of Perdew (P86)^{115,116} or Lee, Yang and Parr (LYP).¹¹⁷ Pople's triple zeta basis set with polarization and diffuse functions, 6-311+G(*d,p*), was used in most calculations.¹⁰⁴ Electron density maps were generated and vibrational modes were identified with GaussView 3.09.¹¹⁸ AIEs were calculated to be the energy difference between the ionic and neutral complexes, where vibrational zero-point energy corrections were included. Metal-ligand bond dissociation energies were calculated to be the energy difference of the metal atoms and ligands from their complexes.

The theoretical calculations of metal complexes begin from geometry optimization of the free ligand. For ligands with several possible conformations, a systematic local minimum search needs to be performed starting from a number of initial guesses. The global minimum energy structure can be located by comparing the energies of all structures. During this search for the minimum energy structure, weak interactions, such as intramolecular hydrogen bonding, should be considered. In addition to these

geometry optimizations, frequency calculations are performed to ensure each structure is a local minimum on the potential energy surface of the molecule.

After calculating structures of the free ligand, a variety of initial geometries for the metal complexes are constructed by attaching the metal atom or ion to various binding sites of the lowest energy ligand structure. The work presented in this dissertation mainly involves Cu binding to nitrogen or aromatic rings. In addition, Cu binding to higher energy ligand structures may be considered, because sometimes a metal complex formed by metal binding to a ligand with higher energy may be more stable than that formed by metal binding to a ligand with lower energy. Moreover, low-lying electronic excited states may need to be considered in addition to the ground states of the neutral and ionic complexes. From my experience, geometry optimization of the ionic state is easier to converge than that of the neutral. Hence, geometry optimizations of the neutral metal complex are carried out using the optimized geometry of the ionic species. Otherwise, the calculation may terminate abnormally. The output of a geometry optimization carries a range of information including the equilibrium geometry, molecular symmetry, electronic state, electronic energy, dipole moment, atomic charges, molecular orbitals, and rotational constants.

Similar to the calculations of the free ligand, all the optimized structures of the metal complex need to be tested by subsequent frequency calculations. The output of a frequency calculation also gives the vibrational modes, frequencies, force constant matrices, and zero-point energies, which are necessary for spectral analysis. Normally, frequency calculations start with the checkpoint files from the geometry optimization at the exact same computational level (same method and basis set). Frequencies and normal modes are calculated by diagonalizing the force constant matrices in mass-weighted Cartesian coordinates. This calculation yields $3N$ eigenvectors, and the program will calculate them again after projecting out the translational and rotational modes. In addition, the roots of $3N$ eigenvalues are calculated and correspond to the

fundamental frequencies. If a minimum is located, the frequencies of the rotational and translational modes should be close to zero ($< 50 \text{ cm}^{-1}$). For some cases, if the vibrational frequencies and modes are contaminated by the rotational and translational modes, some very small imaginary frequencies may be found in the output. One way to solve this problem is to redo the geometry optimization using tighter convergence criteria (e.g. using the keywords `Opt = Tight` or `Opt = VeryTight`). For DFT calculations, the grid step size must be reduced as well [e.g. using the keywords `Integral(Grid=UltraFine)`]. In some cases, high symmetry structures are determined to be first order saddle points according to the frequency calculations. However, by reducing or removing the symmetry constraint, re-optimization may generate the corresponding local minimum energy structure. Otherwise, searching for a different electronic state by orbital switching may help to find a local minimum energy structure. In some cases, the metal complex has lower symmetry upon ionization. Therefore, geometry optimization of the ion must be carried out under a lower symmetry or without symmetry constraints. As a last option, a large step size (e.g. `Opt = Loose`) may be used to find a local minimum energy structure, and the resultant structure needs to be re-optimized under tighter convergence criteria.

1.3.2 Franck-Condon spectral simulations

ZEKE spectra are simulated by calculating multidimensional Franck-Condon (FC) overlap integrals of the vibronic transitions between the neutral and the ion. These integrals are calculated by using the theoretical equilibrium geometries, harmonic vibrational frequencies and normal modes of the neutral and the monocation.¹¹⁹

The eigenvector matrix of the mass-weighted force constant matrix, \mathbf{L} , relates the normal coordinates, \mathbf{q} , with the mass-weighted Cartesian displacement coordinates, \mathbf{d} , by

$$\mathbf{q} = (\mathbf{L})^T \mathbf{d} \quad (1.2)$$

$$\mathbf{q}' = (\mathbf{L}')^T \mathbf{d} \quad (1.3)$$

(Primed quantities are for ions, and unprimed quantities are for neutral molecules.)

The mass-weighted Cartesian displacement coordinates are defined as

$$d_i = \sqrt{m_i} \cdot (x_i - x_i^e), i = 1, 2, \dots, 3n \quad (1.4)$$

where m_i and x_i^e are the masses and equilibrium geometries. From equations (1.2), (1.3), and (1.4), the normal coordinates of the final and initial states can be related to each other by¹²⁰

$$\mathbf{q}' = \mathbf{S} \cdot \mathbf{q} + \mathbf{Q} \quad (1.5)$$

where $\mathbf{S} = \mathbf{L}'^T \cdot \mathbf{L}$, and $\mathbf{Q} = \mathbf{L}'^T \cdot \sqrt{\mathbf{m}} \cdot (\mathbf{x}^e - \mathbf{x}'^e)$.²⁶ \mathbf{S} is the rotational matrix relating the two normal coordinates, and \mathbf{Q} denotes the displacement between them. Duschinsky¹²¹ pointed out that \mathbf{S} is not always a unitary matrix due to the rotation of the normal coordinates upon excitation or ionization. However, when \mathbf{S} is very close to an identity matrix, it can be assumed to be a unitary matrix. By replacing the ion frequencies with the corresponding neutral frequencies,¹²² the multi-dimensional FC factor calculations can be simplified to one-dimensional calculations. In this case, the intensity of transitions between two different vibrational states is proportional to the displacement between the two electronic surfaces. In other words, the intensity of the i^{th} totally symmetric mode is determined by the displacement, B_i , of the i^{th} normal coordinate by,

$$B_i = Q_i \sqrt{\frac{\omega_i'}{\hbar}}, \quad (1.6)$$

where Q_i is a component of the vector \mathbf{Q} . In this way, the FC overlap integrals are reduced to the products of one-dimensional integrals. Moreover, the intensity of the band corresponding to the $\nu = \{\nu_1, \nu_2, \dots, \nu_n\}$ vibrational quantum number is given by

$$I_v = \prod \frac{B_i^{2v_i}}{2^{v_i} v_i!} \quad (1.7).$$

For the case in which the S matrix is quite different from a unitary matrix, the Duschinsky effect needs to be considered. The spectral simulations were implemented by the FCF (v2.3) program written by Shenggang Li. Execution of this FCF program requires an input file (“fcf.inp”) generated by the PreFCF (v2.3) program. This input file contains the atomic masses, equilibrium geometries, harmonic vibrational frequencies, normal coordinates of the neutral and cationic complexes, and input parameters such as temperature, band width, vibrational quanta, resolution, signal threshold, and spectral range. The spectrum is simulated by calculating the contribution of each FC factor to each transition. A Boltzmann distribution is used to simulate finite temperature spectra. Spectral broadening is simulated by giving each transition a Lorentzian line shape with an experimental linewidth.

1.4 The scope of this dissertation

This dissertation focuses on PIE and PFI-ZEKE spectroscopy of Cu complexes containing alkyl and aromatic amines. Experimental measurements are compared to theoretical calculations and simulations to obtain information about the metal-ligand bonding interactions. Although there have been numerous experimental and theoretical studies about Cu σ ¹²³ and π bonding¹²⁴ interactions, little electronic spectroscopy has been done for these systems. In Chapter 2, the copper complexes of ethylenediamine are discussed. Both nitrogen atoms in ethylenediamine provide sp^3 lone pairs for σ bonding. However, the structure of the metal complex is governed by the competition between the copper atom coordination to both nitrogen atoms and intramolecular hydrogen bonding. This competition can be elucidated by investigating methyl-substituted ethylenediamines. Chapter 3 discusses copper coordination to

pyridine, which has both σ - and π -binding capabilities. Chapter 4 presents the study of Cu binding with pyrazine, pyrimidine, and pyridazine. In Chapter 5, the interaction of copper atoms and ions to aminopyridines are investigated. These ligands contain two σ nitrogens, one is in the pyridine ring that has an electron lone pair in an sp^2 hybridized orbital (σ_α), and the other one is in the amino group that has an electron lone pair in an sp^3 hybridized orbital (σ_β). In addition to the σ bonding sites, the aromatic pyridine ring in these ligands may provide π bonding as well. Chapter 6 extends our studies to copper-polypyridines. The polypyridines have multiple binding sites and include 2,2'-bipyridine, 4,4'-bipyridine, 1,10-phenanthroline, and 2,2':6',2''-terpyridine. In Chapter 7, the binding mode of Cu-imidazole is deciphered by comparing with the Al-imidazole complex. The last chapter summarizes the ionization energies and metal-ligand stretching vibrations of the Cu-complexes in this work.

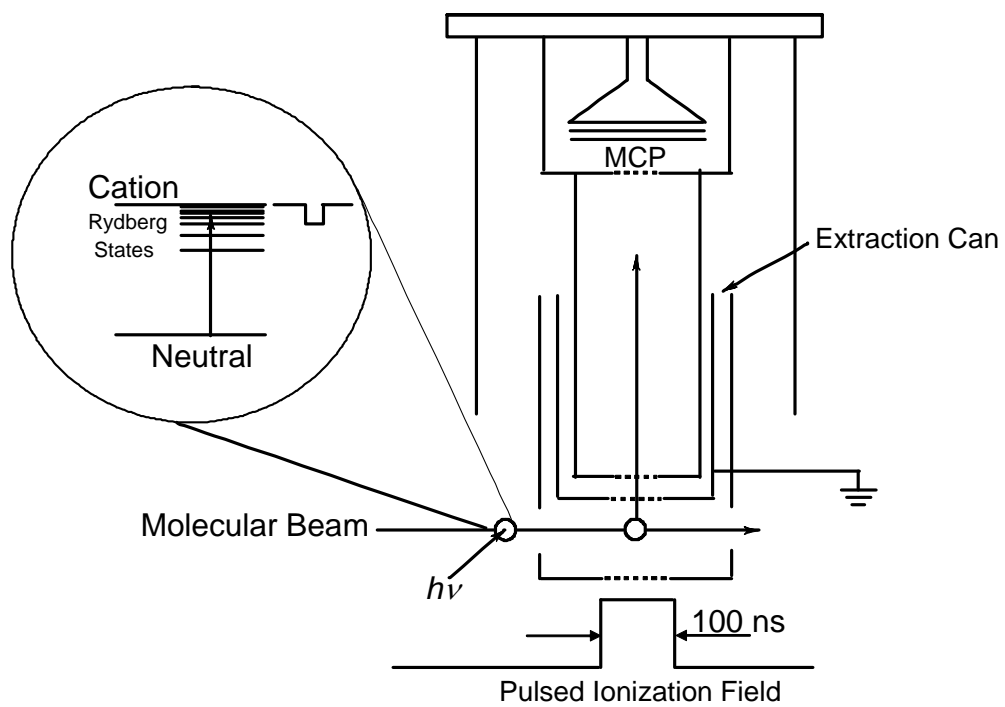


Figure 1.1. Schematic for generating ZEKE electrons.

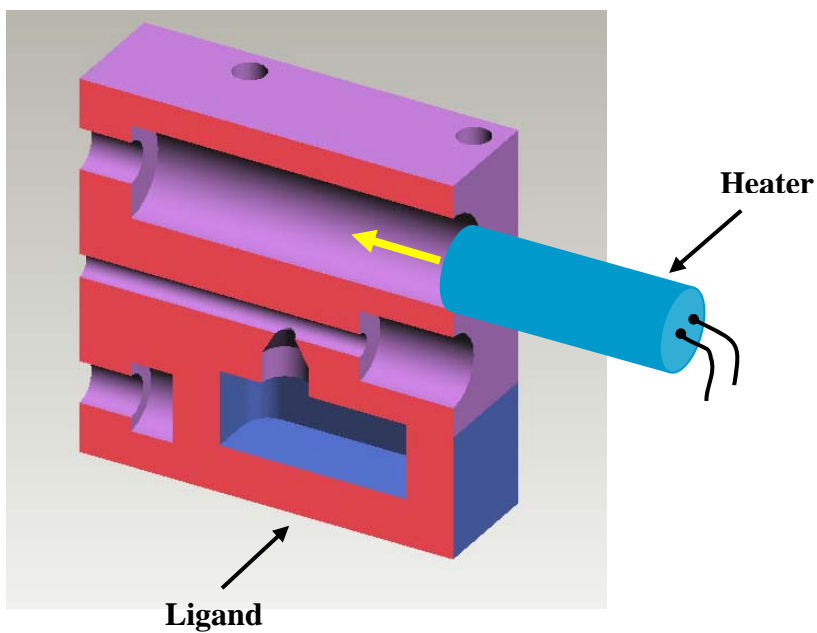


Figure 1.2. Schematic of the copper oven used to vaporize solid ligands.

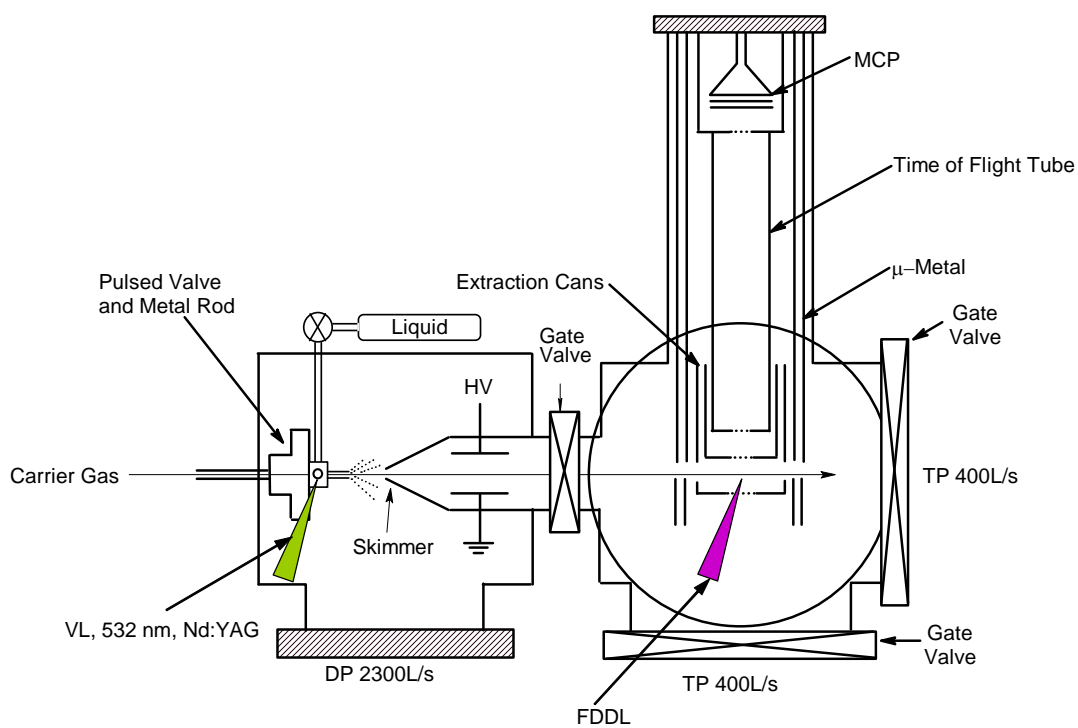
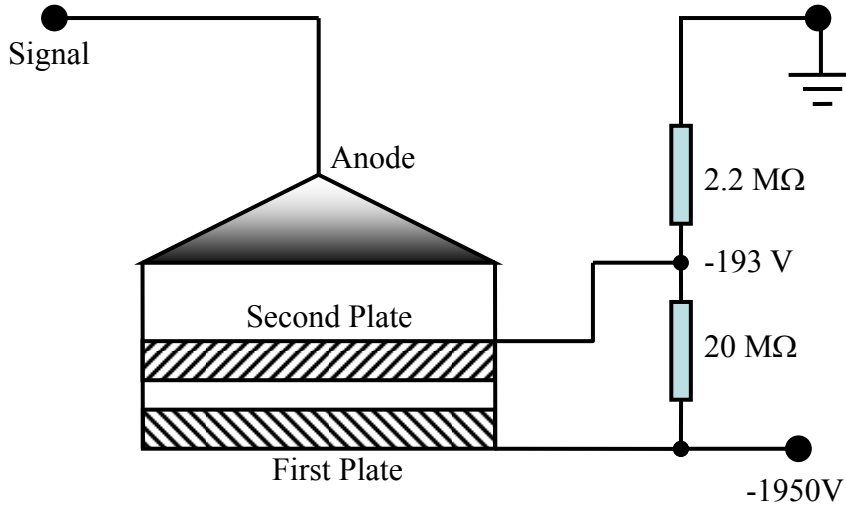
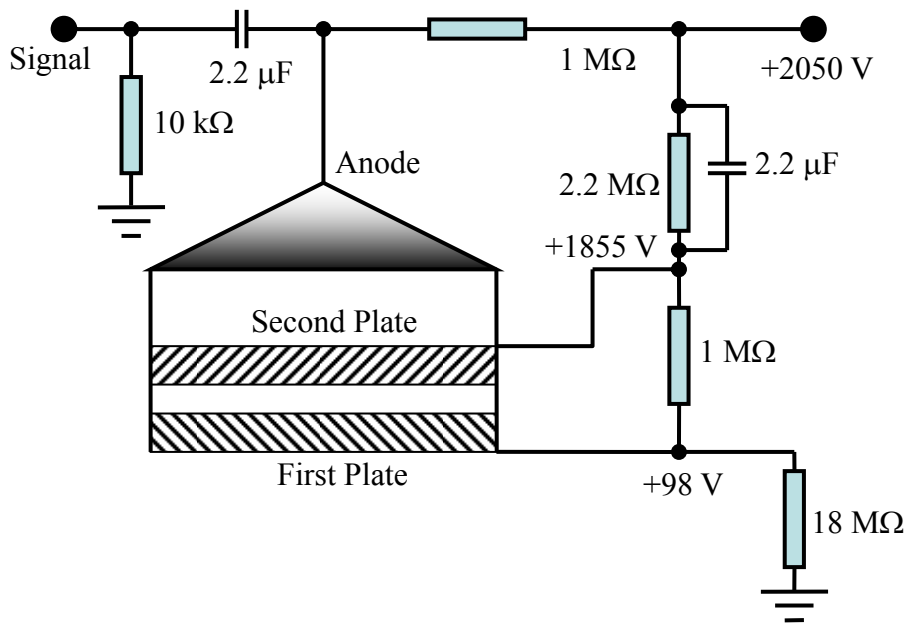


Figure 1.3. Schematic diagram of the PFI-ZEKE spectrometer. DP: oil diffusion pump; TP: turbo molecular pump; VL: vaporization laser; FDDL: frequency-doubled dye laser; MCP: microchannel plate detector.



(a) Ion detection



(b) Electron detection

Figure 1.4. Schematic diagrams of the voltage divider circuits for ion (a) and electron (b) detection.

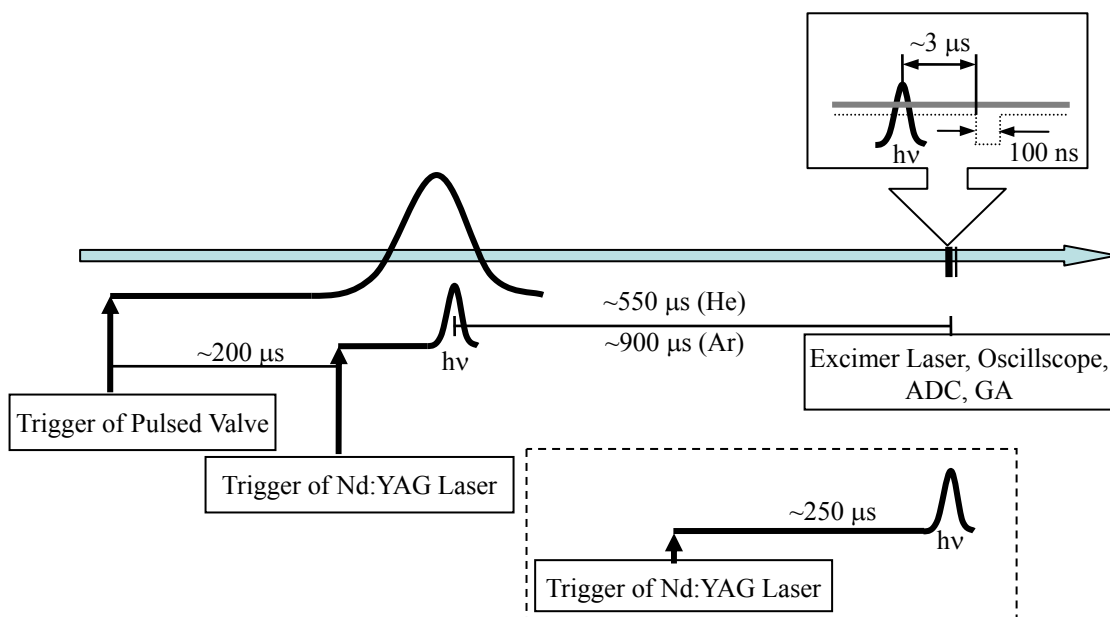


Figure 1.5. Schematic of the trigger sequence. GA: gated integrator; ADC: analog-to-digital adapter. The timing sequence in the dashed square box is applied when a Nd:YAG laser is used for pumping the dye laser.

Chapter 2 Spectroscopy and structures of copper-diamine complexes

Ethylenediamine (en) is one of the most widely used nitrogen-containing ligands in coordination chemistry.^{29,125} The ligand can adopt staggered trans and gauche conformations about the C-C bond. It is entirely trans in the solid state¹²⁶⁻¹²⁸ and largely gauche in the condensed phase.¹²⁹ In the vapor phase, ten rotational isomers have been predicted,¹²⁹⁻¹³⁵ and the most stable ones are two gauche forms, each with an internal NH...N hydrogen-bond.¹³² The two gauche forms have a tendency to convert to the trans form when the temperatures is increased by heating¹³² or absorbing IR radiation.¹³⁵

In the condensed phases, en complexes of metal ions are mainly in the chelating mode, although examples of monodentate and bridging forms also exist.¹²⁵ In the gas phase, experimental and theoretical studies have shown similar bidentate binding modes for a number of metal atoms and ions. Recently, Li et al. studied group 13 (Al, Ga, In) metal-en complexes using PFI-ZEKE spectroscopy and DFT calculations.⁸⁵ Four structural isomers with the metal binding to the gauche and trans forms of en were predicted by the DFT calculations; a five-membered cyclic structure was identified by ZEKE spectroscopy. This ring structure is formed by metal binding to both nitrogen atoms of the gauche en molecule. This bidentate binding mode was also found for Li⁺- and Na⁺-en by HF calculations by Ikuta,^{136,137} K/K⁺-en by PIE measurements and HF/MP2 calculations by Liao and Su,¹³⁸ and Mg⁺-en by photofragmentation experiments and DFT calculations by Liu et al.¹³⁹ At higher energies than the bidentate structure, these calculations located a monodentate form of Li⁺/Na⁺-en with the metal ions binding to a single nitrogen of trans en,^{136,137} a hydrogen-bonded monodentate form of Mg⁺-en with Mg⁺ binding to a single nitrogen atom of gauche en,¹³⁹ and three monodentate forms of

K^+ / K -en with or without internal hydrogen-bonding.¹³⁸ More closely related to this work was a DFT study of the potential energy surface associated with the gas-phase reactions between en and Cu^+ by Alcamí et al..^{140,141} From these DFT calculations, the most stable association complex of Cu^+ -en was a bidentate cyclic structure, a second minimum was a hydrogen-bond stabilized monodentate structure, and two other local minima were found with Cu^+ binding to the trans isomer of en.

In this chapter, I report the ZEKE study of the Cu complexes with en, N-methylethylenediamine (meen), N,N-dimethylethylenediamine (dmen), N,N,N'-trimethylethylenediamine (tren), N,N,N',N'-tetramethylethylenediamine (tmen), 1,3-propanediamine (pn), and 1,4-butanediamine (bn). The ZEKE spectra of Cu-en, -meen, -dmen, -pn and -bn are analyzed by using MP2 and FC calculations. In contrast to the previously reported metal-en complexes, the neutral Cu-en complex prefers a monodentate binding mode, where Cu binds to a nitrogen atom of a hydrogen-bonded gauche en molecule. Interestingly, methyl substitutions of one or more hydrogen atoms of the NH_2 groups switches the Cu binding from the monodentate to bidentate mode. On the other hand, two types of hydrogen-bonded structures of Cu-pn and -bn are identified by the ZEKE experiments.

2.1 Experimental and computational methods

Metal complexes were prepared by reactions of copper atoms with the vapor of a diamine ligand [$NH_2CH_2CH_2NH_2$, 99.5%, Aldrich; $CH_3NHCH_2CH_2NH_2$, 95%, TCI; $(CH_3)_2NCH_2CH_2NH_2$, 99%, Aldrich; $(CH_3)_2NCH_2CH_2NHCH_3$, 96%, TCI; $(CH_3)_2NCH_2CH_2N(CH_3)_2$, 99%, Aldrich; $NH_2(CH_2)_3NH_2$, 99%, Aldrich; $NH_2(CH_2)_4NH_2$, 99%, Aldrich] in molecular beams. Copper atoms were produced by pulsed laser vaporization of a copper rod (99.9%; Alfa Aesar) with the second harmonic output of a Nd:YAG laser (Quanta-Ray, GCR-3, 532 nm, ~ 3 mJ) in the presence of helium or argon

carrier gas with ~ 50 psi of backing pressure. The vapor of the diamine ligand was introduced at room temperature through a stainless capillary to a small reaction chamber (~ 1.5 mL). The ultraviolet photon source used for ionization was a frequency-doubled dye laser (Lumonics, HD-500), pumped by a XeCl excimer laser (Lumonics, PM-800). Prior to ZEKE experiments, ionization thresholds of the 1:1 complexes were located by recording the ion signal as a function of the laser wavelength. ZEKE electrons were produced by photoexcitation of the neutral molecules to high-lying Rydberg states, followed by ~ 3 μs delayed pulsed electric field ionization (1.2 V cm^{-1} , 100 ns) of these Rydberg states. Laser wavelengths were calibrated against vanadium or titanium atomic transitions.¹⁴² Field-dependent measurements were not carried out due to the limited size of the ZEKE signal.

Geometry and frequency calculations were carried out with the MP2 method and 6-311+G(*d,p*) basis, implemented in the GAUSSIAN 03 program package.¹¹³ Multidimensional FC factors were calculated from the equilibrium geometries, harmonic frequencies, and normal coordinates.^{143,144} Spectral broadening was simulated by giving each line a Lorentzian line shape with the linewidth of the experimental spectrum. Transitions from excited vibrational levels of the neutral electronic states were considered by assuming thermal excitations at specific temperatures.

2.2 Results and discussion

2.2.1 Computation

2.2.1.1 Isomers of free ligands

In order to determine the structures of the metal complexes, we first consider the low energy conformers of the free ligands. Although a large number of rotational isomers have been predicted for en, only three of which have been identified by electron

diffraction¹³² or IR spectroscopic measurements.¹³⁵ Figure 2.1 displays the most stable gauche (A, B) and trans isomers of en, and Table 2.1 lists their geometries and relative energies from the MP2/6-311+G(*d,p*) calculations. Both gauche isomers are more stable than the trans form due to stabilization of the internal NH...N hydrogen bond. This prediction is consistent with the previous MP2^{129,133} and B3LYP⁸⁵ calculations. Gauche A has a shorter NH...N distance, a larger \angle N-C-C-N dihedral angle, and a slightly lower energy than gauche B, while both gauche forms have the same \angle H-N...H angles. The two gauche forms are different because of the different orientations of the proton donor NH₂ group. To estimate the hydrogen-bond strength, we calculated a gauche conformer in C₂ symmetry with the two-fold axis passing through the middle point of the C-C bond. This structure has a hydrogen-nitrogen distance of 2.83 Å, which is larger than the sum of the van der Waals radii of nitrogen (1.55 Å) and hydrogen (1.20 Å).¹⁴⁵ By neglecting the hydrogen bonding interaction in this C₂ structure, we estimated the hydrogen-bond dissociation energy of 17.8 kJ mol⁻¹ for the most stable gauche form. This value is larger than the dissociation energy of 12.2 kJ mol⁻¹ for an ammonia dimer.¹⁴⁶

The relative stability of the three isomers of meen and dmen follow the same order as that of the parent diamine (Table 2.1), and the energy differences between the gauche (A, B) and trans forms increase with increasing number of methyl groups. The N-C-C-N framework remains planar in the trans dmen, but it is non-planar in the trans meen because of the asymmetric NHCH₃ group. For the gauche isomers, the \angle N-C-C-N dihedral angle slightly decreases from en through meen to dmen, while the N...H bond distance and \angle N-H...N angle show no significant changes. The calculations of the hydrogen-bond energies of meen and dmen are not straightforward because the energies of the non-hydrogen-bonded configurations depend on the relative orientation of the methyl groups. However, a Mulliken population analysis of gauche A shows the negative charges on the nitrogen atom of the proton acceptor NH₂ [NHCH₃ or N(CH₃)₂] decreases from en (-0.43) to meen (-0.33) to dmen (-0.08). Since the positive charges

on the hydrogen atoms of the proton donor NH_2 groups are almost the same (~ 0.25) in the three amines, the decrease of the negative charges on the nitrogen atom should reduce the Coulomb attraction between the hydrogen and nitrogen atoms. This trend agrees with the previous predictions that methyl substitutions deplete the charges of the proton acceptors of nitrogen bases¹⁴⁷⁻¹⁴⁹ and reduce the strengths of the internal hydrogen bonding in nitrogen- and oxygen-containing dimers.¹⁵⁰⁻¹⁵²

The trimethyl-substituted diamine ligand has only one hydrogen atom available to form a $\text{NH}\cdots\text{N}$ hydrogen bond in the gauche A form. Compared to dmen, the gauche A isomer of tren has a significantly longer $\text{NH}\cdots\text{N}$ distance and smaller $\angle\text{N-H}\cdots\text{N}$ angle (Table 2.1), indicating a weaker hydrogen bond in this trimethyl-substituted derivative. The weakening of the hydrogen bond in tren is due to a weaker electrostatic interaction and an increase in steric hindrance. The weakening observed in the electrostatic attraction arises from the decrease of the positive charge on the hydrogen atom of the proton donor upon additional methyl substitution. For the gauche B isomer, a $\text{CH}\cdots\text{N}$ hydrogen bond is predicted, where the CH_3 group acts as the proton donor [Figure 2.2 (a)]. A $\text{CH}\cdots\text{N}$ hydrogen bond is normally considered to be weak, because the carbon atom is not very electronegative. However, this type of hydrogen bond has been identified in a variety of organic and organometallic compounds.¹⁵³⁻¹⁵⁶ Interestingly, the $\text{CH}\cdots\text{N}$ bond in the gauche B isomer has a shorter $\text{H}\cdots\text{N}$ distance and a larger $\angle\text{C-H}\cdots\text{N}$ angle than the $\text{NH}\cdots\text{N}$ bond in gauche A (Table 2.1), although the hydrogen atom in $\text{CH}\cdots\text{N}$ is less positively charged than that in $\text{NH}\cdots\text{N}$.

The formation of the $\text{NH}\cdots\text{N}$ hydrogen bond is not possible in the tetramethyl-substituted diamine, because all four hydrogen atoms in the two NH_2 groups are replaced by methyl groups. Thus, only a gauche isomer containing a $\text{CH}\cdots\text{N}$ bond is predicted for this molecule [Figure 2.2 (b)]. The gauche tmen shows a shorter $\text{CH}\cdots\text{N}$ distance and larger $\angle\text{C-H}\cdots\text{N}$ and $\angle\text{N-C-C-N}$ angles than the gauche B tren. The larger angles are due to the increased steric effect in the tetramethyl-substituted diamine.

Two hydrogen bonded gauche and one trans structures are also calculated for pn and bn (shown in Figure 2.3), and their geometries and relative energies are listed in Table 2.1. The relative stabilities of the three isomers of pn are different from those of bn. For example, the gauche A isomer of pn is 4.39 kJ mol^{-1} above its gauche B isomer, while the trans isomer of bn is 1.27 kJ mol^{-1} below its gauche B isomer. Moreover, the energy differences among the three isomers decrease with increasing ligand chain length. The trans bn ligand is still in the C_{2h} point group, whereas the tran pn ligand has C_2 symmetry. The C_{2h} structure of pn is calculated to be a transition state (TS). The Mulliken population analysis of the gauche A isomers of pn and bn shows the negative charges on the nitrogen atoms of the proton acceptor NH_2 increase from en (-0.43) to pn (-0.51) to bn (-0.52) and the positive charges on the hydrogen atoms of the proton donor NH_2 also increase from en (0.25) to pn (0.28) to bn (0.31). The changes in these atomic charges lead to an enhanced Coulomb attraction between the hydrogen and nitrogen atoms. Consequently, the hydrogen-bond strengths are enhanced from en to pn to bn.

2.2.1.2 Isomers of Cu-en

Figure 2.4 displays the H-bond I, H-bond II, ring, and trans isomers of Cu-en, with their geometries and relative energies listed in Table 2.2. The H-bond I and II isomers are formed by Cu binding with a single nitrogen of gauche A and B. They have the same Cu-N distances and nearly identical hydrogen-bond lengths. H-bond I is slightly more stable than H-bond II. The major difference between the two hydrogen-bonded monodentate isomers is the $\angle\text{Cu-N-C-C}$ dihedral angle, which is 72.0° in H-bond I and 169.7° in H-bond II. The difference in dihedral angles is due to the different orientations of the proton donor NH_2 groups of the gauche A and B forms. Upon Cu coordination, the hydrogen-bond distances are reduced and the $\angle\text{N-H}\cdots\text{N}$ angles are increased. The negative charge on the nitrogen atom of the proton acceptor is increased

from -0.43 in the free gauche A form to -0.53 in the complex, and the positive charge of the hydrogen atom of the proton donor is increased from 0.27 to 0.30. These changes in the hydrogen-bond geometry and atomic charge suggest that Cu coordination enhances the hydrogen bonding. The ring structure is formed by Cu binding to both nitrogen atoms of the gauche A or B forms and has a 2-fold axis passing through the Cu atom and the middle point of the C-C bond. This bidentate cyclic structure has a slightly higher energy than the monodentate H-bond I complex but a significantly lower ionization energy. The bidentate structure also has a longer Cu-N distance than the monodentate complex, as expected by considering coordination numbers. The fourth conformer of the Cu-en complex is formed when Cu binds to a single nitrogen atom of the trans ligand. This configuration has the highest energy among all isomers. The different stabilities between the monodentate trans and hydrogen-bonded structures are clearly due to the effect of the internal hydrogen bonding.

It is interesting to compare the binding modes of Cu-en with other metal-en complexes, for which structures have been determined.⁸⁵ The hydrogen-bond stabilized monodentate structures of the neutral Cu-en complex are more stable than the bidentate cyclic structure, whereas the most stable structure of the group 13 metal-en complexes is in the bidentate binding mode. Although the en ligand has two equivalent nitrogen binding sites, the actual binding mode depends on the competition between the hydrogen bonding and metal coordination. The group 13 metal atoms have an unpaired *p* electron, and the *p* orbital can orientate itself perpendicularly to the nitrogen lone-pair electron orbital to minimize electron repulsions. On the other hand, the Cu 4s¹ electron has a higher density along the nitrogen lone-pair orbital, which causes stronger electron repulsion. As a result, the group 13 metal atoms bind to nitrogen atoms more strongly than Cu atoms. For example, the metal-ligand bond dissociation energy of the bidentate Al-en complex is calculated to be 78.4 kJ mol⁻¹, while that of the bidentate Cu-en is 50.0 kJ mol⁻¹. Another interesting difference between Cu and group 13 metal atoms concerns

their trans structures. The trans structure of Cu-en has a twisted NCCN chain, while the group 13 metal-en trans forms have C_s symmetry with a planar NCCN framework.⁸⁵ The C_s trans structure of Cu-en is not a local minimum.

Ionization removes the Cu 4s-based electron from the highest occupied molecular orbital (HOMO) of the neutral complex. The removal of the Cu 4s electron reduces the electron repulsion with the nitrogen electron lone pair and creates an additional electrostatic interaction between Cu^+ and en. As a result, the copper-nitrogen bond distance is reduced and the metal-ligand bond energy is dramatically enhanced for all four conformers. As the metal-ligand bond energy increases, the bidentate cyclic ion becomes more stable than the monodentate hydrogen-bonded ions, consistent with the previous DFT calculations.^{140,141} The ratio of the bond energies of the ionized species to the neutral species is about five for the monodentate conformers and seven for the bidentate conformer. The larger binding energy of the cyclic structure of the ion leads to the lower ionization energy of the cyclic structure. In addition to the changes in metal-ligand geometry and thermochemistry, ionization causes further changes in the ligand geometry. For example, the hydrogen-bond distances in H-bond I and II are reduced by as much as 10%. Moreover, the negative charge of the hydrogen-bonded nitrogen atom and the positive charge of the hydrogen-bonded hydrogen atom are slightly increased from the neutral complex (-0.53, 0.30) to the ion (-0.57, 0.33), which suggests that the hydrogen bonding is likely enhanced upon ionization.

2.2.1.3 Isomers of Cu-meen, -dmen, -tren, and -tmen

Similar to Cu-en, the copper complexes of the methyl-substituted derivatives possess low energy structures in the monodentate and bidentate binding modes (Table 2.2). Both H-bond I and II of Cu-meen and -dmen and H-bond I of Cu-tren contain an internal $NH\cdots N$ hydrogen bond, whereas H-bond II of Cu-tren and the only

hydrogen-bonded structure of Cu-tmen have an internal CH...N hydrogen bond. The structures containing the CH...N bond are not stable upon ionization and convert to the bidentate cyclic structure in the ion. Cu-meen and -tren have two trans monodentate structures (trans-L and tran-S), because the monomethyl- and trimethyl-substituted ligands have asymmetric amine groups. All of the methyl-substituted complexes form a bidentate cyclic structure, which becomes more stable with increasing methyl substitutions. As a result, the bidentate structures of the neutral Cu-tren and -tmen complexes have lower energies than the hydrogen-bonded monodentate structures. The increased stability of the bidentate versus hydrogen-bonded structures is due to the weakening of the internal hydrogen bond and the strengthening of the metal coordination upon additional methyl substitutions. Similar methyl effects have been reported for hydroxyl-containing dimers¹⁵¹ and metal-amine complexes.^{77,82,83,157}

2.2.1.4 Isomers of Cu-pn and -bn

Four stable structures in the monodentate and bidentate binding modes are also optimized for the Cu-pn and -bn complexes (Table 2.2). With increasing ligand chain length, the bidentate cyclic structures of Cu-pn and -bn become less stable; and the bidentate Cu-bn has nearly the same energy as its trans structure. The decreased stability of the bidentate versus hydrogen-bonded structures is due to an enhancement of the internal hydrogen bond. Moreover, although the hydrogen bond distances in the Cu-pn and -bn complexes are very close to those in the Cu-en complexes, the bond angles of $\angle\text{N-H}\cdots\text{H}$ are much larger than those of the Cu-en complexes, which are in favor of forming a hydrogen bond.

2.2.2 Spectroscopy

2.2.2.1 ZEKE spectra of Cu-en

Figure 2.5 (a) shows the experimental ZEKE spectrum of Cu-en seeded in argon carrier gas.⁸⁷ The spectrum displays a strong 0-0 transition peak at 43491 (5) cm^{-1} with the full width at the half-maximum (FWHM) of $\sim 5 \text{ cm}^{-1}$, and vibrational intervals of 1013, 474, 296, 214, 141, and 47 cm^{-1} . Additionally, the spectrum exhibits a number of hot transitions originating from excited vibrational levels of the ground electronic state of the neutral complex. The 0-0 transition energy of Cu-en is comparable to the adiabatic ionization energy (AIE) of simple Cu-amine complexes $\text{Cu-NH}_n(\text{CH}_3)_{3-n}$ ($n = 0-3$) but much higher than the AIE of $\text{Cu}(\text{NH}_3)_2$ (Table 3).^{84,88,157,158} The $\text{Cu-NH}_n(\text{CH}_3)_{3-n}$ complexes are formed by single copper-nitrogen coordination, whereas $\text{Cu}(\text{NH}_3)_2$ is formed by Cu binding to two nitrogen atoms.⁸⁸ Thus, the 0-0 transition energy of Cu-en likely corresponds to the AIE from the monodentate neutral complex to the monodentate ion. Among the measured vibrational intervals, the 474 cm^{-1} spacing can be assigned to the Cu^+ -N stretch of Cu^+ -en, because it is comparable to the Cu^+ -N stretching frequencies of $\text{Cu}^+\text{-NH}_3$ (470 cm^{-1}),¹⁵⁸ $\text{Cu}^+\text{-NH}_2\text{CH}_3$ (461 cm^{-1}),¹⁵⁷ and $\text{Cu}^+\text{-NH}(\text{CH}_3)_2$ (482 cm^{-1}).¹⁵⁷ Assignments for other transitions are discussed below in combination with spectral simulations.

Figures 2.5 (b) - (e) show the spectral simulations of H-bond I, H-bond II, ring, and trans isomers. These simulations represent the vibronic transitions from the doublet ground electronic state of the neutral molecule to the singlet ground electronic state of the ion. The theoretical 0-0 transition energies are shifted to the experimental value for simplicity, but the calculated vibrational frequencies are not scaled in these simulations. Electronic transitions between different isomers are not considered because such transitions would have a long FC profile due to large geometry differences between the initial and final states. The simulation of H-bond I [Figure 2.5 (b)] is in nice agreement

with the measured spectrum, while others are very different. Thus, the observed spectrum is attributed to H-bond I, and no significant contributions are from other isomers. This experimental finding is consistent with the MP2 prediction that the H-bond I isomer has the lowest energy for the neutral complex. Other low energy isomers might be formed in the molecular beams, but searches of PFI-ZEKE signals around their predicted AIEs were not successful.

The experimental spectrum can be assigned in comparison with the simulation of the H-bond I isomer. Major progressions involving the excitation of single vibrational modes (e.g. 21_0^n , 28_0^n , 30_0^n , 31_0^n , 32_0^n , and 33_0^n) are labeled in Figure 2.4(a), more detailed assignments are listed in Table 2.4. Six vibrational modes are measured for the ion and three for the neutral complex. The ion modes include N-C (ν_{21}^+), Cu⁺-N (ν_{28}^+), and H-bond stretches (ν_{31}^+), NH₂ rock (ν_{30}^+), Cu⁺-N-C bend (ν_{32}^+), and Cu⁺-N-C-C torsion (ν_{33}^+). The neutral modes include H-bond stretch (ν_{31}), Cu-N-C bend (ν_{32}), and Cu-N-C-C torsion (ν_{33}). Among these measured vibrational modes, the copper-nitrogen and hydrogen-bond vibrations are of the most importance because they provide direct evidence about the metal-ligand binding and molecular structures. The Cu-N stretching frequency increases from the neutral complex (353 cm⁻¹, MP2) to the ion (474 cm⁻¹), as ionization enhances the metal-ligand binding. It is interesting to note that the monodentate Cu⁺-en ion has a very similar Cu⁺-N stretching frequency as [Cu(en)₃]²⁺SO₄²⁻ (485 cm⁻¹) in the condensed phase.¹⁵⁹ The hydrogen-bond stretching frequency of the Cu-en complex increases from the free ligand (193 cm⁻¹, MP2) through the neutral molecule (197 cm⁻¹) to the ion (214 cm⁻¹). This frequency trend is due to the partial charges that become more negative on the hydrogen-bonded nitrogen and more positive on the hydrogen-bonded hydrogen. This increase in the charge difference enhances the hydrogen bonding. The Mulliken charges on nitrogen are calculated to be -0.43, -0.53, and -0.57 in the free ligand, the neutral complex, and ion complex, respectively; whereas the corresponding charges on hydrogen are 0.27, 0.30, and 0.33.

2.2.2.2 ZEKE spectra of Cu-meen

A representative ZEKE spectrum of Cu-meen seeded in He carrier is shown in Figure 2.6 (a). Measurements with Ar carrier were not successful. Compared to the parent diamine complex discussed above, the spectrum of the monomethyl-substituted species exhibits a number of distinctive features. First, the 0-0 transition of Cu-meen is observed at a much lower energy (36022 cm^{-1}) than that of Cu-en (43491 cm^{-1}). The AIE shift (7469 cm^{-1}) from Cu-en to Cu-meen is many times larger than that from Cu-NH₃ to Cu-NH₂CH₃ (974 cm^{-1}) (Table 2.3), a sign that the Cu-en and -meen complexes may have different binding modes. Second, the spectrum of Cu-meen displays a major vibrational progression (201 cm^{-1}) with a relatively long FC profile, indicating a considerable change of the geometry from the initial neutral state to the final ion state. Third, the Cu-meen spectrum displays a broader linewidth (16 cm^{-1}) than Cu-en and other Cu complexes investigated in our laboratory.^{84,88,157,158} The large linewidth is due to unresolved rotational envelopes and perhaps unresolved sequence transitions from vibrationally hot neutral molecules as well.⁷⁸

It is clear that only the simulation from the bidentate ring structure [Figure 2.6 (b)] matches the experimental spectrum. From the experimental spectrum alone, it is not straightforward to determine if the first peak at 36022 cm^{-1} originates from the 0-0 transition. However, the comparison between the measured spectrum and the simulation of the ring structure suggests that this lowest-energy transition is indeed the band origin. The 201 cm^{-1} progression is assigned to the Cu⁺-N stretch (ν_{40}^+), where Cu⁺ is displaced from the equilibrium geometry. The long FC profile observed for this vibrational progression is consistent with a large change ($> 0.15\text{ \AA}$) in the Cu-N distance from the neutral ground electronic state ($2.19/2.16\text{ \AA}$) to the ionic ground state ($2.01/2.01\text{ \AA}$). Two vibrational intervals are assigned to the fundamental excitations of two NCCNC

twists (248 cm^{-1} for ν_{38}^+ and 95 cm^{-1} for ν_{42}^+). These two intervals combine with the major progression 40_0^n to form progressions $38_0^1 40_0^n$ and $40_0^n 42_0^1$ [Figure 2.6 (a)]. The signal for the first few low-energy transitions of $38_0^1 40_0^n$ and $40_0^n 42_0^1$ was too small to be observed, and their expected positions are marked with dotted lines in Figure 2.6 (a). Since the sum of the calculated ν_{38}^+ (259 cm^{-1}) and ν_{40}^+ (213 cm^{-1}) frequencies is virtually the same as ν_{35}^+ (471 cm^{-1}), $35_0^1 40_0^{n-1}$ transitions overlap with $38_0^1 40_0^n$. From the FC factor calculations, the relative intensity of $35_0^1 40_0^{n-1}$ versus $38_0^1 40_0^n$ is $\sim 20\%$ for $n = 2$ and increased to $\sim 50\%$ for $n = 5$. Therefore, the $35_0^1 40_0^{n-1}$ transitions may also contribute to the observed ZEKE spectrum. This assignment yields the experimental ν_{35}^+ frequency of 449 cm^{-1} . The ν_{35}^+ mode is identified as a Cu^+ -N stretch, where a nitrogen atom is displaced from the equilibrium position. The assignment for each ZEKE transition is summarized in Table 2.4.

2.2.2.3 ZEKE spectra of Cu-dmen

The dimethyl-substituted complex exhibits a similar spectral profile as the monomethyl species [Figure 2.7 (a)]. The spectrum begins at 36248 cm^{-1} and extends with a long vibrational progression of 199 cm^{-1} . It shows two more progressions formed by the combination of the 199 cm^{-1} spacing with the 469 and 144 cm^{-1} intervals, respectively, and a few hot transitions. By comparing the measured spectrum with the simulations in Figures 2.6 (b-f), the Cu-dmen complex is identified to be in a bidentate cyclic structure [Figure 2.7 (b)]. The 199 cm^{-1} progression, labeled 49_0^n in Figure 2.7 (a), is assigned to the transitions from the neutral ground state to various Cu^+ -N stretching levels of the ion state. The Cu^+ -N stretching motion of ν_{49}^+ is characterized by the displacement of the Cu^+ ion and has almost the same frequency as the

corresponding stretching mode of Cu^+ -meen (ν_{40}^+ , 201 cm^{-1}). The 469 cm^{-1} interval corresponds to the excitation of another Cu^+ -N stretch with the displacement of the N atoms (ν_{41}^+) and is similar to the corresponding Cu^+ -N stretch in Cu-en (ν_{28}^+ , 474 cm^{-1}) and Cu-meen (ν_{35}^+ , 449 cm^{-1}). The 144 cm^{-1} interval is identified as the excitation of a $\text{N}(\text{CH}_3)_2$ rocking mode (ν_{50}^+) in the ion. The three hot transitions at 36559, 36764, and 36977 cm^{-1} [Figure 2.7 (a)] are assigned to $49_0^2 50_1^0$, $48_0^1 49_0^2 50_1^0$, and $48_0^2 49_0^2 50_1^0$, respectively, which yields vibrational frequencies of 209 cm^{-1} for ν_{48}^+ and 123 cm^{-1} for ν_{50} . ν_{48}^+ is a N- Cu^+ -N bending mode in the ion, and ν_{50} is the $\text{N}(\text{CH}_3)_2$ rocking mode in the neutral complex. Two additional transitions at 37596 and 37999 cm^{-1} (Table 2.4) may be assigned to the excitations of a CH_2 rocking mode (ν_{25}^+) and a NH_2 scissoring mode (ν_{13}^+) in the ion, respectively. The measured CH_2 rocking and NH_2 scissoring frequencies are 1312 and 1646 cm^{-1} , in good agreement with the calculated values of 1334 and 1644 cm^{-1} , respectively. However, because the FC factors of these two excitations are calculated to be small, their assignments are considered to be tentative.

2.2.2.4 Photoionization efficiency spectra of Cu-tren and -tmen

The ZEKE measurements on the trimethyl- and tetramethyl-substituted complexes were not successful. However, PIE measurements yielded approximate ionization energies for these two complexes. Figure 2.8 presents the PIE spectra of Cu-tren (a) and -tmen (b), with the Cu^+ -tren signal beginning at $\sim 36100 \text{ cm}^{-1}$ and the Cu^+ -tmen signal starting at $\sim 34800 \text{ cm}^{-1}$. By drawing a line through the first onset of the signal crossing with the base line, the intersection point gives ionization energies of 36250 (300) cm^{-1} for Cu-tren and 34950 (300) cm^{-1} for Cu-tmen. These values are corrected by $+110 \text{ cm}^{-1}$, the energy shift induced by the electric field (320 V cm^{-1}) used in recording the PIE spectra. The signal below the estimated ionization threshold may be due to ionization of thermally excited molecules. In both PIE spectra, an additional onset is observed. The

energy separation between the first and second onsets is measured to be ~ 400 and ~ 200 cm^{-1} for the trimethyl- and tetramethyl-substituted species, respectively. The second onset may indicate the opening of the first excitation of a vibrational mode in the ion complex, but definitive assignment is difficult because of the large measurement uncertainty. The large uncertainty is due to the slowly rising ion signal as the ionization laser is scanned to shorter wavelengths. The lack of a sharp onset at the ionization threshold may be due to large structural changes upon ionization or significant predisposition. Either of these conditions could have contributed to the failure of the ZEKE experiment. However, since the trimethyl and tetramethyl species have similar ionization energies to the monomethyl and dimethyl derivatives, they are expected to be in the bidentate binding configuration as well. This structural assignment is supported by the MP2 predictions, where the bidentate cyclic structure was calculated to have the lowest energy among all isomers (Table 2.2).

2.2.2.5 ZEKE spectra of Cu-pn

Figure 2.9 (a) shows the experimental ZEKE spectrum of Cu-pn seeded in argon carrier gas. The first strong peak is located at 42578 cm^{-1} with a linewidth of $\sim 5 \text{ cm}^{-1}$ and is assigned to the 0-0 transition. On the higher energy side of the 0-0 transition, the spectrum displays eight vibrational intervals of 506, 487, 388, 315, 303, 236, 170, and 57 cm^{-1} . Additionally, the spectrum exhibits a number of small peaks below the first strong transition with 202, 129 and 97 cm^{-1} spacings. Compared to the ZEKE spectrum of Cu-en, these small peaks possibly arise from the hot transitions originating from excited vibrational levels of the ground electronic state of the neutral complex. The 0-0 transition energy of this complex (42578 cm^{-1}) is fairly close to that of Cu-en (43491 cm^{-1}), which implies a monodentate bonding mode for the Cu-pn neutral and ion complexes. Among the measured vibrational intervals, the 487, 303 and 236 cm^{-1}

spacings could be attributed to the Cu⁺-N stretch, NH₂ rock, and H-bond stretch of Cu⁺-pn on the basis of their comparable values with those of the Cu⁺-en (474, 296 and 214 cm⁻¹, respectively).

Figures 2.9 (b) - (e) present the spectral simulations of the H-bond I, H-bond II, ring, and trans isomers. The theoretical 0-0 transition energies are aligned to the first strong peak of the experimental spectrum, but the calculated vibrational frequencies are not scaled. Similarly, electronic transitions between different isomers are excluded. Although the simulation of the H-bond II isomer has a fairly good match with the experimental spectrum, it does not reproduce the weak transitions below the 0-0 band, even at much higher vibrational temperatures (i.e. 300 K, not shown). Additionally, we have found that the metal complexes seeded in Ar have vibrational temperatures lower than 100 K.^{78,87,93} Furthermore, any of the calculated frequencies of the neutral H-bond II isomer (shown in Table 2.8) do not match the 129 and 202 cm⁻¹ spacings of two weak transitions. Therefore, although the observed spectrum is mainly contributed by the H-bond II isomer, those small peaks below the origin band may arise from other structures. From Figure 2.9 (b), the simulation of the H-bond I isomer includes the 77 and 116 cm⁻¹ progressions with fairly strong intensities, and they are very close to the spacings (73 and 105 cm⁻¹) of the second and third small peaks to the first small peak at 42376 cm⁻¹. Thus, these small peaks are assigned to transitions originating from the H-bond I isomer with its origin band located at 42376 cm⁻¹. Figure 2.9 (f) shows a sum of the two simulated spectra with contributions from the H-bond I and H-bond II structures. In this spectrum, the 0-0 band of the H-bond II isomer is aligned to the small peak located at 42376 cm⁻¹, the intensities of those transitions arising from the H-bond I isomer are taken as 6 % those of the transitions from the H-bond II isomer, which is the ration of the intensity of the first small peak at 42376 cm⁻¹ to the intensity of the first strong peak at 42578 cm⁻¹. Surprisingly, this summed spectrum reproduces those weak transitions very well, which indicates that both hydrogen-bonded isomers are present in

the molecular beam and probed by the ZEKE spectroscopy. This experimental finding is consistent with the MP2 predictions that the H-bond II isomer has the lowest energy for the neutral complex and the H-bond I isomer is the second most stable structure. In addition, the H-bond I isomer is predicted to have a slightly lower ionization energy, consistent with the spectral assignment.

The major progressions (H-bond I: 41_0^n and 42_0^n ; H-bond II, 34_0^n , 35_0^n , 36_0^n , 37_0^n , 38_0^n , 39_0^n , 40_0^n , and 42_0^n) are labeled in Figure 2.9 (a); the rest of the assignments are listed in Table 2.5. Two vibrational modes of H-bond I are ligand chain distortion (ν_{41}^+) and Cu^+NH_2 rock (ν_{42}^+) modes. The vibrational modes of H-bond II include two $\text{Cu}^+\text{-N}$ stretches (ν_{34}^+ and ν_{35}^+), two NH_2 rocks (ν_{36}^+ and ν_{38}^+), a C-C-C bend (ν_{37}^+), a H-bond stretch (ν_{39}^+), a $\text{Cu}^+\text{-N-C}$ bend (ν_{40}^+), and a Cu^+NH_2 rock (ν_{42}^+). Among these measured vibrational modes, the $\text{Cu}^+\text{-N}$ and H-bond stretches show the strongest intensities and slight larger frequencies than the corresponding modes of $\text{Cu}^+\text{-en}$. It should be pointed out that, although only two vibrational modes are observed in this ZEKE measurement, some other vibration transitions should be still excited and distributed on the higher energy side. Nevertheless, such transitions would have much weaker intensities and possibly overlapped by the transitions from the H-bond II isomer due to the fairly low concentration of the H-bond I isomer in the molecular beam.

2.2.2.6 ZEKE spectra of Cu-bn

The ZEKE spectrum of Cu-bn in Ar carrier is shown in Figure 2.10 (a). Compared to the Cu-pn spectrum, this spectrum displays more transitions below the first strong peak at 41638 cm^{-1} . Similar to Cu-pn, two isomers of Cu-bn are probed by the ZEKE spectroscopy. Thus, the peak at 41638 cm^{-1} arises from the 0-0 transition of H-bond I, the most stable Cu-bn isomer, while the peak at 41207 cm^{-1} is attributed to the 0-0 transition of H-bond II, the second most stable Cu-bn isomer. The spectrum displays 10

vibrational intervals (512, 483, 413, 382, 319, 262, 191, 133, 73 and 46 cm^{-1}) with respect to the 0-0 transition of the H-bond I isomer at 41638 cm^{-1} , and five vibrational intervals (370, 283, 234, 142, and 89 cm^{-1}) with respect to the 0-0 transition of the H-bond II isomer at 41207 cm^{-1} . Both the ionization energies of the Cu-bn H-bond I and H-bond II isomers are close to those of the corresponding isomers of Cu-pn, indicating their monodentate bonding structures.

Figures 2.10 (b) - (e) present the spectral simulations of H-bond I, H-bond II, ring, and trans isomers, whereas Figure 2.10 (f) is the sum of the H-bond I and H-bond II simulations. In Figure 2.10 (b) - (e), the calculated AIEs are aligned to the 0-0 transition at 41638 cm^{-1} . In Figure 2.10 (f), the AIEs of H-bond I and H-bond II isomers are aligned to the 0-0 transitions at 41638 and 41207 cm^{-1} , respectively, and the intensities of the H-bond II simulation are modified by 20 %, which is the ratio of the intensity of the 0-0 transition of the H-bond II isomer to the intensity of the 0-0 transition of the H-bond I. The sum of the H-bond I and II simulations is in very nice agreement with the experimental spectrum, which confirms these two isomers are produced in these experiments as well. Therefore, the observed transitions above 41638 cm^{-1} are mainly contributed by the H-bond I isomer, while the transitions below are contributed by the H-bond II isomer.

The spectral assignments [Figure 2.10 (a) and Table 2.6] are based on the good agreement between the experimental spectrum and the summed simulation in Figure 2.10 (f). The vibrational modes of H-bond I include a $\text{Cu}^+\text{-N}$ stretch (ν_{41}^+), two H-bond stretches (ν_{43}^+ and ν_{47}^+), a NH_2 rock (ν_{44}^+), and six ligand chain distortions (ν_{42}^+ , ν_{45}^+ , ν_{48}^+ , ν_{49}^+ , ν_{50}^+ , and ν_{51}^+). The vibrational modes of H-bond II include a $\text{Cu}^+\text{-N}$ stretch (ν_{41}^+), an NH_2 rock (ν_{44}^+), a C-C-C bend (ν_{37}^+), two H-bond stretches (ν_{46}^+ and ν_{47}^+), a $\text{Cu}^+\text{-N-C}$ bend (ν_{40}^+), and a ligand chain distortion (ν_{49}^+). The $\text{Cu}^+\text{-N}$ and H-bond stretching frequencies of these two isomers are larger than those of the $\text{Cu}^+\text{-pn}$ complex. This increase in the $\text{Cu}^+\text{-N}$ and H-bond stretching frequencies from $\text{Cu}^+\text{-en}$ to $\text{Cu}^+\text{-pn}$ to

Cu⁺-bn indicates that metal-ligand binding and hydrogen bonding are enhanced with the ligand chain length.

2.2.2.7 Comparison of experimental measurements and ab initio calculations

Table 2.7 summarizes the AIEs and vibrational frequencies of the Cu complexes with diamines and methyl-substituted ethylenediamines from the ZEKE spectra and MP2 calculations. Overall, the calculated frequencies for vibrational modes larger than ~ 200 cm⁻¹ are in good agreement with the experimental values. However, the ab initio results for lower frequency modes have relative large errors ranging from a few hundredths to a few tenths. For ionization energies, the calculated values are consistently lower than the measured values by 3000-4000 cm⁻¹ (36-48 kJ mol⁻¹). Therefore, experimental measurements of ionization energies and low frequency modes are especially valuable, as the theory is still not able to provide accurate predictions for these quantities consistently and reliably. More expensive methods and basis sets may be used to improve the theoretical results, but this is beyond the current work.

2.3 Conclusion

We have reported a spectroscopic and ab initio study of the copper complexes of diamines and methyl-substituted ethylenediamines. ZEKE spectra were obtained for the Cu complexes of ethylenediamine, N-methylethylenediamine, N,N-dimethylethylenediamine, 1,3-propanediamines, and 1,4-butenediamine; but only PIE spectra could be measured for the Cu complexes of N,N,N'-trimethylethylenediamine and N,N,N',N'-tetramethylethylenediamine. A number of low energy structures are predicted for each of the Cu complexes by MP2 calculations. These structures involve the bidentate Cu binding of two nitrogen atoms

and the monodentate Cu binding of single nitrogen with or without an internal hydrogen bond. The parent diamine complexes are identified in a structure with monodentate Cu coordination and an internal hydrogen bond. In contrast, all methyl-substituted derivatives are determined to have a cyclic structure with bidentate binding. The binding modes of these complexes result from the competition between the Cu coordination and hydrogen bonding. For unsubstituted diamines, monodentate coordination with an internal hydrogen-bond is preferred over bidentate coordination. For all the methyl derivatives, the bidentate binding is more stable. However, all ionic complexes prefer the bidentate binding mode on the basis of the MP2 predictions.

Two hydrogen bonded isomers (H-bond I and H-bond II) are identified for the Cu-pn and -bn complexes. The H-bond II complex is determined to be the major isomer for the Cu-pn, while the H-bond I complex is the predominant isomer for Cu-bn. The AIE differences between these two hydrogen bonded isomers are measured to be 202 and 431 cm^{-1} for Cu-pn and Cu-bn, respectively.

Table 2.1. Relative electronic energies (E_e , kJ mol⁻¹) and geometries (R, Å; \angle , degrees) of ethylenediamine and methyl-substituted derivatives from MP2/6-311+G(*d,p*) calculations.

Molecules	Conformers ^a	E_e	R(H...N)	\angle N-H...N	\angle N-C-C-N
H ₂ N(CH ₂) ₂ NH ₂ , en	gauche A	0	2.450	105.0	63.9
	gauche B	1.6	2.533	105.0	60.2
	trans	8.2			180.0
(CH ₃)HN(CH ₂) ₂ NH ₂ , meen	gauche A	0	2.440	105.7	61.8
	gauche B	1.6	2.534	105.3	58.2
	trans	11.1			177.4
(CH ₃) ₂ N(CH ₂) ₂ NH ₂ , dmen	gauche A	0	2.446	105.7	60.3
	gauche B	1.9	2.549	105.3	56.9
	trans	15.2			180.0
(CH ₃) ₂ N(CH ₂) ₂ NH(CH ₃), tren	gauche A	0	2.595	100.3	51.4
	gauche B	6.5	2.489	120.2 ^b	66.5
	trans	18.0			176.8
(CH ₃) ₂ N(CH ₂) ₂ N(CH ₃) ₂ , tmen	gauche	0	2.367	126.0 ^b	70.2
	trans	15.7			180.0
H ₂ N(CH ₂) ₃ NH ₂ , pn	gauche A	4.39	2.305	130.5	
	gauche B	0	2.266	124.1	
	trans	6.73			
H ₂ N(CH ₂) ₄ NH ₂ , bn	gauche A	0	2.083	146.0	
	gauche B	2.93	2.101	150.0	
	trans	1.66			

^a All conformers are in C₁ point group except for the trans conformers of en (C_{2h}), dmen (C_s), tmen (C_{2h}), pn (C₂), and bn (C_{2h}). All gauche conformers have a NH...N hydrogen bond, except for the gauche B of tren and the gauche form of tmen with a CH...N hydrogen bond.

^b \angle C-H...N.

Table 2.2. Relative electronic energies (E_e , kJ mol⁻¹), adiabatic ionization energies (AIE, eV), bond dissociation energies (D_0 , kJ mol⁻¹), and geometries (R, Å; \angle , degrees) of copper-diamine complexes from MP2/6-311+G(*d,p*) calculations.

Complexes ^a	E_e	AIE	D_0	R(Cu-N)	R(N \cdots H)	\angle N-Cu-N	\angle N-H \cdots N	\angle Cu-N-C	\angle N-C-C-N
Cu-en									
H-bond I	0	5.03	53.5	2.02	2.32		109.3	116.0	58.7
H-bond II	2.2	4.99	52.8	2.02	2.39		108.8	116.3	57.3
ring	4.0	4.08	50.0	2.17		81.6		107.4	56.7
trans	14.5	5.19	47.4	2.03				117.2	176.6
Cu ⁺ -en									
H-bond I	90.6		268.0	1.92	2.13		114.8	118.0	51.4
H-bond II	89.2		270.6	1.91	2.10		117.6	118.6	51.2
ring	0		355.5	2.01		92.6		100.1	58.1
trans	120.9		246.8	1.93				115.2	179.7
Cu-meen									
H-bond I	2.0	4.98	55.3	2.02	2.36		110.3	116.3	54.8
H-bond II	0	5.01	55.9	2.02	2.31			116.0	57.6
ring	2.2	4.05	54.3	2.19/2.16		82.0		105.6/108.1	57.0
trans-L	17.8	5.21	49.5	2.05				111.4	174.5
trans-S	18.6	5.21	48.7	2.03				115.7	177.8
Cu ⁺ -meen									
H-bond I	92.7		274.7	1.91	2.07		119.2	118.8	50.0
H-bond II	93.5		272.5	1.91	2.08		117.5	117.9	49.9
ring	0		363.2	2.01		93.6		99.4/100.6	58.6
trans-L	131.1		246.9	1.93				112.1	171.8
trans-S	132.4		245.6	1.92				116.6	179.7
Cu-dmen									
H-bond I	2.7	4.98	53.4	2.02	2.36		110.8	116.4	53.5
H-bond II	0	5.02	57.4	2.02	2.31		109.7	115.9	56.3
ring	2.4	4.04	54.4	2.23/2.14		82.2		104.2/108.6	56.8
trans-L	23.3	5.20	48.5	2.08				107.3	180
trans-S	22.0	5.19	49.4	2.03				115.7	180

Table 2.2 continued

Cu ⁺ -dmen									
H-bond I	94.6		272.3	1.91	2.04		120.8	118.9	48.7
H-bond II	95.5		272.8	1.91	2.07		118.2	117.7	49.1
ring	0		364.2	2.01/2.00		94.6		98.2/100.0	58.5
trans-L	137.1		246.0	1.94				108.1	180.0
trans-S	134.3		248.1	1.92				116.5	180.0
Cu-tren									
H-bond I	1.3	4.95	57.2	2.03	2.37		109.0	113.2	48.7
H-bond II	10.8		54.0	2.04	2.44		120.3 ^b	115.2	61.3
ring	0	4.00	59.2	2.22/2.16		82.7		104.8/106.4	57.6
trans-L	27.2	5.17	49.5	2.07				107.2	177.9
trans-S	25.0	5.15	51.2	2.05				111.3	168.7
Cu ⁺ -tren									
H-bond I	96.5		279.1	1.91	2.02		122.2	115.1	44.5
ring	0		372.8	2.01/2.00		95.7		97.9/98.5	59.1
trans-L	143.5		250.4	1.94				108.0	173.1
trans-S	138.9		254.1	1.93				112.0	163.5
Cu-tmen									
H-bond	13.0		53.2	2.06	2.33		125.4 ^b	112.9	65.2
ring	0	3.99	66.0	2.20		83.1		105.2	57.1
trans	31.6	5.15	50.0	2.07				107.0	180.0
Cu ⁺ -tmen									
ring	0		380.5	2.00		96.6		97.4	58.9
trans	146.6		252.7	1.94				107.7	180.0
Cu-pn									
H-bond I	4.8	4.83	59.4	2.012	2.133	136.3	136.4	116.1	
H-bond II	0	4.84	60.6	2.015	2.105	101.7	130.9	116.6	
ring	9.3	3.70	52.2	2.117		95.4		115.9	
trans	18.1	5.13	50.0	2.035				115.9	
Cu ⁺ -pn									
H-bond I	109.5		292.6	1.905	1.876	130.9	145.3	118.1	
H-bond II	111.9		345.7	1.909	1.899	109.1	143.7	117.2	
ring	0		394.7	1.930		122.0		103.4	
trans	151.9		254.3	1.932				113.5	

Table 2.2 continued

Cu-bn								
H-bond I	0	4.80	65.5	2.006	1.925	105.7	154.5	118.2
H-bond II	4.4	4.75	64.1	2.007	1.944	118.8	159.2	116.0
ring	17.3	3.27	49.6	2.075		108.6		119.9
trans	18.1	5.18	49.6	2.032				116.0
Cu ⁺ -bn								
H-bond I	136.6		301.6	1.904	1.770	111.6	160.7	116.4
H-bond II	134.7		305.8	1.902	1.765	119.2	162.6	117.0
ring	0		433.4	1.887		149.2		106.6
trans	190.9		249.2	1.924				116.8

^a All complexes are in the C_1 point group, except for the ring structures of Cu/Cu⁺-en (C_2), -tmen (C_2), -pn (C_s), and -bn (C_2) and the trans structures of Cu/Cu⁺-dmn, -tmen, and -bn (C_s). All H-bonded complexes have a NH...N hydrogen bond, except for H-bond II Cu-tren and H-bond Cu-tmen.

^b $\angle C-H\cdots N$.

Table 2.3. Adiabatic ionization energies (AIE) of copper-amine complexes from ZEKE spectra.

Molecules	AIE (cm ⁻¹)	References
Cu-NH ₃	46485	[¹⁵⁸]
Cu-NH ₂ (CH ₃)	45511	[¹⁵⁷]
Cu-NH(CH ₃) ₂	44916	[¹⁵⁷]
Cu-N(CH ₃) ₃	44730	[⁸⁴]
Cu-(NH ₃) ₂	29532	[⁸⁸]
Cu-H ₂ NCH ₂ CH ₂ NH ₂	43491	This work
Cu-(CH ₃)HNCH ₂ CH ₂ NH ₂	36020	This work
Cu-(CH ₃) ₂ NCH ₂ CH ₂ NH ₂	36284	This work
Cu-(CH ₃) ₂ NCH ₂ CH ₂ NH(CH ₃)	36250 ^a	This work
Cu-(CH ₃) ₂ NCH ₂ CH ₂ N(CH ₃) ₂	34950 ^a	This work
Cu-H ₂ N(CH ₂) ₃ NH ₂ , H-bond I	42376	This work
Cu-H ₂ N(CH ₂) ₃ NH ₂ , H-bond II	42578	This work
Cu-H ₂ N(CH ₂) ₄ NH ₂ , H-bond I	41638	This work
Cu-H ₂ N(CH ₂) ₄ NH ₂ , H-bond II	41207	This work

^a From photoionization efficiency measurements.

Table 2.4. ZEKE peak positions and assignments of the Cu-en, -meen, and -dimeen complexes.

Cu-en		Cu-meen		Cu-dimeen			
Positions	Assignments	Positions	Assignments	Positions	Assignments		
43259	$31_0^1 33_0^0$	44027	$31_0^1 32_0^2 33_0^1$	36022	0_0^0	36284	0_0^0
43336	$32_0^1 33_0^0$	44048	$30_0^1 31_0^1 33_0^0$	36224	40_0^1	36428	50_0^1
43456	33_0^1	44061	$28_0^1 33_0^3 / 31_0^2 32_0^1$	36426	40_0^2	36483	49_0^1
43491	0_0^0	44073	$31_0^1 32_0^2 33_0^0$	36472	$38_0^1 40_0^1 / 35_0^1$	36559	$49_0^2 50_0^0$
43511	32_0^1	44107	$28_0^1 32_0^1$	36596	$38_0^1 40_0^2 42_0^0$	36682	49_0^2
43538	33_0^1	44132	31_0^3	36628	40_0^3	36764	$48_0^1 49_0^2 50_0^1$
43587	33_0^2	44146	$30_0^1 31_0^1 32_0^1$	36676	$38_0^1 40_0^2 / 35_0^1 40_0^1$	36881	49_0^3
43632	32_0^1	44178	$28_0^1 31_0^1$	36796	$38_0^1 40_0^3 42_0^0$	36977	$48_0^2 49_0^2 50_0^1$
43648	32_0^2	44219	$28_0^1 31_0^1 33_0^1$	36830	40_0^4	37025	$49_0^3 50_0^1$
43678	$32_0^1 33_0^1$	44247	$28_0^1 32_0^2$	36875	$38_0^1 40_0^3 / 35_0^1 40_0^2$	37079	49_0^4
43705	31_0^1	44258	$28_0^1 30_0^1$	37031	40_0^5	37151	$41_0^1 49_0^2$
43752	$31_0^1 33_0^1$	44291	$28_0^1 32_0^2 33_0^1$	37079	$38_0^1 40_0^4 / 35_0^1 40_0^3$	37219	$49_0^4 50_0^1$
43762	$32_0^2 33_0^1$	44319	$28_0^1 31_0^1 32_0^1$	37126	$40_0^5 42_0^1$	37276	49_0^5
43771	32_0^2	44389	$28_0^1 31_0^2$	37231	40_0^6	37347	$41_0^1 49_0^3$
43787	30_0^1	44436	28_0^2	37277	$38_0^1 40_0^5 / 35_0^1 40_0^4$	37418	$49_0^5 50_0^1$
43816	$32_0^2 33_0^1$	44470	$28_0^1 30_0^1 31_0^1$	37326	$40_0^6 42_0^1$	37468	49_0^6
43836	$30_0^1 33_0^1$	44481	$28_0^2 33_0^1$	37432	40_0^7	37548	$41_0^1 49_0^4$
43847	$31_0^1 32_0^1$	44504	21_0^1	37478	$38_0^1 40_0^6 / 35_0^1 40_0^5$	37596	25_0^1 ^a
43891	$31_0^1 32_0^1 33_0^1$	44575	$28_0^2 32_0^1$			37665	49_0^7
43919	31_0^2	44603	$28_0^1 31_0^3$			37739	$41_0^1 49_0^5$
43965	28_0^1	44647	$28_0^2 31_0^1$			37866	49_0^8
44010	$28_0^1 33_0^1$	44685	$28_0^1 30_0^1 31_0^2$			37941	$41_0^1 49_0^6$
						37999	13_0^1 ^a

^a Tentative assignments, see text.

Table 2.5. ZEKE peak positions (cm^{-1}) and assignments of the Cu-pn complexes.

Positions	Assignments	Positions	Assignments	Positions	Assignments
	H-bond I	43084	34_0^1	43450	$35_0^1 36_0^1$
42376	0_0^0	43113	$38_0^1 39_0^1$	43473	$39_0^3 40_0^1$
42449	42_0^1	43124	$35_0^1 42_0^1 / 37_0^1 39_0^1$	43506	$35_0^1 36_0^1 42_0^1 / 36_0^1 38_0^1 39_0^1$
42481	41_0^1	43142	$34_0^1 42_0^1 / 36_0^1 40_0^1$	43528	39_0^4
	H-bond II	43157	$39_0^1 40_0^2$	43552	35_0^2
42578	0_0^0	43180	$38_0^2 / 35_0^1 42_0^2$	43565	$34_0^1 35_0^1$
42635	42_0^1	43190	$36_0^1 40_0^1 42_0^1$	43595	34_0^2
42691	42_0^2	43199	$36_0^1 39_0^1 / 37_0^1 38_0^1$	43610	$35_0^2 42_0^1$
42750	40_0^1	43205	37_0^2	43645	$35_1^1 39_0^1 40_0^2$
42814	39_0^1	43215	$39_0^1 40_0^2 42_0^1$	43665	$35_0^2 42_0^2$
42870	$39_0^1 42_0^1$	43236	$35_0^1 40_0^1$	43691	$35_0^1 36_0^1 39_0^1$
42881	38_0^1	43269	$36_0^1 38_0^1$	43722	$35_0^2 40_0^1$
42893	37_0^1	43293	$39_0^3 / 35_0^1 40_0^1 42_0^1$	43751	$35_0^1 36_0^1 38_0^1$
42922	40_0^2	43303	$35_0^1 39_0^1$	43789	$35_0^2 39_0^1$
42939	$38_0^1 42_0^1$	43322	$34_0^1 39_0^1$	43808	$34_0^1 35_0^1 39_0^1$
42947	$37_0^1 42_0^1$	43354	36_0^2	43833	$35_0^1 36_0^2$
42966	36_0^1	43367	$35_0^1 38_0^1$	43851	$35_0^2 39_0^1 42_0^1$
42985	$39_0^1 40_0^1$	43381	$35_0^1 37_0^1$	43871	$34_0^1 35_0^1 38_0^1$
43000	$38_0^1 42_0^2$	43387	$34_0^1 38_0^1$	43892	$35_0^1 36_0^2 42_0^1$
43021	$36_0^1 42_0^1$	43409	$36_0^2 42_0^1$	43911	$35_0^2 38_0^1 42_0^1$
43045	39_0^2	43425	$35_0^1 38_0^1 42_0^1$	43932	$35_0^2 36_0^1$
43065	35_0^1	43433	$36_0^1 39_0^2$	43991	$35_0^2 36_0^1 42_0^1$

Table 2.6. ZEKE peak positions (cm^{-1}) and assignments of the Cu-bn complexes.

Positions	Assignments	Positions	Assignments	Positions	Assignments
H-bond I		41887	?	42370	$43_0^1 45_0^1 / 47_0^2 49_0^1 50_0^1$
41207	0_0^0	41900	47_0^1	42380	$42_0^1 47_0^1$
41296	50_0^1	41947	$47_0^1 51_0^1$	42409	$41_0^1 47_0^1$
41349	49_0^1	41957	45_0^1	42426	47_0^3
41384	50_0^2	41975	$47_0^1 50_0^1$	42455	$41_0^1 47_0^1 51_0^1$
41441	47_0^1	41992	$47_0^1 51_0^2$	42472	$47_0^3 51_0^1$
41489	46_0^1	42020	44_0^1	42500	$47_0^3 50_0^1$
41530	$47_0^1 50_0^1$	42031	$47_0^1 49_0^1$	42516	$47_0^3 51_0^2$
41577	44_0^1	42051	43_0^1	42544	$44_0^1 47_0^2$
41583	$47_0^1 49_0^1$	42066	$44_0^1 51_0^1$	42575	$41_0^1 44_0^1 51_0^1$
41618	$47_0^1 50_0^2$	42078	$47_0^1 49_0^1 51_0^1$	42584	$44_0^1 47_0^2 51_0^1$
41676	47_0^2	42093	$43_0^1 51_0^1 / 44_0^1 50_0^1$	42589	$44_0^1 47_0^2 51_0^1$
41724	$46_0^1 47_0^1$	42108	$47_0^1 49_0^1 50_0^1$	42604	$47_0^3 49_0^1 51_0^1$
41800	41_0^1	42121	$42_0^1 / 43_0^1 50_0^1$	42618	$44_0^1 47_0^2 50_0^1$
H-bond II		42150	41_0^1	42630	$41_0^1 42_0^1 / 43_0^1 45_0^1 47_0^1$
41611	51_0^0	42163	$47_0^2 / 42_0^1 51_0^1$	42687	47_0^4
41638	0_0^0	42181	$43_0^1 49_0^1$	42732	$47_0^4 51_0^1$
41684	51_0^1	42197	$41_0^1 51_0^1$	42760	$47_0^4 50_0^1$
41711	50_0^1	42208	$47_0^2 51_0^1$	42807	$44_0^1 47_0^3$
41731	51_0^2	42238	$47_0^2 50_0^1$	42826	$47_0^4 49_0^1$
41758	$50_0^1 51_0^1$	42255	$47_0^2 51_0^2 / 42_0^1 49_0^1$	42836	$43_0^1 47_0^3$
41770	49_0^1	42280	$44_0^1 47_0^1 / 41_0^1 49_0^1$	42850	$44_0^1 47_0^3 51_0^1$
41783	50_0^2	42297	$47_0^2 49_0^1$	42882	$44_0^1 47_0^3 50_0^1$
41817	$49_0^1 51_0^1$	42310	$43_0^1 47_0^1$	42893	$47_0^4 49_0^1 51_0^1$
41827	48_0^1	42326	$44_0^1 47_0^1 51_0^1$	42937	$44_0^1 47_0^3 49_0^1$
41844	$49_0^1 50_0^1$	42338	$47_0^2 49_0^1 51_0^1$	42953	47_0^5
41863	$49_0^1 51_0^2$	42349	$45_0^1 47_0^1 49_0^1 ?$	42993	$47_0^5 51_0^1$
41871	$48_0^1 51_0^1$	42356	$43_0^1 47_0^1 51_0^1$		

Table 2.7. Adiabatic ionization energies (AIE, eV) and vibrational frequencies (cm^{-1}) of Cu-diamine complexes from ZEKE measurements and MP2/6-311+G(*d,p*) calculations.

Complexes	Vibrational Description		ZEKE	MP2
Cu-en		AIE	43491(5)	40600
	N-C stretch	ν_{21}^+	1013	1062
	Cu-N stretch (with N displacement)	ν_{28}^+	474	473
	NH ₂ rock	ν_{30}^+	296	318
	H-bond stretch	ν_{31}^+ / ν_{31}	214 / 197	223 / 197
	Cu-N-C bend	ν_{32}^+ / ν_{32}	141 / 121	150 / 133
	Cu-N-C-C torsion	ν_{33}^+ / ν_{33}	47 / 35	57 / 62
Cu-meen		AIE	36022 (16)	32665
	Cu-N stretch (with N displacement)	ν_{35}^+	449	471
	NCCNC twist	ν_{38}^+	248	259
	Cu-N stretch (with Cu displacement)	ν_{40}^+	201	213
	NCCNC twist	ν_{42}^+ / ν_{42}	95 / 80	109 / 79
Cu-dmen		AIE	36284 (20)	32590
	NH ₂ scissor	ν_{13}^+	1646	1644
	CH ₂ rock	ν_{25}^+	1312	1334
	Cu-N stretch (with N displacement)	ν_{41}^+	469	494
	N-Cu-N bend	ν_{48}^+	209	212
	Cu-N stretch (with Cu displacement)	ν_{49}^+	199	207
	N-(CH ₃) ₂ rock	ν_{50}^+ / ν_{50}	144 / 123	160 / 119
Cu-tren		IE	36250(300) ^a	32260
Cu-tmen		IE	34950(300) ^a	32180
Cu-pn				
H-bond I		AIE	42380 (5)	38987
	Ligand chain distortion	ν_{41}^+	105	116
	CuNH ₂ rock	ν_{42}^+	73	77
H-bond II		AIE	42582 (5)	39623
	Cu-N stretch (with C-C-C bend)	ν_{34}^+	506	505
	Cu-N stretch	ν_{35}^+	487	483
	NH ₂ rock (with H-bond stretch)	ν_{36}^+	388	408
	C-C-C bend	ν_{37}^+	315	356
	NH ₂ rock	ν_{38}^+	303	328
	H-bond stretch	ν_{39}^+	236	248
	Cu-N-C bend	ν_{40}^+	170	180
	CuNH ₂ rock	ν_{42}^+	57	68

Table 2.7 continued

Cu-bn			
H-bond I	AIE	41638	38749
Cu-N stretch (with chain distortion)	ν_{41}^+	512	514
Ligand chain distortion	ν_{42}^+	483	490
H-bond stretch (with chain distortion)	ν_{43}^+	413	444
NH ₂ rock (with chain distortion)	ν_{44}^+	382	396
Ligand chain distortion	ν_{45}^+	319	341
H-bond stretch	ν_{47}^+	262	270
Ligand chain distortion	ν_{48}^+	191	194
Ligand chain distortion	ν_{49}^+	133	138
Ligand chain distortion	ν_{50}^+	73	77
Ligand chain distortion	ν_{51}^+	46	53
H-bond II		41207	38281
Cu-N stretch with N-C-C bend	ν_{41}^+	593	590
NH ₂ rock (with chain distortion)	ν_{44}^+	370	371
H-bond stretch	ν_{46}^+	283	296
H-bond stretch (with chain distortion)	ν_{47}^+	234	238
Ligand chain distortion	ν_{49}^+	142	145
Cu-N-C bend	ν_{50}^+	89	93

^a From photoionization efficiency measurements.

Table 2.8. Vibrational frequencies (cm^{-1}) of the observed isomers of Cu-en, -meen, -dmen, -pn, and -bn from MP2/6-311+G(*d,p*) calculations.

complexes	isomers	vibrational frequencies	
		neutral	ion
Cu-en	H-bond I	3647, 3568, 3549, 3467, 3148	3635, 3544, 3539, 3359 3182
		3138, 3059, 3054, 1652, 1613	3132, 3103, 3075 1658, 1588
		1522, 1514, 1451, 1416, 1356	1528, 1516, 1447, 1415, 1371
		1348, 1256, 1204, 1132, 1093	1349, 1296, 1223, 1158, 1121
		1065, 992, 934, 900, 840 587	1062, 1003, 954, 912, 862
		496, 353, 317, 251 197, 133 62	696, 524, 473, 337, 318 223 150, 57
Cu-meen	ring	3609, 3557, 3514, 3188, 3151	3583, 3535, 3506, 3207 3181
		3143, 3117, 3072, 3036, 3031	3174, 3146, 3110 3083, 3080
		1639, 1529 1522, 1511, 1498	1644, 1533 1525, 1517, 1504
		1482 1465, 1426, 1402, 1344	1479 1469, 1431, 1406, 1351
		1311, 1256, 1188, 1161 1122	1332, 1257, 1203, 1154 1135
		1088, 1028, 1007, 952, 908	1092, 1063, 1020, 1005, 976
		874, 821, 554 432, 411 368	878, 833, 626 527, 471, 438
		255, 216, 178, 161 128, 79	333, 259 218, 213, 180, 109
Cu-dmen	ring	3605, 3510, 3186, 3184, 3154	3583, 3506, 3201, 3200, 3176
		3138, 3134, 3105 3070, 3005	3163, 3161, 3131, 3108, 3060
		3001, 3000, 1638, 1526, 1520	3058, 3058 1644, 1530, 1527
		1514, 1509, 1498, 1496, 1476	1520, 1516, 1505, 1501, 1483
		1451, 1433, 1402, 1350, 1319	1461, 1440, 1405, 1354, 1334
		1299, 1278, 1208, 1150, 1127	1280, 1265, 1227 1150, 1135
		1116, 1073, 1065, 1017, 1001	1122, 1083, 1050, 1027, 1013
		933, 898, 796, 562, 448, 428	955, 890 795, 622, 528, 494
		420, 381, 298, 277, 245, 224	442, 408, 358, 292, 283, 245
		171, 126, 119, 73	212, 207, 160, 104

Table 2.8 continued

Cu-pn	H-bond I	3622, 3540, 3527, 3427 3151	3606, 3519, 3510, 3170, 3143
		3123, 3111, 3091, 3056, 3041	3135, 3109, 3095, 3080, 3070
		1662, 1646, 1528, 1510, 1485	1673, 1646, 1528, 1515, 1487
		1441, 1420, 1410, 1389, 1348	1448, 1441, 1419, 1391, 1355
		1308, 1252, 1203, 1141, 1100	1332, 1277, 1257, 1142, 1118
		1089, 1034, 978, 968 879, 870	1080, 1050, 1013, 959, 901
		825, 592, 520, 439, 332, 308	885, 839, 742, 587, 489, 382
	261, 174, 139 97, 58	339, 302, 224, 176, 116, 77	
	H-bond II	3616, 3551, 3518, 3423, 3135	3608, 3524, 3523, 3166, 3144
		3129, 3107, 3069, 3050, 3039	3142, 3137, 3095, 3082, 3056
		1647, 1617, 1532, 1519, 1486	1650, 1620, 1535, 1519, 1485
		1453, 1440, 1399, 1373, 1339	1458, 1437, 1412, 1388, 1358
		1317, 1231, 1219, 1152, 1104	1318, 1280, 1242, 1160, 1130
		1097, 1060, 971, 968, 908	1091, 1052, 1009, 965, 912
869, 833, 615, 497, 407, 330		881, 838, 746, 505, 483, 408	
326, 300, 236, 147, 97, 55	356, 328, 248, 180, 83, 68		
Cu-bn	H-bond I	3612, 3533, 3519, 3286, 3130	3592, 3514, 3509, 3159, 3131
		3121, 3116, 3110, 3061, 3050	3124, 3122, 3089, 3072, 3067
		3044, 3043, 1659, 1640, 1528	3036, 2888, 1674, 1643, 1528
		1517, 1489, 1486, 1454, 1441	1525, 1493, 1488, 1478, 1441
		1413, 1395, 1391, 1349, 1318	1427, 1413, 1391, 1351, 1327
		1295, 1250, 1212, 1152, 1133	1308, 1272, 1236, 1157, 1150
		1120, 1060, 1039, 1032, 937	1115, 1087, 1048, 1021, 963
	923, 872, 855, 778, 640, 483	934, 874, 869, 783, 757, 514	
	451, 365, 346, 318, 302, 244	491, 444, 396, 341, 310, 271	
	159, 130, 71, 51	194, 138, 77, 53	
	H-bond II	3614, 3534, 3522, 3306, 3146	3591, 3508, 3507, 3164, 3133
		3115, 3107, 3105, 3087, 3053	3129, 3123, 3100, 3077, 3065
		3049, 3042, 1667, 1644, 1529	3058, 2871, 1689, 1641, 1529
		1510, 1489, 1486, 1440, 1434	1514, 1492, 1488, 1481, 1443
1410, 1409, 1389, 1345, 1320		1420, 1416, 1392, 1357, 1341	
1290, 1252, 1223, 1154, 1122		1319, 1284, 1250, 1153, 1126	
1105, 1060, 1045, 1001, 945		1105, 1089, 1030, 1026, 973	
924, 872, 832, 772, 650, 503	943, 874, 843, 783, 779, 590		
474, 361, 338, 322, 265, 211	494, 417, 371, 333, 296, 237		
136, 116, 74, 49	170, 145, 93, 68		

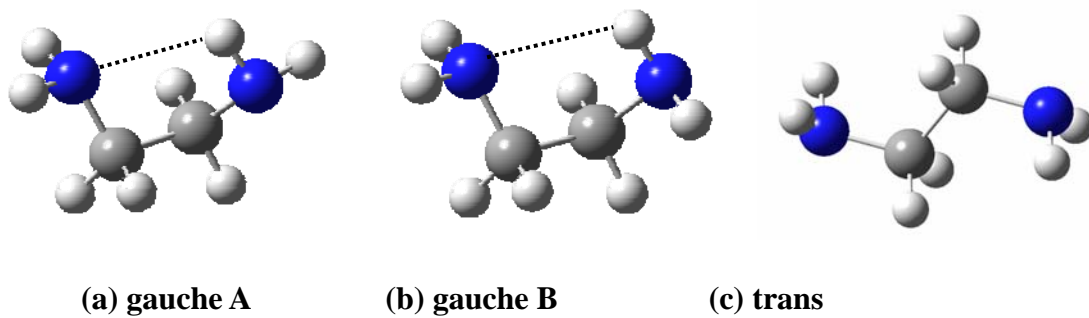


Figure 2.1. Low-energy rotational isomers of ethylenediamine.

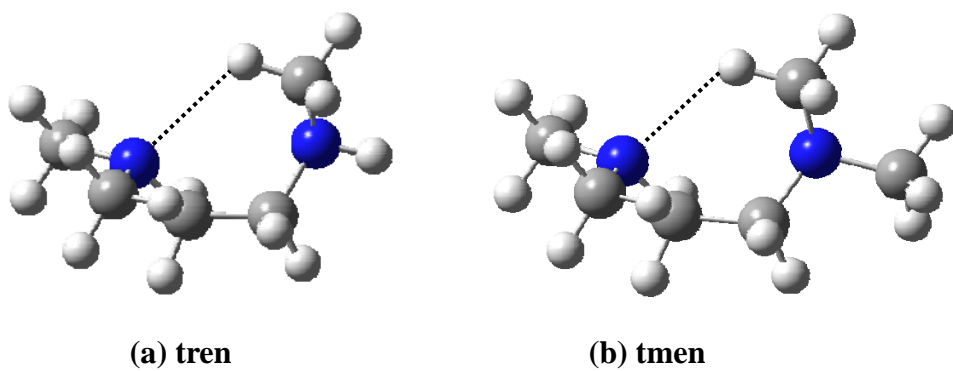
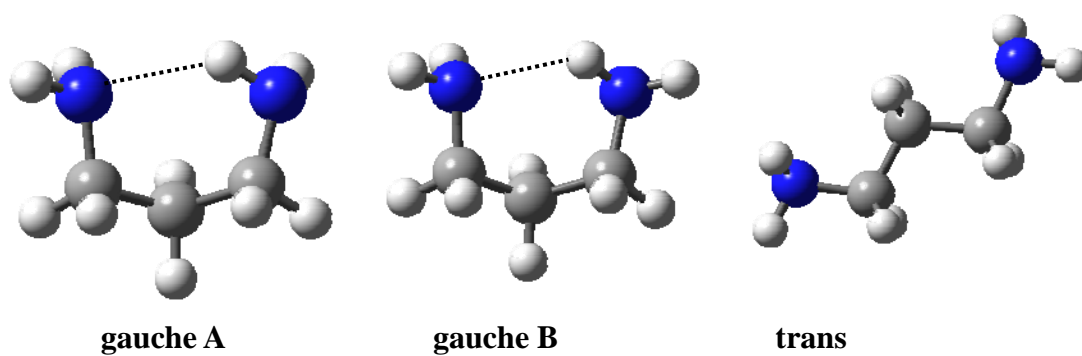
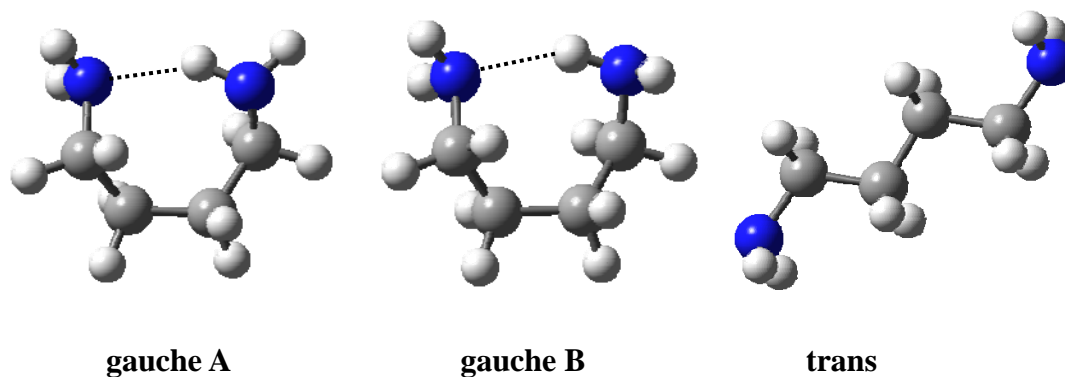


Figure 2.2. CH...N hydrogen-bonded isomers of N,N,N'-trimethylethylenediamine (a) and N,N,N',N'-tetramethylethylenediamine (b).

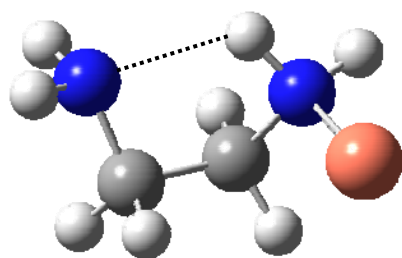


(a) 1, 3-propanediamine

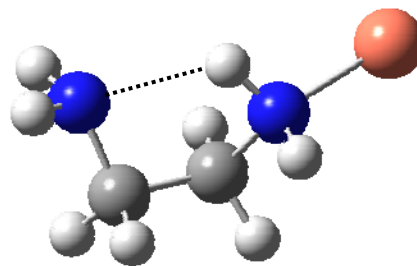


(b) 1, 4-butanediamine

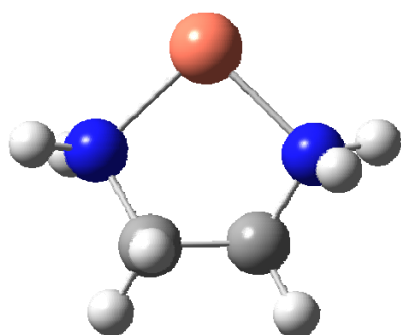
Figure 2.3. Low-energy rotational isomers of 1,3-propanediamine (a) and 1,4-butanediamine (b).



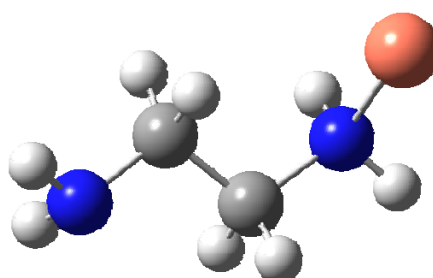
(a) H-bond I



(b) H-bond II



(c) ring



(d) trans

Figure 2.4. Rotational isomers of Cu-ethylenediamine.

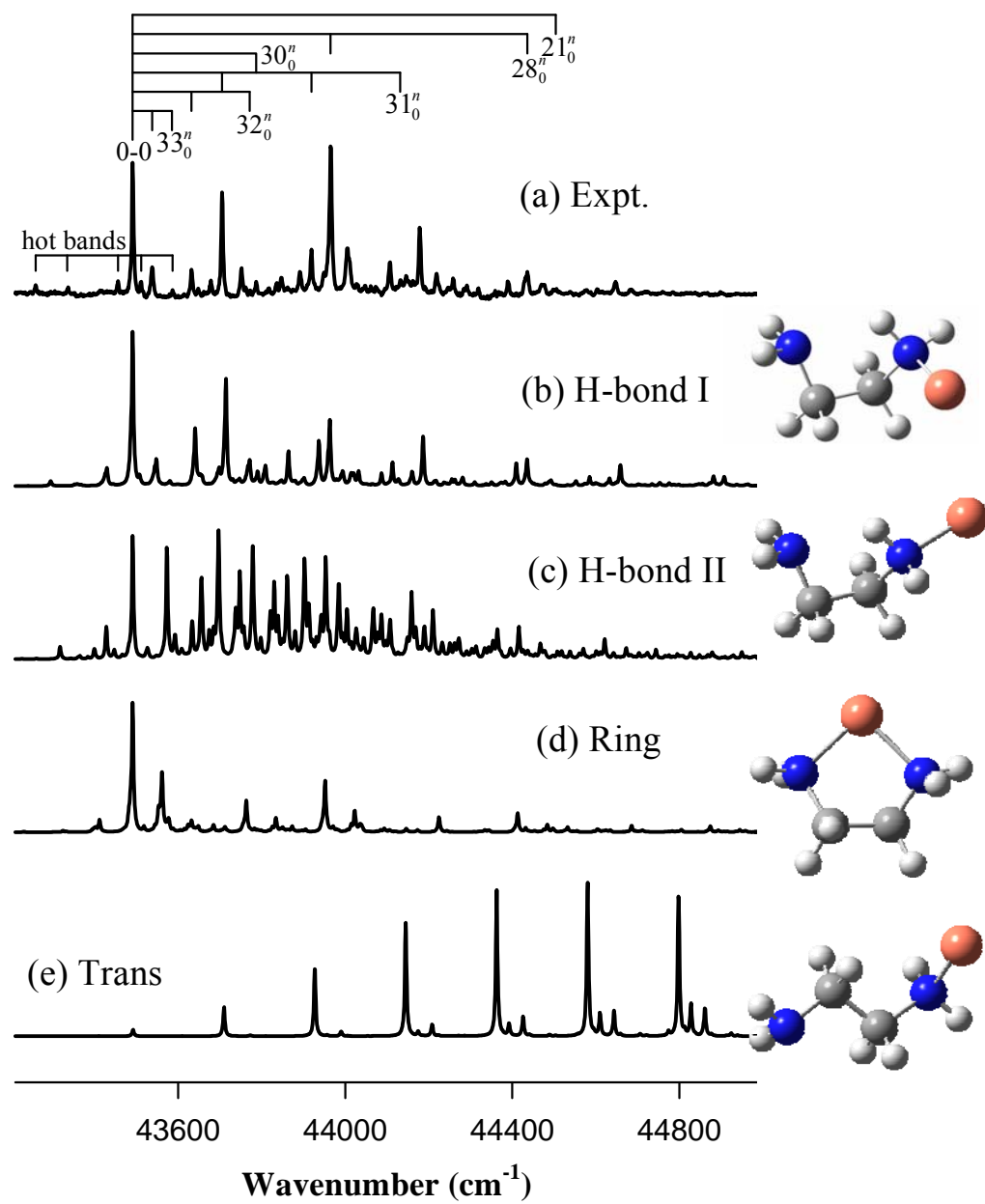


Figure 2.5. Experimental ZEKE spectrum of Cu-ethylenediamine and simulations of four Cu-ethylenediamine isomers (b) - (e).

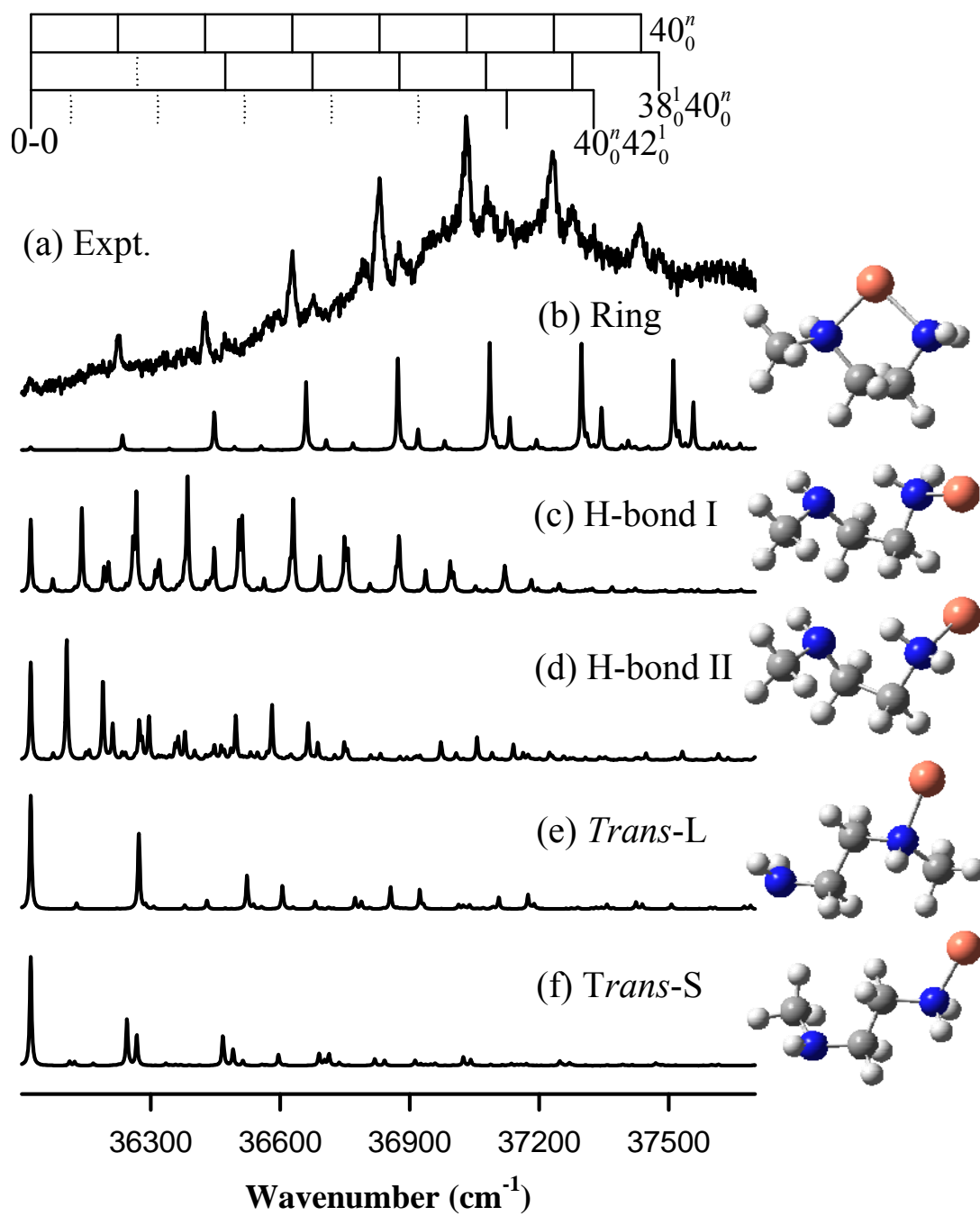


Figure 2.6. Experimental ZEKE spectrum of Cu-(N-methylethylenediamine) (a) and simulations of five Cu-(N-methylethylenediamine) isomers (b) - (f).

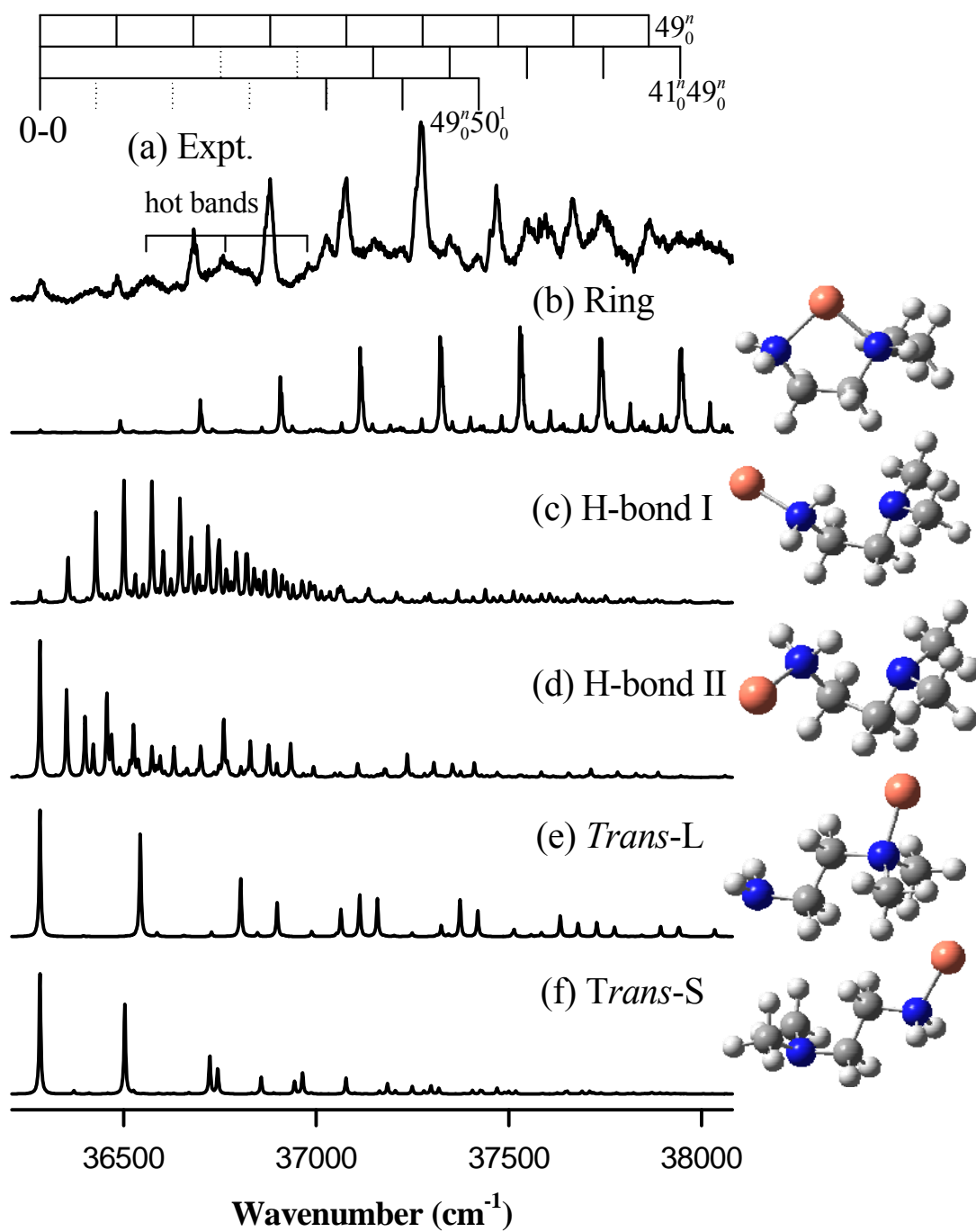


Figure 2.7. Experimental ZEKE spectrum of Cu-(N,N-dimethylethylenediamine) (a) and simulations of five Cu-(N,N-dimethylethylenediamine) isomers (b) - (f).

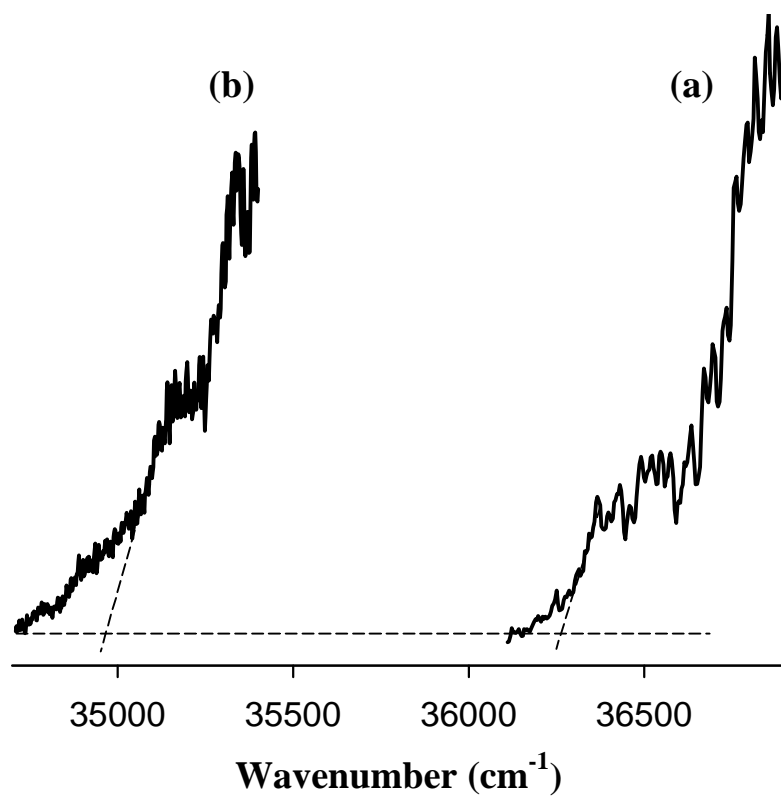


Figure 2.8. Photoionization efficiency spectra of Cu-(N,N,N'-trimethylethylenediamine) (a) and -(N,N,N',N'-tetramethylethylenediamine) (b).

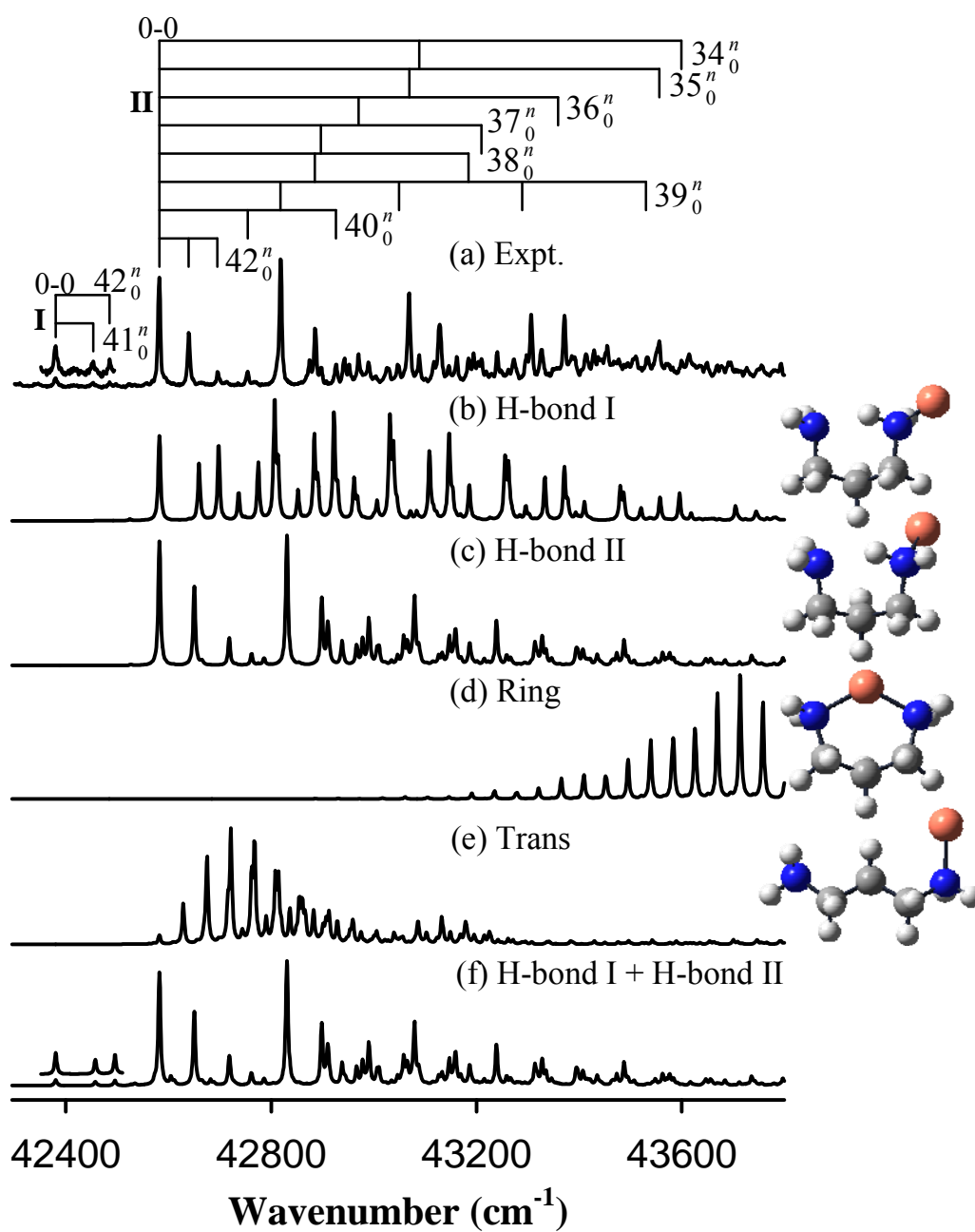


Figure 2.9. Experimental ZEKE spectrum and simulations from H-bond I (b), H-bond II (c), Ring (d), Trans (e), and a mixture of H-bond I and II (f) isomers of Cu(1,3-propanediamine).

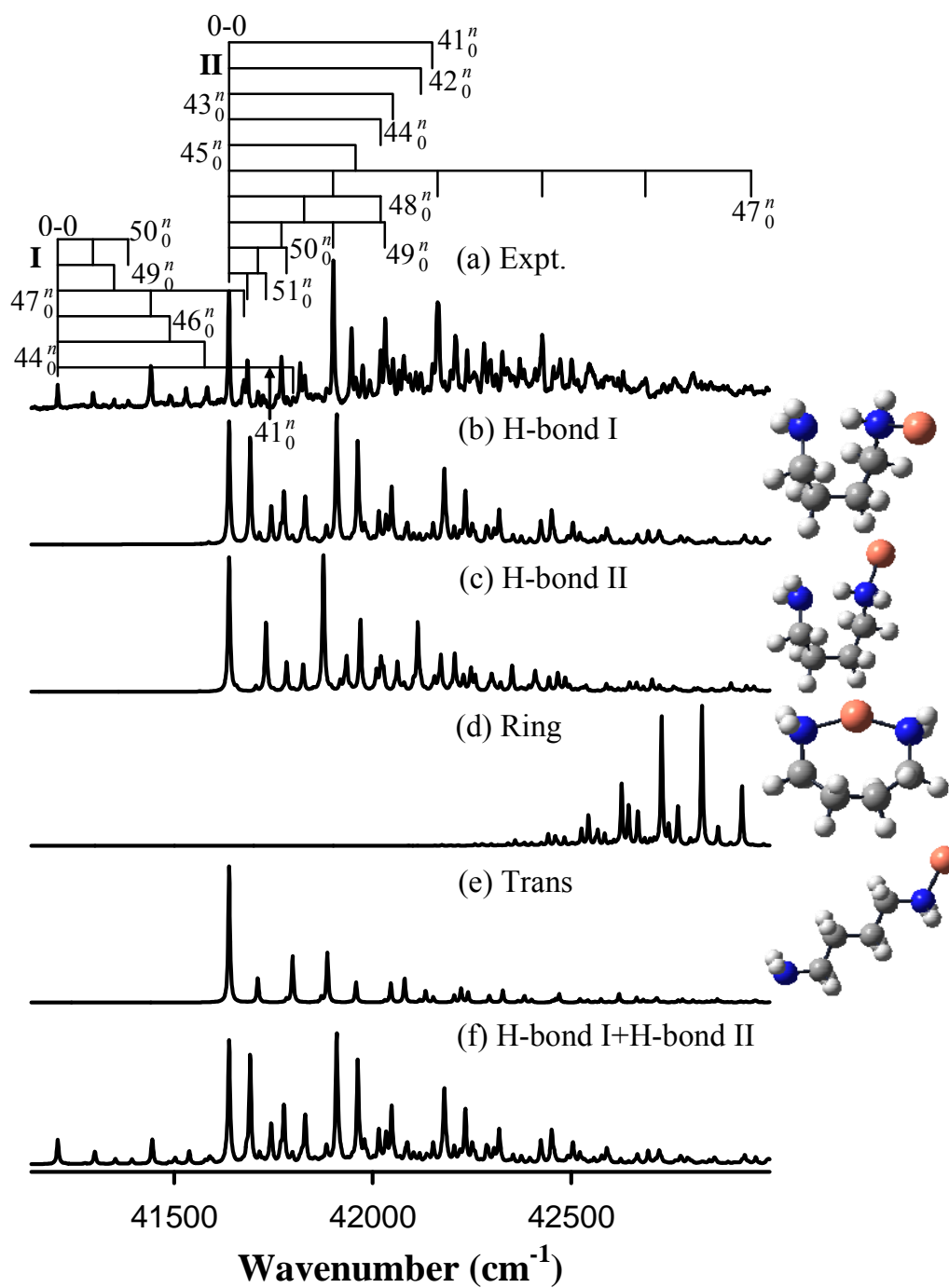


Figure 2.10. Experimental ZEKE spectrum (a) and simulations (20 K) from H-bond I (b), H-bond II (c), Ring (d), Trans (e), and a mixture of H-bond I and II (f) isomers of Cu(1,4-butanediamine).

Copyright © Xu Wang 2007

Chapter 3 Spectroscopy and structures of copper-(pyridine)_n (n=1,2) complexes

Pyridine (Figure 3.1), a six-membered cyclic aromatic molecule with σ and π binding capabilities through its nitrogen electron lone pair and π system, respectively, has inspired considerable interests in its bonding with metals over the last ten years. A number of experimental and theoretical investigations have established that most metal-pyridine complexes are σ complexes.¹⁶⁰⁻¹⁶⁸ The bond energies of pyridine σ complexes with various metal atoms and ions have been measured by photodissociation,¹⁶⁰ CID,¹⁶⁹ and ion-ligand reaction kinetics via mass spectrometry.¹⁷⁰ On the other hand, a few of π complexes (i.e. Mg⁺- and Au⁺-pyridine) have been predicted by theoretical calculations to be local minimum energy structures but with relatively higher energies.^{162,164,168} In addition, the bonding of pyridine to copper surfaces has been described by both σ and π interactions.¹⁷¹⁻¹⁷³ In fact, a recent photoelectron spectroscopic and ab initio theoretical study by Edmonds and coworkers suggests that the anionic Co⁻-pyridine and Co⁻-(pyridine)₂ complexes are formed via π bonding.¹⁷⁴ Therefore, it would be interesting to determine the bonding interaction between pyridine and other transition metal atoms such as copper.

Miyawaki and Sugawara reported the PFI-ZEKE spectrum of Cu-pyridine seeded in helium carrier gas.¹⁷⁵ This spectrum is dominated by vibrational progressions that belong to the metal-ligand stretching vibrations of the neutral and ionic complexes. In addition to these major progressions, satellite peaks were assigned to sequence bands. Unfortunately, these spectral assignments were made without changing the carrier gas conditions (vibrational temperatures) or by performing theoretical calculations. However, our previous studies have demonstrated that argon more efficiently cools the

molecular beam.^{78,94} Thus, the intensity of the sequence bands should decrease if argon is used in stead of helium, assuming their spectral assignment is correct. In addition, theoretical calculations can be used to simulate the spectra at finite temperatures to estimate the vibrational temperature of the metal complexes seeded in a molecular beam. Furthermore, theoretical calculations will provide insight into the bonding and structures of these pyridine complexes.

In this chapter, the ZEKE spectra of Cu-pyridine and Cu-(pyridine)₂ are presented. Compared to the previous work on the Cu-pyridine complex, our spectrum has a higher signal-noise ratio and shows more transitions.¹⁷⁵ In addition, we have combined quantum chemistry and FC factor calculations with our experimental results to determine bonding modes and molecular conformations of the Cu-pyridine and Cu-(pyridine)₂ complexes. From these comparisons, we have also determined that some of the assignments in the previous work were incorrect.

3.1 Experimental and computational methods

Copper complexes were prepared by reactions of copper atoms with the vapor of pyridine (99.9+%, Aldrich) in molecular beams. The metal atoms were produced by pulsed laser vaporization of a copper rod (99.9%, Alfa Aesar) with the second harmonic output of a Nd:YAG laser (Quanta-Ray, GCR-3, 532 nm, ~ 3 mJ) in the presence of a carrier gas (He or Ar, ultra-high purity, Scott-Gross) at ~ 50 psi. At room temperature, ligand vapor was introduced downstream from the ablation region by a stainless steel capillary to a small reaction chamber (~ 1.5 mL). Metal complexes were formed by the interactions between these ligand molecules and copper atoms entrained in the carrier gas.

Ionization was carried out by a frequency-doubled dye laser (Lumonics HD-500), pumped by a XeCl excimer laser (Lumonics, PM-884, 308 nm). The production of the

1:1 and 1:2 Cu-pyridine complexes was maximized by optimizing the timing and power of the vaporization and photoionization lasers, the amount of the ligand vapor, and the backing pressure of the carrier gas. ZEKE electrons were produced by photoexcitation of neutral molecules to high-lying Rydberg states, followed by a $\sim 3 \mu\text{s}$ delayed, pulsed electric field ionization (1.2 V cm^{-1} , 100 ns) of these Rydberg states. Laser wavelengths were calibrated against titanium or vanadium atomic transitions.¹⁷⁶

Calculations of the molecular geometries and vibrational frequencies were carried out using the B3P86 and MP2 methods and 6-311+G(*d,p*) basis, implemented in the GAUSSIAN 03 program.⁸⁵ Multidimensional FC factors were computed from the theoretical equilibrium geometries, harmonic frequencies, and normal modes of the neutral and ionic complexes.^{143,177} Spectral broadening was simulated by giving each line a Lorentzian line shape with the linewidth of the experimental spectrum. Boltzmann distributions were used to simulate spectra at specific temperatures.

3.2 Results and discussion

3.2.1 Cu-pyridine

Figure 3.2 (a) shows the ZEKE spectrum of Cu-pyridine seeded in He carrier gas. The spectrum has a linewidth of 7 cm^{-1} , which is 3 cm^{-1} narrower than the reported ZEKE spectrum of Cu-pyridine with the same carrier by Miyawaki and Sugawara.¹⁷⁵ In addition, several more peaks are observed compared to the previous work. The first strong peak at 43703 cm^{-1} is assigned to the 0-0 transition between the ground vibronic states of the neutral and ionic species. Above the 0-0 transition, the spectrum displays two vibrational intervals (167 and 654 cm^{-1}) and a major vibrational progression with five 272 cm^{-1} intervals. A number of satellite peaks separated by $\sim 34 \text{ cm}^{-1}$ intervals are superimposed on the 272 cm^{-1} vibrational progression. On the lower energy side of the 0-0 transition are two small peaks at 196 and 161 cm^{-1} relative to the origin band. A

sharp line marked by an asterisk located at 44915 cm^{-1} arises from the Cu $^4D_{1/2}^0 \leftarrow ^2S_{1/2}$ atomic transition.¹⁴²

Miyawaki and Sugawara assigned the 272 cm^{-1} and 196 cm^{-1} vibrational intervals to the Cu-pyridine symmetric stretch of the ionic and neutral Cu-pyridine complexes, respectively.¹⁷⁵ Furthermore, the satellite peaks in their spectrum were assigned to two series of transitions. The first series of satellite peaks near the major stretch progression were attributed to sequence transitions from the first of the Cu-pyridine in-plane bending level of the neutral molecule to the first Cu⁺-pyridine in-plane bending level of the ion. The second series of bands were assigned to the transitions from the first Cu-pyridine symmetric stretching level of the neutral molecule up to the fourth Cu⁺-pyridine symmetric stretching level of the ion. However, the latter assignment is suspicious, because direct transitions from the first vibrational level of the neutral molecule to the third or fourth vibrational levels in the ionic complex are not reasonable and are rarely observed in our previous ZEKE measurements on nitrogen containing copper complexes.^{85,90,92,94} To verify our suspicion and assign additional ZEKE bands in our spectra, the theoretical calculations are performed using both the B3P86 and MP2 methods with 6-311+G(*d,p*) basis set.

In our calculations of the Cu-pyridine complexes, σ and π structures were considered to be formed by Cu binding to the nitrogen atom and to the six-membered π ring, respectively. However, no minimum energy π structure was found for the neutral and ionic species. Table 3.1 lists point groups, electronic states and energies, equilibrium geometries, and vibrational frequencies of the Cu-pyridine σ complexes from the B3P86 and MP2 calculations. Both B3P86 and MP2 calculations predict a σ configuration in C_{2v} symmetry, where the Cu atom is coplanar to the six-membered π ring. Both methods predict very little geometry change of the pyridine ring upon complexation. The Cu-N distance is predicted to be 0.03 \AA longer by the B3P86 method than the MP2 method. Upon ionization, the Cu-N distance is shortened due to reduced repulsion

between the Cu $4s^1$ and N lone-pair electrons and additional charge-dipole attraction. The B3P86 method predicts a slightly larger reduction (~ 0.13 Å) of the Cu-N distance than the MP2 method (~ 0.11 Å).

Figure 3.2 (b) and (c) show the spectral simulations of the $^1A_1 \leftarrow ^2A_1$ transition of the Cu-pyridine σ complexes from the B3P86 and MP2 calculations at 60 K. The simulations are obtained using the B3P86 or MP2 geometries, harmonic vibrational frequencies, and force fields of the neutral and ionic states. The calculated 0-0 transition energies are shifted to the measured value for easy comparison of the experimental and calculated spectral profiles. Both simulations are in fairly good agreement with the ZEKE spectrum, but the B3P86 simulation has slightly longer progressions compared to the experimental spectrum. The longer progressions in the B3P86 simulation are consistent with the B3P86 prediction of a larger reduction in the Cu-N distance upon ionization. Furthermore, the B3P86 simulation does not reproduce the sequence bands as clearly as the MP2 simulation. Therefore, the MP2 method yields a better overall prediction of the FC profile arising from the geometry changes upon ionization of the Cu-pyridine σ complex. Hence, the spectral assignments will be discussed by comparison to the MP2 simulations only.

The reported assignments of the 272 and 196 cm^{-1} intervals (ν_{11}^+/ν_{11}) by Miyawaki and Sugawara are confirmed by comparison of the experimental and simulated spectra in this work. However, the satellite peaks were not assigned correctly in their work. According to our simulation, the satellite peaks and the 161 cm^{-1} interval above the 0-0 band originate from the first or second excited Cu-pyridine out-of-plane bending level (ν_{20}) of the neutral molecule. From this assignment, the frequency difference of the Cu-pyridine out-of-plane bending mode in the neutral (ν_{20}) and ionic molecule (ν_{20}^+) is determined to be 34 cm^{-1} . The 167 cm^{-1} interval is assigned to an overtone transition of the Cu^+ -pyridine out-of-plane bend. This vibration mode has b_1 symmetry and follows the selection rule $\Delta v = \pm 2, \pm 4, \dots$. Thus, the Cu/ Cu^+ -pyridine (ν_{20}/ν_{20}^+) out-of-plane

bending frequencies are derived to be 50 and 84 cm^{-1} , respectively. The 654 cm^{-1} (ν_{10}^+) interval is attributed to a ring breathing vibration localized on the ligand. All the peak positions and assignments are listed in Table 3.2.

The hot transitions in this ZEKE spectrum were confirmed by measurements with Ar as the carrier gas. In this spectrum [Figure 3.3 (a)], the hot transitions observed with He carrier are largely depressed due to the lower vibrational temperature of the molecular beam. In addition, the linewidth is reduced from 7 to 5 cm^{-1} due to a lower rotational temperature of the argon-seeded complex. Two cold transitions of 10_0^1 and $11_0^2 20_0^2$ are not clearly displayed in this spectrum due to the limited size of the ZEKE signal in Ar carrier. To estimate the vibrational temperature of the argon-seeded complex, we performed simulations at various temperatures. By comparing each simulation to the experimental spectrum, we found that the vibration temperature is approximately 5 K [Figure 3 (b)].

3.2.2 Cu-(pyridine)₂

Figure 3.4 (a) presents the ZEKE spectrum of Cu-(pyridine)₂ seeded in He carrier gas. This spectrum displays a remarkably different profile from that of Cu-pyridine. First of all, the origin band is located at 29917 cm^{-1} , about 14000 cm^{-1} lower in energy than the IE of the Cu-pyridine complex. Secondly, the linewidth of each band in the ZEKE spectrum of the Cu-(pyridine)₂ complex is much wider, FWHM \sim 40 cm^{-1} . Furthermore, many more different vibrational intervals are identified in this spectrum. Six vibrational intervals are labeled in the spectrum by *a*, *b*, *c*, *d*, *e*, and *f*. Intervals *a*, *b*, *c*, *d*, and *f* have frequencies of 194, 658, 1023, 1089, and 1626 cm^{-1} , respectively. Interval *e* is formed by the combination of *c* and a frequency of \sim 1225 cm^{-1} .

All peak positions and the corresponding assignments are listed in Table 3.2. These assignments were made by comparing the ZEKE spectrum to the spectral (B3P86 and

MP2) simulations of eclipsed and staggered isomers. The theoretical work of Cu-(pyridine)₂ presented in this dissertation excludes the π structure, because such a local minimum energy structure was not located for the Cu-pyridine complex. Therefore, the Cu-(pyridine)₂ complex should be formed by Cu atom σ binding to the nitrogen of each pyridine molecule. Two structures were considered in these calculations, an eclipsed D_{2h} structure and a staggered D_{2d} structure. The optimized structures are illustrated in Figures 3.5 and the corresponding point groups, electronic states, equilibrium energies and geometries, and vibrational frequencies predicted by B3P86 and MP2 theories are listed in Table 3.3.

According to the B3P86 calculations, the ground electronic states of the neutral and ionic Cu-(pyridine)₂ complexes are ²B_{3u} and ¹A_g under D_{2h} symmetry (eclipsed structures). A staggered D_{2d} structure of the ion complex in ¹A₁ state is located at ~ 170 cm⁻¹ above the ground ¹A_g electronic state. Calculations of the corresponding neutral Cu-(pyridine)₂ molecule in the staggered configuration were converged back to the eclipsed structure. The optimized Cu-N distance in the Cu-(pyridine)₂ complex is much shorter than that in the Cu-pyridine complex as seen in Table 3.3. Accordingly, the pyridine rings in Cu-(pyridine)₂ undergo slightly larger geometry changes than the one in Cu-pyridine upon complexation.

Ionization of the ²B_{3u} state will generate the ¹A_g state, where the Cu-N distance is slightly elongated and the pyridine rings have nearly the same geometry as that in free ligand. Mulliken population analysis of the ²B_{3u} state shows a negative charge (-0.25) on the Cu atom, and this charge is mainly localized in the HOMO consisting primarily of a Cu 3p _{π} orbital directed perpendicular to the ligand plane. Thus, the metal-ligand bonds are largely enhanced by electron donation from the π clouds of the ligands to the Cu 3p _{π} orbital. Such electron donation explains the shorter Cu-N bond length in the neutral species compared to the ions. Upon ionization, the Cu cations of the ionic complexes in ¹A_g and ¹A₁ states are predicted to bare a less negative charge (-0.13) and

positive charge (+0.18), respectively. The Cu-N bond lengths in the ion are slightly longer than those in the neutral complex due to the lack of π electron donation.

Although the calculated eclipsed 1A_g state lies $\sim 170\text{ cm}^{-1}$ above the staggered 1A_1 state, transitions to the 1A_1 state will have a much longer FC profile than the experimental spectrum due to the large structural difference between the eclipsed and staggered configurations. Therefore, the Cu-(pyridine)₂ ZEKE spectrum is compared only to the $^1A_g \leftarrow ^2B_{3u}$ transition as shown in Figure 3.4 (b). The good agreement between the experimental and calculated spectra confirms our assignment of the $^1A_g \leftarrow ^2B_{3u}$ electronic transition. Moreover, the vibrational intervals can be easily assigned to specific modes on the basis of the one-to-one correspondence between the experimental and calculated transitions. The 194 cm^{-1} interval is assigned to the symmetric ring-Cu⁺-ring stretch (ν_{11}^+). The much shorter stretch progression in the di-ligand complex compared to that of the mono-ligand complex is consistent with the calculated structures, which predicts smaller structural differences between the neutral and ionic Cu-(pyridine)₂ complexes ($\sim 2\%$) compared to that of the Cu-pyridine complexes ($\sim 5\%$). The $658, 1023, 1089, 1225,$ and 1626 cm^{-1} vibrational intervals are attributed to a symmetric ring distortion (ν_{10}^+), a symmetric ring breath (ν_9^+), two C-H in-plane bends (ν_7^+ and ν_6^+), and a symmetric ring distortion mixed with a C-H in-plane bend (ν_4^+), respectively. According to the calculated FC factors, the much larger linewidth in the Cu-(pyridine)₂ ZEKE spectrum are attributed to unresolved $\Delta v = 0$ sequence transitions of the torsion mode (ν_{63}) and two rings in-plane bending mode (ν_{56}). In a previous study of other metal di-ligand complexes, spectral broadening was also observed due to unresolved vibrational structure of the torsion mode.¹⁷⁸ ZEKE measurements of the di-ligand complex seeded in Ar carrier gas were also performed. Although the spectral linewidth is reduced from 40 cm^{-1} in He to 27 cm^{-1} in Ar due to a lower rotational temperature and depressing of the unresolved sequence transitions, no additional vibrational band was resolved in that spectrum (not shown). Since the MP2 method provides better predictions for

Cu-(pyridine)₂, the MP2 calculations for Cu-(pyridine)₂ are also performed in this work. Like the B3P86 calculations, the MP2 geometry optimization on the neutral Cu-(pyridine)₂ complex in D_{2d} symmetry did not converge either. However, an additional geometry optimization without symmetry constraint, i.e. under the C₁ point group, yielded an essentially D_{2d} structure. This structure was determined to be a local minimum energy structure by a subsequent frequency calculation. The corresponding ionic complex was converged to a minimum energy structure in D_{2d} symmetry, as tested by the frequency analysis. Unlike the B3P86 calculations, the D_{2h} eclipsed conformers of the neutral and ionic species were predicted by the MP2 theory to have one small imaginary frequency each (Table 3.3). Subsequent calculations without symmetry constraint (i.e. C₁ symmetry), on the other hand, still reported one imaginary frequency in the neutral and ion. Such small imaginary frequencies (less than 30i cm⁻¹) are usually the result of numerical errors generated from the calculations. Accordingly, these two eclipsed conformers are considered to be local minimum energy structures in our spectral analysis. Surprisingly, the staggered D_{2d} conformers were calculated to be about 3800 cm⁻¹ lower in energy than the corresponding eclipsed D_{2h} isomers by the MP2 method.

Figure 3.4 shows that the simulations for both the D_{2h} and D_{2d} structures reproduce the lower energy portion of the experimental spectrum (29900 - 30800 cm⁻¹). However, only simulations from the eclipsed D_{2h} isomers match the higher energy region of the experimental spectrum. Therefore, the D_{2h} eclipsed structure is the predominant conformer of Cu-(pyridine)₂ prepared in the molecular beam.

3.3 Summary of the ZEKE spectroscopic measurements

Table 3.4 summarizes the AIEs, metal-ligand bond energies, and vibrational frequencies of the Cu-pyridine and Cu-(pyridine)₂ complexes from the ZEKE spectra and the B3P86 and MP2 calculations. By comparison to the ZEKE measurements, both the

B3P86 and MP2 methods predict the vibrational frequencies quite well, except for the Cu/Cu⁺-L out-of-plane bending mode of the mono-ligand complex. Both methods, however, give large errors in the AIE values. The B3P86 calculations overestimates the AIEs by ~ 5000 cm⁻¹ for Cu-pyridine and ~ 8000 cm⁻¹ for Cu-(pyridine)₂. The MP2 calculations, on the other hand, underestimates the AIEs by ~ 3000 cm⁻¹ for Cu-pyridine and by ~ 10,000 cm⁻¹ for Cu-(pyridine)₂.

Metal-ligand bond energies of the ionic Cu⁺-pyridine and Cu⁺-(pyridine)₂ complexes have been measured by mass spectrometry-based techniques.^{169,170} With the measured AIEs of the these ions, the bond energies of the neutral complexes can be calculated by a thermochemical relationship: $AIE(M-L_{n-1}) - AIE(M-L_n) = D_0^+(M-L_n) - D_0(M-L_n)$, where D_0^+ and D_0 are the bond energies of M-L_n and M⁺-L_n, respectively, and AIE(M-L_{n-1}) and AIE(M-L_n) are the adiabatic ionization energies of M-L_{n-1} and M-L_n, respectively. Through this relation, Miyawaki and Sugawara have calculated the bond energy of the Cu-pyridine¹⁷⁵ complex to be 23.2 kJ mol⁻¹ using the AIE(Cu-pyridine) of 522.8 kJ mol⁻¹ from their ZEKE measurement and the D_0^+ (Cu⁺-pyridine) of 245.9 kJ mol⁻¹ from a previous CID experiment.¹⁶⁹ This neutral bond strength is about half as weak as that in Cu-pyrimidine,¹⁷⁹ although these two complexes have very close Cu-L stretching frequencies and molecular masses. This bond energy difference may be due to the large experimental uncertainties in measuring the bond energies of Cu⁺-pyridine (± 10.1 kJ mol⁻¹)¹⁶⁹ and Cu⁺-pyrimidine (± 9.5 kJ mol⁻¹)¹⁸⁰ by the CID method. Using AIE(Cu), AIE[Cu-(pyridine)₂], and D_0^+ [Cu⁺-(pyridine)₂] (494.5 kJ mol⁻¹),¹⁷⁰ the bond energy of Cu-(pyridine)₂ is calculated to be 106.9 kJ mol⁻¹. Therefore, the metal-ligand bonding in the Cu-(pyridine)₂ complexes is strongly enhanced by the large electron donation from the ligand π clouds. Furthermore, the Cu-(pyridine)₂ has a much larger IE shift than the Cu-pyridine from the bare Cu atom, because the metal-ligand bonding in the di-ligand complex is more strongly enhanced upon ionization.

In Table 3.4, the Cu⁺-L stretching mode of Cu-pyridine and the L-Cu⁺-L stretching

mode of Cu-(pyridine)₂ are two completely different vibrational modes, the former has a fairly large Cu displacement, while the latter has no Cu displacement and is essentially a two pyridine stretching motion along L-Cu⁺-L. The frequencies of these two vibrational modes are different. The ring breathing vibrational frequencies in both complexes is blue shifted by about 50 cm⁻¹ compared to that in the free ligand.¹⁸¹ A similar blue shift has also been observed in some other ligand based vibrations in the ionic Cu-(pyridine) complex.¹⁸¹ This blue shift indicates a fairly strong Cu⁺ coordination induced by the large electron donation in this complex and is consistent with the previous reports on metal-pyridine systems.^{163,166,167,182-184}

3.4 Conclusion

The Cu-pyridine and Cu-(pyridine)₂ complexes were studied by PFI-ZEKE spectroscopy and quantum chemistry calculations. Although pyridine provides both σ and π -bonding capabilities towards metal atoms and ions, the mono-ligand and di-ligand Cu-pyridine complexes are determined to be σ structures. In the di-ligand complex, the two pyridine rings prefer the eclipsed to the staggered form.

Due to an additional Cu-N σ bond and stronger ligand π electron donation, the di-ligand complex possesses a stronger metal ligand interaction than the mono-ligand complex. Upon ionization, the metal-ligand bonding in the di-ligand complex is more strongly enhanced compared to the mono-ligand complex. Consequently, the ionization energy of the di-ligand complex is red shifted with respect to the mono-ligand complex. The ZEKE spectrum of Cu-pyridine seeded in He carrier gas shows a strong progression in the metal-ligand stretch, a number of hot transitions for the metal-ligand bending vibrations, and a ligand-based vibration. However, the spectrum of Cu-(pyridine)₂ displays several ligand-based intervals and a very short L-Cu⁺-L symmetric stretch progression. Such spectral differences are consistent with a larger change on the Cu-N

distance of Cu-pyridine upon ionization compared to Cu-(pyridine)₂ predicted by the theoretical calculations.

Table 3.1. Point groups, electronic states, equilibrium energies (E_e , a.u.), geometries (R, Å; \angle , °), and vibrational frequencies (cm^{-1}) of the Cu-pyridine σ complexes from the B3P86 and MP2 calculations using 6-311+G(d,p) basis set.

B3P86, C_{2v}
2A_1
$E_e = -1890.2220812$
Geometries:
Cu-N = 2.034, C-N = 1.339, C-C = 1.386, C-C = 1.389, Cu-N-C = 120.9, N-C-C = 122.7, C-C-C = 118.8
Frequencies:
a_1 : 3217, 3195, 3180, 1654, 1513, 1235, 1093, 1051, 1033, 636, 184; a_2 : 1002, 893, 378; b_1 : 1017, 960, 758, 709, 419, 41; b_2 : 3211, 3181, 1631, 1479, 1375, 1324, 1174, 1091, 662, 123
1A_1
$E_e = -1890.0016694$
Geometries:
Cu-N = 1.904, C-N = 1.348, C-C = 1.382, C-C = 1.389, Cu-N-C = 120.6, N-C-C = 122.0, C-C-C = 119.0
Frequencies:
a_1 : 3232, 3215, 3208, 1664, 1520, 1246, 1102, 1063, 1046, 667, 271; a_2 : 1004, 891, 392; b_1 : 1039, 966, 768, 706, 423, 111; b_2 : 3228, 3212, 1626, 1488, 1387, 1324, 1189, 1106, 658, 168
MP2, C_{2v}
2A_1
$E_e = -1886.87529$
Geometries:
Cu-N = 2.005, C-N = 1.350, C-C = 1.396, C-C = 1.397, Cu-N-C = 120.9, N-C-C = 122.7, C-C-C = 119.0
Frequencies:
a_1 : 3243, 3222, 3213, 1643, 1508, 1241, 1088, 1047, 1027, 630, 186; a_2 : 938, 878, 361; b_1 : 927, 908, 723, 565, 377, 66; b_2 : 3237, 3216, 1615, 1481, 1399, 1381, 1178, 1086, 655, 130
1A_1
$E_e = -1886.6902916$
Geometries:
Cu-N = 1.899, C-N = 1.358, C-C = 1.393, C-C = 1.397, Cu-N-C = 120.7, N-C-C = 122.1, C-C-C = 119.3
Frequencies:
a_1 : 3255, 3239, 3231, 1659, 1517, 1251, 1098, 1063, 1029, 658, 266; a_2 : 943, 878, 368; b_1 : 955, 913, 731, 581, 380, 100; b_2 : 3252, 3234, 1616, 1496, 1399, 1390, 1191, 1099, 652, 166

Table 3.2. ZEKE peak positions (cm^{-1}) and assignments of the Cu-pyridine and -(pyridine)₂ complexes.

Cu-pyridine		Cu-(pyridine) ₂			
Positions	Assignments	Positions	Assignments	Positions	Assignments
43507	11_1^0	44316	$11_0^2 20_2^2$	29917	0_0^0
43542	$11_1^0 20_1^1$	44357	10_0^1	30111	11_0^1
43703	0_0^0	44412	$11_0^2 20_0^2$	30308	11_0^2
43737	20_1^1	44516	11_0^3	30575	10_0^1
43771	20_2^2	44550	$11_0^3 20_1^1$	30940	9_0^1
43870	20_0^2	44585	$11_0^3 20_2^2$	31006	7_0^1
43975	11_0^1	44782	11_0^4	31142	6_0^1
44009	$11_0^1 20_1^1$	44817	$11_0^4 20_1^1$	31543	4_0^1
44044	$11_0^1 20_2^2$	44854	$11_0^4 20_2^2$	31963	9_0^2
44146	$11_0^1 20_0^2$	44915*	${}^4D_{1/2}^0 \leftarrow {}^2S_{1/2}$	32177	$6_0^1 9_0^1$
44247	11_0^2	45051	11_0^5		
44281	$11_0^2 20_1^1$				

Table 3.3. Point groups, electronic states, energies (a.u.), equilibrium geometries (R, Å; \angle , °), and vibrational frequencies of the eclipsed and staggered isomers of the Cu(pyridine)₂ complexes from the B3P86 and MP2 calculations using 6-311+G(*d,p*) basis set.

B3P86	
D_{2h}	
²B_{3u}	
E _e = -2139.3650957	
Geometries:	
Cu-N = 1.860, C-N = 1.369, C-C = 1.373, C-C = 1.402, N-Cu-N = 180.0, Cu-N-C = 121.8, N-C-C = 123.1, C-C-C = 120.1, C-N-N-C = 0.0	
Frequencies:	
a _g : 3223, 3206, 3190, 1668, 1488, 1234, 1070, 1051, 1032, 649, 198; b _{1g} : 958, 830, 412; b _{2g} : 956, 838, 710, 666, 375, 107; b _{3g} : 3209, 3190, 1523, 1418, 1362, 1319, 1133, 1085, 658, 147; a _u : 958, 832, 413, 35; b _{1u} : 3223, 3206, 3189, 1609, 1488, 1212, 1073, 1049, 987, 665, 357; b _{2u} : 3209, 3190, 1523, 1416, 1361, 1323, 1132, 1089, 659, 250, 39; b _{3u} : 956, 837, 711, 667, 395, 168, 34	
¹A_g	
E _e = -2139.1975907	
Geometries:	
Cu-N = 1.897, C-N = 1.346, C-C = 1.383, C-C = 1.389, N-Cu-N = 180.0, Cu-N-C = 120.8, N-C-C = 122.5, C-C-C = 119.0, C-N-N-C = 0.0	
Frequencies:	
a _g : 3231, 3213, 3206, 1668, 1522, 1247, 1104, 1067, 1048, 664, 186; b _{1g} : 1004, 894, 393; b _{2g} : 1034, 965, 770, 709, 426, 108; b _{3g} : 3227, 3209, 1628, 1485, 1385, 1323, 1186, 1102, 661, 145; a _u : 1003, 893, 391, 15; b _{1u} : 3231, 3213, 3205, 1668, 1522, 1244, 1104, 1069, 1048, 673, 338; b _{2u} : 3227, 3209, 1630, 1487, 1386, 1325, 1186, 1105, 661, 237, 40; b _{3u} : 1034, 966, 772, 711, 439, 180, 35;	
D_{2d}	
¹A₁	
E _e = -2139.1983542	
Geometries:	
Cu-N = 1.896, C-N = 1.347, C-C = 1.383, C-C = 1.389, N-Cu-N = 180.0, Cu-N-C = 120.8, N-C-C = 122.4, C-C-C = 119.0, C-N-N-C = 90.0	
Frequencies:	
a ₁ : 3231, 3213, 3206, 1667, 1522, 1246, 1104, 1067, 1047, 664, 187; a ₂ : 1005, 894, 393; b ₁ : 1005, 895, 394, 28; b ₂ : 3231, 3213, 3206, 1667, 1522, 1244, 1104, 1069, 1047, 673, 339; e: 3227, 3209, 1628, 1486, 1385, 1323, 1186, 1103, 1033, 967, 771, 710, 661, 431, 213, 121, 37	

Table 3.3 continued

MP2
D_{2h} ² B _{3u} E _e = -2134.483272 Geometries: Cu-N = 1.838, C-N = 1.358, C-C = 1.355, C-C = 1.393, N-Cu-N = 180.0, Cu-N-C = 121.8, N-C-C = 123.2, C-C-C = 120.0, C-N-N-C = 0.0 Frequencies: a _g : 3262, 3238, 3217, 1892, 1548, 1285, 1161, 1105, 1060, 667, 209; b _{1g} : 1061, 945, 454; b _{2g} : 1025, 917, 744, 630, 335, 41; b _{3g} : 3243, 3215, 1622, 1446, 1383, 1268, 1160, 1111, 687, 151; a _u : 1063, 947, 458, -27; b _{1u} : 3264, 3243, 3216, 2326, 1550, 1377, 1247, 1096, 1052, 689, 374; b _{2u} : 3243, 3214, 1624, 1443, 1385, 1265, 1163, 1103, 688, 267, 36; b _{3u} : 1027, 919, 748, 628, 377, 218, 15 ¹ A _g E _e = -2134.400602 Geometries: Cu-N = 1.862, C-N = 1.357, C-C = 1.393, C-C = 1.397, N-Cu-N = 180.0, Cu-N-C = 120.8, N-C-C = 122.2, C-C-C = 119.2, C-N-N-C = 0.0 Frequencies: a _g : 3255, 3240, 3230, 1659, 1517, 1249, 1103, 1069, 1032, 661, 195; b _{1g} : 940, 879, 367; b _{2g} : 950, 910, 728, 586, 380, 96; b _{3g} : 3251, 3237, 1615, 1493, 1398, 1386, 1189, 1096, 653, 153; a _u : 939, 877, 366, -21; b _{1u} : 3255, 3240, 3230, 1660, 1516, 1247, 1104, 1071, 1031, 673, 354; b _{2u} : 3251, 3236, 1616, 1494, 1388, 1189, 1099, 654, 254, 41; b _{3u} : 950, 911, 729, 583, 395, 178, 34
C₁ ² A E _e = -2134.5007558 Geometries: Cu-N = 1.863, C-N = 1.355, C-C = 1.394, C-C = 1.397, N-Cu-N = 180.0, Cu-N-C = 120.9, N-C-C = 122.4, C-C-C = 119.2, C-N-N-C = 90.0 Frequencies: a: 3274, 3253, 3249, 3240, 3236, 3233, 3233, 3224, 3208, 3206, 1810, 1653, 1615, 1606, 1511, 1487, 1471, 1393, 1382, 1378, 1326, 1258, 1251, 1245, 1182, 1123, 1098, 1093, 1092, 1068, 1049, 1031, 993, 988, 968, 954, 945, 926, 883, 879, 846, 773, 731, 668, 667, 654, 650, 621, 588, 461, 407, 376, 370, 365, 236, 229, 204, 165, 120, 78, 33, 27, 14

Table 3.3 continued

1A_1

$E_e = -2134.4018194$

Geometries:

Cu-N = 1.896, C-N = 1.347, C-C = 1.383, C-C = 1.389,

N-Cu-N = 180.0, Cu-N-C = 120.8, N-C-C = 122.4, C-C-C = 119.0, C-N-N-C = 90.0

Frequencies:

a_1 : 3240, 3230, 1658, 1516, 1249, 1102, 1069, 1031, 662, 196; a_2 : 954, 884, 373; b_1 : 954, 854, 377, 18; b_2 : 3240, 3230, 1660, 1516, 1247, 1104, 1071, 1031, 674, 354; e : 3255, 3251, 3236, 1615, 1494, 1399, 1387, 1189, 1097, 959, 926, 735, 653, 623, 402, 226, 121, 36

Table 3.4. Adiabatic ionization energies (AIE, cm^{-1}), bond dissociation energies (D_0^+/D_0 , kJ mol^{-1}) and vibrational frequencies (cm^{-1}) of Cu-pyridine and $-(\text{pyridine})_2$ from ZEKE measurements and the B3P86 and MP2 calculations using 6-311+G(*d,p*) basis set.

		ZEKE	B3P86 // MP2	
Cu-pyridine	AIE ^a	43703	48623 // 40823	
	D_0^+ / D_0	245.9 / 23.2	280.1 / 45.6 // 258.7 / 47.4	
	Cu ⁺ /Cu-L stretch	$\nu_{11}^+ / \nu_{11}, a_1$	272/196	271/183 // 266/186
	Cu ⁺ -L o.p. bend	$\nu_{20}^+ / \nu_{20}, b_1$	85/51	111/41 // 100/66
	pyridine ring distortion ^b	ν_{10}^+, a_1	654	667 // 658
Cu-(pyridine) ₂	AIE ^a	29917	37713 // 17211	
	D_0^+ / D_0	494.5 / 106.9	524.6 / 159.6 // 517.3 / 23.5	
	L-Cu-L symm. stretch	ν_{11}^+, a_g	194	186 // 195
	pyridine rings distortion ^b	ν_{10}^+, a_g	658	664 // 658
	pyridine rings breath ^b	ν_9^+, a_g	1023	1048 // 1032
	C-H i.p. bend ^b	ν_7^+, a_g	1089	1104 // 1103
	C-H i.p. bend ^b	ν_6^+, a_g	1225	1247 // 1249
	pyridine rings distortion ^b	ν_4^+, a_g	1626	1668 // 1659

^aThe uncertainty of the AIE values is $\sim 5 \text{ cm}^{-1}$. D_0^+ (Cu⁺-pyridine) is from reference [169], with an uncertainty of 10.1 kJ mol^{-1} , and D_0 [Cu⁺-(pyridine)₂] is from reference [170], with an uncertainty of 25.1 kJ mol^{-1} . D_0 values are obtained by using the thermodynamic relation discussed in text. D_0 (Cu-pyridine) was also reported by reference [175]. i.p., in-plane; o.p., out-of-plane. ^bThe analogous vibrations in the free ligand have been measured to be 601 (ν_{10}), 991 (ν_9), 1072 (ν_7), 1218 (ν_6), and 1584 (ν_4) in reference [181].

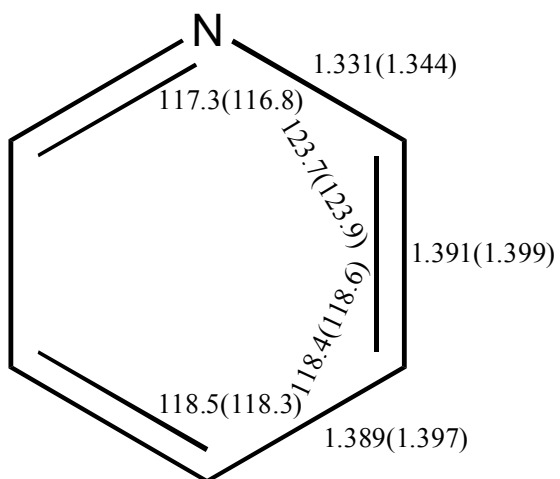


Figure 3.1. Structure of pyridine from B3P86/6-311+G(*d,p*) and MP2/6-311+G(*d,p*) (in parenthesis) calculations: bond lengths, Å, bond angles, °.

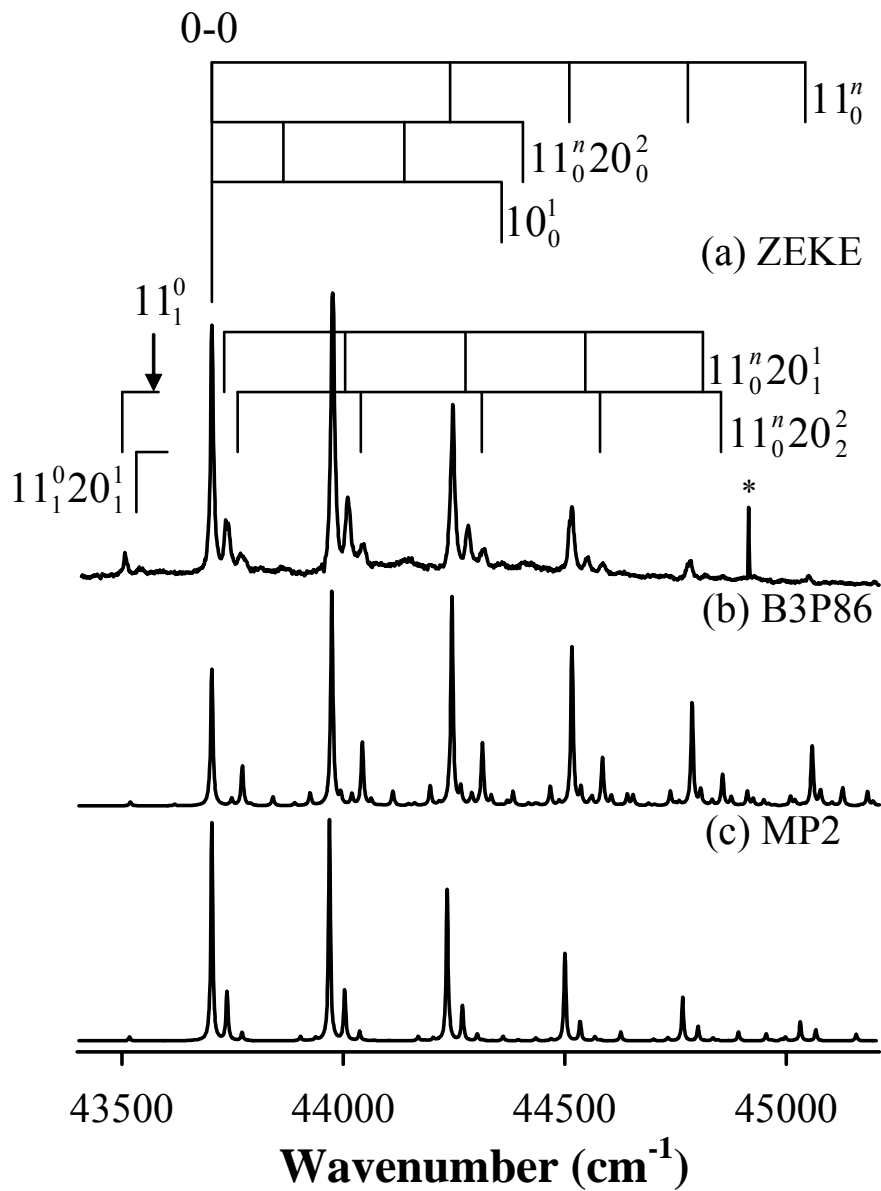


Figure 3.2. ZEKE spectrum of Cu-pyridine seeded in helium (a) and simulations from B3P86 (b) and MP2 (c) calculations at 60 K. The peak with asterisk is a Cu atomic transition.

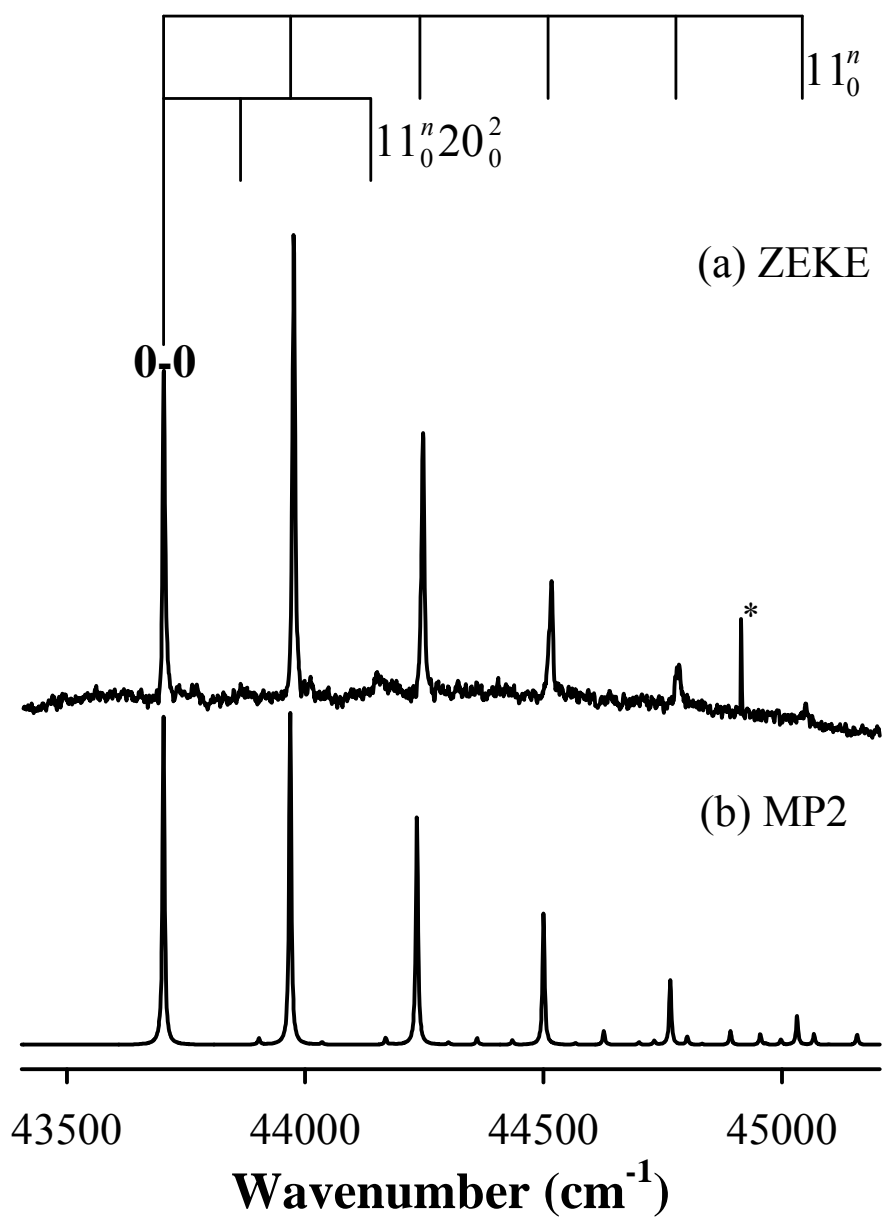


Figure 3.3. ZEKE spectrum of Cu-pyridine seeded in argon (a) and MP2 simulation at 5 K (b). The peak with an asterisk is a Cu atomic transition.

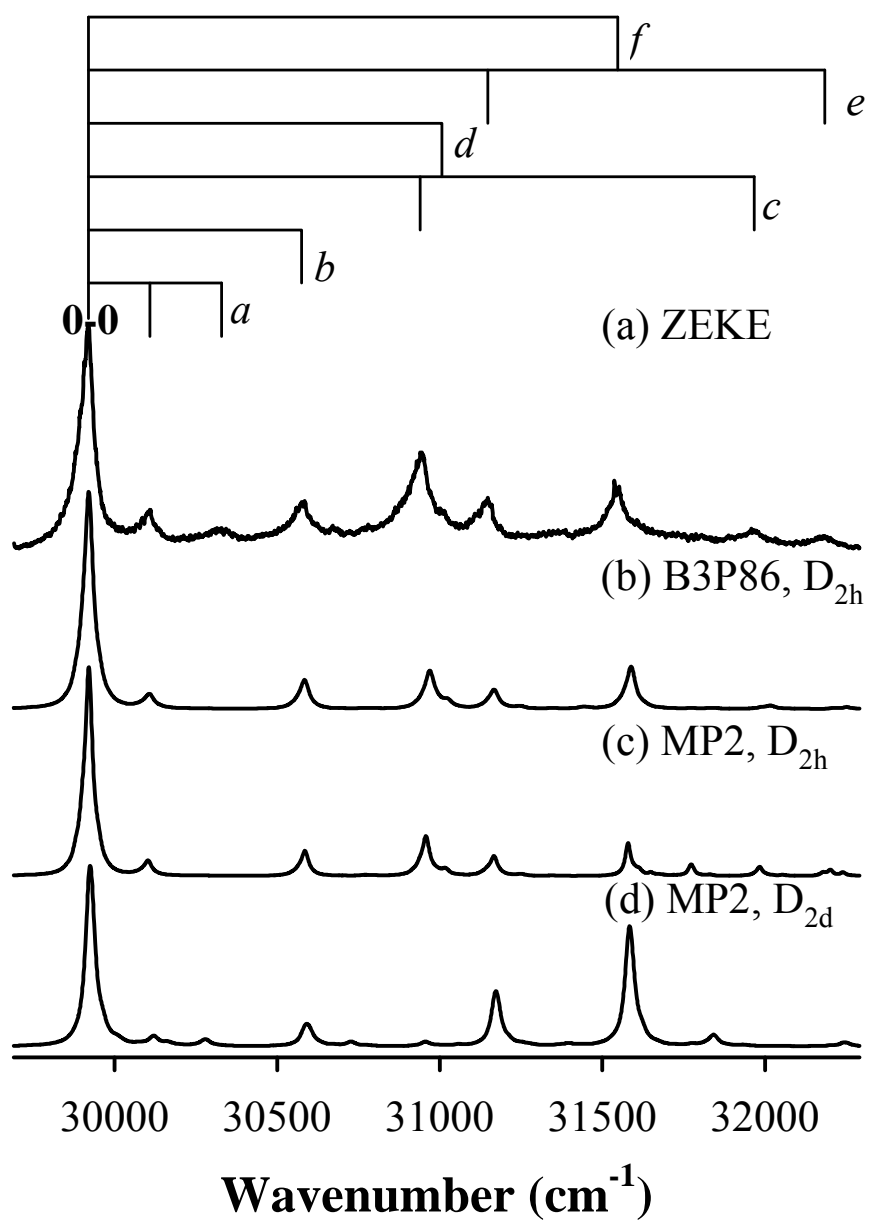


Figure 3.4. Experimental ZEKE spectrum of Cu-(pyridine)₂ and simulations (80 K) of the D_{2h} structures from B3P86 (b) and MP2 calculations (c) and the D_{2d} structure from MP2 calculations (d).

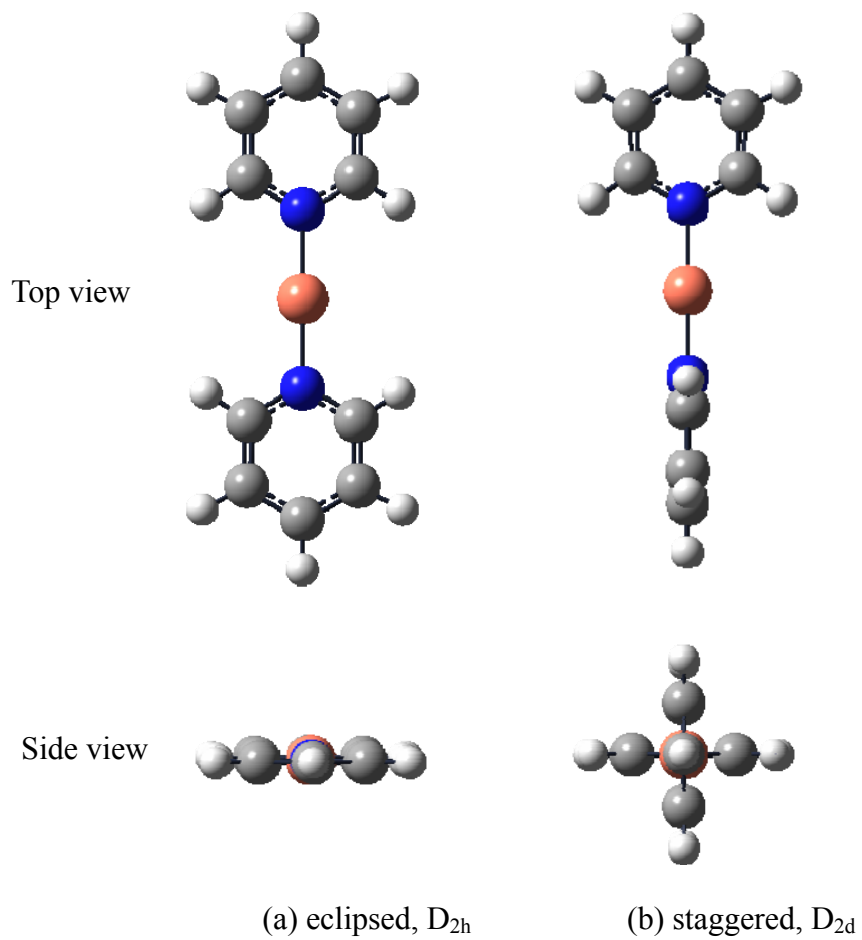


Figure 3.5. Eclipsed and staggered structures of $\text{Cu}-(\text{pyridine})_2$.

Chapter 4 Spectroscopy and structures of copper-diazine complexes

Diazines are heteroaromatic molecules with the formula $C_4H_4N_2$. In these molecules, two of benzene's six CH groups are replaced by nitrogen atoms. Depending on mutual positions of the nitrogen atoms, diazine exists in three isomers: pyrazine (1,4-diazine), pyrimidine (1,3-diazine), and pyridazine (1,2-diazine) (Figure 4.1). The diazine rings are important constituents of both natural and synthetic compounds.¹⁸⁵⁻¹⁸⁹ For example, three nucleobases found in nucleic acids, cytosine, thymine, and uracil, are pyrimidine derivatives. In deoxyribonucleic and ribonucleic acids, these bases form hydrogen bonds with their complementary purines. Since the diazine molecules contain nitrogen bases and an aromatic ring, they can function as a σ -donor, π -acceptor, or π -donor.^{189,190} Their aromaticity, however, should be less than benzene because the substituted nitrogen atoms disturb the π -system.

A number of studies about the interaction of copper atoms and ions with these diazine molecules have been reported previously. Adsorption of pyrazine on a Cu (110) surface was studied by angle resolved photoemission and low energy electron diffraction,¹⁹¹ near-edge X-ray absorption fine structure,¹⁹² and semi-empirical molecular orbital calculations.¹⁹³ These studies were motivated by the use of Cu surfaces as selective catalysts for syntheses of nitrogen-containing compounds.^{194,195} In these studies, pyrazine was determined to interact with the Cu surface through one of the nitrogen atoms in the vertical orientation. The orientation of pyrazine on Cu(110) was the same as that on Au(210),¹⁹⁶ but different from that on Ag(111) where the pyrazine molecular plane was parallel to the silver surface.¹⁹⁷ Cu^{2+} -diazine complexes in the condensed phases were studied by IR absorption spectroscopy, and these spectroscopic

measurements identified the metal-ligand and diazine ring-based vibrations of these stable compounds.^{198,199} In the gas phase, the bond dissociation energy of Cu⁺-pyrimidine was measured by CID experiment.¹⁸⁰ However, there has been no electron spectroscopy reported for the Cu-diazine complexes, which should provide direct evidence about the binding and structures of these systems.

In this work, we have measured the electronic spectra of all three Cu-diazine complexes using PFI-ZEKE spectroscopy. The motivations of this study are: (1) to probe the metal-ligand binding and structures in the neutral and ionic forms of these complexes and compare the metal atomic binding with surface adsorption, (2) to measure the metal-ligand vibrational frequencies and compare them with those of the coordinately saturated compounds in the condensed phases, and (3) to determine the metal-ligand bond dissociation energies of the neutral complexes through ionization energy measurements.

4.1 Experimental and computational methods

Copper complexes were prepared by reactions of copper atoms with pyrazine (99+%, Aldrich), pyrimidine (98%, TCI), or pyridazine (98%, Aldrich) in molecular beams. The metal atoms were produced by pulsed laser vaporization of a copper rod (99.9%, Alfa Aesar) with the second harmonic output of a Nd:YAG laser (Quanta-Ray, GCR-3, 532 nm, ~ 3 mJ) in the presence of a carrier gas (He or Ar, ultra high purity, Scott-Gross) at ~ 50 psi. At room temperature, vapor of the ligand was introduced down stream of the ablation by a stainless steel capillary to a small reaction chamber (~ 1.5 mL), where the organic molecules interacted with the metal atoms entrained in the carrier gas.

Ionization was carried out by a frequency-doubled dye laser (Lumonics HD-500), pumped by a XeCl excimer laser (Lumonics, PM-884, 308 nm) or the third harmonic output (355 nm) of a Nd:YAG laser (~ 180 mJ, Continuum, surelite-III). Prior to ZEKE

experiments, ionization thresholds of the 1:1 complexes were measured by recording the ion signals as a function of laser wavelength. ZEKE electrons were produced by photoexcitation of neutral molecules to high-lying Rydberg states, followed by a $\sim 3 \mu\text{s}$ delayed, pulsed electric field ionization (1.2 V cm^{-1} , 100 ns) of these Rydberg states. A small dc field of $\sim 0.08 \text{ V cm}^{-1}$ was applied to help separate ZEKE from kinetic electrons produced by direct photoionization. The pulsed electric field was generated by a delay pulsed generator (Stanford Research System, DG535). The ion and electron signals were detected by a dual MCP detector (Galileo), amplified by a preamplifier (Stanford Research System, SR445), averaged by a gated integrator (Stanford Research System, SR250), and recorded in a laboratory computer. Laser wavelengths were calibrated against vanadium or titanium atomic transitions.¹⁴² Field-dependent measurements were not performed due to the limited size of the ZEKE signal.

Calculations of molecular geometries and vibrational frequencies were carried out using the MP2 method and 6-311+G(*d,p*) basis, implemented in the GAUSSIAN 03 program.²⁰⁰ Multidimensional FC factors were computed from the theoretical equilibrium geometries, harmonic frequencies, and normal modes of the neutral and ionic complexes.^{143,144} The Duschinsky effect²⁰¹ was considered to account for normal mode differences between the neutral molecule and ion in the FC calculations. Spectral broadening was simulated by giving each line a Lorentzian line shape with the linewidth of the experimental spectrum. Boltzmann distributions were used to simulate spectra at specific temperatures.

4.2 Results and discussion

4.2.1 Equilibrium structures and vibrational frequencies

In calculating the structures of Cu-pyrazine, -pyrimidine and -pyridazine, we considered both σ - and π -bonding modes. The σ -complex is formed by Cu binding to

one of the nitrogen atoms, and the π -complex is formed by Cu binding to the six-membered π -ring. In the case of pyridazine with two adjacent nitrogen atoms, we also consider an initial geometry with Cu chelating to both nitrogen atoms. Figure 4.2 presents the optimized structures for the σ - and π -complexes and their relative energies, and Table 4.1 lists the bond distances, bond angles, and vibrational frequencies for the σ -complexes.

4.2.1.1 Cu-pyrazine

The σ -complex of Cu-pyrazine has C_{2v} symmetry with the metal atom being coplanar to the six-membered ring. The optimized Cu-N distance is 2.011 Å at the MP2/6-311+G(*d,p*) level of theory. This distance is within the range of the Cu-N bond lengths (2.00-2.05 Å) in coordinately saturated copper compounds that contain pyrazine,²⁰²⁻²⁰⁴ but shorter than the Cu-N distance (2.096 Å) calculated for Cu-pyridine.^{184,205} Cu coordination has a very small perturbation on the pyrazine geometry (Figure 4.1 and Table 4.1). The changes are less than 0.005 Å in bond lengths and 2° in bond angles. The small changes in the pyrazine geometry are also evident from vibrational analyses, which yield similar frequencies for the ligand-based modes in the free ligand and complex. Upon ionization, the Cu-N distance shrinks by 0.102 Å, whereas other bond lengths and angles remain virtually the same. The shorter Cu-N distance in the ion is due to the reduced repulsion between Cu 4s¹ and N lone-pair electrons and the additional charge-dipole attraction. A search for the π -bonding configuration was not successful for the neutral complex. However, a cationic π -complex was located 110.7 kJ mol⁻¹ above the ionic σ -complex [Figure 4.2 (a)], but it was not a minimum energy structure.

4.2.1.2 Cu-pyrimidine

Both σ - and π -configurations are found for Cu-pyrimidine and its positive ion. The existence of a stable π -configuration in the neutral species is attributed to the aromaticity of the six-membered ring of pyrimidine. Previous studies have shown that the aromaticity of the three diazine molecules follows the order of pyrimidine > pyrazine > pyridazine.¹⁹⁰ This sequence is consistent with the relative energies of pyrimidine (0 kJ mol⁻¹), pyrazine (14.2 kJ mol⁻¹), and pyridazine (94.4 kJ mol⁻¹) predicted by the MP2 calculations.

The σ -bonded Cu-pyrimidine has a lower molecular symmetry (C_s) than Cu-pyrazine because of the *meta* arrangement of the two nitrogen atoms. The Cu-N bond distances in the neutral and ionic species are almost identical to the corresponding distances in the pyrazine complexes, and the geometry of pyrimidine is only slightly perturbed by Cu coordination. Ionization causes Cu to bend toward the molecular dipole moment of pyrimidine, in addition the Cu-N distance shrinks. The dipole moment of pyrimidine is pointed along the C_δ - C_β axis. As a result, the Cu-N₁-C $_\alpha$ bond angle is increased, and the Cu-N₁-C $_\delta$ angle is reduced in the ion (Table 4.1). This bending is expected as Cu⁺ tries to sample an optimal position to maximize the charge-dipole interaction, while maintaining the σ donor-acceptor bonding between the Cu 4s⁰ and the electron lone pair of the nitrogen atom (N₁).

The π -structure of Cu-pyrimidine has a Cu-ring distance of 3.416 Å in the neutral species. This distance is larger than the sum of van der Waals radii of Cu (1.40 Å) and N (1.55 Å) or C (1.70 Å),²⁰⁶ suggesting little bonding between the metal atom and ligand. Our calculations show that this long-range π structure is 281.1 kJ mol⁻¹ above the σ -structure. Upon ionization, Cu⁺ ion moves away from the ring's center, with the longest distance of 3.100 Å for Cu⁺-C $_\delta$ and the shortest distance of 2.07 Å for Cu⁺-C $_\beta$. The stronger Cu⁺ binding with C $_\beta$ correlates with a higher π electron density of the C $_\beta$ atom, which enhances the π -electron donation to the metal ion.

4.2.1.3 Cu-pyridazine

Because of the adjacent positions of the two nitrogen atoms, pyridazine is expected to have different bonding properties from the other two diazine molecules. It has the largest electric dipole moment (4.22 D) among the three diazine molecules.²⁰⁷ It is less stable due to the large electron repulsion between the nitrogen electron lone pairs. Furthermore, it offers the possibility for metal chelating to both nitrogen atoms. Thus, in searching for minimum energy σ structures, we considered initial geometries with Cu being along the N_1-C_γ axis or between two nitrogen atoms. However, both converged to the same structure with an almost linear $Cu-N_1-C_\gamma$ configuration to reduce the electron repulsion between Cu and the other nitrogen atom. For the π -configuration, a local minimum was found only for the ionic form. In this π -configuration, the Cu^+ ion is off the ring's center and has a much higher energy than the σ -form [Figure 4.2 (c)].

In the neutral σ -complex, the Cu atom is 2.000 Å from N_1 and 2.884 Å from N_2 , and the $Cu-N_1-C_\gamma$ angle is 179.4°. The $Cu-N_1$ distance and Cu orientation is almost the same as those in Cu-pyrazine and -pyrimidine. However, the $Cu-N_2$ distance is smaller than the van der Waals radii of Cu (1.40 Å) and N (1.55 Å),²⁰⁶ suggesting a possible interaction between Cu and N_2 . In the ionic form of the σ -complex, the $Cu-N_1-C_\gamma$ bond angle is reduced to 170.0°, with Cu^+ bending toward the second nitrogen. This Cu orientation arises from the charge-dipole interaction, as the molecular dipole points between the two nitrogen atoms. A similar Cu reorientation is also predicted in Cu^+ -pyrimidine, but to a much smaller extent. In addition, the Cu^+-N_1 and Cu^+-N_2 distances are reduced due to the addition of the charge-dipole interaction and the reduction of the electron-electron repulsion.

4.2.2 ZEKE spectra

The ZEKE spectra of the three Cu-diazine complexes are presented in Figures 4.3-4.6, and the peak positions and assignments of the observed transitions are listed in Table 4.2. The spectral assignments are discussed by comparing the experimental and simulated spectra. The simulations are obtained by using the MP2 geometries, harmonic vibrational frequencies, and force fields of the neutral and ionic states. The calculated 0-0 transition energies are shifted to the measured values for simplicity, while the vibrational frequencies are not scaled in these simulations.

4.2.2.1 Cu-pyrazine

Figure 4.3 (a) shows the ZEKE spectrum of Cu-pyrazine seeded in He carrier gas. The spectrum originates at 46038 cm^{-1} and has a linewidth of 7 cm^{-1} . Above the 0-0 transition, the spectrum shows a main progression of 265 cm^{-1} interval, a weak transition at 906 cm^{-1} , and a series of sequence peaks of 41 cm^{-1} spacing. These sequence transitions are located at the higher energy side of the 265 cm^{-1} progression and the 906 cm^{-1} peak. Below the 0-0 transition, the spectrum displays two hot transitions from excited vibrational levels of the neutral electronic ground state, and one of which is partially overlapped with a sharp peak at 45879.6 cm^{-1} . This and two other sharp peaks at 45820.6 and 46174.1 cm^{-1} arise from Cu atomic transitions and are assigned to ${}^2P_{3/2}^0 \leftarrow {}^2S_{1/2}$, ${}^2P_{1/2}^0 \leftarrow {}^2S_{1/2}$, and ${}^2D_{3/2}^0 \leftarrow {}^2S_{1/2}$, respectively.¹⁴²

Figure 4.3 (b) shows the spectral simulation of the ${}^1A_1 \leftarrow {}^2A_1$ transition of the σ -complex at 80 K. The theoretical and experimental spectra are in good agreement, although the intensity is somewhat overestimated by theory. The 265 cm^{-1} progression is assigned to the symmetric Cu^+ -pyrazine stretching vibrations of the ion (ν_{10}^+). The Cu^+ -pyrazine stretching frequency is slightly lower than the values of the Cu^{2+} -pyrazine

stretches in the condensed-phase $[\text{Cu}(\text{pyrazine})_2](\text{ClO}_4)_2$ (279 cm^{-1}) and $[\text{Cu}(\text{pyrazine})\text{Cl}_2]_n$ (287 cm^{-1}) compound¹⁹⁸ and the Cu^+ -pyridine stretch in the gaseous Cu^+ -pyridine (274 cm^{-1}) complex.²⁰⁸ The 906 cm^{-1} interval is attributed to a ring breathing vibration (ν_8^+) of the ligand. The ring breathing mode of free pyrazine was measured to be 1015 cm^{-1} for the neutral ground state²⁰⁹ and 1004 cm^{-1} for the ionic ground state.²¹⁰ The large red shift of the breathing frequency from the free to coordinated pyrazine is due to the weakening of the C-N(C) bonds caused by metal coordination. The assignment of the hot transitions gives a neutral Cu-pyrazine stretching frequency of 190 cm^{-1} (ν_{10}) and Cu-pyrazine out-of-plane bending frequencies of 115 cm^{-1} (ν_{18}^+) in the ion and 74 cm^{-1} (ν_{18}) in the neutral complex. The Cu-pyrazine stretching frequency of the neutral complex is comparable to the value of Cu-pyridine stretch (195 cm^{-1}).²⁰⁸

4.2.2.2 Cu-pyrimidine

The ZEKE spectrum of Cu-pyrimidine seeded in He carrier is shown in Figure 4.4 (a). It displays a similar spectral profile to and a broader linewidth (10 cm^{-1}) than that of Cu-pyrazine. This line broadening is the result of the expansion of the unresolved rotational envelope at a higher rotational temperature of the complex.⁷⁸ The 0-0 transition is measured to be 45332 cm^{-1} , 706 cm^{-1} lower than that of Cu-pyrazine. The major progression with up to four vibrational quanta has a spacing of 270 cm^{-1} . Superimposed on the main progression are sequence transitions with an interval of 38 cm^{-1} . In addition, the spectrum shows a weak peak at 160 cm^{-1} above the band origin and its combinations with the 270 cm^{-1} interval. Below the 0-0 transition, two weak peaks are observed from excited vibrational levels of the neutral ground electronic state. As in Cu-pyrazine, three sharp atomic transitions are located in the spectrum; one of which (45879.6 cm^{-1} , $^2\text{P}_{3/2}^0 \leftarrow ^2\text{S}_{1/2}$) partially overlaps with the second-quantum transition of the

270 cm⁻¹ progression at 45872 cm⁻¹.

The spectral simulations of the σ - and π -complexes of Cu-pyrimidine are presented in Figures 4.4 (b) and 4.4 (c). A quick comparison of the experiment and theory excludes contribution of the π -complex to the observed spectrum and confirms the ${}^1A' \leftarrow {}^2A'$ transition of the σ -structure. The 270 cm⁻¹ progression is assigned to transition from the ground vibrational level of the neutral ${}^2A'$ state to the Cu⁺-pyrimidine symmetric stretching (ν_{18}^+) levels of the ionic ${}^1A'$ ground state. The 160 cm⁻¹ interval is assigned to the Cu⁺-pyrimidine in-plane bend (ν_{19}^+) of the ionic state. The assignment of the hot transitions yields the Cu-pyrimidine stretching and in-plane bending frequencies of 189 (ν_{18}) and 151 cm⁻¹ (ν_{19}) in the neutral 2A_1 state and a frequency difference of 38 cm⁻¹ between the ionic and neutral metal-ligand out-of-plane bending motions. The Cu⁺-pyrimidine stretching frequency is slightly higher than the values of Cu⁺-pyrazine (265 cm⁻¹) discussed above and Cu²⁺-pyrimidine in [Cu(pyrimidine)₄](ClO₄)₂ (267 cm⁻¹) and [Cu(pyrimidine)Cl₂]_n (247 cm⁻¹).¹⁹⁸

To confirm the assignment for the hot transitions, ZEKE measurements with Ar or Ar/He carrier gases were carried out in the 45100-46000 cm⁻¹ range. A representative spectrum with 1:2 Ar/He is shown in Figure 4.5 (a). The use of the Ar/He mixture quenches all the hot transitions observed in He because of a lower vibrational temperature and reduces the linewidth from 10 to 6 cm⁻¹ because of a lower rotational temperature. The atomic transitions are also suppressed in the Ar/He beam, as previously observed for other Cu complexes.⁸⁴ To estimate the vibrational temperature of the complex seeded in Ar/He, we performed simulations at various temperatures and found that the simulation at 20 K had the best match with the experimental spectrum [Figure 4.5 (b)].

4.2.2.3 Cu-pyridazine

The Cu-pyridazine complex exhibits more ZEKE peaks [Figure 4.6 (a)] and a lower 0-0 transition energy (43054 cm^{-1}) than both Cu-pyrazine and -pyrimidine. The spectral linewidth is about 6 cm^{-1} . The rich ZEKE transitions are the result of a large geometry change upon ionization, as predicted by the MP2 calculations. The low AIE indicates a large increase of the metal-ligand binding energy in the ionized complex. The spectrum displays a vibrational progression of 273 cm^{-1} with up to four quanta and 131 cm^{-1} with three quanta. It also shows a progression consisting of the combination of the 273 and 131 cm^{-1} intervals. In addition to these cold transitions, the spectrum exhibits many weak peaks originating from excited vibrational levels of the neutral ground electronic state.

This spectrum is assigned by comparison to the simulation of the ${}^1A' \leftarrow {}^2A'$ transition of the σ -complex. The 273 cm^{-1} progression is assigned to the excitation of the Cu^+ -pyridazine symmetric stretch (ν_{18}^+) and 131 cm^{-1} to the Cu^+ -pyridazine in-plane bend (ν_{19}^+) in the ionic ${}^1A'$ state. The assignment of the hot transitions gives vibrational frequencies of 192 cm^{-1} for the Cu-ligand stretch (ν_{18}) and 123 cm^{-1} for the Cu-ligand in-plane bend (ν_{19}) in the neutral ${}^2A'$ state. Interestingly, the Cu^+ -pyridazine stretching frequency is nearly identical to those of the Cu^{2+} -pyridazine stretches in $[\text{Cu}(\text{pyridazine})_4](\text{ClO}_4)_2$ (271 cm^{-1}) and $[\text{Cu}(\text{pyridazine})\text{Cl}_2]_n$ (271 cm^{-1}).¹⁹⁸

The major spectral difference between Cu-pyridazine and the other two complexes is the excitation of the symmetric Cu-diazine bending vibration. For the Cu-pyrazine complex, no symmetric bending excitation is observed, although a non-symmetric out-of-plane bend (b_1, ν_{18}) is identified via hot transitions. The Cu-pyrimidine spectrum shows only the fundamental excitation of the Cu^+ -ligand symmetric in-plane bend (ν_{19}^+), whereas three-quantum excitations of this mode are observed for the Cu-pyridazine complex. This difference suggests that changes of the $\text{Cu-N}_1\text{-C}_\alpha$ angle from the neutral complex to the ion must follow the order of Cu-pyrazine < Cu-pyrimidine <

Cu-pyridazine. Indeed, the differences between $\angle\text{Cu}^+\text{-N}_1\text{-C}_\alpha$ and $\angle\text{Cu-N}_1\text{-C}_\alpha$ are predicted to be -0.3, 1.6, and 8.6 degrees for the pyrazine, pyrimidine, and pyridazine complexes, respectively.

4.2.3 Ionization and bond dissociation energies

Table 4.3 summarizes the AIEs, metal-ligand bond energies, and vibrational frequencies from the ZEKE spectra and MP2/6-311+G(*d,p*) calculations of the three Cu-diazine complexes. The measured and calculated metal-ligand stretching frequencies are in good agreement, but the theoretical results are mixed for the low frequency bending modes in the neutral state. The MP2 method yields the correct trend of the ionization energies for the three complexes, although it underestimates the AIE values by about 3000 cm^{-1} . Similar MP2 results have been reported for other Cu complexes.^{84,87,157}

The ionization energies of the Cu-diazine complexes follow the trend of Cu-pyridazine < Cu-pyrimidine < Cu-pyrazine. As a result, the difference between the ionic and neutral binding strengths must be in the order of Cu-pyridazine > Cu-pyrimidine > Cu-pyrazine. Bond energies of ions can be conveniently measured with mass spectrometry-based techniques, but measurements of neutral bond energies are not straightforward for lack of mass information. With AIE measurements, however, the bond energy of neutral complexes can be calculated by using the thermochemical relation: $\text{AIE}(\text{Cu}) - \text{AIE}(\text{Cu-L}) = D_0^+(\text{Cu-L}) - D_0(\text{Cu-L})$, where D_0^+ and D_0 are the bond energies of the ionic and neutral complexes, and AIE (Cu) and AIE (Cu-L) are the adiabatic ionization energies of the Cu atom and complex. Recently, Amunugama and Rodgers measured the D_0^+ value of 249.6 kJ mol^{-1} for Cu^+ -pyrimidine with the CID method.¹⁸⁰ Using D_0^+ (Cu^+ -pyrimidine), AIE (Cu),²⁰⁷ and AIE (Cu-pyrimidine), D_0 (Cu-pyrimidine) is calculated as 46.4 kJ mol^{-1} , which is five times smaller than D_0^+ (Cu^+ -pyrimidine).

The stronger ion bonding is the result of the diminished electron repulsion and additional charge-dipole attraction in the ion. For Cu-pyrazine and -pyridazine, experimental ion dissociation energies have not been reported. Their D_0^+ values, however, may be obtained from the corrected MP2 values. This correction can be taken as the D_0^+ (Cu⁺-pyrimidine) difference between the experimental (CID) and theoretical (MP2) values, 20.1 (249.6 – 229.5) kJ mol⁻¹. Thus, the D_0^+ values of Cu⁺-pyrazine and -pyridazine are estimated to be 243.2 (223.1 + 20.1) and 286.6 (266.5 + 20.1) kJ mol⁻¹, respectively. Using these ion bond energies, we have obtained neutral bond energies of 48.5 kJ mol⁻¹ for Cu-pyrazine and 56.2 kJ mol⁻¹ for Cu-pyridazine.

Among the three Cu-diazine complexes, Cu-pyridazine has the largest bond dissociation energies in both the neutral and ionic states, whereas the bond energies are comparable for Cu-pyrazine and -pyrimidine. A similar binding pattern has also been observed in alkali metal ion-diazine complexes.²¹¹ The enhanced binding of pyridazine is attributed to its large dipole moment (4.22 D) and its ability to act as a bidentate ligand. Although the overall dipole moments of pyrazine (0.000 D) and pyrimidine (2.334 D) are extremely different, the local dipoles of the two diazines should be comparable and similar to that of pyridine (2.215 D).²⁰⁷ Thus, both pyrazine and pyrimidine have similar binding strengths.

4.3 Conclusion

Three Cu-diazine complexes are examined by PFI ZEKE spectroscopy and MP2 calculations. Although the diazine molecules have both σ - and π -binding sites, the most stable structure of the Cu complexes has σ -binding between the nitrogen and copper atoms. The preferred binding mode in these Cu complexes is the same as that in diazine adsorption on Cu (110) surfaces. A π -bonding structure at higher energy is predicted for all three Cu⁺-diazine ions, but is found only for the neutral Cu-pyrimidine complex.

The ability to form the stable neutral π -complex of pyrimidine may be attributed to its higher aromaticity.

For the neutral σ -complexes, Cu-pyridazine has the lowest ionization energy and the highest metal-ligand bond dissociation energy. The stronger σ -binding of pyridazine is due to its larger dipole moment and possibly bidentate binding. For the singly charged ions, the bond dissociation energies are about five times larger than that of the corresponding neutral molecules. The enhanced ion binding is due to the reduced electron repulsion and additional charge-dipole attraction. The Cu^+ -N stretch frequencies in these binary complexes are comparable to those of coordinately saturated Cu^{2+} complexes.

Table 4.1. Electronic states, equilibrium geometries (Å, degree), and vibrational frequencies (cm⁻¹) of the Cu-diazine σ -complexes from MP2/6-311+G(*d,p*) calculations. The N and C atom labeling scheme is depicted in Figure 4.1.

	Bond lengths	Bond angles	Vibrational frequencies
Cu-pyrazine (C _{2v})			
² A ₁	Cu-N ₁ = 2.011 N ₁ -C _{α} = 1.348 C _{α} -C _{β} = 1.397 C _{β} -N ₂ = 1.344	\angle Cu-N ₁ -C _{α} = 121.7 \angle C _{α} -N ₁ -C _{δ} = 116.5 \angle N ₁ -C _{α} -C _{β} = 121.3 \angle C _{α} -C _{β} -N ₂ = 122.8	a ₁ : 3234, 3217, 1623, 1502, 1256, 1151, 1056, 1023, 624, 175 a ₂ : 944, 920, 329 b ₁ : 931, 791, 671, 404, 62 b ₂ : 3231, 3216, 1558, 1451, 1372, 1366, 1095, 706, 128
¹ A ₁	Cu-N ₁ = 1.909 N ₁ -C _{α} = 1.357 C _{α} -C _{β} = 1.397 C _{β} -N ₂ = 1.341	\angle Cu-N ₁ -C _{α} = 121.4 \angle C _{α} -N ₁ -C _{δ} = 117.2 \angle N ₁ -C _{α} -C _{β} = 120.6 \angle C _{α} -C _{β} -N ₂ = 122.8	a ₁ : 3248, 3231, 1633, 1508, 1267, 1148, 1085, 1020, 651, 257 a ₂ : 961, 900, 330 b ₁ : 938, 793, 673, 415, 105 b ₂ : 3246, 3230, 1555, 1457, 1382, 1370, 1106, 703, 167
Cu-pyrimidine (C _s)			
² A'	Cu-N ₁ = 2.021 N ₁ -C _{α} = 1.347 C _{α} -C _{β} = 1.393 C _{β} -C _{γ} = 1.396 N ₂ -C _{γ} = 1.343 N ₂ -C _{δ} = 1.337 N ₁ -C _{δ} = 1.348	\angle Cu-N ₁ -C _{α} = 121.0 \angle Cu-N ₁ -C _{δ} = 122.0 \angle C _{α} -N ₁ -C _{δ} = 117.0 \angle N ₁ -C _{δ} -N ₂ = 126.2 \angle C _{α} -C _{β} -C _{γ} = 117.2 \angle C _{β} -C _{γ} -N ₂ = 122.3 \angle C _{γ} -N ₂ -C _{δ} = 116.0	a': 3249, 3231, 3217, 3211, 1629, 1603, 1493, 1442, 1397, 1327, 1242, 1156, 1097, 1083, 1030, 690, 637, 174, 127 a'': 964, 959, 929, 787, 680, 385, 328, 62
¹ A'	Cu-N ₁ = 1.908 N ₁ -C _{α} = 1.357 C _{α} -C _{β} = 1.389 C _{β} -C _{γ} = 1.397 N ₂ -C _{γ} = 1.343 N ₂ -C _{δ} = 1.327 N ₁ -C _{δ} = 1.358	\angle Cu-N ₁ -C _{α} = 122.6 \angle Cu-N ₁ -C _{δ} = 120.2 \angle C _{α} -N ₁ -C _{δ} = 117.2 \angle N ₁ -C _{δ} -N ₂ = 125.5 \angle C _{α} -C _{β} -C _{γ} = 117.5 \angle C _{β} -C _{γ} -N ₂ = 122.1 \angle C _{γ} -N ₂ -C _{δ} = 117.0	a': 3260, 3238, 3232, 3229, 1648, 1599, 1501, 1457, 1408, 1328, 1251, 1159, 1113, 1068, 1044, 704, 644, 261, 167 a'': 985, 954, 936, 795, 677, 394, 327, 104

Table 4.1 continued

Cu-pyridazine (C _s)			
² A'	Cu-N ₁ = 2.000	∠Cu-N ₁ -C _α = 121.0	a': 3247, 3236, 3227, 3221,
	Cu-N ₂ = 2.884	∠Cu-N ₁ -N ₂ = 118.0	1614, 1601, 1484, 1428,
	N ₁ -C _α = 1.346	∠C _α -N ₁ -N ₂ = 120.9	1331, 1307, 1173, 1096,
	C _α -C _β = 1.397	∠N ₁ -N ₂ -C _δ = 118.1	1090, 1081, 997, 675, 636,
	C _β -C _γ = 1.390	∠C _α -C _β -C _γ = 117.2	182, 129
	C _γ -C _δ = 1.400	∠C _β -C _γ -C _δ = 117.0	a'': 945, 935, 919, 754, 601,
	N ₂ -C _δ = 1.342	∠C _γ -C _δ -N ₂ = 124.2	353, 344, 58
	N ₂ -N ₁ = 1.341		
¹ A'	Cu-N ₁ = 1.904	∠Cu-N ₁ -C _α = 129.6	a': 3257, 3249, 3243, 3237,
	Cu-N ₂ = 2.656	∠Cu-N ₁ -N ₂ = 108.3	1626, 1605, 1495, 1438,
	N ₁ -C _α = 1.347	∠C _α -N ₁ -N ₂ = 122.0	1352, 1312, 1186, 1123,
	C _α -C _β = 1.398	∠N ₁ -N ₂ -C _δ = 117.8	1100, 1080, 997, 691, 641,
	C _β -C _γ = 1.390	∠C _α -C _β -C _γ = 117.6	266, 135
	C _γ -C _δ = 1.402	∠C _β -C _γ -C _δ = 117.6	a'': 965, 957, 926, 767, 622,
	N ₂ -C _δ = 1.340	∠C _γ -C _δ -N ₂ = 123.7	369, 351, 112
	N ₂ -N ₁ = 1.346		

Table 4.2. ZEKE peak position (cm⁻¹) and assignment of the Cu-diazine σ -complexes.

Cu-pyrazine		Cu-pyrimidine		Cu-pyridazine			
Position	Assignment	Position	Assignment	Position	Assignment	Position	Assignment
45820.6*	${}^2P_{1/2}^0 \leftarrow {}^2S_{1/2}$	45143	18_1^0	42862	18_1^0	43651	$18_0^1 19_0^2 27_1^1$
45848	10_1^0	45181	19_1^0	42931	19_1^0	43665	$18_1^2 19_0^2$
45879.6*	${}^2P_{3/2}^0 \leftarrow {}^2S_{1/2}$	45332	0_0^0	42994	$18_1^0 19_0^1$	43715	$18_0^1 19_0^3$
45891	18_2^0	45370	27_1^1	43054	0_0^0	43841	$18_0^1 19_0^4$
46038	0_0^0	45407	27_2^2	43111	27_1^1	43862	$18_0^2 19_0^2$
46079	18_1^1	45492	19_0^1	43124	$18_1^0 19_0^2$	43869	18_0^3
46119	18_2^2	45602	18_0^1	43185	19_0^1	43939	$18_1^3 19_0^2$
46160	$10_0^1 18_2^0$	45640	$18_0^1 27_1^1$	43200	$18_0^1 19_1^0$	43985	$18_0^2 19_0^3$
46174.1*	${}^2D_{3/2}^0 \leftarrow {}^2S_{1/2}$	45679	$18_0^1 27_2^2$	43243	$19_0^1 27_1^1$	44000	$18_0^3 19_0^1$
46303	10_0^1	45764	$18_0^1 19_0^1$	43267	$18_1^1 19_0^1$	44072	$18_1^3 19_0^3$
46346	$10_0^1 18_1^1$	45820.6*	${}^2P_{1/2}^0 \leftarrow {}^2S_{1/2}$	43315	19_0^2	44129	$18_0^3 19_0^2$
46390	$10_0^1 18_2^2$	45872	18_0^2	43327	18_0^1	44137	18_0^4
46428	$10_0^2 18_2^0$	45879.6*	${}^2P_{3/2}^0 \leftarrow {}^2S_{1/2}$	43372	$19_0^2 27_1^1$	44260	$18_0^3 19_0^3$
46568	10_0^2	45909	$18_0^2 27_1^1$	43388	$18_0^1 27_1^1$	44269	$18_0^4 19_0^1$
46610	$10_0^2 18_1^1$	45948	$18_0^2 27_2^2$	43395	$18_1^1 19_0^2$		
46692	$10_0^3 18_2^0$	46034	$18_0^2 19_0^1$	43445	19_0^3		
46832	10_0^3	46140	18_0^3	43459	$18_0^1 19_0^1$		
46943	8_0^1	46174.1*	${}^2D_{3/2}^0 \leftarrow {}^2S_{1/2}$	43520	$18_0^1 19_0^1 27_1^1$		
46983	$8_0^1 18_1^1$	46215	$18_0^3 27_2^2$	43588	$18_0^1 19_0^2$		
		46406	18_0^4	43598	18_0^2		

*Atomic transitions of Cu (I).

Table 4.3. Adiabatic ionization energies (AIE, cm^{-1}), metal-ligand bond energies (D_0 , D_0^+ , kJ mol^{-1}), and vibrational frequencies (cm^{-1}) of the Cu-diazine σ -complexes from ZEKE measurements and MP2/6-311+G(*d,p*) calculations. D_0 and D_0^+ are metal-ligand bond dissociation energies for the neutral and ionic complexes, respectively.

		ZEKE ^a	MP2	
Cu-pyrazine	AIE	46038	43127	
	D_0^+ / D_0	243.2 / 48.5	223.1 / 39.4	
	Cu-pyrazine stretch	$\nu_{10}^+ / \nu_{10}, a_1$	265 / 190	257 / 175
	Cu-pyrazine o.p. bend	$\nu_{18}^+ / \nu_{18}, b_1$	115 / 74	105 / 62
	ring breath	ν_8^+, a_1	906	1020
Cu-pyrimidine	AIE	45332	42485	
	D_0^+ / D_0	249.6 / 46.4	229.5 / 38.1	
	Cu-pyrimidine stretch	$\nu_{18}^+ / \nu_{18}, a'$	270 / 189	261 / 174
	Cu-pyrimidine i.p. bend	$\nu_{19}^+ / \nu_{19}, a'$	160 / 151	167 / 127
	Cu-pyrimidine o.p. bend	$\nu_{27}^+ / \nu_{27}, a''$	$\nu_{27}^+ - \nu_{27} = 38$	$\nu_{27}^+ - \nu_{27} = 42$
Cu-pyridazine	AIE	43054	39965	
	D_0^+ / D_0	286.6 / 56.2	266.5 / 44.9	
	Cu-pyridazine stretch	$\nu_{18}^+ / \nu_{18}, a'$	273 / 192	266 / 182
	Cu-pyridazine i.p. bend	$\nu_{19}^+ / \nu_{19}, a'$	131 / 123	135 / 129
	Cu-pyridazine o.p. bend	$\nu_{27}^+ / \nu_{27}, a''$	$\nu_{27}^+ - \nu_{27} = 57$	$\nu_{27}^+ - \nu_{27} = 54$

^a The uncertainty of the AIE values is $\sim 5 \text{ cm}^{-1}$. D_0^+ (Cu⁺-pyrimidine) is from reference [180], with an uncertainty of 9.5 kJ mol^{-1} , and other D_0^+ values are from the corrected MP2 results (see text). D_0 values are obtained by using the thermodynamic relation discussed in the text. i.p., in-plane; o.p., out-of-plane.

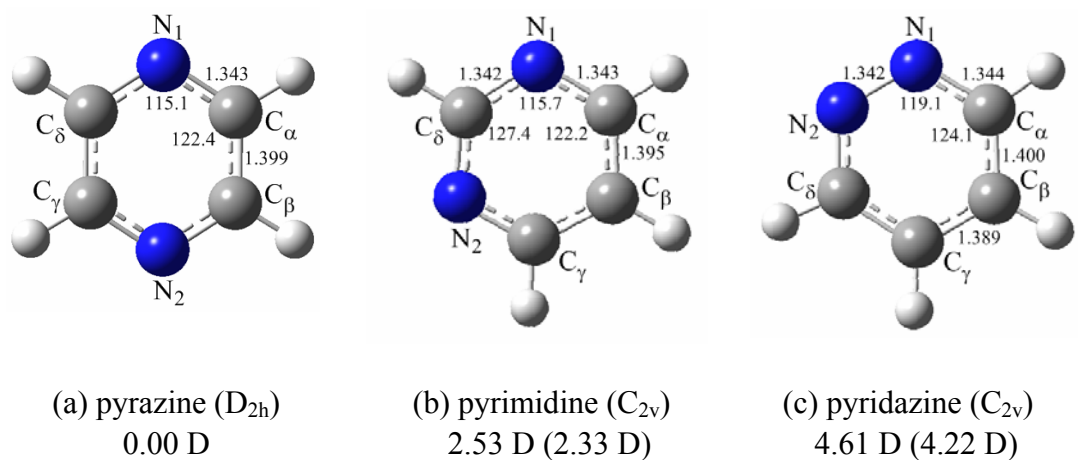


Figure 4.1. Structures and permanent electric dipole moments of diazine molecules from MP2/6-311+G(*d,p*) calculations. Bond distances are in Angstrom, and bond angles are in degrees. The dipole moments in parentheses are experimental values from reference [207].

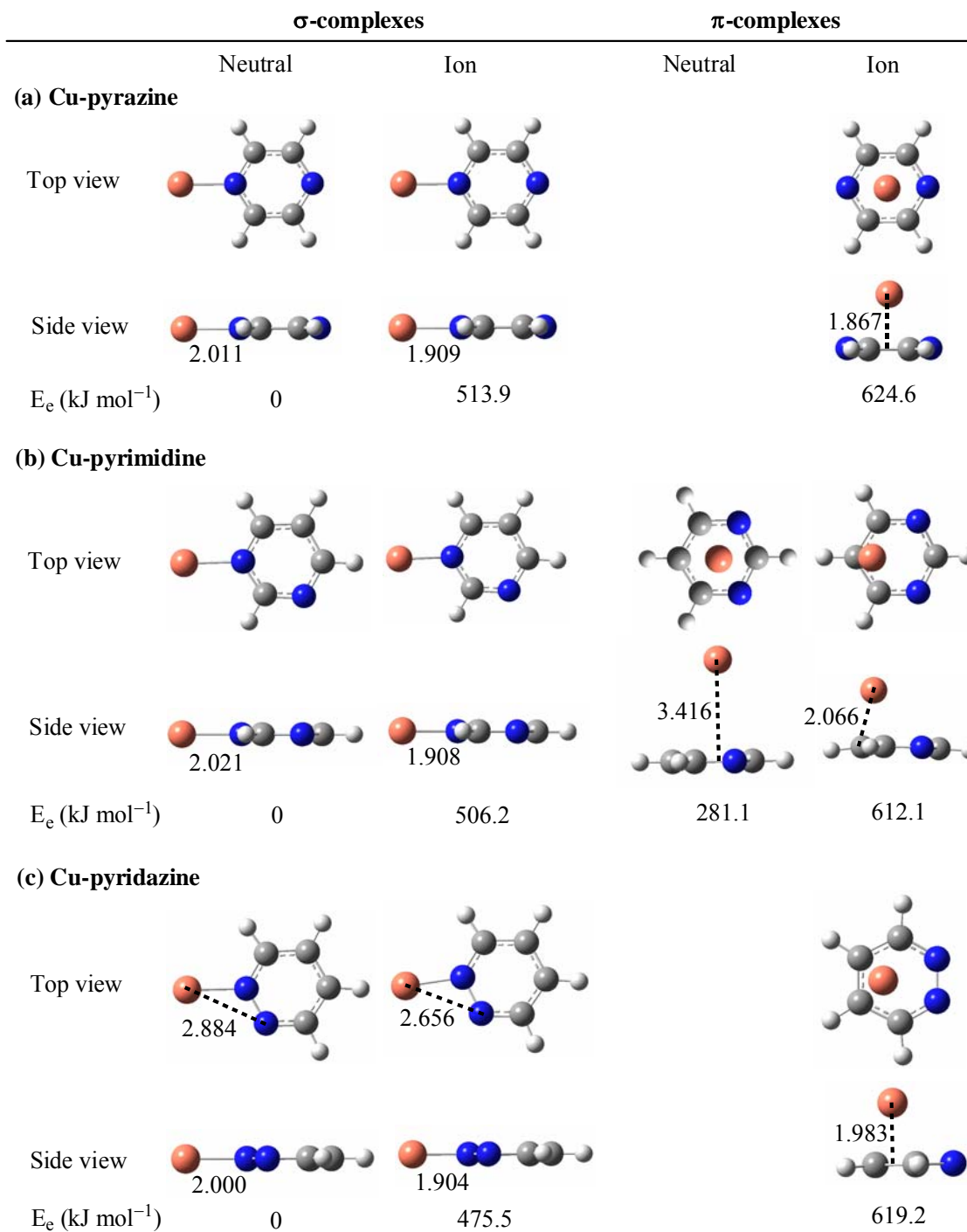


Figure 4.2. Structural isomers and relative electronic energies of Cu-pyrazine (a), -pyrimidine (b), and -pyridazine (c) from MP2/6-311+G(*d,p*) calculations. Bond distances are in Angstrom. The atomic labeling of the diazine molecules is the same as that in Figure 4.1.

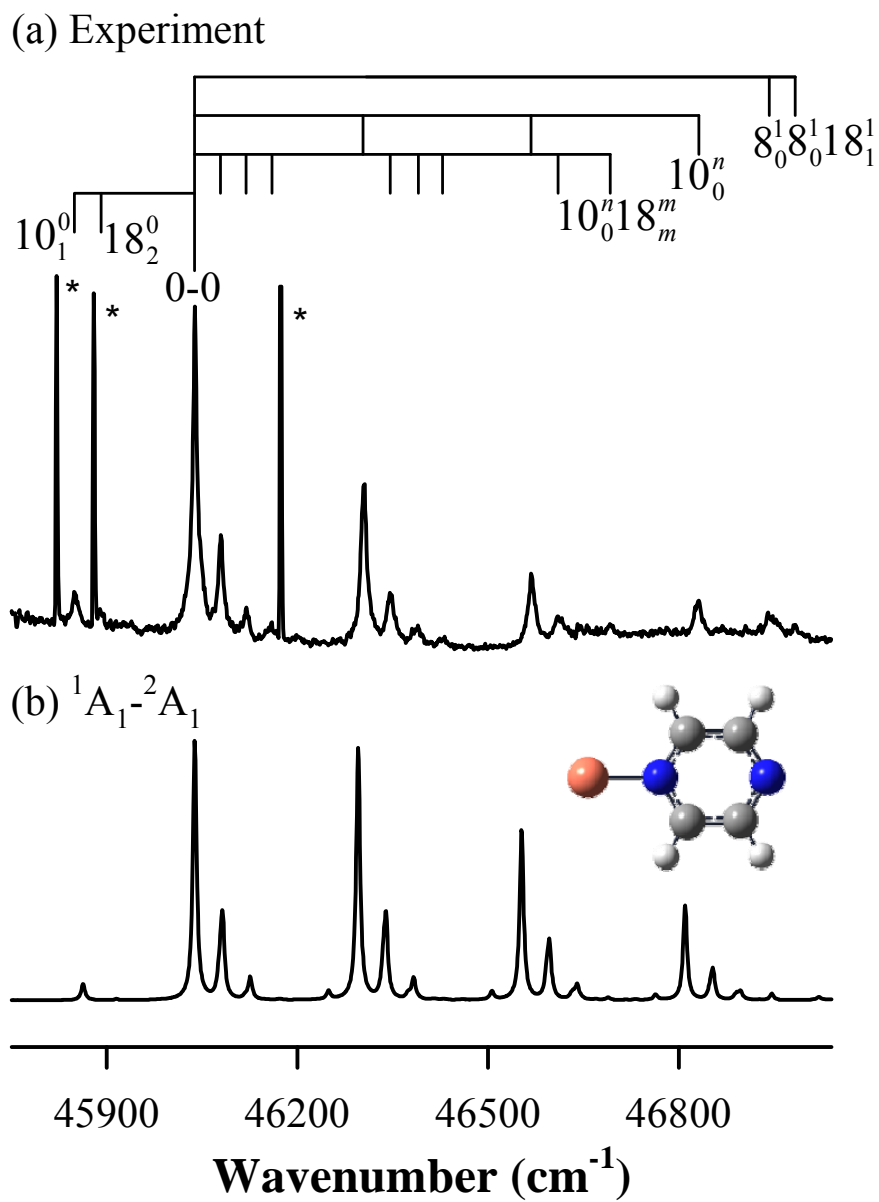


Figure 4.3. ZEKE spectrum of Cu-pyrazine seeded in helium (a) and simulation (b) of the σ -complex at 80 K. Peaks with asterisks are Cu atomic transitions.

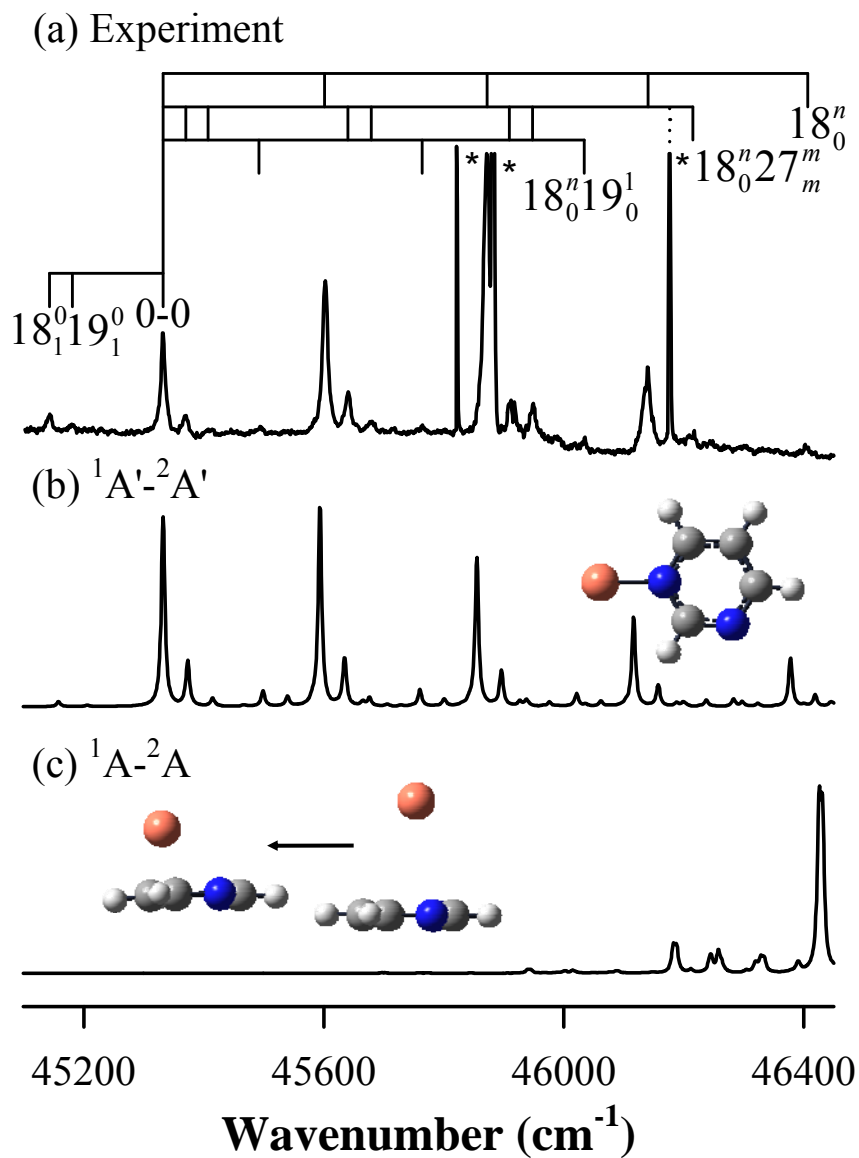


Figure 4.4. ZEKE spectrum of Cu-pyrimidine seeded in helium (a) and simulations of the σ - (b) and π - (c) complexes at 80 K. Peaks with asterisks are Cu atomic transitions.

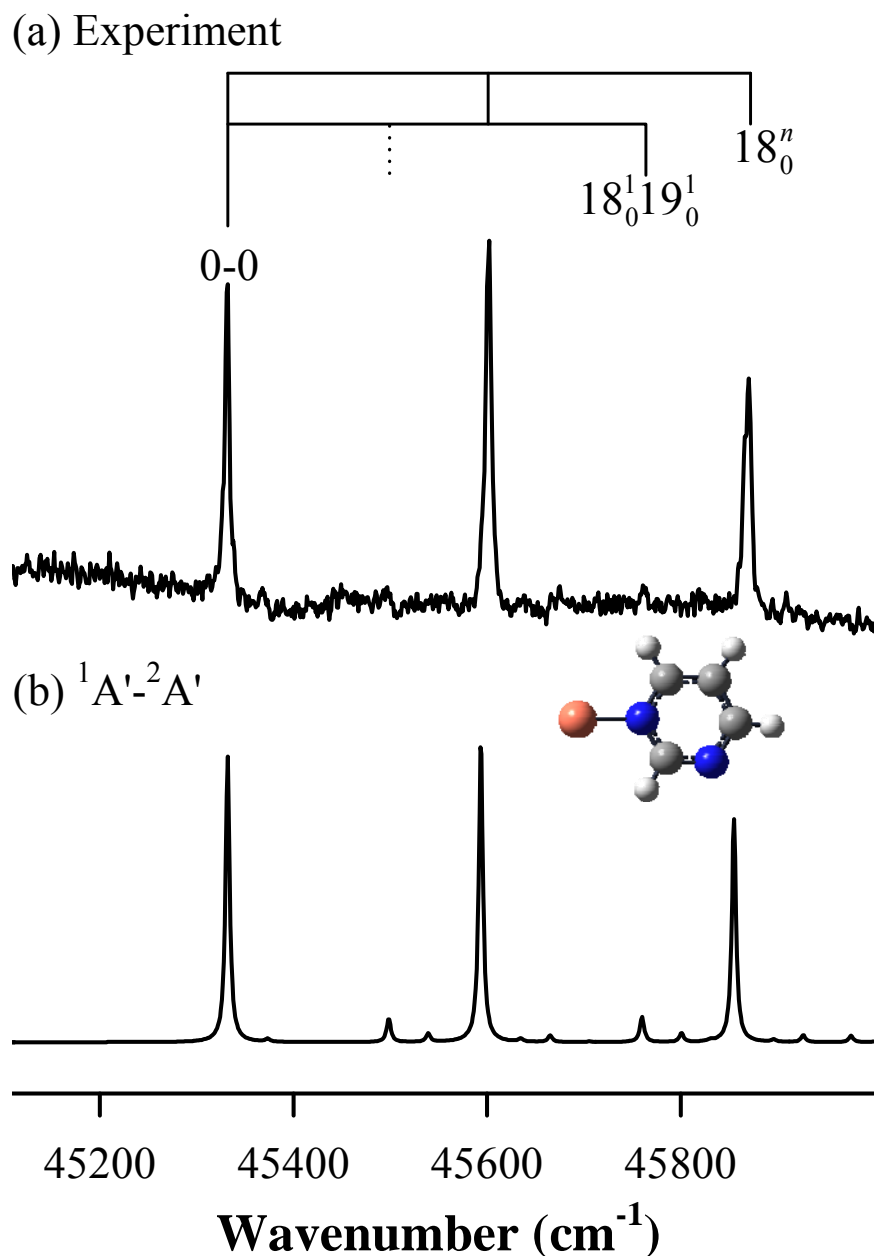


Figure 4.5. ZEKE spectrum of Cu-pyrimidine seeded in a 1:2 Ar/He mixture (a) and simulation (b) of the σ -complex at 20 K.

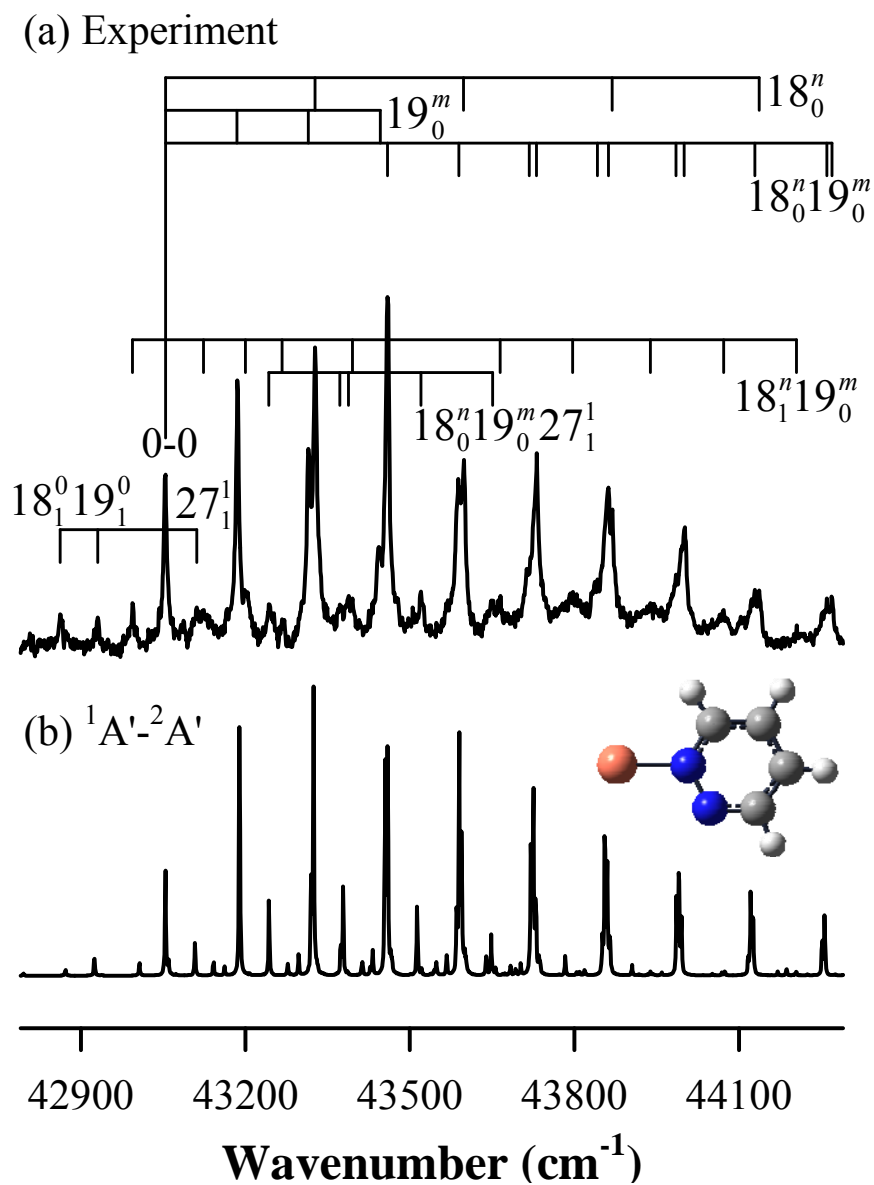


Figure 4.6. ZEKE spectrum of Cu-pyridazine seeded in helium (a) and simulation (b) of the σ -complex at 80 K.

Chapter 5 Spectroscopy and structures of copper-aminopyridine complexes

Aminopyridine has three isomers based on the positions of amino group, and these isomers include 4-aminopyridine (4AP), 3-aminopyridine (3AP) and 2-aminopyridine (2AP). These ligands have two nitrogens providing σ bonding abilities as illustrated in Figure 5.1. One is in the pyridine ring that has a lone pair of electrons in an sp^2 hybridized orbital (σ_α), and the other one is in the amino group which has a lone pair of electrons in an sp^3 hybridized orbital (σ_β). In addition to these σ binding sites, the aromatic pyridine ring in these ligands can function as a π donor or acceptor. It would be interesting to examine how these bonding modes compete with each other in the formations of Cu complexes. In a previous study, Rodgers and coworkers measured the bond energies of alkali metal ion-aminopyridine complexes by CID experiments.²¹² Their experiments were interpreted using ab initio calculations of a σ bonding structure.²¹² Moreover, vibrational analyses of metal-aminopyridine complexes were performed by combining FT-IR spectroscopy and theoretical calculations, where only the σ structure was considered.²¹³⁻²¹⁶ On the other hand, the π bonding mode was identified for the 2-aminopyridine•Ar_n van der Waals complexes by REMPI and ZEKE/MATI spectroscopy and ab initio calculations.^{217,218}

Here, I report the ZEKE spectra of Cu complexes of 4AP, 3AP and 2AP. The molecular structures are identified by comparing the ZEKE spectra with MP2 calculations and spectral simulations. AIEs and metal-ligand and ligand-based vibrational frequencies are measured from the ZEKE spectra.

5.1 Experimental and computational methods

Cu complexes were prepared by reactions of Cu atoms with 4AP (98%, Aldrich), 3AP (99%, Aldrich) or 2AP (99%, Aldrich) in molecular beams. The metal atoms were produced by pulsed laser vaporization of a Cu rod (Cu, 99.9%, Alfa Aesar) with the second harmonic output of a Nd:YAG laser (Quanta-Ray GCR-3, 532 nm, ~ 3 mJ) in the presence of a carrier gas (He or Ar, ultra high purity, Scott-Gross) at ~ 50 psi. The carrier gas was delivered by a piezoelectric pulsed valve.²¹⁹ The metal rod was translated and rotated by a motor-driven mechanism to ensure that each laser pulse ablated a fresh surface. Since 4AP is a solid (m.p.: 155-158 °C) and has a low vapor pressure at room temperature, the Cu oven was used to obtain sufficient ligand vapor.²²⁰ Although 3AP and 2AP are also solids (m.p.: 3AP, 65 °C; 2AP, 57-60 °C) at room temperature, these ligands have higher vapor pressures compared to 4AP. Therefore, these two ligands were housed in a glass bulb directly mounted inside the source chamber, and the ligand vapor interacted with the metal atoms entrained in the carrier gas.

Ionization was carried out by a frequency-doubled dye laser (Lumonics HD-500), pumped by a XeCl excimer laser (Lumonics PM-884, 308 nm) or the third harmonic output (355 nm) of a Nd:YAG laser (~ 180 mJ, Continuum, surelite-III). The production of the 1:1 metal-ligand complexes was maximized by optimizing the timing and power of the vaporization and photoionization lasers, the amount of ligand vapor, and the backing pressure of the carrier gas. Prior to ZEKE experiments, ionization thresholds of these complexes were measured by recording the ion signals as a function of the laser wavelength. ZEKE electrons were produced by photoexcitation of neutral molecules to high-lying Rydberg states, followed by delayed (~ 3 μ s), pulsed electric field ionization (1.2 V cm⁻¹, 100 ns) of these Rydberg states. A small DC field of ~ 0.08 V cm⁻¹ was applied to help separate ZEKE from kinetic electrons produced by direct photoionization. The pulsed electric field was generated by a delay pulsed generator (Stanford Research System, DG535). The ion and electron signals were detected by a

dual MCP detector (Galileo), amplified by a preamplifier (Stanford Research System, SR445), averaged by a gated integrator (Stanford Research System, SR250), and recorded in a laboratory computer. Laser wavelengths were calibrated against vanadium atomic transitions in regions of the ZEKE spectra.²²¹ The field dependence of the ZEKE signal was not measured. However, the energy shift from the small electric field ($\sim 1 \text{ V cm}^{-1}$) has been shown to be much smaller than the spectral linewidth.¹⁷⁸

Calculations of molecular geometries and vibrational frequencies were carried out using the MP2/6-311+G(*d,p*) method, implemented in the GAUSSIAN 03 program.¹¹³ Multidimensional FC factors were computed from the equilibrium geometries, harmonic frequencies, and normal modes of the neutral and ionic complexes.^{143,144} The Duschinsky effect²⁰¹ was considered to account for normal mode differences between the neutral molecule and ion in the FC calculations. Spectral broadening was simulated by giving each line a Lorentzian line shape with the linewidth of the experimental spectrum. Boltzmann distributions were used to simulate spectra at specific vibrational temperatures.

5.2 Results and discussion

5.2.1 Equilibrium structures and vibrational frequencies

In our theoretical survey of Cu-4AP, -3AP and -2AP, a π and two σ (σ_α and σ_β) structures are considered for both neutral and ionic species. The σ_α and σ_β complexes are formed by Cu binding to N_α or N_β (Figure 5.1), and the π complex is formed by Cu binding atop of the pyridine ring. Figure 5.2 presents the calculated metal-ligand distances and energies of the σ_α , σ_β , and π complexes. These theoretical results are discussed below.

5.2.1.1 Cu-4AP

The σ_α -complex of Cu-4AP has C_s symmetry, where the Cu- N_β moiety is nearly coplanar to the pyridine ring, and the two N_β -H bonds slightly bend out of the pyridine plane. This out-of-plane bending has also been found in the free ligand (Figure 5.1), and it is due to the sp^3 hybridized nature of the N_β atom, which tends to remain a tetrahedral configuration. The Cu- N_α distance is calculated to be 1.988 Å, which is somewhat shorter than that in the Cu-pyridine complex (2.005 Å) calculated at the same level of theory.²²² The Cu-N bond in Cu-4AP σ_α complex is about 10.9 kJ mol⁻¹ weaker than the one in Cu-pyridine (47.4 kJ mol).²²²

The σ_β -complex also belongs to the C_s point group and is ~ 1800 cm⁻¹ less stable than the σ_α -complex. This structure has more distortion about the amino group because the copper atom is coordinated directly to this nitrogen atom. The σ_β complex has a longer Cu-N distance (2.096 Å) and smaller bond dissociation energy than the σ_α complex. The Cu-N bond in the σ_β complex is weaker than that in the Cu-NH₃ complex,²²³ due to the large steric repulsion from the pyridine ring. Like in the σ_α complex, the pyridine ring geometry remains virtually the same upon Cu coordination as in the free ligand. This small perturbation of the ligand geometry has been found in other Cu heterocyclic nitrogen containing complexes.⁹³ Upon ionization, the Cu-N distance shrinks by 0.102 Å in the σ_α complex and 0.156 Å in the σ_β complex. The smaller Cu-N distances in the ionic complexes are due to the reduced repulsion between the Cu 4s¹ and N lone pair electrons and an additional charge-dipole attraction. Interestingly, although the σ_α complex undergoes a smaller reduction of the Cu-N bond, it has a larger Cu-N bond energy difference between the neutral and ionic species compared to the σ_β complex [Figure 5.2 (a)]. This energy difference leads to a lower AIE for the σ_α complex (38207 cm⁻¹) compared to the σ_β complex (45781 cm⁻¹). Moreover, the Cu⁺-N bond in the ionic σ_α complex is predicted to be 30.8 kJ mol⁻¹ stronger in energy than the one in the Cu⁺-pyridine complex,²²² but the Cu-N bonds in the

corresponding neutral species have the opposite order. This difference is due to a so-called π -resonance delocalization effect, which induces a more negative charge on the N_α atom of 4AP than that on the N_β atom. The larger negative charge on N_α leads to an increased repulsion towards the Cu $4s^1$ electron, but an enhanced attraction towards the Cu cation. On the other hand, the Cu⁺-N bond in the σ_β complex is much weaker than that in the Cu⁺-NH₃ complex, indicating that electron withdrawing and steric effects from the pyridine ring play an important role in the σ_β bonding. Therefore, the metal-ligand bonding strengths in these Cu-aminopyridines are determined by π -resonance delocalization, electron withdrawing, and steric effects.

Neutral π -complex is not predicted by our theoretical calculations of the Cu-4AP molecule. However, a stable ionic π complex is located about 7400 cm⁻¹ above the lowest-energy ionic σ_α complex [Figure 5.2(a)]. The vertical distance between the Cu cation and the pyridine ring center is calculated to be 1.849 Å. The Cu⁺-ligand bond dissociation energy in this π complex (202.6 kJ mol⁻¹) is slightly larger than the σ_β complex (197.3 kJ mol⁻¹) but much smaller than that of the σ_α complex (289.5 kJ mol⁻¹).

5.2.1.2 Cu-3AP

The σ_α complex of Cu-3AP has a slightly longer Cu-N distance but stronger bond strength compared to the Cu-4AP σ_α complex [Figure 5.2(b)]. Similar to the Cu-4AP σ_α complex, both the Cu and N_β atoms in the Cu-3AP σ_α complex are nearly coplanar to the pyridine ring, but the amino group is slightly tilted from this plane. Upon Cu σ_α complexation, the local configuration of the amino group is almost identical to that in the free ligand, which indicates weaker σ_α bonding in the Cu-3AP complex compared to the Cu-4AP complex. Like in Cu-4AP, the Cu-3AP σ_β complex is relatively higher in energy (1733 cm⁻¹) than the corresponding σ_α structure. Similarly, the Cu-N distance is longer, and the amino group is more distorted in the Cu-3AP σ_β complex compared to the

corresponding σ_α complex. Moreover, the Cu-N distances of both the σ_α and σ_β are shortened upon ionization.

The Cu-3AP π complex is located 3090 cm^{-1} higher in the electronic energy than the lowest-energy σ_α complex [Figure 5.2 (b)]. In this π structure, the Cu atom is closest to the C₄ and C₅ atoms, and the vertical Cu-ring distance is calculated to be 2.154 Å. The longer Cu-ligand distance compared to the σ complexes indicates a weaker bonding interaction in the π configuration. Upon ionization, the Cu ion moves towards the pyridine ring center, and the vertical Cu-ring distance is decreased to 1.855 Å. The much smaller Cu-ring distance is the result of an additional electrostatic interaction between the copper ion and π surface of the ligand. Accordingly, the bond dissociation energy of the ionic π complex (198.9 kJ mol^{-1}) is calculated to be much larger than the corresponding neutral complex (15.2 kJ mol^{-1}). The bond dissociation energy of the Cu-3AP ionic π complex is predicted to be close to that of the Cu-4AP ionic π complex.

5.2.1.3 Cu-2AP

Due to the close proximity of the two nitrogen atoms, 2AP is considered to have different bonding capabilities compared to the other two aminopyridines. For example, if the amino group is rotated by 90°, Cu can bind to both the N _{α} and N _{β} atoms to form a four membered ring. Thus, in our theoretical search for stable σ structures, we consider two initial geometrical configurations for both the neutral and ionic complexes: (1) Cu binding to the N _{α} atom with the amino group fixed in the same local configuration as that in the free ligand, and (2) Cu binding to both the N _{α} and N _{β} atoms, where the amino group is rotated by $\sim 90^\circ$ and perpendicular to the plane of the pyridine ring. For the neutral complexes, only the geometry optimization of the former initial guess is converged to a local minimum energy σ_α structure [Figure 5. 2(c)]. The geometry optimization of the latter initial guess results in a transition state energy structure according to a subsequent frequency analysis, where one imaginary frequency (330i cm^{-1})

was calculated. In that σ_α structure, the Cu atom monodentately binds to the N_α atom, and the N_β atom is nearly coplanar to the pyridine ring with each N-H bond slightly tilted out of the plane. In order to minimize the repulsion from the amino group, the Cu atom bends about 10° out of the plane of the ring. The Cu-N distance of this structure is slightly longer than those of the Cu-4AP and Cu-3AP σ_α complexes, whereas the bond energies are in the order of Cu-4AP < Cu-2AP < Cu-3AP. For the ionic species, only the bidentate configuration is converged, where the copper ion binds to both nitrogen atoms [Figure 5.2(c)]. No ionic monodentate structure was predicted by our theoretical calculations. The ionic bidentate structure has C_s symmetry, where the copper ion is coplanar to the pyridine ring. Although there are two σ bonding interactions between Cu^+ and the ligand, the bond energy of this Cu-2AP complex is 7 kJ mol^{-1} smaller than that of the Cu-4AP monodentate σ_α complex. This smaller bond dissociation energy should be due to ample strain on the four-membered $Cu^+-N_\alpha-C_2-N_\beta$ ring. This ring strain also explains the longer Cu-N distances in the Cu-2AP bidentate ionic σ complex compared to its monodentate neutral species and the Cu-4AP and Cu-3AP monodentate ionic σ_α complexes. The monodentate Cu-2AP σ_β complex is predicted to be 1275 cm^{-1} higher energy than the σ_α complex [Figure 5.2 (c)]. This structure has a similar Cu-N distance and bond dissociation energy to those of the Cu-4AP and Cu-3AP σ_β complexes.

For the π configuration, a local minimum energy structure is predicted only for the ionic species. In this π configuration, the Cu^+ cation is calculated to be closest to the C_5 atom. The vertical Cu^+ -ring distance and bond dissociation energy are predicted to be nearly the same as those in the Cu^+ -4AP and -3AP ionic π complexes. Thus, the mutual position between the amino group and the N_α atom plays a trivial role in the π bonding interaction of copper to these aminopyridines

5.2 ZEKE spectra and vibrational analysis

5.2.1 Cu-4AP

Figure 5.3 (a) shows the ZEKE spectrum of Cu-4AP seeded in He carrier gas. The first strong peak at $41377 (5) \text{ cm}^{-1}$ has a linewidth of 8 cm^{-1} and is assigned to the 0-0 transition between the ground vibronic levels of the neutral and ionic complexes. Above the 0-0 transition, the spectrum displays a main progression (ν_0^n) of 260 cm^{-1} intervals with up to four vibrational quanta. Superimposed on the 260 cm^{-1} progression are a number of satellite peaks separated by 15 and 36 cm^{-1} intervals from the respective cold bands, labeled $\nu_0^n \omega_1^j \delta_s^t$ in the figure. Below the 0-0 transition, the spectrum displays a fairly strong hot transition at 193 cm^{-1} with two sequence bands on the higher energy side, labeled $\nu_1^0 \omega_n^m \delta_m^m$. An additional progression is formed by combinations of one or more 260 cm^{-1} spacings with a 210 cm^{-1} interval. In order to identify hot transitions, ZEKE measurements were carried out with Ar carrier. In this ZEKE spectrum [Figure 5.4(b)], the intensities of all hot transitions ($\nu_0^n \omega_1^j \delta_s^t$ and $\nu_1^0 \omega_n^m \delta_m^m$) are largely reduced due to a lower vibrational temperature of the argon seeded molecules. In addition, the spectral linewidth is reduced from 8 to 5 cm^{-1} due to a lower rotational temperature of the molecules. Furthermore, in comparison to the ZEKE spectra of He-seeded complexes, additional cold transitions that have been overlapped by hot bands are resolved. One of these resolved cold bands is formed by combination of the 260 cm^{-1} spacing with a 514 cm^{-1} interval, labeled $\tau_{a_0}^1 \nu_0^n$ in the spectrum. Another cold band is formed by a 565 cm^{-1} spacing labeled $\tau_{b_0}^1$. A third cold band is determined to be the combination of 260 and 790 cm^{-1} , labeled $\rho_0^1 \nu_0^n$.

Previously, we have observed the Cu^+ -ligand stretching vibrations in the ZEKE spectra of the Cu complexes of pyridine and diazines. Those stretching frequencies are

in the range of 265 - 275 cm^{-1} . From these previous measurements, the main 260 cm^{-1} progression in the Cu-4AP ZEKE spectra is assigned to the Cu^+ -4AP stretching vibration of the σ_α structure. Moreover, the spectral profile of Cu-4APseeded in He is very similar to the ZEKE spectra of the Cu-pyridine and -diazines complexes seeded in the same carrier gas. In those Cu-pyridine and -diazine complexes, the satellite bands have been assigned to the sequence transitions of the Cu-ring in-plane and/or out-of-plane bend and the neutral Cu-ring stretch modes. Thus, the sequence peaks labeled by $v_0^n \omega_i^j \delta_s^t$ and $v_1^0 \omega_i^j \delta_s^t$ in the Cu-4AP ZEKE spectrum [Figure 5.3(a)] can be attributed to such bending and stretching modes. Moreover, from a previous FT-IR spectroscopic measurement of Cu^{2+} -(4Apy)₂Ni(CN)₄,²¹⁴ the 514, 565 and 790 cm^{-1} intervals in the ZEKE spectra should arise from ligand-based vibrations of two ligand out-of-plane distortion and a C-H out-of-plane bend.

In our MP2 calculations, both σ_α and σ_β structures are predicted for the neutral and ionic Cu-4AP complexes, but only one ionic π complex has been found. Since the energy difference between the σ_α and σ_β complexes is small, both structures may have been produced in the molecular beam. In our spectral analysis, we thus consider both the σ isomers by comparing the experimental and calculated AIEs, vibrational frequencies, and FC intensities. Transitions between two different isomers are excluded, because such transitions are expected to have a very different FC intensity profile from the experimental spectra. The AIEs of the σ_α and σ_β complexes are calculated to be 37336 and 44195 cm^{-1} . Our previous studies have shown that MP2 calculations typically underestimate the AIEs of the Cu-ligand complexes by about 3000 cm^{-1} .^{84,157,224} By applying the 3000 cm^{-1} correction, the AIEs are estimated to be 40336 cm^{-1} for the σ_α structure and 47195 cm^{-1} for the σ_β structure, respectively. After such a correction, the theoretical AIE of the σ_α structure better matches the measured value of 41377 cm^{-1} , and the σ_α structure is most likely to be the ZEKE carrier.

Figures 5.3 and 5.4 compare the experimental ZEKE spectra to the spectral

simulations of the σ_α and σ_β complexes at 50 and 10 K. In the simulations at 50 K, 150 K is used for the neutral Cu-4AP stretching mode, because it has a much larger frequency than other observed neutral vibrations and may not be populated to excited levels at a low temperature. The σ_α simulations show a main progression with 256 cm^{-1} intervals, whereas the σ_β simulations display three strong cold progressions with 67, 201, and 422 cm^{-1} intervals and their combination bands. Moreover, the σ_β simulation at 50 K does not reproduce the hot transitions well. Overall, the simulations of the σ_α complex are in much better agreement with the experimental spectra compared to those of the σ_β complex. Thus, the ZEKE spectrum is assigned to the σ_α isomer.

Based on the good agreement between the σ_α simulations and the experimental spectra, the 260 cm^{-1} major progression is confirmed to be the transitions from the ground vibrational level of the neutral Cu-4AP molecule to the Cu^+ -4AP symmetric stretching levels of the ion. The stretch frequency in the neutral Cu-4AP complex is measured to be 193 cm^{-1} . A least squares fit of the peak positions of ν_0^n to $G(\nu) = \omega_s^+(\nu^+ + 1/2) + x_{ss}^+(\nu^+ + 1/2)^2$ yields a harmonic frequency of 261.1(5) cm^{-1} and an anharmonicity of -0.6 (1) cm^{-1} for the ion stretching mode. The 15 and 36 cm^{-1} spacings arise from $\Delta\nu = 0$ sequence transitions of the Cu-ring out-of-plane and in-plane bending vibrations, respectively. The 210 cm^{-1} interval is ascribed to the $3 \leftarrow 1$ sequence transition of the Cu-ring in-plane bend. Therefore, the neutral and ionic Cu-ring in-plane bending frequencies are derived to be 56 and 89 cm^{-1} , respectively. Moreover, the 514, 565 and 790 cm^{-1} are confirmed to be the vibrational frequencies of two ligand out-of-plane distortions (τ_a^+ and τ_b^+) and a C-H out-of-plane bend (ρ^+) in the ion, which have nearly the same frequencies as those in the previous IR measurement of Cu^{2+} -(4Apy)₂Ni(CN)₄.²¹⁴

5.2.2 Cu-3AP

The ZEKE spectra of Cu-3AP seeded in He and Ar carriers are presented in Figure 5.5 (a) and 5.6 (a), respectively. Both spectra have a similar spectral profile to and slightly narrower linewidths (6 cm^{-1} in He and 5 cm^{-1} in Ar) than those of Cu-4AP. The 0-0 band is located at 42541 cm^{-1} , 1164 cm^{-1} higher in energy than that of Cu-4AP. The main progression labeled ν_0^n has an interval of 268 cm^{-1} . Superimposed on the main progression are a number of sequence transitions with 29 cm^{-1} spacings. Additionally, the spectrum shows a small peak at 131 cm^{-1} above the origin band and its combinations with one or more 268 cm^{-1} intervals. The ZEKE spectrum of the helium-seeded complex shows a fairly strong hot band 194 cm^{-1} below the 0-0 transition and a small peak 29 cm^{-1} above the 0-0 transition. In the spectrum using Ar carrier, all hot transitions are vanished. By comparing these two experimental ZEKE spectra, two cold progressions containing 268 cm^{-1} intervals combined with 482 or 564 cm^{-1} intervals are found to be overlapped with some of the sequence transitions. By comparing to the ZEKE spectrum of Cu-4AP [Figure 5.3 (a)], the 268 and 194 cm^{-1} intervals in the Cu-3AP ZEKE spectra are assigned to the Cu^+ -3AP and Cu-3AP stretching modes; the 484 and 564 cm^{-1} intervals to ligand-based frequencies; and the sequence bands to Cu-3AP bending vibrations.

The spectral simulations of the Cu-3AP σ_α , σ_β and π complexes at 60 and 10 K are presented in Figures 5.5 (b, c, d) and 5.6 (b, c, d), respectively. In the simulations at 60 K, 150 K is used for the neutral Cu-4AP stretching mode. A comparison of the experimental and calculated spectra excludes contribution of the π complex to the observed spectrum. The simulation of the σ_β complex shows more cold transitions and a shorter spectral profile than the experimental spectrum. Simulation from the σ_α complex matches the experimental spectrum quite well. Moreover, the AIEs of σ_α , σ_β and π complexes are predicted to be 39816 , 43758 , and 43133 cm^{-1} by the MP2 method, respectively. By applying the 3000 cm^{-1} correction, the AIEs are calculated to be 42816 ,

46758, and 46133 cm^{-1} for the σ_α , σ_β and π complexes, respectively. The AIE of the σ_α complex (42816 cm^{-1}) has the best match with the experimental value (42541 cm^{-1}). Therefore, the observed spectrum is attributed to the σ_α structure of the Cu-3AP complex. The 268 and 194 cm^{-1} intervals are assigned to the ionic (ν^+) and neutral (ν) metal-ligand stretching frequencies. A least squares fit of the peak positions of ν_0^n to $G(\nu) = \omega_s^+(\nu^+ + 1/2) + x_{ss}^+(\nu^+ + 1/2)^2$ yields a harmonic frequency of 271.6 (11) cm^{-1} and an anharmonicity of -1.1 (2) cm^{-1} for this ion stretching mode. The 482 and 564 cm^{-1} intervals are attributed to two ligand out-of-plane distortions, τ_a^+ and τ_b^+ . The τ_b^+ mode is largely mixed with an NH_2 wagging motion. The 131 cm^{-1} interval and its combinations are determined to be a number of cold transitions arising from the Cu^+ -3AP out-of-plane bending vibration (ω^+). Due to the limited size of the ZEKE signal, these peaks were not observed in the ZEKE spectrum using Ar carrier gas. From the calculated FC factors, the superimposed sequence bands are attributed to both Cu-3AP in-plane (δ^+) and out-of-plane bending (ω^+) vibrations, which overlap in the simulation, because the calculated differences between the neutral and ionic in-plane bending vibrations (δ/δ^+) and between the neutral and ionic out-of-plane bending vibrations (ω/ω^+) are almost the same. The measured frequency difference between the ionic and neutral Cu-ring in-plane bending vibrations is 29 cm^{-1} . Thus, the neutral Cu-ring out-of-plane bending frequency (ω) is derived to be 102 cm^{-1} .

5.2.3 Cu-2AP

The ZEKE spectrum of the Cu-2AP complex has been obtained using a 1:1 gas mixture of He and Ar as the carrier. The vibrational levels could not be well resolved using pure He carrier, and the ZEKE signal with Ar carrier was too weak. The Cu-2AP ZEKE spectrum [Figure 5.7(a)] shows a broader linewidth ($\sim 25 \text{ cm}^{-1}$) and a lower signal/noise ratio compared to the spectra of Cu-4AP and Cu-3AP. The first strong peak

at 43742 cm^{-1} is assigned to the 0-0 transition. The spectrum displays a major vibrational progression of 256 cm^{-1} (ν_0'') with up to three quanta, a progression of 446 cm^{-1} (τ_a'') with up to two quanta, an interval of 660 cm^{-1} (τ_b^1), and a few combinations of the 256 and 446 cm^{-1} intervals. Two sequence bands are inconspicuously superimposed on the right shoulders of the 0-0 and ν_0^1 peaks.

Our MP2 calculations predict two monodentate structures (σ_α and σ_β) for the neutral Cu-2AP complex and one bidentate structure for the ion. On the basis of the 0-0 transition energy in the ZEKE spectrum, the experimental IE of Cu-2AP complex is 43742 cm^{-1} , about 1200 cm^{-1} higher than that of the Cu-3AP complex and about 2400 cm^{-1} higher than that of the Cu-4AP complex. Generally, more σ bonding interactions should lead to larger IE shifts from the bare metal atom. In other words, if the Cu-2AP complex possesses a bidentate configuration, its IE should be much smaller than those of the Cu-3AP and Cu-4AP complexes. Thus, this IE measurement indicates that the Cu-2AP complex is formed by a monodentate binding. Moreover, the ZEKE spectrum of Cu-2AP exhibits a fairly short FC profile and fewer bands, which indicates a small geometry change upon ionization. Furthermore, the 256 cm^{-1} spacing of the major progression is very close that in the Cu-3AP (271 cm^{-1}) and Cu-4AP (261 cm^{-1}) ZEKE spectra. Therefore, both the neutral and ionic Cu-2AP complexes should have a monodentate structure. Unfortunately, the predicted structural changes are large and the simulation is not consistent with the experimental spectrum (not shown). Nevertheless, the spectral assignments can be carried out by comparison to the Cu-3AP and Cu-4AP ZEKE spectra. Consequently, the 256 cm^{-1} spacing is assigned to the Cu^+ -2AP stretch (ν^+), the 446 and 660 cm^{-1} intervals are attributed to two ligand distortions (τ_a^+ and τ_b^+), and the 51 cm^{-1} intervals to the frequency difference between the ionic and neutral Cu-ring out-of-plane bend.

5.3 Ionization energies and vibrational frequencies

Table 5.3 summarizes the AIEs, metal-ligand bond energies, and vibrational frequencies from the ZEKE spectra and MP2/6-311+G(*d,p*) calculations of the three Cu-aminopyridine complexes. The AIEs of the Cu-aminopyridine complexes are in the order Cu-4AP < Cu-3AP < Cu-2AP, with $\sim 1200 \text{ cm}^{-1}$ increment. This small increment is consistent with the similar σ_α bonding interaction in these Cu-aminopyridine complexes. The MP2 method provides quite good predictions for most of the Cu-ligand stretching and ligand-based vibrational frequencies but have large errors for the Cu-ligand bending frequencies. The measured and calculated ionization energies of Cu-4AP and Cu-3AP are in good agreement, if the 3000 cm^{-1} IE correction is considered.

In the neutral and ionic Cu-aminopyridine complexes, the Cu/Cu⁺-N bond strengths are determined by the balance of ion-dipole attractions, electron withdrawing, steric repulsions, and π -resonance effects. The π -resonance effect seems to play a more significant role for the neutral species compared to the other interactions. In the Cu-4AP and Cu-2AP σ_α complexes, the π -resonance effect leads to an additional negative charge on the N $_\alpha$ atom, which enhances the repulsion to the Cu 4s¹ electron. Compared to Cu-4AP, the Cu-2AP has an additional steric repulsion from the amino group, which forces the Cu-N bond to bend out of the pyridine plane. Unlike Cu-4AP and -2AP, the Cu-3AP σ_α complex has little π -resonance and steric repulsion due to the meta-position of its amino group. Consequently, the Cu-N bonding strengths of the Cu-4AP, Cu-3AP, and Cu-2AP σ_α neutral complexes are in the order of Cu-4AP < Cu-2AP < Cu-3AP. The sequence for the bond energies of the Cu⁺-4AP and Cu⁺-3AP ions is also consistent with the π -resonance effect, i.e., Cu⁺-4AP > Cu⁺-3AP; The bond energy of the Cu⁺-2AP ion is not considered in this trend since a bidentate binding mode, rather than a monodentate mode is predicted for this ion.

The Cu⁺-ligand stretching vibration (ν^+) shows the strongest FC activities in the ZEKE spectra of the three Cu-aminopyridine complexes. The stretching frequencies are

in the range of $263 \pm 8 \text{ cm}^{-1}$ and close to the Cu^+ -L stretching frequencies of the Cu^+ -diazine and Cu^+ -pyridine complexes. In addition, the neutral Cu-L stretching frequencies of the Cu-4AP and Cu-3AP are measured to be nearly identical and are also very close to the Cu-L stretching frequencies of the Cu-diazine and Cu-pyridine complexes. The similar frequencies among these three copper-aminopyridine complexes indicate that they share the similar bonding mode with Cu binding to the N_α atom of the pyridine ring.

5.4 Conclusion

Adiabatic ionization energies and various vibrational frequencies of three Cu-aminopyridine complexes are measured by ZEKE spectroscopy. The Cu-N bond strength are in order of $\text{Cu-4AP} < \text{Cu-2AP} < \text{Cu-3AP}$, while the ionization energies are in the order of $\text{Cu-4AP} < \text{Cu-3AP} < \text{Cu-2AP}$. The Cu^+ -L stretching frequencies of the Cu-4AP, -3AP and -2AP ionic complexes are measured to be 261, 271, and 256 cm^{-1} , respectively. The ZEKE spectra are analyzed using MP2 calculations and FC simulations. Structures formed by σ_α , σ_β , and π bonding are considered, but only the σ_α configuration is identified in our experimental measurements. Moreover, the MP2 method failed to predict a monodentate ionic structure for Cu^+ -2AP, spectral comparisons indicate that this complex is also formed by a monodentate σ_α binding scheme.

Table 5.1. Molecular symmetries, equilibrium geometries (Å, degree), and vibrational frequencies (cm⁻¹) of the Cu-aminopyridine $\sigma\alpha$ -complexes from MP2/6-311+G(d,p) calculations. The N and C atom labeling scheme is depicted in Figure 5.1.

	Bond lengths	Bond angles	Vibrational frequencies
Cu-4AP (C_s)			
² A'	Cu-N: 1.988	\angle Cu-N _{α} -C ₂ : 121.9	a': 3641, 3310, 3223, 2503,
	N _{α} -C ₂ : 1.343	\angle C ₆ -N _{α} -C ₂ : 116.3	1675, 1625, 1414, 1301,
	C ₂ -C ₃ : 1.374	\angle N _{α} -C ₂ -C ₃ : 124.4	1254, 1030, 990, 985, 817,
	C ₃ -C ₄ : 1.405	\angle C ₂ -C ₃ -C ₄ : 118.8	657, 588, 543, 501, 204, 192,
	C ₄ -N _{β} : 1.364	\angle C ₃ -C ₄ -C ₅ : 117.3	27
		\angle C ₃ -C ₄ -N _{β} : 121.3	a'': 3745, 3229, 3203, 1718,
		\angle Cu-N _{α} -C ₂ -C ₃ : 179.6	1523, 1386, 1379, 1158,
¹ A'		\angle C ₂ -C ₃ -C ₄ -N _{β} : 177.7	1090, 1031, 857, 687, 453,
		\angle C ₃ -C ₄ -N _{β} -H: 18.1	395, 392, 116
	Cu-N: 1.886	\angle Cu-N _{α} -C ₂ : 121.4	a': 3617, 3241, 3226, 1704,
	N _{α} -C ₂ : 1.362	\angle C ₆ -N _{α} -C ₂ : 117.1	1668, 1563, 1392, 1250,
	C ₂ -C ₃ : 1.382	\angle N _{α} -C ₂ -C ₃ : 123.1	1089, 1045, 905, 866, 784,
	C ₃ -C ₄ : 1.413	\angle C ₂ -C ₃ -C ₄ : 120.0	585, 558, 502, 440, 256, 209,
	C ₄ -N _{β} : 1.355	\angle C ₃ -C ₄ -C ₅ : 116.7	69
		\angle C ₃ -C ₄ -N _{β} : 121.6	a'': 3741, 3240, 3227, 1603,
		\angle Cu-N _{α} -C ₂ -C ₃ : 179.8	1532, 1390, 1376, 1147,
		\angle C ₂ -C ₃ -C ₄ -N _{β} : 177.7	1063, 924, 839, 671, 458,
	\angle C ₃ -C ₄ -N _{β} -H: 14.1	392, 380, 151	
Cu-3AP(C₁)			
² A	Cu-N: 1.999	\angle Cu-N _{α} -C ₂ : 120.1	3704, 3594, 3238, 3223,
	N _{α} -C ₂ : 1.345	\angle C ₆ -N _{α} -C ₂ : 117.1	3205, 3193, 1670, 1641,
	C ₂ -C ₃ : 1.406	\angle N _{α} -C ₂ -C ₃ : 123.1	1623, 1519, 1483, 1443,
	C ₃ -C ₄ : 1.405	\angle C ₂ -C ₃ -C ₄ : 117.5	1370, 1329, 1222, 1160,
	C ₄ -C ₅ : 1.394	\angle C ₃ -C ₄ -C ₅ : 119.1	1097, 1067, 1038, 912, 880,
	C ₅ -C ₆ : 1.396	\angle C ₄ -C ₅ -C ₆ : 119.6	864, 859, 757, 651, 649, 551,
	C ₆ -N _{α} : 1.350	\angle C ₅ -C ₆ -N _{α} : 121.7	550, 484, 387, 379, 291, 203,
	C ₃ -N _{β} : 1.392	\angle C ₂ -C ₃ -N _{β} : 120.6	185, 111, 66
		\angle Cu-N _{α} -C ₂ -C ₃ : 178.7	
		\angle N _{α} -C ₂ -C ₃ -N _{β} : 176.6	
		\angle C ₂ -C ₃ -N _{β} -H: 25.2	

Table 5.1 continued

¹ A	Cu-N: 1.894	∠Cu-N _α -C ₂ : 120.6	3727, 3611, 3253, 3240,
	N _α -C ₂ : 1.356	∠C ₆ -N _α -C ₂ : 119.5	3219, 3218, 1684, 1654,
	C ₂ -C ₃ : 1.408	∠N _α -C ₂ -C ₃ : 112.6	1621, 1541, 1494, 1448,
	C ₃ -C ₄ : 1.411	∠C ₂ -C ₃ -C ₄ : 117.3	1381, 1361, 1229, 1167,
	C ₄ -C ₅ : 1.390	∠C ₃ -C ₄ -C ₅ : 119.6	1090, 1081, 1036, 929, 883,
	C ₅ -C ₆ : 1.394	∠C ₄ -C ₅ -C ₆ : 120.0	880, 833, 754, 670, 560, 551,
	C ₆ -N _α : 1.358	∠C ₅ -C ₆ -N _α : 120.9	522, 489, 390, 387, 350, 262,
	C ₃ -N _β : 1.371	∠C ₂ -C ₃ -N _β : 120.7	195, 141, 94
		∠Cu-N _α -C ₂ -C ₃ : 179.4	
		∠N _α -C ₂ -C ₃ -N _β : 176.7	
		∠C ₂ -C ₃ -N _β -H: 21.9	
Cu-2AP			
² A (C ₁)	Cu-N: 2.008	∠Cu-N _α -C ₂ : 1.227	3687, 3536, 3248, 3230,
	N _α -C ₂ : 1.349	∠C ₆ -N _α -C ₂ : 118.9	3215, 3213, 1687, 1663,
	C ₂ -C ₃ : 1.412	∠N _α -C ₂ -C ₃ : 121.4	1629, 1522, 1470, 1417,
	C ₃ -C ₄ : 1.390	∠C ₂ -C ₃ -C ₄ : 119.4	1352, 1338, 1187, 1165,
	C ₄ -C ₅ : 1.403	∠C ₃ -C ₄ -C ₅ : 119.1	1107, 1073, 1027, 910, 902,
	C ₅ -C ₆ : 1.391	∠C ₄ -C ₅ -C ₆ : 118.3	891, 839, 746, 666, 646, 593,
	C ₆ -N _α : 1.357	∠C ₅ -C ₆ -N _α : 123.1	569, 477, 416, 382, 348, 201,
	C ₂ -N _β : 1.383	∠N _α -C ₂ -N _β : 117.6	179, 128, 62
		∠Cu-N _α -C ₂ -C ₃ : 168.5	
		∠C ₄ -C ₃ -C ₂ -N _β : 175.9	
		∠C ₃ -C ₂ -N _β -H: 30.6	
¹ A' (C _s) ^a	Cu-N: 2.019	∠Cu-N _α -C ₂ : 95.8	a': 3501, 3255, 3244, 3240,
	N _α -C ₂ : 1.349	∠C ₆ -N _α -C ₂ : 119.3	3230, 1662, 1627, 1610,
	C ₂ -C ₃ : 1.392	∠N _α -C ₂ -C ₃ : 123.0	1507, 1472, 1418, 1321,
	C ₃ -C ₄ : 1.400	∠C ₂ -C ₃ -C ₄ : 117.7	1263, 1190, 1130, 1067,
	C ₄ -C ₅ : 1.398	∠C ₃ -C ₄ -C ₅ : 119.4	1038, 1012, 834, 652, 582,
	C ₅ -C ₆ : 1.396	∠C ₄ -C ₅ -C ₆ : 119.2	243, 140
	C ₆ -N _α : 1.349	∠C ₅ -C ₆ -N _α : 121.3	a'': 3581, 1188, 951, 942,
	C ₂ -N _β : 1.450	∠N _α -C ₂ -N _β : 110.7	896, 771, 602, 494, 425, 388,
		∠Cu-N _α -C ₂ -C ₃ : 180.0	203, 74
		∠C ₄ -C ₃ -C ₂ -N _β : 180.0	
		∠C ₃ -C ₂ -N _β -H: 59.5	

^a The theoretical values of the Cu-2AP bidentate ion are listed.

Table 5.2. ZEKE peak positions (cm^{-1}) and assignments of the Cu-aminopyridine complexes.

Cu-4AP		Cu-3AP		Cu-2AP	
Positions	Assignments	Positions	Assignments	Position	Assignments
41184	ν_1^0	42347	ν_1^0	43742	0_0^0
41199	$\nu_1^0\omega_1^1$	42378	$\nu_1^0\omega_1^1$	43793	ω_1^1
41219	$\nu_1^0\delta_1^1$	42541	0_0^0	43886	?
41377	0_0^0	42570	ω_1^1/δ_1^1	43944	?
41392	ω_1^1	42613	ν_1^1	44005	ν_0^1
41410	δ_1^1	42666	ω_0^1	44052	$\nu_0^1\omega_1^1$
41427	$\omega_1^1\delta_1^1$	42691	ω_1^2	44188	τ_{a0}^1
41445	δ_2^2/ν_1^1	42809	ν_0^1	44223	h_c
41588	δ_1^3	42838	$\nu_0^1\omega_1^1/\nu_0^1\delta_1^1$	44266	ν_0^2
41637	ν_0^1	42929	$\nu_0^1\omega_0^1$	44400	τ_{b0}^1
41652	$\nu_0^1\omega_1^1$	42943	$\nu_0^1\delta_0^1$	44449	$\tau_{a0}^1\nu_0^1$
41673	$\nu_0^1\delta_1^1$	42957	$\nu_0^1\omega_1^2$	44527	ν_0^3
41687	$\nu_0^1\omega_1^1\delta_1^1$	43023	τ_{a0}^1	44633	τ_{a0}^2
41705	$\nu_0^1\delta_2^2$	43076	ν_0^2	44707	$\tau_{a0}^1\nu_0^2$
41846	$\nu_0^1\delta_1^3$	43105	$\nu_0^2\omega_1^1/\nu_0^2\delta_1^1/\tau_{b0}^1$	44894	$\tau_{a0}^2\nu_0^1$
41891	τ_{a0}^1	43137	$\tau_{b0}^1\omega_1^1/\tau_{b0}^1\delta_1^1$	44915.2	${}^4D_{1/2}^0 \leftarrow {}^3S_{1/2}$
41896	ν_0^2	43212	$\nu_0^2\omega_0^1/\nu_0^2\omega_1^2$	44966	$\tau_{a0}^1\nu_0^3$
41911	$\nu_0^2\omega_1^1$	43283	$\tau_{a0}^1\nu_1^1$		
41929	$\nu_0^2\delta_1^1$	43343	ν_0^3		
41942	$\nu_0^2\omega_1^1\delta_1^1/\tau_{b0}^1$ ^a	43372	$\nu_0^3\omega_1^1/\nu_0^3\delta_1^1/\tau_{b0}^1\nu_0^1$		
41960	$\nu_0^2\delta_2^2$	43401	$\tau_{b0}^1\nu_0^1\omega_1^1/\tau_{b0}^1\nu_0^1\delta_1^1$		
41986	$\nu_0^2\omega_0^2$	43445	?		
42105	$\nu_0^2\delta_1^3$	43466	$\nu_0^3\omega_0^1$		
42147	$\tau_{a0}^1\nu_0^1$	43489	$\nu_0^3\omega_1^2$		
42153	ν_0^3	43604	ν_0^4		
42167	$\nu_0^3\omega_1^1/\rho_0^1$ ^a	43638	$\nu_0^4\omega_1^1/\nu_0^4\delta_1^1/\tau_{b0}^1\nu_0^2$		
42187	$\nu_0^3\delta_1^1$	43661	$\tau_{b0}^1\nu_0^2\omega_1^1/\tau_{b0}^1\nu_0^2\delta_1^1$		
42222	$\nu_0^3\delta_2^2$	43864	ν_0^5		
42360	$\nu_0^3\delta_1^3$	43903	$\nu_0^5\omega_1^1$		
42400	$\tau_{a0}^1\nu_0^2/\tau_{a0}^2$				
42410	ν_0^4				
42427	$\nu_0^4\omega_1^1/\rho_0^1\nu_0^1$ ^a				
42448	$\nu_0^4\delta_1^1$				
42468	$\nu_0^4\delta_2^2$				

Table 5.3. Adiabatic ionization energies (AIE, cm^{-1}), metal-ligand bond energies (D_0 , D_0^+ , kJ mol^{-1}), and vibrational frequencies (cm^{-1}) of the Cu-aminopyridine σ -complexes from ZEKE measurements and MP2/6-311+G(*d,p*) calculations.

			ZEKE ^a	MP2
Cu-4AP	AIE		41377	37336
	D_0^+ / D_0			289.5 / 36.5
	Cu-4AP stretch	$\nu^+ / \nu, a'$	261 ^b / 193	256 / 192
	Cu-4AP o.p. bend	$\omega^+ / \omega, a''$	$\omega^+ - \omega = 15$	67/27
	Cu-4AP i.p. bend	$\delta^+ / \delta, a'$	89 / 56	151 / 116
	ligand o.p. distortion	τ_a^+, a'	514	502
	ligand o.p. distortion	τ_b^+, a'	565	558
	C-H o.p. bend	ρ^+, a'	790	784
Cu-3AP	AIE		42541	39816
	D_0^+ / D_0			274.7 / 51.4
	Cu-3AP stretch	$\nu^+ / \nu, a$	271 ^b / 194	262 / 185
	Cu-3AP o.p. bend	$\omega^+ / \omega, a$	131/102	94 / 66
	Cu-3AP i.p. bend	$\delta^+ / \delta, a$	$\delta^+ - \delta = 29$	141/111
	ligand o.p. distortion	τ_a^+, a	482	489
	NH ₂ wag & ligand o.p. distortion	τ_b^+, a	564	522
Cu-2AP	AIE		43742	
	D_0^+ / D_0			-- / 48.0
	Cu-2AP stretch	ν^+, a	256	
	Cu-2AP o.p. bend	ω^+ / ω	$\omega^+ - \omega = 51$	
	ligand distortion	τ_a^+, a	446	
	ligand distortion	τ_b^+, a	660	

^a The uncertainty of the AIE values is $\sim 5 \text{ cm}^{-1}$. i.p., in-plane; o.p., out-of-plane.

^b Harmonic frequencies from least squares fits.

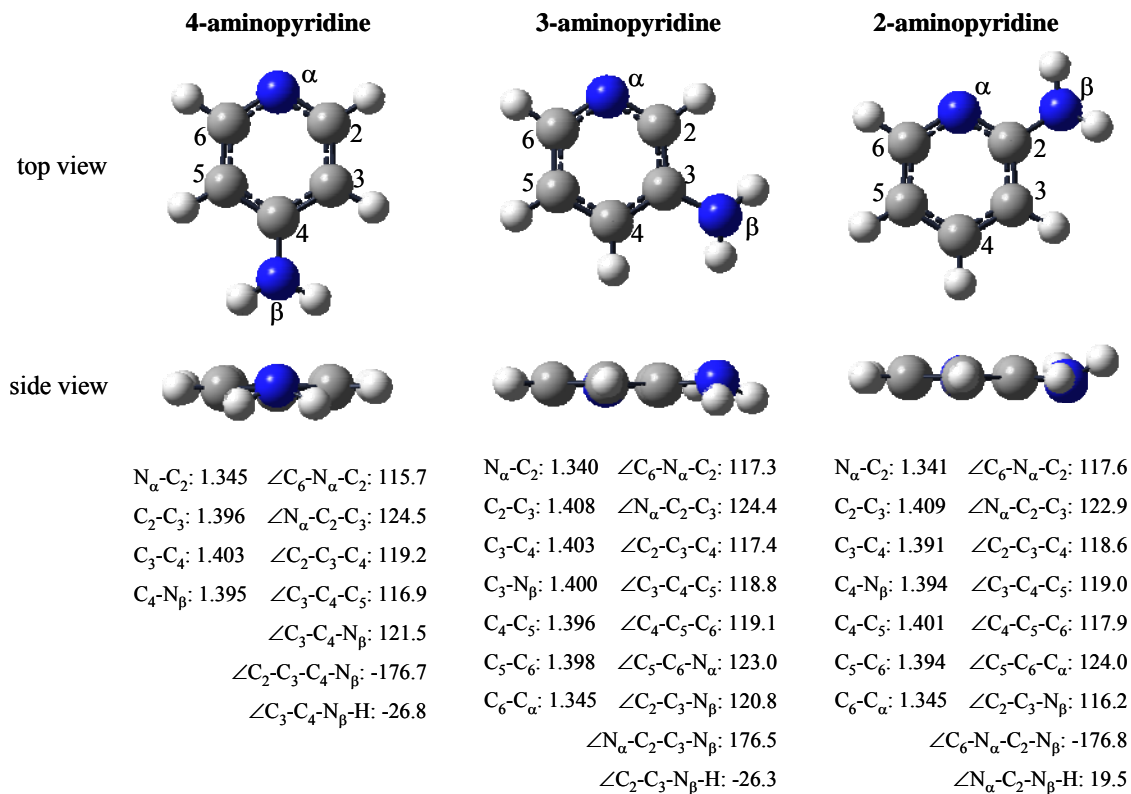


Figure 5.1. Structures of 4- (a), 3- (b), and 2- (c) aminopyridine from MP2/6-311+G(*d,p*) calculations. The bond distances are in angstroms and the bond angles are in degrees.

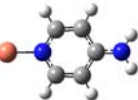
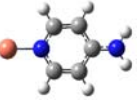

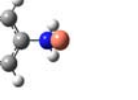
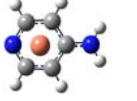

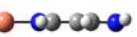
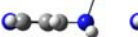

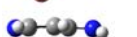





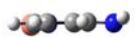
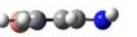
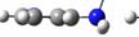



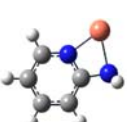



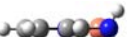
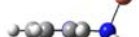

	σ_α -complex		σ_β -complex		π -complex	
	neutral	ion	neutral	ion	neutral	ion
(a) Cu-4AP						
top view						
side view						
E_e (cm ⁻¹)	0	38207	1799	45781	45589	
AIE (cm ⁻¹)	37333		44195			
D_0 (kJ mol ⁻¹)	6.5	289.5	26.4	197.3	202.6	
Cu-L (Å)	1.988	1.886	2.096	1.940	1.849	
(b) Cu-3AP						
top view						
side view						
E_e (cm ⁻¹)	0	39644	1733	45282	3090	46132
AIE (cm ⁻¹)	39815		43758		43133	
D_0 (kJ mol ⁻¹)	1.4	274.7	29.1	205.2	15.2	198.9
Cu-L (Å)	1.999	1.894	2.085	1.939	2.154	1.855
(c) Cu-2AP						
top view						
side view						
E_e (cm ⁻¹)	0	38657	1275	45305		
AIE (cm ⁻¹)						
D_0 (kJ mol ⁻¹)	48.0	282.3	31.0	204.7		
Cu-L (Å)	2.008	2.019/2.166	2.078	1.885		

Figure 5.2. Structural isomers and relative electronic energies, adiabatic ionization energies (AIE) and bond dissociation energies (D_0) of Cu-(4-aminopyridine) (a), -(3-aminopyridine) (b), and -(2-aminopyridine) (c) from MP2/6-311+G(*d,p*) calculations. The bond distances are in angstroms; for σ -complexes the Cu-N distance is given, while for π -complexes the vertical Cu-ring distance is given.

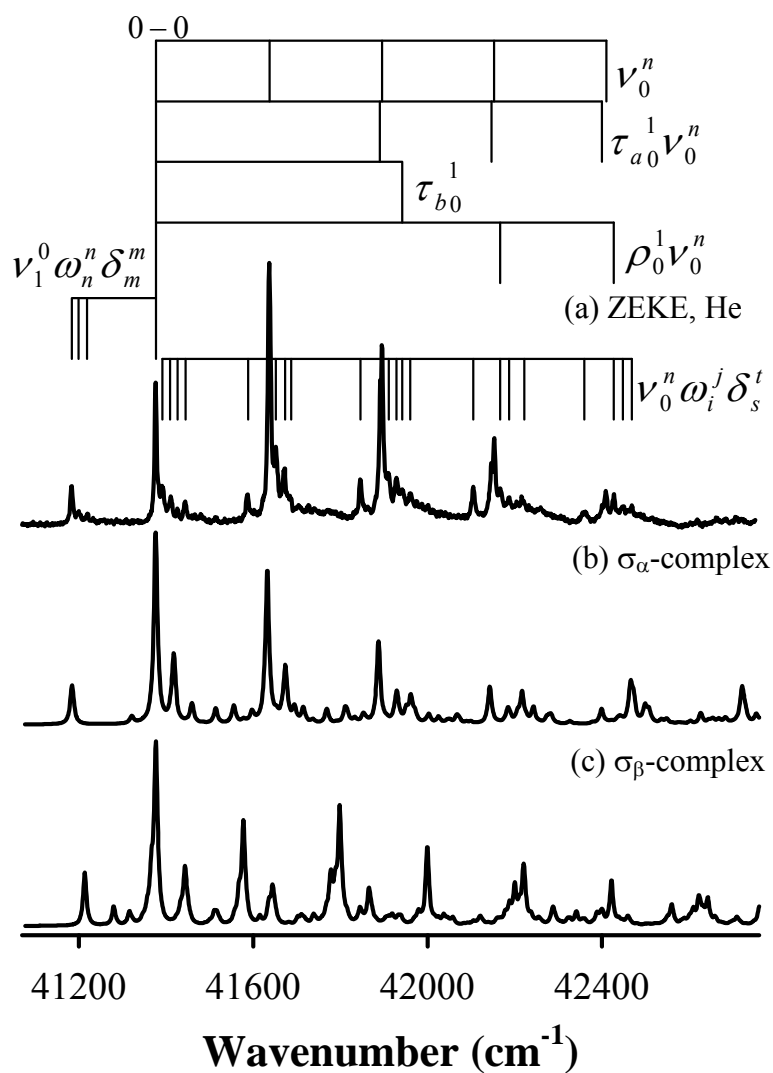


Figure 5.3. Experimental ZEKE spectrum of Cu-(4-aminopyridine) seeded in helium (a) and simulations of the σ_α (b) and σ_β (c) complexes at 50 K, except for the neutral Cu-4AP stretching mode where 150 K was specified.

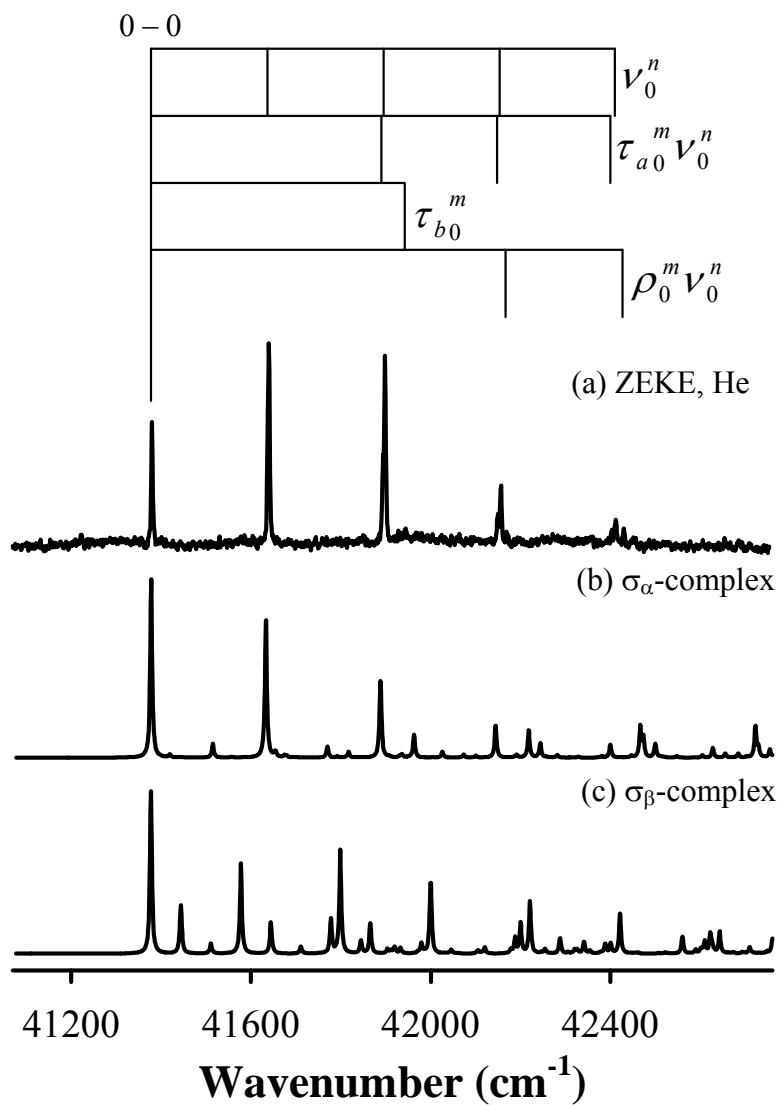


Figure 5.4. Experimental ZEKE spectrum of Cu-(4-aminopyridine) seeded in argon (a) and simulations of the σ_α (b) and σ_β (c) complexes at 10 K.

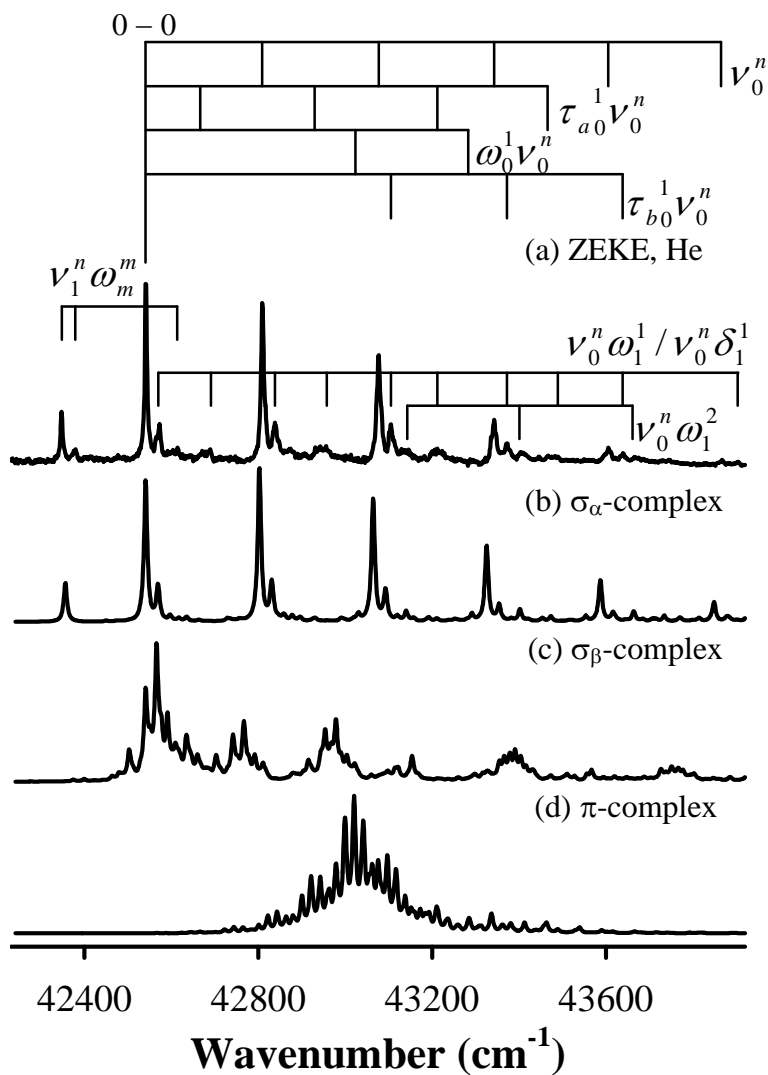


Figure 5.5. Experimental ZEKE spectrum of Cu-(3-aminopyridine) seeded in helium (a) and simulations of the σ_α (b), σ_β (c) and π (d) complexes at 60 K, except for the neutral Cu-3AP stretching mode where 150 K was specified.

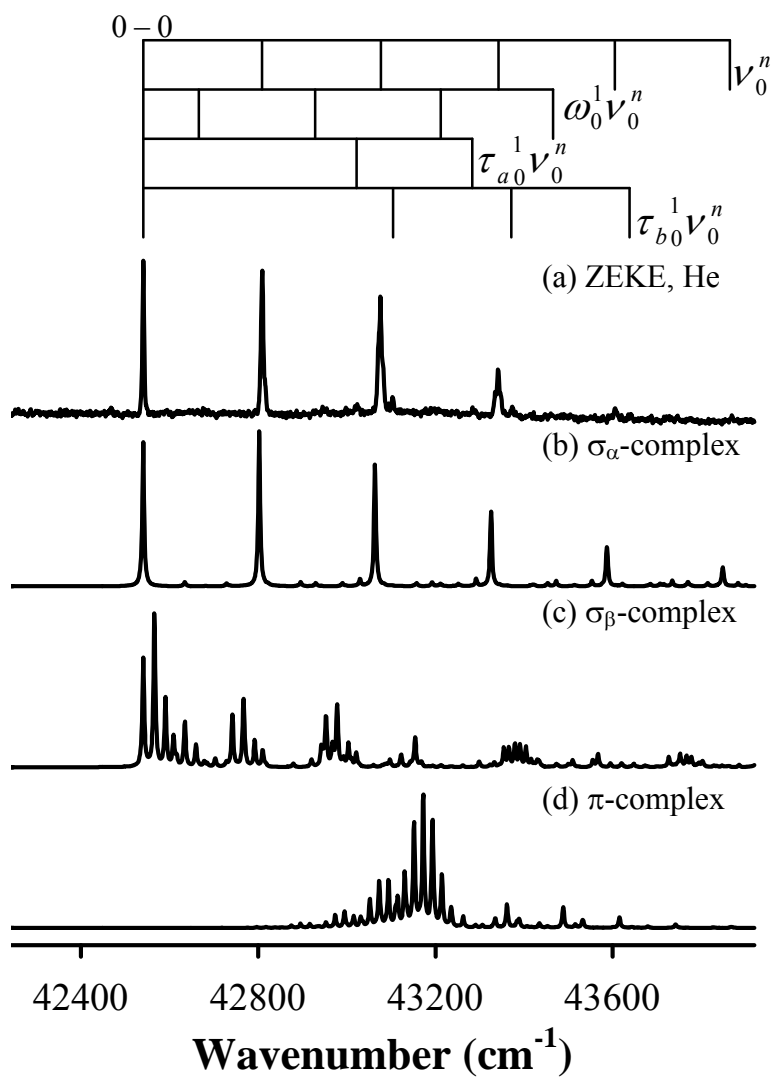


Figure 5.6. Experimental ZEKE spectrum of Cu-(3-aminopyridine) seeded in argon (a) and simulations of the σ_α (b), σ_β (c) and π complexes at 10 K.

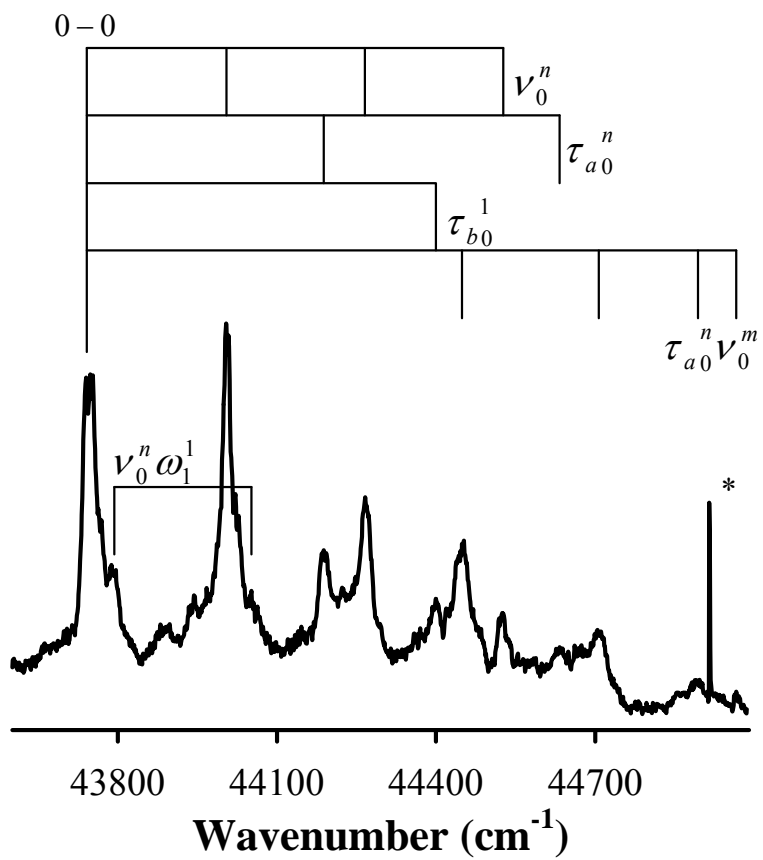


Figure 5.7. Experimental ZEKE spectrum of Cu-(2-aminopyridine) seeded in the 1:1 mixture of helium and argon.

Chapter 6 Spectroscopy and structures of Copper-polypyridine complexes.

Polypyridines are a class of molecules that contain two or more pyridine rings joined by C-C junction bond (s) or consist of fused pyridine rings. The chemical structure for each of these ligands is shown in Figure 6.1. In this chapter, the Cu complexes of 2,2'-bipyridine (22BIPY), 4,4'-bipyridine (44BIPY), 2,2':6',2''-terpyridine (TERPY) and 1,10-phenanthroline (PHEN) are discussed.

These molecules have been extensively used as multidentate ligands in coordination, and supramolecular chemistry due to their strong binding affinities to metal ion.²²⁵ Moreover, the metal complexes of these ligands and their derivatives play important roles in photochemical and photophysical processes, synthetic chemistry, biological and medicinal applications.^{226,227} For example, the metal complexes of bipyridines are widely used for investigating fundamental photophysical processes and have been considered to be potentially valuable systems for solar energy conversion and nanotechnology.^{6,228-232} In addition, some transition metal polypyridine complexes can serve as the active sites of many catalysts and are essential for the activities of several enzymes.²³³⁻²³⁸ The transition metal complexes of PHEN and its derivatives have been used as molecular probes or footprinting agents for the structures and conformations along the DNA and RNA helices.^{226,227,239-241}

22BIPY is one of the most important representative of the bipyridine ligands with the presence of two adjacent coordinating sites.²⁴² The stereochemistry of 22BIPY has been the subject of many experimental and theoretical investigations. Various experimental approaches, such as electron diffraction,²⁴³ X-ray analysis²⁴⁴, NMR²⁴⁵, and ultraviolet absorption spectroscopy^{246,247} have been employed to determine the structures

of 22BIPY in the gas phase, solid state, aqueous and organic solvents. A number of theoretical calculations have been performed to analyze the conformational behavior of 22BIPY regarding to the rotation angle (ϕ) between the two pyridine rings. These computational studies include semiempirical,^{242,248,249} force field,²⁵⁰ ab initio HF and MP2,^{251,252} and DFT calculations.^{252,253} In these studies, the global minimum energy structure was determined to be planar with the nitrogen atoms oriented trans to each other ($\phi = 180^\circ$). A local minimum energy structure was located with the pyridine rings being twisted in a cis configuration ($35^\circ < \phi < 50^\circ$). The corresponding local maximum energy structures ($\phi = 0^\circ$ and $75^\circ < \phi < 90^\circ$) were predicted as transition states between these stable structures.

44BIPY has two nitrogen atoms at the opposite ends and, therefore, is considered as a bifunctional, non-chelating molecule used as a bridging ligand in coordination chemistry. Several previous experimental and theoretical investigations have been carried out on the rotational conformations of 44BIPY. Electron diffraction measurements have identified the rotation angle between two pyridine rings in the 44BIPY to be 37.3° in the gas phase.²⁴³ X-ray diffraction experiments have determined rotation angles of $\sim 18.2^\circ$ and $\sim 34.5^\circ$ for two crystallographically independent molecules of 44BIPY,^{254,255} and a rotation angle of 41.6° for two crystallographically independent molecules of the 44BIPY dihydrate in the asymmetric unit.²⁵⁶ A recent theoretical work studied the torsional potential of 44BIPY with respect to the rotation angle. In that work, a global minimum with a rotation angle of 36.9° in D_2 symmetry was obtained by using MP2 and B3LYP methods with (aug)cc-pVTZ Dunning correlation-consistent basis sets.²⁵⁷

Compared to bipyridines, TERPY possesses more structural possibilities due to the possible rotations of the three pyridine rings. In the gas phase, several conformations of TERPY and its mono- and di-protonated forms were calculated by HF/6-31G(d) calculations.²⁵⁸ These include trans-trans (C_{2v} , 180° , 180°), cis-trans (C_1 , 43.0° , 176.1°)

and cis-cis (C_s , 47.9°, 47.9°) isomers in the energy order of trans-trans < cis-trans < cis-cis.²⁵⁸ The crystal structure of TERPY was determined to be the trans-trans configuration by single-crystal X-ray diffraction studies.²⁵⁹ In this trans-trans configuration, the three pyridine rings are nearly coplanar with the rotation angles of 5.1 and 7.2°, respectively.²⁵⁹ The trans-trans configuration is also found in the basic and organic solutions. On the other hand, the cis-trans and cis-cis forms are favored in the acidic solutions, where the ligand exists as the mono-cation and bi-cation, respectively.^{247,258,260}

PHEN is much different from the above three ligands, because it is formed by fused pyridines rings. Consequently, PHEN has a very rigid molecular framework and provides σ and π binding sites through the nitrogen atoms and six-membered aromatic rings, respectively.

The extensive applications of these metal-polypyridine complexes have inspired considerable interests in their reactions, bonding and structures. A large number of experimental and theoretical investigations about the complexes of transition metal cations with bipyridines and their derivatives have been reported previously.^{246,261-268} Three studies in 1980's²⁶⁹⁻²⁷¹ and a more recently study in 2003²⁶⁶ have reported that the geometries of the 22BIPY and its methyl-substituted derivatives in the bis-ligand complexes of Cu(I), Cu(II), and Ag(I) are nonplanar and are slightly twisted about the carbon-carbon bond between the two pyridine rings. A recent theoretical investigation by Hazell concluded that the 22BIPY conformation is seldom planar in metal complexes.²⁷² Unfortunately, to our knowledge, no electronic spectra with resolved metal-ligand vibrational structure have been reported to support or oppose this conclusion. For 44BIPY, experimental and theoretical investigations have shown that the ligand binds to the surface of metal electrodes and transfer electronic charge to the metal surface in a monodentate fashion.²⁷³⁻²⁷⁶ Such electron transfer properties have been recognized to have potential applications in nanodevices.²⁷⁷

Metal-TERPY complexes are commonly formed by a tridentate bonding mode,^{6,232,278} although monodentate²⁷⁹ or bidentate modes have been found as well.²⁸⁰⁻²⁸² Metal-PHEN complexes are typically in a bidentate bonding configuration with the metal ions binding to two nitrogen atoms. Numerous studies were reported on the binding affinity, charge transfer, and molecular structures for the tridentate metal-TERPY complexes,^{6,232,259,260,278,283-293} and the bidentate metal-PHEN.^{226,239-241,293-298} In spite of the extensive studies, little electronic spectroscopy is known about these systems, which should provide direct evidence about their binding and structures.

In this chapter, I present the PFI-ZEKE spectra of Cu-22BIPY, Cu-44BIPY, Cu-PHEN, and Cu-TERPY. The spectra are analyzed by comparison to theoretical calculations. From this comparison, the preferred geometry conformations and bonding modes of the neutral and ionic metal complexes are determined.

6.1 Experimental and computational methods

The Cu complexes were produced by the reactions of laser-vaporized Cu atoms with 22BIPY (99.0%, Aldrich), 44BIPY (99.0%, Aldrich), TERPY (99.0%, Aldrich) and PHEN (99.0%, Aldrich). The vaporization laser was the second harmonic output of a Nd:YAG (YAG-yttrium aluminum garnet) laser (Quanta-Ray, GCR-3, 532nm, ~ 3 mJ). Since these ligands are in solid state at room temperature (22BIPY, mp: 170 °C, 44BIPY, mp: 110-114 °C, TERPY, mp: 89-94 °C, PHEN, mp: 117 °C), a Copper oven (See section 1.2.2 and Figure 1.2) was used to generate enough ligand vapors.

Ionization thresholds of the 1:1 complexes were located by recording the mass-selected ion signal while the laser wavelength was scanned. The production of 1:1 complexes was maximized by optimized the timing and power of the vaporization and ionization lasers, backing pressure of the carrier gas, and the temperature of the heating oven. ZEKE measurement was performed by photoexcitation of the molecules to

high-lying Rydberg levels and then pulsed-field-ionization of these Rydberg states. A typical field of 1.2 V cm^{-1} was applied $3 \mu\text{s}$ after laser excitation for 100 ns. The resulting ZEKE electron signal was capacitively decoupled from the dual MCP anode, amplified by the preamplifier, and collected and stored in a computer. A 0.08 V cm^{-1} DC field was applied to help discriminate ZEKE from prompt electron.

Calculations of molecular geometries and vibrational frequencies were carried out by using the B3LYP and MP2 methods with 6-311+G(*d,p*) basis set, implemented in the GAUSSIAN 03 program.¹¹³ Multidimensional FC factors were computed from the equilibrium geometries, harmonic frequencies, and normal modes of the neutral and ionic complexes.^{143,144} The Duschinsky effect²⁰¹ was considered to account for normal mode differences between the neutral molecule and ion in the FC calculations. Spectral broadening was simulated by giving each line a Lorentzian line shape with the linewidth of the experimental spectrum. Boltzmann distributions were used to simulate spectra at specific vibrational temperatures.

6.2 Results and discussion

6.2.1 Cu-22BIPY

6.2.1.1 Theoretical geometries, electronic states and energies

To calculate the structures of Cu-(22BIPY), we first considered stable rotational conformers of the free ligand. Figure 6.2 illustrates two conformers of 22BIPY in cis and trans configurations, and Table 6.1 lists their symmetries, geometries and relative energies from the B3LYP/6-311+G(*d,p*) and MP2/6-311+G(*d,p*) calculations. The trans conformer has a planar structure in the C_{2h} point group and is about 2000 cm^{-1} more stable than the cis conformer. The cis conformer is calculated to be in C_2 symmetry with a rotation angle of 40.5° by the B3LYP method and a rotation angle of 47.0° by the

MP2 method.

Considering both the trans and cis conformations of 22BIPY, Cu may bind with one nitrogen in the trans conformer to form a monodentate structure [Figure 6.3 (a)] or with both nitrogen atoms in the cis conformer to form a bidentate structure [Figure 6.3 (b)]. Table 6.2 lists the low-lying electronic states, point groups, relative energies, metal-ligand BDEs, and equilibrium geometries of the optimized structures of Cu-22BIPY from the B3LYP/6-311+G(*d,p*) and MP2/6-311+G(*d,p*) calculations. A twisted monodentate trans structure and a planar bidentate cis structure are predicted by the B3LYP method. The trans structure has no symmetry and is about 3000 cm⁻¹ higher in electronic energy than the cis structure. In this trans configuration, the two pyridine rings are twisted by about 22° compared to the free ligand, and the Cu atom bends off the pyridine plane to which it is attached by ~ 31° (i.e. the ∠Cu-N-C₂-C₃ dihedral angle is 149.2°). The C₂-C₂' bond length in the complex remains nearly the same as that in the free ligand. Upon ionization, the Cu-N bond distance decreases by about 0.1 Å due to reduced repulsion between the Cu 4s¹ and N lone-pair electrons and the additional charge-dipole attraction. In addition, the rotation angle between two rings increases by about 20°, whereas the ∠Cu⁺-N-C₂-C₃ dihedral angle increase by 26° (∠Cu⁺-N-C₂-C₃ = 175.2°). The AIE of this trans isomer is calculated to be 42625 cm⁻¹, and it is close to the measured ionization energy of the monodentate Cu-pyridine complex (43703 cm⁻¹).

The bidentate cis isomer has C_{2v} symmetry with the ground electronic states of ²B₁ for the neutral species and ¹A₁ for the ion. Upon Cu coordination, the C₂-C₂' bond length is reduced from 1.494 Å in the cis conformer of the free ligand to 1.443 Å in the complex. Cu coordination leads to a rotation of the two pyridine rings and a reduction in the ring-ring distance. Surprisingly, the Cu-N distances increase by about 0.05 Å upon ionization. A Mulliken population analysis of the bidentate neutral isomer shows the Cu atom carries a positive charge of (+0.46) due to a large electron back donation from the Cu 3d_π to the lowest unoccupied molecular orbital (LUMO) of the ligand. This

LUMO consists of a p_π orbital directed perpendicular to the ligand plane. It explains the 2B_1 ground state of the neutral complex. Mulliken population analysis shows only a partial positive charge (+0.64) on the Cu cation of the ionic species due to for ligand an electron donation to the HOMO of the Cu. This HOMO consists of a $3p_\sigma$ orbital in the molecular plane, which should have a larger radius along the Cu^+-N bond and leads to a longer bond distance compare to the neutral species. The BDEs of both the neutral and ionic species in the bidentate form are much higher than the trans isomers due to a stronger bidentate bonding interaction between the Cu and the ligand. Moreover, the difference between the ionic forms is much larger than the neutral forms, leading to a lower AIE of the bidentate isomer.

The MP2 method also predicts a twisted trans structure for the monodentate neutral and ionic Cu-22BIPY complexes. However, the AIE of this monodentate complex from the MP2 calculations is about 8000 cm^{-1} lower than that predicted from the B3LYP calculations. Surprisingly, the MP2 method predicts a twisted bidentate cis isomer as a local minimum energy structure. This cis structure is calculated to be only 80 cm^{-1} higher in electronic energy than the trans isomer. However, the twisted bidentate conformation is calculated to be the global minimum of the ionic species. Compared to the B3LYP predictions, the MP2 method predicts different structural changes induced by ionization. Upon ionization of the bidentate structure, for example, the rotation angle between the two rings is decreased from 22.0° in the neutral complex to 15.9° in the ion, the Cu-N bond distance shrinks from 2.149 to 1.979 Å, and the $\angle N-Cu-N'$ bond angle is increased by about 11° . In addition, the calculated AIE of this bidentate isomer is about 7000 cm^{-1} lower than that predicted by the B3LYP calculations. From these calculations alone, we can not determine which of the Cu-22BIPY structures are more stable.

6.2.1.2 ZEKE spectroscopy

Figure 6.4 (a) shows the ZEKE spectrum of Cu-22BIPY seeded in Ar carrier gas. The peak positions and assignments are listed in Table 6.3. For clarity, vertical expansions are plotted for the ranges of 37660 to 37700 cm^{-1} and 37950 to 39000 cm^{-1} . The first strong band is located at 37641 cm^{-1} and has a linewidth of 6 cm^{-1} . This band corresponds to the onset of the ion signal in the photoionization efficiency spectrum (not shown) and is assigned to the 0-0 transition between the ground vibronic levels of the neutral and ionic complexes. Above the 0-0 band, the spectrum displays a main progression of 224 cm^{-1} spacings and weak bands with vibrational intervals of 72, 192, 370, 711, 757, 1027, 1181, and 1295 cm^{-1} .

In our theoretical calculations, the AIEs of the cis isomer from the B3LYP calculations and the trans isomer from the MP2 calculations are close to the measured AIE. Thus, we can not determine which of the structures is observed by comparing the calculated and measured AIEs alone. Figure 6.4 (b) - (d) show the simulations of the trans and cis isomers within the harmonic oscillator and FC approximations, using the equilibrium geometries, vibrational frequencies and normal coordinates of their neutral and ion species from the B3LYP and MP2 calculations. Transitions between monodentate and bidentate isomers are not considered, because the resultant FC profile will be drastically different from the experimental spectrum. From Figure 6.4 (a) - (d), it is evident that the simulation of the bidentate cis isomer from B3LYP calculations is in excellent agreement with the experimental spectrum; while others do not match the experimental spectrum at all. Therefore, the Cu-22BIPY complex observed in our ZEKE experiments should have a planar bidentate cis structure, and the MP2 method does not provide good predictions for the structures of the Cu-22BIPY complex.

Spectral assignments are based on the good agreement between the experimental spectrum and the simulation (B3LYP) of the bidentate structure [Figure 6 (a) and (b)]. The 224 cm^{-1} progression is assigned to the transitions from the ground vibrational level

of the 2B_1 state to excited levels of the $\text{Cu}^+\text{-L}$ stretch (mixed with a ligand in-plane bending mode) in the 1A_1 state. This mode is labeled ν_{19}^+ in Figure 6.4 (a) and Table 6.3. The 193 cm^{-1} interval is attributed to the $\text{Cu}^+\text{-L}$ stretch with Cu displacement, ν_{20}^+ . The observation of these two vibrations is consistent with the predicted geometrical changes of the Cu-22BIPY complex upon ionization. For example, the N-Cu-N angle decreases from 90.2° in the neutral complex to 86.4° in the ion, the Cu-N-C angle increases from 106.4° in the neutral complex to 109.3° in the ion, and the Cu-N distance increases from 1.961 \AA in the neutral complex to 2.010 \AA in the ion. Assignments of the small peaks yield fundamental vibrational frequencies of 370 cm^{-1} for a $\text{C}_2\text{-C}_2'$ stretch (ν_{18}^+), 711 , 757 , and 1027 cm^{-1} for three symmetric pyridine ring in-plane distortions (ν_{15}^+ , ν_{16}^+ , and ν_{17}^+), 1181 cm^{-1} for a C-H in-plane bend (ν_{11}^+), and 1295 cm^{-1} for a C-H in-plane bend (mixed with a $\text{C}_2\text{-C}_2'$ stretch) (ν_{10}^+). The weak intensities of these transitions indicate little geometry change of the ligand from the neutral complex to the ion. The peak at 37677 cm^{-1} is assigned to a hot transition from the first vibrational level of the pyridine rings rotation in the neutral to the first vibrational level of this mode in the ion, labeled 38_1^1 . Consequently, this assignment yields the frequency difference of 36 cm^{-1} between ν_{38}^+ and ν_{38} . In the first-order approximation, the ZEKE transitions of the non-totally-symmetric vibrational modes should follow the normal selection rule of $\Delta v = 0, \pm 2, \pm 4, \dots$. Therefore, the peak at 37712 cm^{-1} is assigned to the overtone transition of the pyridine ring out-of-plane bend (29_0^2), and this assignment yields the fundamental frequency of 36 cm^{-1} for ν_{29} . Due to the limited size of the ZEKE signal, the assignments for those weak peaks are tentative.

6.2.2 Cu-44BIPY

6.2.2.1 Theoretical geometries, electronic states, and energies

As 44BIPY has only one stable conformation with two equivalent nitrogen atoms positioned at opposite ends, the Cu complex should be formed by Cu atom σ binding to one nitrogen along the C_2 axis of the ligand. Therefore, the geometry optimizations of Cu-44BIPY are performed on an initial structure in C_2 symmetry by the B3LYP/6-311+G(*d,p*) and MP2/6-311+G(*d,p*) methods. The resultant electronic states, AIEs, BDEs, and geometries are listed in Table 6.4. The geometries of the free ligand are also calculated by these two methods and listed in Table 6.4 for comparison. Surprisingly, although the geometry optimizations for both the neutral complex and ion in C_2 symmetry are successfully converged in the B3LYP calculations, the subsequent frequency calculations yield one imaginary frequency for the neutral species. In order to search for the minimum energy structure for the neutral complex, an additional B3LYP calculation was performed without symmetry constraint. This calculation generated a minimum energy structure because no imaginary frequencies were predicted in the subsequent frequency analysis. In this structure, the Cu atom is bent off the C_2 axis of the ligand (i.e. $\angle\text{Cu-N-C}_2\text{-C}_3=168.4^\circ$). Upon ionization, the Cu-N distance is reduced from 2.070 Å to 1.918 Å. The rotation angle between the two pyridine rings is slightly decreased from 38.6° in the free ligand to 37.2° in the neutral complex and to 35.5° in the ion.

Unlike the B3LYP calculation, the MP2 calculations predicted a C_2 configuration for both the neutral and ionic species. In this configuration, the Cu atom is in the plane of the ligand. The ligand geometry remains virtually unchanged upon Cu coordination and ionization of the complex.

6.2.2.2 ZEKE spectroscopy

Figure 6.5 shows the ZEKE spectrum of Cu-44BIPY with a He/Ar (1:1) mixture as the carrier gas. The 0-0 transition in this spectrum is located at 43705 cm^{-1} and has a linewidth of 4 cm^{-1} . This spectrum consists of a major progression with 200 cm^{-1} intervals, and two additional progressions of one or more 200 cm^{-1} spacings combined with 379 or 63 cm^{-1} intervals. Additionally, a set of sequence bands are superimposed on the major progression with a 9 cm^{-1} separation. Since the B3LYP and MP2 methods generated different geometrical structures for the neutral Cu-44BIPY complex, two sets of simulations were carried out using the equilibrium geometries, vibrational frequencies and normal coordinates of the neutral and ionic complexes from these calculations. The resultant simulations from MP2 and B3LYP are shown in Figure 6.5 (b) and (c), respectively. The B3LYP simulation displays more transitions and a longer FC profile than the experimental spectrum due to a large geometry change regarding the Cu-N bond bend upon ionization. On the other hand, the MP2 simulation is in very nice agreement with the experimental spectrum. Therefore, both the neutral and ionic Cu-44BIPY complexes should have C_2 symmetry with the Cu atom or cation positioned along the C_2 axis.

The spectral assignments are made based on the good agreement between the experimental and simulated (MP2) spectra. The 200 cm^{-1} progression is assigned to the Cu-N⁺ stretch (ν_{26}) with Cu displacement. The 379 cm^{-1} and 63 cm^{-1} intervals are attributed to a Cu⁺-N stretch (ν_{24}^+) with N displacement and a pyridine rings torsion (ν_{27}^+), respectively. Although the assignments of the sequence bands do not yield the fundamental frequency of the Cu-L out-of-plane bending mode (ν_{57}^+), the frequency difference between the neutral and ion is determined to be 9 cm^{-1} . This small frequency difference indicates little change of the $\angle\text{Cu-N-C}_2\text{-C}_3$ upon ionization and is consistent with the MP2 calculations that predicted no Cu displacement from the plane of the 44BIPY ligand.

6.2.3 Cu-TERPY

6.2.3.1 Theoretical geometries, electronic states, and energies

Compared to bipyridines, TERPY possesses more conformational possibilities with respect to the rotation angles about two C-C bonds. In order to systematically investigate such conformational behavior, a relaxed 3-dimensional potential energy surface scan was carried out at the B3LYP/6-311+G(*d,p*) level of theory. The resultant potential energy surface diagram is shown in Figure 6.6. In this scan, the rotation angle of ϕ' is scanned from -180° to 180° , and the rotational angle of ϕ'' is scanned from 0° to 180° , so that a whole picture of the rotational conformational behavior is illustrated by the potential energy surface. The potential energy surface displays a global minimum (labeled I) for the trans-trans planar conformation with both rotation angles at 180° . A local minimum energy structure (labeled II) is in cis-trans form with rotational angles of $\phi' = 37.1^\circ$ and $\phi'' = 177.3^\circ$. In addition, the potential energy surface diagram shows two additional local minima (labeled III and IV): one in C_2 symmetry and the other in C_s symmetry. The rotation angles in the C_2 structure (42.6°) are slightly larger than those in the C_s structure (41.6°). The C_2 structure was not calculated in the previous theoretical investigation by Drew and coworkers.²⁵⁸ Table 6.6 displays the molecular structures of these four conformers, along with their relative energies, symmetries, and dipole moments. The trans-trans I configuration is about 53.3 kJ mol^{-1} more stable than the cis-cis IV conformer. Compared to the cis-cis IV conformer, the cis-cis III form has a slightly lower energy but a larger dipole moment. The larger dipole moment is a result of both side-rings twisting towards the same orientation relative to the middle-ring. The energy order of the four conformers is trans-trans I < trans-cis II < cis-cis III < cis-cis IV. Except for the rotation angles, the geometries of the three pyridine rings and two bridging C-C bonds are very similar among the four conformers.

Copper atoms and ions can bond to TERPY in a mono-, bi-, or tridentate mode. Thus geometry optimizations are carried out for the mono-, bi-, and tridentate structures of the Cu-TERPY complex. Initial monodentate structures are formed by attaching a Cu atom or ion to one nitrogen atom in each of the four different ligand conformations, initial bidentate structures are constructed by positioning Cu or Cu⁺ in equidistance from both nitrogen atoms of the cis part of the trans-cis and two cis-cis conformations, and initial tridentate structures are constructed by positioning Cu or Cu⁺ nearly equidistance to all three nitrogen atoms of the two cis-cis conformers (i.e. no symmetry constraint).

The geometry optimizations yield five local minimum energy structures: a tridentate (T), a bidentate (B), and three monodentate isomers (M_I, M_{II}, and M_{III}). Table 6.7 lists geometries, relative electronic energies, and BDEs of these isomers. The lowest energy structure is the T isomer, and the second lowest energy structure corresponds to the B isomer and is located ~ 6000 cm⁻¹ higher in electronic energy than the T isomer. The M_I, M_{II}, and M_{III} isomers are separated by about 1000 cm⁻¹, with the most stable M conformer being about 2000 cm⁻¹ higher in electronic energy than the B form.

The M_I complex is formed by Cu σ binding to one of the side-rings of the trans-trans ligand. Due to steric effects between the Cu and adjacent hydrogen atom, the ring (with Cu attaching to it) and the middle-ring is twisted by about 27° with respect to the free ligand, and the Cu atom bends off the attached pyridine plane by about 33°. Upon ionization of this monodentate structure, the rotation angle is increased by about 20°, while the Cu ion bends back towards the pyridine plane. This geometry change is in accord with an enhance metal-ligand bonding in the ion which strongly prefers lying along the local dipole moment of the pyridine ring.

The M_{II} structure is formed by Cu σ binding to the middle-ring of the trans-trans conformation of the TERPY ligand and has a C_s symmetry. In a similar fashion, the M_{III} structure is formed by Cu σ binding to the side-ring of the trans part of the trans-cis conformation has a C₁ symmetry. Similar to the M_I isomer, the trans configurations in

the M_{II} and M_{III} isomers are twisted with respect to the corresponding free ligand configurations, and Cu atoms bend away from the pyridine rings as well. In addition, the twisted angles are increased and the bending angles are also increased upon ionization. Interestingly, the ionic M_{II} complex is not in C_s symmetry any more, because the Cu^+ ion is slightly closer to one side-ring than the other. The molecular symmetry may have been compromised due to an additional π interaction between the Cu cation and one side-ring after a fairly large torsion upon ionization.

In the B isomer, Cu binds to two pyridine rings. In this bidentate structure, the two pyridine rings that bind with Cu are nearly coplanar, while the third ring is twisted about 20° . This twisted angle maintains a balance between the steric repulsion of the Cu and adjacent hydrogen atoms and the π -conjugation of the aromatic system. In the neutral species, the Cu atom is slightly closer to the middle-ring than the side-ring. Upon ionization, the ligand geometry undergoes little change, but the Cu-N bonds are slightly elongated.

The T isomer has a planar configuration in C_{2v} symmetry, and the Cu atom or ion has equidistance from the two nitrogen atoms the side-rings and a slightly shorter distance from the nitrogen atom of the middle ring. Table 6.8 lists the electronic states and geometries of the neutral and ionic T isomer. Upon Cu coordination, the C-C bridging bond lengths are slightly decreased, but the geometries of three pyridine rings are virtually unchanged. These structural changes indicate that the Cu coordination brings the three rings coplanar to each other and relatively closer to each other without disturbing their local pyridine geometries. Surprisingly, the three rings are no longer coplanar in the ionic complex. Instead, the middle ring is tilted off the co-plane of two side-rings with a rotation angle of $\sim 8^\circ$. The resultant C_s structure of the ionic Cu complex is predicted to be in the $^1A'$ electronic state. In addition to the middle ring rotation, the Cu-N bond lengths and the two C-C bridging bond lengths are slightly increased upon ionization.

Due to the different numbers of Cu-N σ bonds in the monodentate, bidentate, and tridentate forms, the predicated BDEs are in the order of $M_I \sim M_{II} \sim M_{III} < B < T$ for both the neutral and ionic isomers. Moreover, the AIEs of M_I , M_{II} , M_{III} , B, and T are also predicted to be in the same order as the calculated BDEs. In this work, no MP2 calculation was performed for the TERPY and Cu-TERPY complexes due to a fairly high computational cost for the relatively larger molecules. Although five isomers of the Cu complex are predicted by the B3LYP calculations, the tridentate T-complex has much lower energy than others. Thus, the monodentate and bidentate isomers are not likely to be produced in the supersonic molecular beam.

6.2.3.2 ZEKE spectroscopy

Figure 6.7 (a) shows the ZEKE spectrum of Cu-TERPY seeded in helium carrier. The peak positions and assignments are listed in Table 6.9. This spectrum has a linewidth of 12 cm^{-1} , which is broader than those of the Cu-22BIPY and Cu-44BIPY spectra seeded in heavier carriers. In addition to the broad linewidth, this spectrum has a fairly high noise background possibly due to a predissociation or a low productivity of the Cu complex. The first strong photoelectron band is located at 35190 cm^{-1} . This band corresponds to the onset of the ion signal in the photoionization efficiency spectrum (not shown) and is assigned to be the 0-0 transition. Surprisingly, above this 0-0 band, the spectrum displays another strong peak with an interval of 26 cm^{-1} and a weaker band with the same separation but partially overlapped by the shoulder of the second peak. Additionally, the spectrum exhibits a number of weak at 1062, 1472, and 1594 cm^{-1} from the 0-0 band.

Among the five isomers, the AIEs of three monodentate isomers lie far from the measured 0-0 transition of 35190 cm^{-1} , whereas the AIE of T complex has the best match with the experimental value. Therefore, the tridentate T complex should be the only

ZEKE carrier. Nevertheless, to confirm such assignment, we have performed spectral simulations for all five structures [shown in Figure 6.8 (c-g)], using the equilibrium geometries, vibrational frequencies and normal coordinations of their neutral and ion complexes. The calculated AIEs are aligned to the experimental value, and the transitions between different bonding structures are excluded. Apparently, the simulations of the monodentate and bidentate isomers [Figure 6.8 (c-f)] have no similarity with the experimental spectrum. However, the simulated spectrum of the tridentate structure is in excellent agreement with the experimental one, and interestingly, it nicely reproduces the position and intensity of the 26 cm^{-1} progression. Consequently, this progression is assigned to the transitions from the ground vibrational level of the 2B_1 state to the excited levels of middle-ring out-of-plane bend in the ${}^1A'$ state. This spectral finding confirms the middle-ring rotation upon ionization predicted by the theory, and the quick degressive intensity of the 26 cm^{-1} progression are consistent with the small value ($\sim 8^\circ$) of that rotation angle. Three small peaks are assigned to be the fundamental frequencies of 1062 cm^{-1} for a middle-ring distortion characterized by the displacement of N' (ν_{21}^+), 1472 and 1594 cm^{-1} for two C-H in-plane bends mixed with pyridine rings distortion (ν_{12}^+ and ν_{10}^+). The assignments of these ligand-based vibrations are tentative due to their fairly low intensities.

6.2.4 Cu-PHEN

6.2.4.1 Theoretical geometries, electronic states, and energies

Different from the other three ligands, PHEN may only function as a bidentate ligand to metal atoms or ions. The geometry optimizations are performed by placing the copper atom or ion equidistance to both nitrogen atoms and in the plane of the PHEN ligand. Figure 6.8 (a) presents the optimized bidentate structures of the neutral and ionic Cu-PHEN complexes from the B3LYP/6-311+G(*d,p*) calculations. Similar to

Cu-22BIPY, the Cu-N bond length is slightly decreased from the neutral to the ionic Cu-PHEN complex. The shorter Cu-N distance in the neutral species is explained by the strong electron back donation from a Cu $3d_{\pi}$ orbital atom to the p_{π} LUMO of the ligand.

Because PHEN contains a benzene ring that is fused together with two pyridine rings, it may have a π bonding capability. Searches for a π binding structure were carried out by placing the Cu atom on the top of the benzene ring. However, only the ionic π complex was found in these calculations. In this π configuration, the Cu^+ cation is closer to the C_6 and C_7 atoms than others and has a much higher energy than the σ form [Figure 6.8 (b)]. Moreover, this ionic π complex possesses only about half the metal-ligand bond strength than the ionic σ complex. No MP2 calculation was performed for the PHEN and its Cu complexes due to the higher computational cost.

6.2.4.2 ZEKE spectroscopy

Figure 6.9 (a) shows the ZEKE spectrum of Cu-PHEN seeded in Ar carrier gas. The spectrum originates at 37333 cm^{-1} , with a linewidth of 4 cm^{-1} . Above the 0-0 transition, the spectrum displays a major progression with an energy interval of 201 cm^{-1} , a number of small peaks with 159, 430, 681, and 726 cm^{-1} intervals. Additionally, a small peak locates below the 0-0 transition with a 274 cm^{-1} spacing. The corresponding peak positions and assignments are listed in Table 6.10.

The simulation of the bidentate isomer is present in Figure 6.9 (b). This simulation matches the experimental spectrum well, which makes assignment of each vibrational interval straightforward. The 201 cm^{-1} progression is assigned to the symmetric $\text{Cu}^+\text{-L}$ stretch (ν_{22}^+) characterized by Cu^+ displacement mixed with a ligand in-plane distortion. The 430 and 726 cm^{-1} intervals are attributed to two ligand in-plane distortions (ν_{20}^+ and ν_{18}^+), respectively. The 159 cm^{-1} interval is assigned to the $\Delta v = 2$ transition of the

asymmetric Cu⁺-L out-of-plane bend (ν_{42}^+). This transition follows the selection rule of $\Delta v = 0, \pm 2, \pm 4 \dots$ for non-totally symmetric vibrational modes. Accordingly, the fundamental frequency of this mode is derived to be 79 cm^{-1} . The small peak below the 0-0 band was assigned to a hot transition from the first excited level of the Cu-PHEN stretch in the neutral 2B_1 state to the zero vibrational level of the ionic 1A_1 state. This hot band is not reproduced in the simulation, even at higher vibrational temperatures (i.e. 300 K, simulation not shown). The 681 cm^{-1} interval is not predicted in the simulation, and does not match any of the calculated Cu⁺-PHEN fundamental frequencies with a_1 symmetry. If this band is assigned to an overtone, the fundamental frequency of the corresponding asymmetric mode will be 340 cm^{-1} . This frequency does not match any of the calculated Cu⁺-PHEN fundamental frequencies for the asymmetric mode. Thus, this band may arise from other species, but further investigation is required to confirm its assignment.

6.3. Summary of the ZEKE measurements and theoretical calculations

Table 6.11 summarizes the AIEs, BDEs, and vibrational frequencies from the ZEKE spectra and calculations of the Cu-polypyridine complexes. All the theoretical values are from the B3LYP/6-311+G(*d,p*) calculations, except the frequencies of the Cu-44BIPY complexes, where the MP2/6-311+G(*d,p*) results are listed. Overall, the measured and calculated vibrational frequencies are in good agreement, except for the Cu-L stretch frequency of the neutral Cu-PHEN complex, where the calculated frequency was overestimated by about 30%. The B3LYP method yields the correct trend of the ionization energies for these complexes, although it overestimates the AIE values by about 1000 cm^{-1} . For geometries, it is interesting to find the B3LYP method gives better predictions for Cu-22BIPY, while the MP2 method generates better results for Cu-44BIPY.

The BDEs of both the neutral and ionic Cu-polypyridine complexes follow the trend of Cu-44BIPY < Cu-22BIPY \approx Cu-PHEN < Cu-TERPY. This trend is in accord with the number of Cu-N bonds in these complexes. Moreover, the difference between the ionic and neutral binding strength is also in the order of the Cu-44BIPY < Cu-22BIPY \approx Cu-PHEN < Cu-TERPY, because the metal-ligand bonding interactions in the multidentate complexes are more strongly enhanced compared to the monodentate complex upon ionization. The Cu⁺-L stretch with Cu displacement is mainly observed for the Cu-22BIPY, Cu-44BIPY and Cu-PHEN ionic complexes. This spectral finding is consistent with the major geometry change with respect to the Cu-N bonds upon ionization of these complexes. On the other hand, the ligand based vibrations of these complexes show relatively low intensities in the ZEKE spectra due to the rigid structure of these ligands. For Cu-TERPY, two five-membered C-N-Cu-N-C rings are formed by Cu coordination to each of the three nitrogen atoms. Consequently, this molecule has less displacement freedom along each Cu-N bond, while the vibrational transition of the middle-ring out-of-plane bend (ν_{44}^+) appears to have the strongest FC activity in the ZEKE spectrum.

6.4 Conclusion

The Cu complexes of 2,2'-bipyridine, 4,4'-bipyridine, 2,2':6',2''-terpyridine and 1,10-phenanthroline are studied by PFI-ZEKE spectroscopy. This work reports the first vibrationally resolved electronic spectra for metal-polypyridine complexes. A monodentate structure for Cu-(4,4'-bipyridine), bidentate structures for Cu-(2,2'-bipyridine) and Cu-(1,10-phenanthroline), and a tridentate structure for Cu-(2,2':6',2''-terpyridine) are identified in our experimental measurements. The monodentate structures of neutral and ionic Cu-(4,4'-bipyridine) have C₂ symmetry with about 40° rotation angles between the two pyridine rings, while the neutral and ionic Cu-2,2'-bipyridine and the neutral

Cu-(1,10-phenanthroline) complexes have planar conformations in C_{2v} symmetry. Interestingly, although the neutral Cu-(1,10-phenanthroline) complex has a planar conformation, the corresponding ion has a twisted shape with C_s symmetry. Moreover, the AIEs of the complexes are decreased with the number of Cu-N bonds.

Table 6.1. Point groups, relative energies (E_e , cm^{-1}), geometric structures (R, Å; \angle , degree) of 2,2'-bipyridine isomers from B3LYP/6-311+G(*d,p*) and MP2/6-311+G(*d,p*) calculations.

	B3LYP/6-311+G(<i>d,p</i>)		MP2/6-311+G(<i>d,p</i>)	
	C_{2h}	C_2	C_{2h}	C_2
E_e	0	2253	0	1725
R(C_2 - C_2')	1.491	1.494	1.488	1.486
R(C_2 -N)	1.342	1.340	1.350	1.348
R(N- C_6)	1.333	1.333	1.342	1.343
R(C_6 - C_5)	1.394	1.394	1.399	1.400
R(C_5 - C_4)	1.393	1.391	1.398	1.397
R(C_4 - C_3)	1.389	1.391	1.395	1.396
R(C_3 - C_2)	1.402	1.401	1.405	1.404
$\angle C_2'$ - C_2 -N	117.0	117.1	116.6	116.8
$\angle C_2$ -N- C_6	118.3	118.1	117.6	117.1
\angle N- C_6 - C_5	123.6	123.8	123.8	124.0
$\angle C_6$ - C_5 - C_4	118.0	118.0	118.2	118.4
$\angle C_5$ - C_4 - C_3	119.0	118.8	118.8	118.4
$\angle C_4$ - C_3 - C_2	118.8	119.1	118.8	119.0
$\angle C_3$ - C_2 -N	122.2	122.2	122.8	123.1
ϕ^a	180.0	40.5	180.0	47.0

^a ϕ is the rotation angle between the two pyridine rings.

Table 6.2. Electronic states, point groups, relative energies (E_e and E_0 , cm^{-1})^a, bond dissociation energies (D_0 , kJ mol^{-1}), and geometric structures (R , Å; \angle , degree) of Cu-(2,2-bipyridine) complexes from B3LYP/6-311+G(d,p) and MP2/6-311+G(d,p) calculations.

	B3LYP				MP2			
	cis, C_{2v}		trans, C_I		cis, C_2		trans, C_I	
	2B_1	1A_1	2A	1A	2A	1A	2A	1A
E_e	0	37821	2979	45402	154	31000	0	38075
E_0	0	38529	3239	45864	80	31229	0	38217
D_0	91.4	405.9	26.6	292.1	63.0	390.1	42.0	284.5
R(Cu-N)	1.961	2.010	2.086	1.980	2.149	1.979	2.029	1.960
R(C ₂ -C ₂ ')	1.443	1.500	1.483	1.489	1.483	1.491	1.480	1.483
R(C ₂ -N)	1.395	1.356	1.356	1.356	1.352	1.362	1.356	1.362
\angle N-Cu-N'	90.2	86.4			76.9	87.9		
\angle Cu-N-C ₂	106.4	109.3	122.8	108.2	114.6	108.2	123.7	105.1
\angle C ₂ -N-C ₆	119.5	119.9	118.3	119.5	118.6	119.3	118.2	119.1
\angle N-C ₆ -C ₅	123.9	122.6	123.4	121.8	122.8	122.5	123.0	121.6
\angle C ₆ -C ₅ -C ₄	117.7	118.2	118.4	118.9	118.6	118.6	118.7	119.3
\angle C ₅ -C ₄ -C ₃	119.5	119.3	118.9	119.4	118.8	119.0	118.7	119.2
\angle C ₄ -C ₃ -C ₂	121.1	119.8	121.4	121.5	119.0	119.5	119.3	118.2
ϕ^b	0.0	0.0	22.6	39.8	22.0	15.9	34.5	44.3
\angle Cu-N-C ₂ -C ₃	0.0	0.0	149.2	175.2	162.4	168.1	159.6	174.6

^a E_e is the electronic energy; E_0 is the electronic energy including vibrational zero point energy correction. ^b ϕ is the rotation angle between the two pyridine rings.

Table 6.3. Peak positions (cm^{-1}) and assignments of the Cu-(2,2'-bipyridine) ZEKE spectrum

Positions	Assignments	Positions	Assignments
37641	0_0^0	38308	19_0^3
37677	38_1^1	38352	17_0^1
37712	29_0^2	38374	18_0^2
37833	20_0^1	38398	16_0^1
37865	19_0^1	38671	15_0^1
38011	18_0^0	38823	12_0^1
38053	$19_0^1 20_0^1$	38891	$15_0^1 29_0^1$
38088	19_0^2	38941	10_0^1

Table 6.4. Electronic states, adiabatic ionization energies (AIE, cm⁻¹), dissociation energies (D₀, kJ mol⁻¹) and geometric structures (R, Å; ∠, degree), of Cu-(4,4'-bipyridine) complexes and free ligand from B3LYP/6-311+G(*d,p*) and MP2/6-311+G(*d,p*) calculations

	B3LYP			MP2		
	neutral	ion	ligand	neutral	ion	ligand
	C ₁ , ² A	C ₂ , ¹ A		C ₂ , ² A	C ₂ , ¹ A	
AIE	44733	--		40900	--	
D ₀	36.4	276.7		46.2	256.6	
R(Cu-N)	2.070	1.918		2.007	1.896	
R(N-C ₂)	1.344	1.354	1.336	1.350	1.360	1.345
R(C ₂ -C ₃)	1.387	1.381	1.392	1.395	1.390	1.395
R(C ₃ -C ₄)	1.401	1.404	1.400	1.404	1.406	1.404
R(C ₃ '-C ₄ ')	1.400	1.400	1.400	1.403	1.404	1.404
R(C ₂ '-C ₃ ')	1.392	1.393	1.392	1.398	1.399	1.395
R(N'-C ₂ ')	1.336	1.335	1.336	1.345	1.344	1.345
R(C ₄ -C ₄ ')	1.481	1.477	1.483	1.477	1.473	1.477
∠C ₂ -N-C ₆	117.6	118.1	116.9	117.9	118.1	116.5
∠N-C ₂ -C ₃	123.1	122.4	123.8	122.8	122.3	124.0
∠C ₂ -C ₃ -C ₄	119.7	120.3	119.3	119.5	120.1	119.1
∠C ₃ -C ₄ -C ₅	116.8	116.7	116.9	117.4	117.2	117.3
∠C ₃ '-C ₄ '-C ₅ '	117.0	117.7	116.9	117.5	118.1	117.3
∠C ₂ '-C ₃ '-C ₄ '	119.2	118.8	119.3	119.0	118.6	119.1
∠N'-C ₂ '-C ₃ '	123.8	123.5	123.8	123.9	123.8	124.0
∠C ₂ '-N'-C ₆ '	116.9	117.6	116.9	116.6	117.1	116.5
∠Cu-N-C ₂ -C ₃	168.4	180.0		179.9	179.8	
φ ^a	37.2	35.5	38.6	44.1	41.9	44.0

^a φ is the rotation angle between the two pyridine rings.



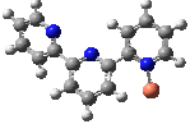
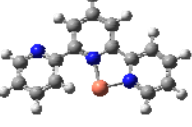

Table 6.5. Peak positions (cm^{-1}) and assignments of the Cu-(4,4'-bipyridine) ZEKE spectrum

Positions	Assignments	Positions	Assignments
43705	0_0^0	44084	24_0^1
43714	57_1^1	44104	26_0^2
43768	27_0^1	44114	$26_0^2 57_1^1$
43904	26_0^1	44281	24_0^1
43914	$26_0^1 57_1^1$	44302	26_0^3
43968	$26_0^1 27_0^1$	44480	$24_0^1 26_0^2$

Table 6.6. Relative energies (kJ mol^{-1}), symmetries, dipole moments, and geometric structures (R , Å; \angle , degree) of 2,2':6',2''-terpyridine from B3LYP/6-311+G(d,p) calculations

	trans-trans I	trans-cis II	cis-cis III	cis-cis IV
top view				
side view				
symmetry	C_{2v}	C_1	C_2	C_s
E_e	0	22.1	51.5	53.3
Dipole	2.123	1.927	3.418	2.576
$R(\text{C}_2-\text{C}_2')$	1.492	1.492	1.495	1.495
$R(\text{C}_6'-\text{C}_2'')$	1.492	1.494	1.495	1.495
$\angle\text{N}-\text{C}_2-\text{C}_2'-\text{N}'$	180	177.3	42.6	41.6
$\angle\text{N}-\text{C}_6'-\text{C}_2''-\text{N}''$	180	37.1	42.6	41.6

Table 6.7. Relative energies (cm^{-1}), bond dissociation energies (kJ mol^{-1}) and geometries (R, Å; \angle , degree) of different binding isomers of Cu-(2,2':6':2''-terpyridine) from B3LYP/6-311+G(*d,p*) calculations.

	M_I		M_{II}		M_{III}		B		T	
										
	M _I	M _I ⁺	M _{II}	M _{II} ⁺	M _{III}	M _{III} ⁺	B	B ⁺	T	T ⁺
E _e	7885	49101	8637	50198	9633	50904	5570	42426	0	35423
D ₀	27.5	307.4	19.6	295.4	28.5	307.8	81.0	407.1	177.6	517.2
Cu-N	2.088	1.993	2.096	1.974	2.089	1.987	1.991 (1.977)	2.019 (2.018)	2.029 (2.006)	2.057 (2.054)
C ₂ -C ₂ '	1.484	1.491	1.483	1.483	1.484	1.490	1.485	1.487	1.469	1.497
C ₆ '-C ₂ ''	1.491	1.484	1.487	1.488	1.493	1.488	1.451	1.499	1.469	1.497
φ' ^a	154.9	136.1	160.0	140.8	157.8	139.5	156.8	150.6	0.0	7.5
φ'' ^a	175.2	179.5	160.0	147.4	37.0	31.0	1.4	5.2	0.0	7.5

^a φ' and φ'' are the rotation angles between the middle-ring and two side-rings, respectively.

Table 6.8. Electronic states and geometries (R, Å; \angle , degree) of the tridentate Cu-(2,2':6':2'')-terpyridine) from B3LYP/6-311+G(*d,p*) calculations.

	2B_1	$^1A'$		2B_1	$^1A'$
R(Cu-N')	2.029	2.057	$\angle C_2'-C_2-N$	116.2	116.3
R(Cu-N'')	2.006	2.054	$\angle C_2-N-C_6$	117.8	118.7
R(C ₂ -N)	1.387	1.364	$\angle N-C_6-C_5$	124.0	123.1
R(N-C ₆)	1.350	1.340	$\angle C_6-C_5-C_4$	118.5	118.5
R(C ₆ -C ₅)	1.381	1.391	$\angle C_5-C_4-C_3$	118.6	119.0
R(C ₅ -C ₄)	1.406	1.389	$\angle C_4-C_3-C_2$	120.6	119.7
R(C ₄ -C ₃)	1.383	1.392	$\angle C_3-C_2-N$	120.5	121.1
R(C ₃ -C ₂)	1.401	1.392	$\angle C_2-C_2'-N'$	112.5	112.9
R(C ₂ -C ₂ ')	1.469	1.497	$\angle C_2'-N'-C_6'$	124.4	124.6
R(C ₂ '-N')	1.346	1.326	$\angle C_5'-C_4'-C_3'$	121.0	121.2
R(C ₄ '-C ₃ ')	1.403	1.396	$\angle C_4'-C_3'-C_2'$	118.2	117.7
R(C ₃ '-C ₂ ')	1.394	1.398	$\angle C_3'-C_2'-N'$	119.1	119.4
$\angle N-Cu-N'$	80.1	79.3	$\angle N-C_2-C_2'-N'$	0.0	7.5
$\angle N-Cu-N''$	160.2	158.5	$\angle Cu-N-N'-N''$	0.0	1.2
$\angle N-N'-N''$	100.7	100.8			

Table 6.9. Peak positions (cm^{-1}) and assignments of the Cu-(2,2':6':2''-terpyridine) ZEKE spectrum.

Positions	Assignments
35190	0_0^0
35216	44_0^1
35242	44_0^2
36252	21_0^1
36662	12_0^1
36784	10_0^1
36808	$10_0^1 44_0^1$

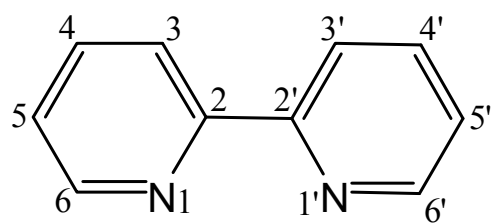
Table 6.10. Peak positions (cm^{-1}) and assignments of the Cu-(1,10-phenanthroline) ZEKE spectrum

Positions	Assignments
37059	22_1^0
37333	0_0^0
37492	42_0^2
37534	22_0^1
37733	22_0^2
37763	20_0^1
38014	?
38059	18_0^1
38258	$18_0^1 22_0^1$

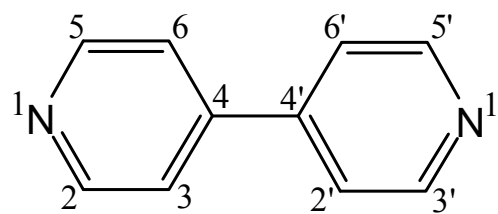
Table 6.11. Adiabatic ionization energies (AIE, cm^{-1}), metal-ligand bond dissociation energies (D_0 and D_0^+ , kJ mol^{-1}), and vibrational frequencies (cm^{-1}) of the Cu-polypyridine complexes from the ZEKE spectra and calculations.

		Experiment	Calculation ^a	
Cu-22BIPY	AIE	37641	38529	
	D_0/D_0^+		91.4 / 405.9	
	C-H in-plane bend with C_2-C_2' stretching	ν_{10}^+ , a_1	1295	1308
	C-H in-plane bend	ν_{12}^+ , a_1	1181	1207
	pyridine rings i.p. distortion	ν_{15}^+ , a_1	1027	1037
	pyridine rings i.p. distortion	ν_{16}^+ , a_1	757	772
	pyridine rings i.p. distortion	ν_{17}^+ , a_1	711	672
	C_2-C_2' stretch	ν_{18}^+ , a_1	370	367
	Cu^+-L stretch (with ligand i.p. bend)	ν_{19}^+ , a_1	224	232
	Cu^+-L stretch (with Cu displacement)	ν_{20}^+ , a_1	192	194
	pyridine rings i.p. torsion	ν_{29}^+ , a_2	36	34
	pyridine rings o.p. bend	ν_{38}/ν_{38}^+ , b_1	$\Delta\nu_{38} = 36$	54/79
	Cu-44BIPY	AIE	43705	44733
D_0/D_0^+			36.4 / 276.7	
Cu^+-L stretch (with N displacement)		ν_{24}^+ , a	379	374
Cu^+-L stretch (with Cu displacement)		ν_{26}^+ , a	200	197
pyridine rings i.p. torsion		ν_{27}^+ , a	63	69
$\text{Cu}/\text{Cu}^+-\text{L}$ o.p. bend		ν_{57}/ν_{57}^+ , b	$\Delta\nu_{57} = 9$	34/44
Cu-TERPY	AIE	35190	36431	
	D_0/D_0^+		177.6 / 517.2	
	C-H i.p. bend with rings distortion	ν_{10}^+ , a'	1594	1494
	C-H i.p. bend with rings distortion	ν_{12}^+ , a'	1472	1438
	middle-ring i.p. distortion	ν_{21}^+ , a'	1062	1040
middle-ring o.p. bend	ν_{44}^+ , a'	26	24	
Cu-PHEN	AIE	37333	38281	
	D_0/D_0^+	92.4	413.0	
	ligand i.p. distortion	ν_{18}^+ , a_1	726	735
	ligand i.p. distortion	ν_{20}^+ , a_1	430	432
	$\text{Cu}/\text{Cu}^+-\text{L}$ stretch (with Cu displacement)	ν_{22}/ν_{22}^+ , a_1	274/201	213/203
	$\text{Cu}-\text{L}$ o.p. bend	ν_{42}^+ , b_1	80	74

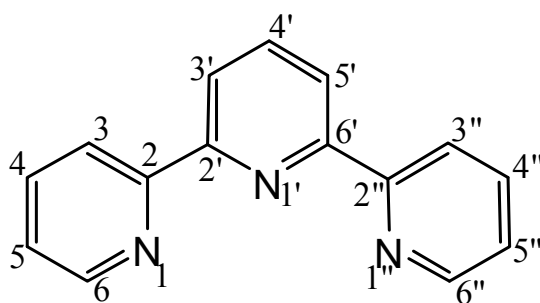
^a All the theoretical values from the B3LYP/6-311+G(d,p) calculations, except for the Cu-44BIPY frequencies that are from the MP2/6-311+G(d,p) results are listed instead. i.p.: in-plane; o.p.: out-of-plane.



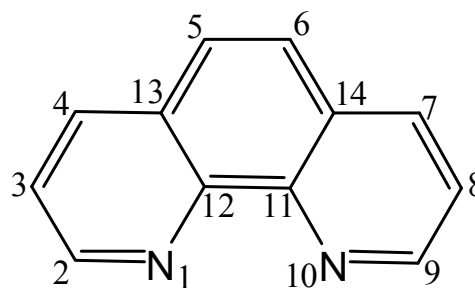
(a) 2,2'-bipyridine



(b) 4,4'-bipyridine



(c) 2,2':6',2''-terpyridine



(d) 1,10-phenanthroline

Figure 6.1. Structures of 2,2'-bipyridine (a), 4,4'-bipyridine (b), 2,2':6',2''-terpyridine (c), and 1,10-phenanthroline (d).

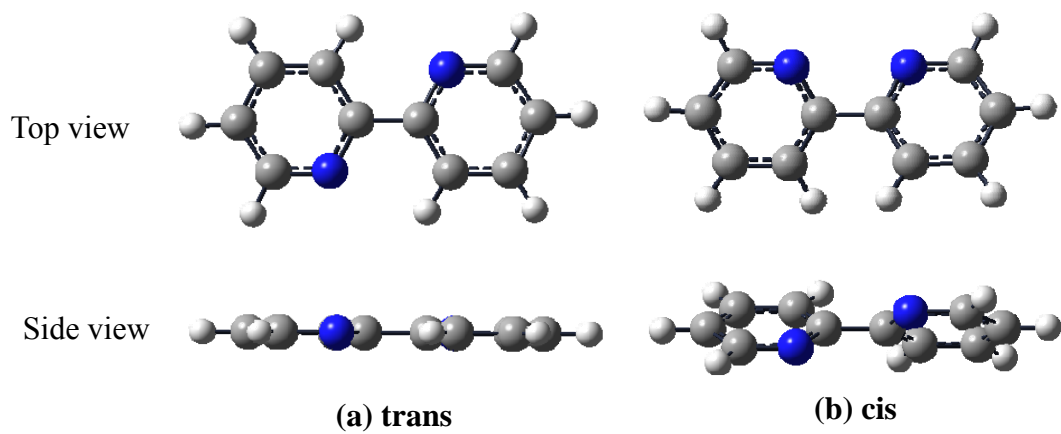


Figure 6.2. Stable rotational isomers of the trans (a) and cis (b) 2,2'-bipyridine.

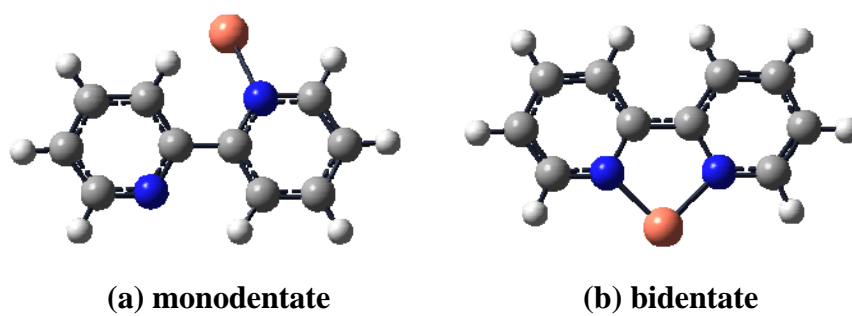


Figure 6.3. Isomers of Cu-(2,2'-bipyridine).

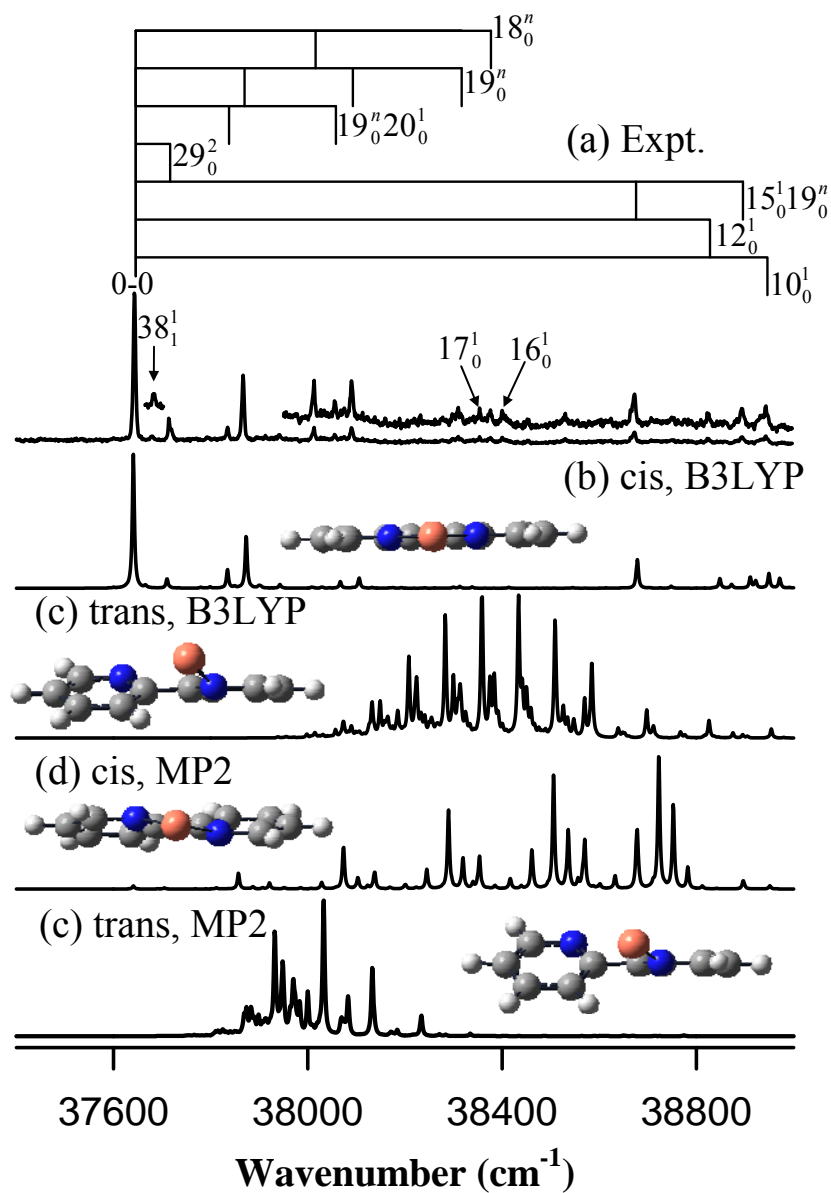


Figure 6.4. ZEKE spectrum of Cu-22BIPY seeded in Ar (a) and simulations of the cis (b) and trans (c) structures obtained by B3LYP calculations and the simulation (d) of the cis structure at 20 K obtained by MP2 calculations.

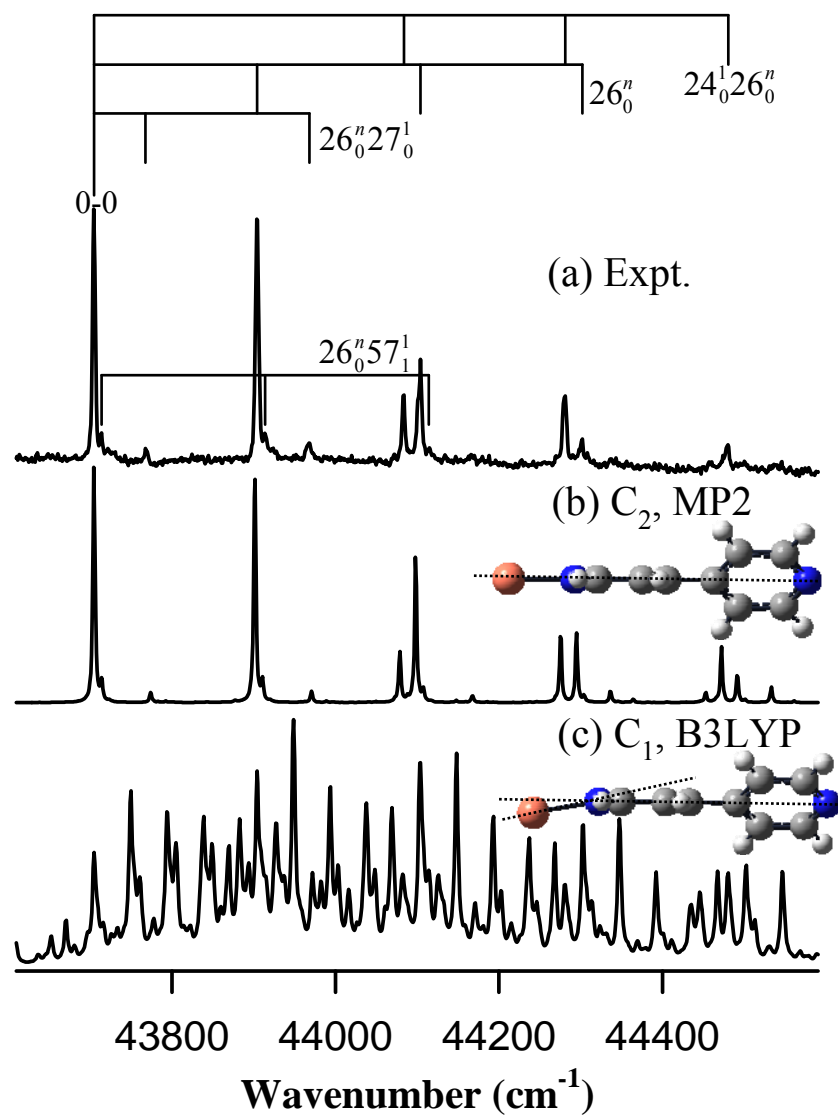


Figure 6.5. ZEKE spectrum of Cu-44BIPY seeded in 1:1 Ar/He mixture gas (a) and simulations from the B3LYP (b) and MP2 (c) at 20 K calculations.

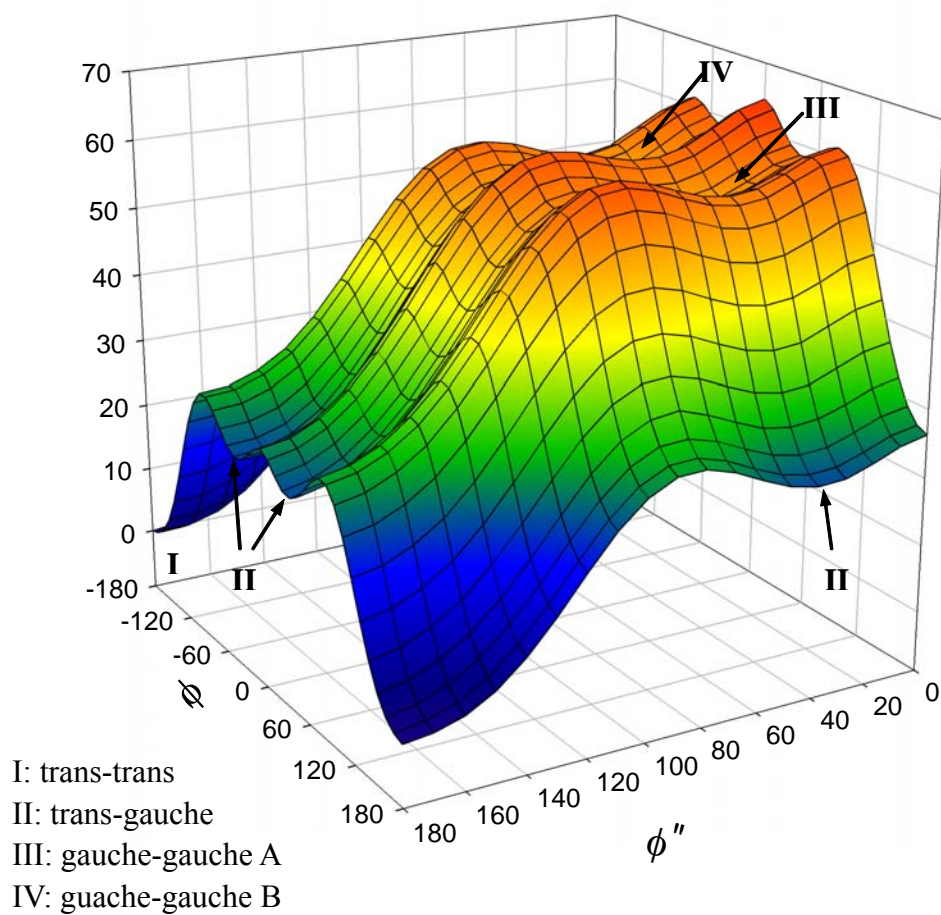


Figure 6.6. Potential energy surface for TERPY with respect to the rotation angles (ϕ' and ϕ'') among three pyridine rings calculated at the B3LYP/6-311+G(*d,p*) level of theory. Energies are relative to the global minimum.

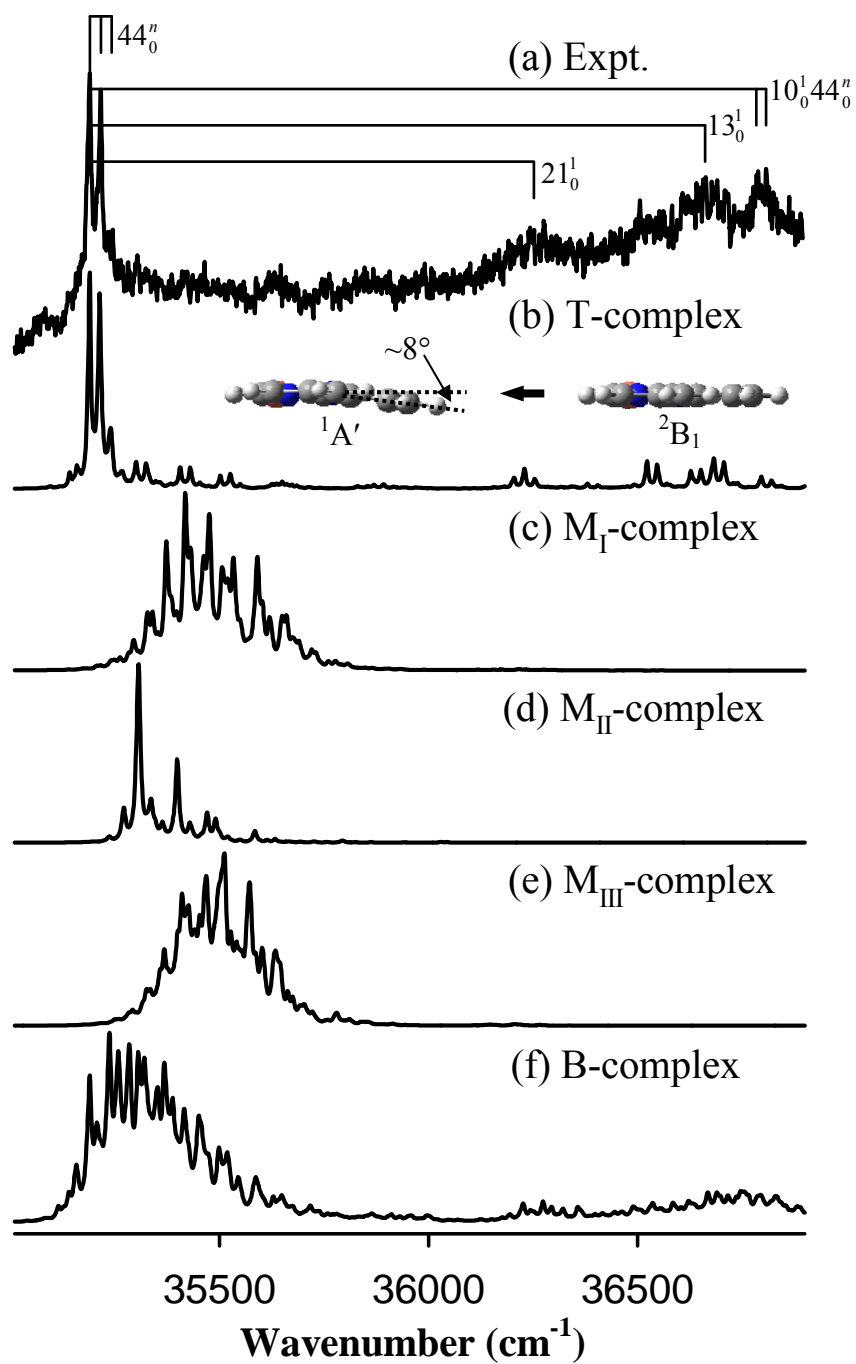


Figure 6.7. ZEKE spectrum of Cu-(2,2':6'',2-terpyridine) seeded in He (a) and spectral simulations of the T (b), M_I (c), M_{II} (d), M_{III} (e), and B (f) complexes at 50K (b) from the B3LYP/6-311+G(d,p) calculations.

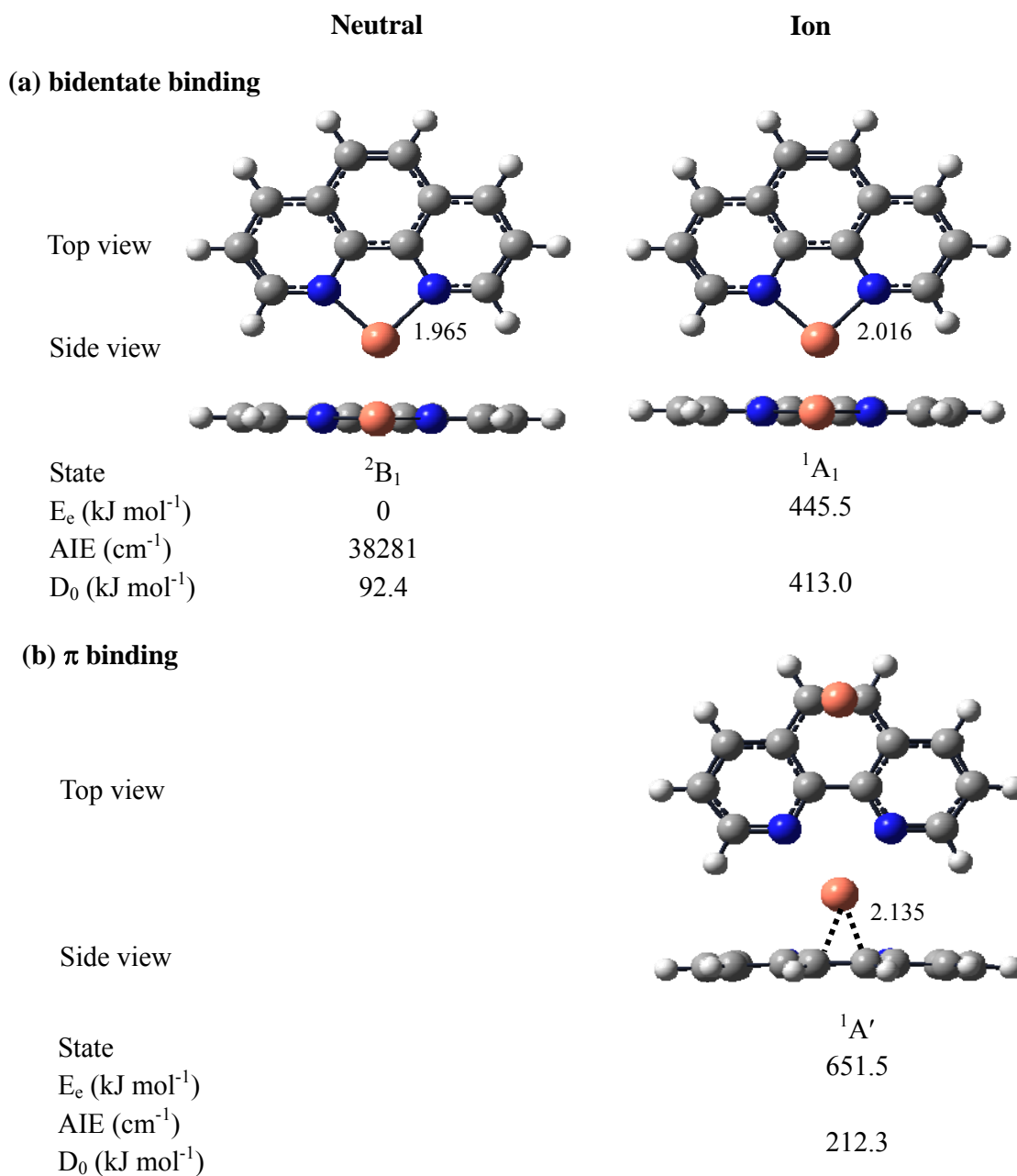


Figure 6.8. Bidentate and π bonding structures of Cu-(1,10-phenanthroline) from B3LYP/6-311+G(*d,p*) calculations. Bond distances are in angstrom. AIE, adiabatic ionization energy; D_0 , metal-ligand bond dissociation energy.

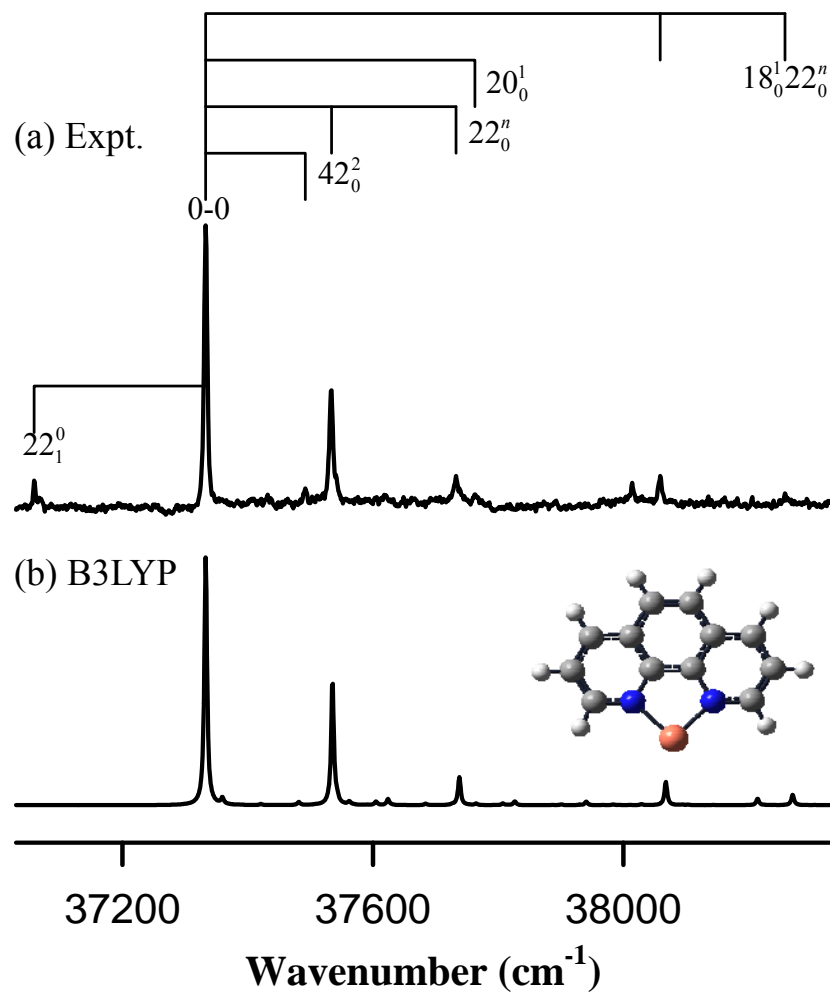


Figure 6.9. ZEKE spectrum of Cu-1,10-phenanthroline seeded in Ar (a) and spectral simulation at 20 K (b) from the B3LYP/6-311+G(d,p) calculations.

Chapter 7 Spectroscopy and structures of Cu- and Al-imidazole complexes

Imidazole or 1,3-diazole has a five-membered planar ring structure (Figure 7.1) and occurs as an essential constituent in common biological compounds and is one of the most versatile binding sites in proteins. Familiar examples of these biological chemicals include biogenic histamine, amino acid histidine, and nucleobases adenine and guanine. Derivatives of imidazole are present in antibacterial, antifungal, antiprotozoal, and antihelminthic medications;^{190,299} metal ion complexes containing imidazole rings are used as metal corrosion inhibitors^{300,301} and potential anticancer agents.³⁰² In the imidazole ring structure, N1 contributes two p electrons; N3 and three carbon atoms each provide one p electron to form the sextet aromatic π system. Additionally, N3 has a lone pair of electrons in the plane of the molecule. Thus, imidazole is expected to function as an aromatic π ligand or a simple σ ligand in binding with atomic or molecular species.³⁰³

The widespread applications and multiple binding sites of imidazole have stimulated considerable interest in the binding and structures of its complexes with noble gases, nonpolar and polar molecules, and metal ions. A π bound structure of neutral imidazole-Ar complex with Ar on top of the five-membered ring has been determined by rotational millimeter wave spectroscopy in a supersonic jet.³⁰⁴ The π bonding in imidazole-Ar is, however, changed to the H bonding in (imidazole)⁺-Ar and -N₂, as probed by gas-phase IR photodissociation spectroscopy and MP2 theoretical calculations.³⁰⁵ In binding with water, N-H...OH₂ and N...H-OH H-bond isomers of imidazole-H₂O have been detected by matrix isolation IR³⁰⁶ and Rydberg electron transfer spectroscopy.³⁰⁷ For metal complexes, binding energies of a series of metal ions

(Li⁺, Na⁺, K⁺, Mg⁺, Al⁺, Ca⁺, Sc⁺, Ti⁺, V⁺, Cr⁺, Mn⁺, Fe⁺, Co⁺, Ni⁺, Cu⁺, and Zn⁺) have been measured by CID experiments,³⁰⁸⁻³¹¹ and the metal ions in these complexes have been predicted to be σ -bound to the N3 group of imidazole.³⁰⁸⁻³¹⁴ However, there has been no electronic-vibrational spectroscopy reported for any metal-imidazole complexes, and such spectroscopic measurements should provide direct and quantitative evidence about their bonding and structures.

In the previous chapters, applications in molecular beam PFI-ZEKE spectroscopy have been reported to examine copper complexes of diamines, pyridine, diazines, and polypyridines. In this chapter, we extend our studies to copper complexation with the five-membered aromatic molecule, imidazole, using ZEKE spectroscopy and MP2 calculations, and a study on the Al-imidazole complex is reported for comparison. Neutral and ionic ground electronic states of these complexes are established by comparing the experiment to theory. AIEs and metal-ligand vibrational frequencies are measured from the ZEKE spectra, and the neutral metal-ligand bond energies are derived using a thermochemical relation.

7.1. Experimental and computational methods

Cu- and Al-imidazole were prepared by reactions of metal atoms with imidazole vapor in molecular beams. The metal atoms were produced by pulsed laser vaporization of a Cu or an Al rod (Cu, 99.9%, Alfa Aesar; Al, 99.9999%, Aldrich) with the second harmonic output of a Nd:YAG laser (Quanta-Ray GCR-3, 532 nm, ~ 3 mJ) in the presence of a carrier gas (He or Ar, ultra high purity, Scott-Gross) at ~ 50 psi. The carrier gas was delivered by a piezoelectric pulsed valve.²¹⁹ The metal rod was translated and rotated by a motor-driven mechanism to ensure that each laser pulse ablated a fresh surface. Since imidazole is a solid (m.p.: 89-91 °C) and has a relatively low vapor pressure at room temperature, a Cu oven (See section 1.2.2 and Figure 1.2)

was used to obtain sufficient ligand vapor. During the experiment, the oven was heated to about 45 °C by a heating cartridge, and the temperature was maintained by a thermo-controller (Omega CN2110). The vaporized ligand interacted with the metal atoms entrained in the carrier gas.

The Al- and Cu-imidazole complexes in the molecular beams were identified by photoionization TOF mass spectrometry. Ionization was carried out by a frequency-doubled dye laser (Lumonics HD-500), pumped by a XeCl excimer laser (Lumonics PM-884). The production of the 1:1 metal-ligand complexes was maximized by optimizing the timing and power of the vaporization and photoionization lasers, the amount of ligand vapor, and the backing pressure of the carrier gas. Prior to ZEKE experiments, ionization thresholds of these complexes were measured by recording the ion signals as a function of the laser wavelength. ZEKE electrons were produced by photoexcitation of neutral molecules to high-lying Rydberg states, followed by a $\sim 3 \mu\text{s}$ delayed, pulsed electric field ionization (1.2 V cm^{-1} , 100 ns) of these Rydberg states. A small DC field of $\sim 0.08 \text{ V cm}^{-1}$ was applied to help separate ZEKE from kinetic electrons produced by direct photoionization. The pulsed electric field was generated by a delay pulse generator (Stanford Research System, DG535). The ion and electron signals were detected by a dual MCP detector (Galileo), amplified by a preamplifier (Stanford Research System, SR445), averaged by a gated integrator (Stanford Research System, SR250), and recorded in a laboratory computer. Laser wavelengths were calibrated against vanadium or titanium atomic transitions in regions of the ZEKE spectra.²²¹

Calculations of molecular geometries and vibrational frequencies were carried out by using the MP2/6-311+G(*d,p*) method, implemented in the GAUSSIAN 03 program.¹¹³ Multidimensional FC factors were computed from the equilibrium geometries, harmonic frequencies, and normal modes of the neutral and ionic complexes.^{143,144} The Duschinsky effect²⁰¹ was considered to account for normal mode differences between the

neutral molecule and ion in the FC calculations. Spectral broadening was simulated by giving each line a Lorentzian line shape with the linewidth of the experimental spectrum. Boltzmann distributions were used to simulate spectra at specific vibrational temperatures.

7.2. Ab Initio Calculations

Both σ and π bonding modes are considered in search for the structures of the Cu- and Al-imidazole complexes and their ions. Metal binding to N3 is considered for the σ structure, and metal binding at the top of imidazole ring is assumed for the π structure. Figure 7.2 presents the optimized metal-ligand distances, electronic energies, and ionization and dissociation energies of the σ and π structures. The bond lengths and angles of imidazole in these complexes are similar to those of the free ligand in Figure 7.1.

7.2.1 Cu-Imidazole

The σ structure of the neutral Cu-imidazole complex has C_s symmetry and a $^2A'$ ground electronic state (Figure 7.2). The HOMO of the $^2A'$ ground state is formed by an antiphase σ^* interaction between the Cu $4s^1$ and N lone-pair electrons. The electron repulsion is strong since both the Cu $4s$ and N lone-pair orbitals are along the Cu-N axis. Because of the spherical shape of the s orbital, this complex has no $^2A''$ electronic state. Ionization of the $^2A'$ neutral ground state yields a $^1A'$ ion ground state in C_s symmetry. From the $^2A'$ to $^1A'$ state, the Cu-N distance is reduced from 1.978 Å to 1.881 Å, and the metal-ligand dissociation energy is increased from 52.9 to 284.2 kJ mol⁻¹. These bonding and structural changes are due to the removal of the antibonding σ^* electron in the $^2A'$ neutral state and the addition of a charge-dipole interaction in the $^1A'$ ion state.

The neutral 2A ground electronic state of the π structure is located 39.5 kJ mol^{-1} above the ${}^2A'$ state of the σ structure. In this π structure, the Cu atom is nearly on top of the C4-C5 bond, and the Cu-C4 and Cu-C5 distances are calculated to be 2.269 and 2.328 Å, respectively. Distances between Cu and other ring atoms are much longer and in the 2.940 – 3.240 Å range. The stronger Cu binding to C4 and C5 atoms (compared to other ring atoms) is also evident from a larger increase of the C4-C5 bond length (from 1.382 Å in the free ligand to 1.399 Å in the π complex). The longer metal-ligand distances and smaller dissociation energy (13.7 kJ mol^{-1}) than that of the σ structure are consistent with the common wisdom that imidazole is a weak π ligand. In free imidazole, N3, C4, and C5 atoms carry negative π charges, whereas N1 and C2 bear positive ones.¹⁹⁰ The prediction of the preferred Cu binding sites of C4 and C5 indicates that the ligand functions as a weak π donor, in agreement with the viewpoint that imidazole is a weakly π -excessive system.¹⁹⁰ Upon ionization, the Cu ion moves close to C4 and C5, with the Cu-C4 and -C5 distances being reduced to 2.035 and 2.254 Å, respectively, and the C4-C5 bond length is increased to 1.422 Å. These structural changes are in line with the increase of the metal-ligand dissociation energy in the ion.

7.2.2 Al-Imidazole

Similarly, our initial calculations on the Al-imidazole σ -complexes are performed under the C_s point group with Al binding to N3 (Figures 7.1 & 7.2). The ground electron configuration of Al is $3s^23p^1$. The $3p^1$ electron should be located in one of two $3p_\pi$ orbitals to minimize the repulsion with the N lone-pair electrons. These $3p_\pi$ orbitals are either perpendicular to or in the molecular plane, but either way perpendicular to the Al-N bond. If the $3p^1$ electron is filled in the $3p_\pi$ orbital in the molecular plane, the σ complex will have a ${}^2A'$ electronic state. On the other hand, if the $3p^1$ electron is filled in the $3p_\pi$ orbital perpendicular to the plane, it will have a ${}^2A''$ state. In both cases, the

Al $3p_{\pi}^1$ electron will be located in the HOMO, as it has a higher energy than the HOMO of the ligand. Our geometry optimizations show the ${}^2A'$ state is 15.7 kJ mol^{-1} lower than the ${}^2A''$ state. However, subsequent frequency calculations yield an imaginary frequency of $100i \text{ cm}^{-1}$ for the ${}^2A'$ state, and this imaginary frequency still exists in calculations with more stringent convergence criteria. Thus, the ${}^2A'$ state can be considered a saddle point on the potential energy surface. To search for a minimum energy structure associated with this Al $3p_{\pi}^1$ electron configuration, we carried out additional calculations without symmetry constrain, i.e., under the C_1 point group. The optimization of the C_1 initial geometry yields an essentially planar C_s structure, with dihedral angles (e.g., $\angle \text{Al-N3-C2-N1}$ and $\angle \text{Al-N3-C4-C5}$) smaller than 0.01 degrees, and the resultant electronic state can be described as ${}^2A'$ under C_s symmetry. This ${}^2A'$ state is a minimum (no imaginary frequency); it has a slightly lower electronic energy (2.2 kJ mol^{-1}) than and slightly different bond lengths and angles from the ${}^2A'$ saddle point obtained by the optimization of the C_s initial geometry.

This ${}^2A'$ state is 17.9 kJ mol^{-1} more stable and has an Al-N distance 0.089 \AA shorter than the ${}^2A''$ state. The geometries of the ligand, however, are quite similar in the two doublet states of the complex and the singlet ground state of free imidazole. Although the interaction between the Al $3p_{\pi}^1$ and N lone-pair electrons is small and comparable in these doublet states, the Al $3p_{\pi}^1$ electron of the ${}^2A'$ state should have a certain degree of repulsion with the $1s^1$ electrons of the adjacent hydrogen atoms, whereas the Al $3p_{\pi}^1$ electron of the ${}^2A''$ state should have some repulsion with the π electron cloud of the imidazole ring. The stronger metal-ligand bonding of the ${}^2A'$ state probably suggests a smaller repulsion between the Al $3p_{\pi}^1$ and H $1s^1$ electrons than that between the Al $3p_{\pi}^1$ and the π -electron cloud. Ionization of either the ${}^2A'$ or ${}^2A''$ states removes the Al $3p_{\pi}$ -based nonbonding electron from the HOMO and yields the ion ground electronic state of ${}^1A'$. From the neutral ${}^2A'$ or ${}^2A''$ state to the ion ${}^1A'$ state, the ligand geometry undergoes a small change in bond lengths ($< 0.020 \text{ \AA}$) and bond angles ($< 1.50^\circ$), but the

Al-N distance is reduced by more than 0.2 Å. The small change in the ligand framework is not surprising as the ejected electron has an Al-based nonbonding character. The large reduction in the Al-N bond length is due to an additional charge-dipole attraction. Consistent with the reduction of the Al-N bond length is a large increase of the bond dissociation energy from 62.7 ($^2A'$) or 42.0 ($^2A''$) kJ mol⁻¹ to 208.5 kJ mol⁻¹.

In addition, our calculations predict a less stable π structure at 36.4 kJ mol⁻¹ relative to the ground electronic $^2A'$ state. In this π structure, Al is located above the five-membered ring and closer to N3 and C4. The Al-N3 and Al-C4 distances are calculated to be 2.901 and 2.990 Å, whereas the distances between Al and other ring atoms are in the range of 3.240 – 3.580 Å. Like Cu-imidazole, the metal-ring distances are longer, and the bond energy is smaller than that of the σ structure. A significant difference from Cu-imidazole is that ionization of the π complex yields the same σ ion structure as the one from ionization of the σ complex. The conversion from the neutral π structure to the ionic σ structure shows that the predominant binding in the ionized species is the charge-dipole attraction.

7.3 ZEKE Spectra

Figures 7.3-7.6 present the experimental and theoretical ZEKE spectra, and Table 7.1 lists the energies of the observed transitions and their assignments. The spectral assignments are discussed by comparing with similar molecular species and with spectral simulations. In these simulations, the theoretical vibrational frequencies are not scaled, while the calculated 0-0 transition energies are shifted to the measured values for simplicity.

7.3.1 Cu-Imidazole

Figures 7.3 (a) and 7.4 (a) present the spectra of Cu-imidazole seeded in He and Ar carriers, respectively. The 0-0 transition energy is measured to be 42054 (5) cm^{-1} , with spectral linewidths of 7 cm^{-1} in He and 5 cm^{-1} in Ar. Both Figures 7.3 (a) and 7.4 (a) show a major progression of the 305 cm^{-1} spacing and its combinations with 173 ($16_0^m 17_0^l$) and 1129 cm^{-1} ($13_0^l 16_0^l$) intervals. In addition to these cold transitions, Figure 7.3 (a) displays a number of progressions formed by sequence transitions, which are labeled $16_0^m 17_m^m$, $16_0^m 24_i^j$, and $16_0^m 17_m^m 24_i^i$. These peaks vanish in Figure 7.4(a) because of lower vibrational temperatures of the complex in the heavier gas.

To assign the spectra in more details, Figures 7.3 and 7.4 compare the experimental spectra with the simulations of the σ and π structures at 80 and 10 K. For the simulations of the π structure, although the frequency interval of the major progression (316 cm^{-1}) is comparable to the experimental value (305 cm^{-1}), the calculated FC intensity is significantly larger. Moreover, an additional cold progression with the spacing of 86 cm^{-1} is predicted, but not observed in the experimental spectra. In contrast, the simulations of the σ structure have very good agreement with the experimental spectra in both the FC intensity and vibrational frequencies. In addition, the AIE of the σ structure is predicted to be closer to the experimental value. Our previous studies have shown that the MP2 calculations typically underestimate AIE values of Cu-ligand complexes by about 3000 cm^{-1} .^{84,157,224} By correcting the 3000 cm^{-1} error, the AIEs are estimated to be 42147 cm^{-1} for the σ structure and 46535 cm^{-1} for the π structure. Thus, the corrected theoretical AIE of the σ structure has a much better match with the measured value of 42054 cm^{-1} . Therefore, the comparisons in the FC intensity, vibrational frequencies, and AIE value show that the observed spectra must arise from ionization of the $^2A'$ state of the σ structure, rather than the 2A state of the π structure.

The spectral assignments are straightforward with the good agreement between the experimental spectra and the ${}^1A' \leftarrow {}^2A'$ simulations of the σ structure. The 305 cm^{-1} progression is assigned to the Cu^+ -imidazole symmetric stretch (ν_{16}^+), the 173 cm^{-1} interval to a Cu^+ -imidazole in-plane bend (ν_{17}^+) in the ${}^1A'$ ion state. Moreover, the 1129 cm^{-1} interval is due to the excitation of the ν_{13}^+ ring distortion characterized by an in-plane C-H bend. The assignment of the hot transitions yields the Cu-imidazole in-plane bending frequency of 124 cm^{-1} (ν_{17}) in the ${}^2A'$ neutral state and the Cu-imidazole out-of-plane bending (ν_{24}) frequencies of 111 and 74 cm^{-1} in the ${}^1A'$ and 2A states, respectively. A least squares fit of the peak positions of 16_0^n to $G(v) = \omega_s^+(v^+ + 1/2) + x_{ss}^+(v^+ + 1/2)^2$ yields a harmonic ν_{16}^+ frequency of $303(1)\text{ cm}^{-1}$ and an anharmonicity of $-0.2(2)\text{ cm}^{-1}$. Interestingly, the stretch frequency of the isolated Cu^+ -imidazole complex is almost identical to that of $[\text{Cu}^{2+}(\text{imidazole})_2]\text{Cl}_2$ (306.5 cm^{-1}) and $[\text{Cu}^+(\text{imidazole})_2]\text{Br}_2$ (307.0 cm^{-1}) measured in the condensed phase.³¹⁵ A similar observation has also been reported for the Cu^+ -diazine complexes.²²⁴ These observations suggest that the concept of formal oxidation states widely used in inorganic and organometallic chemistry may not reflect true electric charges on coordinated metal positive ions. In addition to anion ligands, the number and type of coordinated neutral ligands affects the amount of the charge on the metal ion.

7.3.2 Al-Imidazole

Figure 7.5 (a) shows the ZEKE spectrum of Al-imidazole seeded in He carrier gas. The first strong peak at $35343(5)\text{ cm}^{-1}$ has a linewidth of 10 cm^{-1} and is assigned to the 0-0 transition between the ground vibronic levels of the neutral and ionic complexes. This 0-0 transition energy is lower than that of the Cu-imidazole complex. The lower transition energy is in line with the lower ionization energy of Al atom. Furthermore, this spectral linewidth is significantly broader than those of Cu-imidazole. This is

consistent with larger rotational constants of Al-imidazole, which may lead to a higher rotational temperature and a more spread rotational envelop. Above the 0-0 transition, the spectrum shows a main progression (16_0^n) of 310 cm^{-1} spacing with up to five vibrational quanta and three other progressions formed by combinations of the 310 cm^{-1} spacing with 127 ($16_0^n 17_0^1$), 1065 ($13_0^1 16_0^n$), or 1192 cm^{-1} ($11_0^1 16_0^n$) intervals. Additionally, sequence transitions are observed at the higher wavenumber side of these progressions and are measured to be ~ 35 or $2 \times \sim 35\text{ cm}^{-1}$ from the respective cold transitions. These sequence transitions are labeled $16_0^n 24_m^m$, $16_0^n 17_0^1 24_1^1$, and $13_0^1 16_0^n 24_1^1$ in the figure. Below the 0-0 transition, a very small peak appears at 224 cm^{-1} (16_1^0) from an excited vibrational level of the neutral electronic ground state to the ground vibrational level of the ionic state. All of these hot transitions disappear in the spectrum recorded with Ar carrier [Figure 7.6 (a)], because vibrational temperatures of molecules seeded in Ar are lower.⁷⁸ Associated with this vibrational cooling, the molecules seeded in Ar also have lower rotational temperatures, as evident from the reduction of the spectral linewidth from 10 to 7 cm^{-1} .

Previously, vibrational spectra of imidazole have been measured by argon matrix-isolation^{306,316} and vapor-phase³¹⁷ IR spectroscopy and by solid state inelastic neutron scattering.³¹⁸ From these measurements and associated ab initio calculations,^{306,318} all vibrational modes of this organic compound are larger than 500 cm^{-1} , and four of which are in the range of 1050 - 1200 cm^{-1} . Therefore, the 1065 and 1192 cm^{-1} intervals in the ZEKE spectra should arise from ligand-based vibrations and the 127 and 309 cm^{-1} intervals from metal-ligand vibrations. Furthermore, previous ZEKE measurements^{83,85,319} have found that the Al^+ -N stretch frequencies of Al-amine complexes are around $300 \pm 60\text{ cm}^{-1}$. This frequency range suggests that the 308 cm^{-1} spacing may correspond to the Al^+ -N stretch as well.

Our MP2 calculations predict the ${}^2A'$ and ${}^2A''$ electronic states for the σ structure

and the 2A ground state for the π structure of the neutral complex, and the ${}^1A'$ ground state of the ionic complex. Since the three neutral states, especially the two neutral states of the σ structure, are predicted to be close in energy, transitions from these neutral states to the ${}^1A'$ ion state may be all possible. However, because of their large structural changes, the electronic transition from 2A state of the neutral π complex to the ${}^1A'$ state of the σ ion is expected to have a much longer FC profile than what is observed in the experiment. This transition can thus be excluded from the spectral assignment.

Figures 7.5 (b,c) and 7.6 (b,c) show the spectral simulations of the ${}^1A' \leftarrow {}^2A'$ and ${}^1A' \leftarrow {}^2A''$ transitions of the σ complex, in comparison with the experimental spectra [Figures 7.5 (a) and 7.6 (a)]. The ${}^1A' \leftarrow {}^2A''$ simulations have a significantly longer FC profile and many more transitions than the observed spectra, whereas the ${}^1A' \leftarrow {}^2A'$ simulations have a very good match with the measured ones. The longer FC profile in the ${}^1A' \leftarrow {}^2A''$ simulation is due to a larger Al-N distance change from the initial neutral state to the final ion state. Based on the agreement between the ${}^1A' \leftarrow {}^2A'$ simulations and the experimental spectra, we have assigned each of the observed peaks to specific vibronic transitions (Table 7.1). The 310 cm^{-1} major progression is assigned to the transitions from the ground vibrational level of the neutral ${}^2A'$ state to the Al^+ -imidazole symmetric stretch levels of the ionic ${}^1A'$ state, ν_{16}^+ . A least squares fit of the peak positions of 16_0^n yields a harmonic frequency of $312.6(8)\text{ cm}^{-1}$ and an anharmonicity of $-1.9(1)\text{ cm}^{-1}$ for this ion stretch mode. The 127 cm^{-1} interval is attributed to an in-plane Al^+ -imidazole symmetric bend, ν_{17}^+ ; the 1065 and 1192 cm^{-1} are ascribed to in-plane imidazole ring distortions, ν_{13}^+ and ν_{11}^+ . ν_{13}^+ is largely characterized by an in-plane C-H bend, whereas ν_{11}^+ is described by a C-N stretch. The ν_{13} frequency of the free ligand has been measured to be 1074 cm^{-1} in the vapor phase,³¹⁷ 1076 or 1074 cm^{-1} in the argon matrix,^{306,316} and 1061 cm^{-1} in the solid.³¹⁸ Al coordination seems to have a small effect to this in-plane C-H bending vibration. The ν_{11} frequency of imidazole has not been reported in the vapor phase, but measured as 1124 or 1130 cm^{-1} in the argon

matrix^{306,316} and 1142 cm^{-1} in the solid state.³¹⁸ These frequencies are significantly smaller than that in Al^+ -imidazole. However, this difference may not be used to assess the effect of Al coordination to the C-N stretching vibration, as the matrix interaction and H-bonding affect its frequency as well. Although the assignment of the sequence transitions above the band origin does not yield any additional fundamental frequency, a difference between the Al-imidazole out-of-plane bends in the ionized and neutral complexes is determined to be 35 cm^{-1} . The 224 cm^{-1} peak below the band origin is assigned to the Al-imidazole stretch excitation in the neutral complex, ν_{16} .

7.4. Metal-Ligand Binding in Cu- and Al-Imidazole

Table 7.2 summarizes the measured ionization and metal-ligand bond dissociation energies and vibrational frequencies of the two complexes. The dissociation energies of the ions are determined by Rodgers and coworkers with CID experiments,³¹⁰ and that of the neutral complexes are derived from a thermochemical cycle by involving the ion dissociation energies and AIEs of the complexes and metal atoms.²⁰⁷ These measured values are compared with those predicted from the MP2 calculations. The theory predicts a correct order of the ionization and dissociation energies, but underestimates their values. The calculated vibrational frequencies are generally in good agreement with the experimental measurements, although the computational accuracy remains to be improved.

For both complexes, ionization enhances the binding between the metal and ligand, and the stronger ion binding leads to an AIE reduction from the metal atom to the complex. This AIE shift is measured to be 20263 cm^{-1} for Cu and 12935 cm^{-1} for Al. The bond dissociation energy of Cu^+ -imidazole is larger than that of Al^+ -imidazole, but the opposite order is observed for the neutral complexes. The stronger Cu^+ ion bonding is easy to understand because Cu^+ is smaller and thus has a stronger charge-dipole

interaction with the ligand. The valence shell radius of Cu^+ (3d) is calculated to be 0.33 Å, whereas the radius of Al^+ (3s) is 1.11 Å.⁶⁶ In addition to the ion size effect, orbital interactions or electron repulsions also contribute to the binding difference between the two metals. The HOMO of the $^2\text{A}'$ neutral state of Al-imidazole has largely Al $3p_\pi$ character, whereas that of the $^2\text{A}'$ neutral state of Cu-imidazole is formed by the antiphase σ^* interaction between the Cu 4s and N lone-pair orbitals. Removal of the σ^* electron by ionization should substantially increase the metal-ligand binding, whereas removal of the mainly nonbonding Al $3p_\pi$ electron should have a small effect. The σ^* interaction also explains why the large bond energy of the Cu^+ ion complex is not carried over into the neutral species, even though the Cu-N bond is shorter than the Al-N bond (Figure 2). The charge-dipole and orbital interactions can also be used to rationalize metal-ligand binding in complexes containing the same metal atoms but different ligands. For example, the bond dissociation energy of Cu^+ -imidazole (287.5 kJ mol^{-1}) is larger than that of Cu^+ -pyrimidine (249.6 kJ mol^{-1}),¹⁸⁰ because imidazole has a larger electric dipole (3.8 D) and stronger basicity (8.0 pK_b) than pyrimidine (2.334 D, 3.4 pK_b).^{207,320,321} On the other hand, the bond energies of the neutral Cu-imidazole (45.1 kJ mol^{-1}) and -pyrimidine (46.4 kJ mol^{-1})²²⁴ are comparable, since the σ^* interactions or electron repulsions are similar in both cases.

The major vibrational progression observed in the ZEKE spectra of the two complexes is from excitation of the cation-ligand symmetric stretch (ν_{16}^+). This spectroscopic observation is consistent with the MP2 prediction, which shows that the largest structural change upon ionization occurs at the metal-nitrogen bond. The harmonic frequency of this stretch mode is measured to be 303 cm^{-1} in Cu^+ -imidazole and 313 cm^{-1} in Al^+ -imidazole. If one assumes that the metal-ligand stretch in these complexes behaves as diatomic molecules, then the force constant ($k = 4\pi^2c^2\omega^2\mu$, where k is force constant, c the speed of light, ω is the harmonic frequency, and μ is the reduced mass) of the Al^+ -imidazole stretch is estimated about 63% of that of the Cu^+ -imidazole

stretch. The ratio of the metal-ligand bond energies of these two complexes is about 81%.

7.5. Conclusions

This chapter presents a joint ZEKE spectroscopic and MP2 computational study of Cu- and Al-imidazole. ZEKE spectroscopy measures the AIEs and several vibrational frequencies, and the MP2 calculations predict the σ and π structures of these complexes with the former being more stable. By comparing these measurements and calculations, we have determined that the observed spectra arise from ionization of the σ structure. The ground electronic states of the σ Cu/Al- and Cu⁺/Al⁺-imidazole complexes are ²A' and ¹A' in C_s symmetry, respectively. The adiabatic ionization and bond dissociation energies are, respectively, 42054 (5) cm⁻¹ and 45 (7) kJ mol⁻¹ for the ²A' state of the Cu σ complex, and 35343 (5) cm⁻¹ and 78 (8) kJ mol⁻¹ for the ²A' state of the σ Al complex. The weaker Cu bonding is due to a stronger electron repulsion and σ^* interaction between the Cu 4s and N lone pair electrons. The major vibrational progression observed is the metal-ligand stretch, which has frequencies of 303 cm⁻¹ in Cu⁺-imidazole and 313/224 cm⁻¹ in Al⁺/Al-imidazole. The stretch frequency in the coordinately unsaturated Cu⁺-imidazole complex is nearly identical to those in the stable [Cu²⁺-(imidazole)₂]X₂ (X = Cl, Br) compounds.³¹⁵

Table 7.1. Peak positions (cm⁻¹) and assignments for the ZEKE spectra of Cu- and Al-imidazole σ complexes.

Cu-imidazole				Al-imidazole			
¹ A' ← ² A'				¹ A' ← ² A'			
Positions	Assignments	Positions	Assignments	Positions	Assignments	Positions	Assignments
42054	0 ₀ ⁰	42747	16 ₀ ² 17 ₁ ¹ 24 ₁ ¹	35119	16 ₁ ⁰	36386	16 ₀ ³ 17 ₀ ¹
42088	24 ₁ ¹	42754	16 ₀ ² 17 ₂ ²	35343	0 ₀ ⁰	36408	13 ₀ ¹
42103	17 ₁ ¹	42796	16 ₀ ² 17 ₂ ² 24 ₁ ¹	35378	24 ₁ ¹	36535	11 ₀ ¹
42137	17 ₁ ¹ 24 ₁ ¹	42836	16 ₀ ² 17 ₀ ¹	35413	24 ₂ ²	36555	16 ₀ ⁴
42227	17 ₀ ¹	42922	16 ₀ ² 24 ₁ ³	35470	17 ₀ ¹	36599	16 ₀ ⁴ 24 ₁ ¹
42359	16 ₀ ¹	42965	16 ₀ ³	35506	17 ₀ ¹ 24 ₁ ¹	36629	16 ₀ ⁴ 24 ₂ ²
42397	16 ₀ ¹ 24 ₁ ¹	43001	16 ₀ ³ 24 ₁ ¹	35653	16 ₀ ¹	36682	16 ₀ ⁴ 17 ₀ ¹
42410	16 ₀ ¹ 17 ₁ ¹	43015	16 ₀ ³ 17 ₁ ¹	35689	16 ₀ ¹ 24 ₁ ¹	36717	13 ₀ ¹ 16 ₀ ¹
42436	16 ₀ ¹ 24 ₂ ²	43053	16 ₀ ³ 17 ₁ ¹ 24 ₁ ¹	35730	16 ₀ ¹ 24 ₂ ²	36758	13 ₀ ¹ 16 ₀ ¹ 24 ₁ ¹
42450	16 ₀ ¹ 17 ₁ ¹ 24 ₁ ¹	43104	16 ₀ ³ 17 ₂ ² 24 ₁ ¹	35781	16 ₀ ¹ 17 ₀ ¹	36843	11 ₀ ¹ 16 ₀ ¹
42459	16 ₀ ¹ 17 ₂ ²	43132	16 ₀ ³ 17 ₀ ¹	35817	16 ₀ ¹ 17 ₀ ¹ 24 ₁ ¹	36848	16 ₀ ⁵
42485	16 ₀ ¹ 17 ₁ ¹ 24 ₂ ²	43183	13 ₀ ¹	35956	16 ₀ ²	37022	13 ₀ ¹ 16 ₀ ²
42532	16 ₀ ¹ 17 ₀ ¹	43238	16 ₀ ³ 24 ₁ ³	35995	16 ₀ ² 24 ₁ ¹	37060	13 ₀ ¹ 16 ₀ ² 24 ₁ ¹
42580	16 ₀ ¹ 24 ₀ ²	43269	16 ₀ ⁴	36033	16 ₀ ² 24 ₂ ²		
42615	16 ₀ ¹ 24 ₁ ³	43325	16 ₀ ⁴ 17 ₁ ¹	36085	16 ₀ ³ 17 ₀ ¹		
42662	16 ₀ ²	43438	16 ₀ ⁴ 17 ₀ ¹	36258	16 ₀ ³		
42703	16 ₀ ² 24 ₁ ¹	43489	13 ₀ ¹ 16 ₀ ¹	36296	16 ₀ ³ 24 ₁ ¹		
42710	16 ₀ ² 17 ₁ ¹	43573	16 ₀ ⁵	36332	16 ₀ ³ 24 ₂ ²		

Table 7.2. Adiabatic ionization energies (AIE, cm^{-1}), metal-ligand bond dissociation energies (D_0 and D_0^+ , kJ mol^{-1}), and vibrational frequencies (cm^{-1}) of Cu- and Al-imidazole σ complexes from the ZEKE spectra and MP2/6-311+G(*d,p*) calculations. D_0 and D_0^+ are metal-ligand bond dissociation energies of the neutral and ionic complexes, respectively.

		Experiment ^a	MP2
Cu-imidazole			
AIE		42054	39147
D_0^+ / D_0		287.5/45.1	284.2/52.9
Ring distortion	ν_{13}^+, a'	1129	1112
Cu-imidazole symmetric stretch	ν_{16}^+, a'	303 ^b	296
Cu-imidazole in-plane bend	$\nu_{17}^+ / \nu_{17}, a'$	173/124	179/131
Cu-imidazole out-of-plane bend	$\nu_{24}^+ / \nu_{24}, a''$	111/74	117/78
Al-imidazole			
AIE		35343	33399
D_0^+ / D_0		232.4/77.7	208.5/62.7
Ring distortion	ν_{11}^+, a'	1192	1164
Ring distortion	ν_{13}^+, a'	1065	1100
Al-imidazole symmetric stretch	$\nu_{16}^+ / \nu_{16}, a'$	313 ^b /224	289/202
Al-imidazole in-plane bend	ν_{17}^+, a'	127	129
Al-imidazole out-of-plane bend	$\nu_{24}^+ / \nu_{24}, a''$	$\nu_{24}^+ - \nu_{24} = 35$	$\nu_{24}^+ - \nu_{24} = 16$

^a The uncertainty of the AIE values is $\sim 5 \text{ cm}^{-1}$. D_0^+ values are taken from Ref. 13 with an uncertainty of 7.4 kJ mol^{-1} in Cu^+ -imidazole and 8.2 kJ mol^{-1} in Al^+ -imidazole. D_0 values are obtained by using a thermochemical relation.

^b Harmonic frequencies from least squares fits.

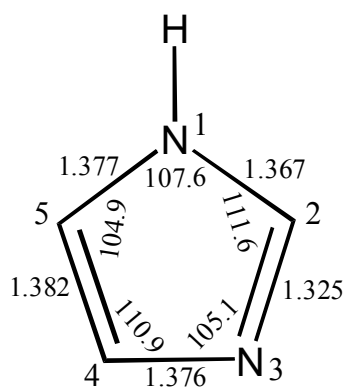


Figure 7.1. Structure of imidazole from MP2/6-311+G(*d,p*) calculations. Bond distances are in angstrom, and bond angles are in degrees. This molecule has a permanent electric dipole moment of 3.8 D (Ref. ²⁰⁷).

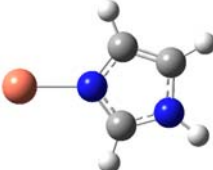

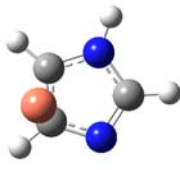
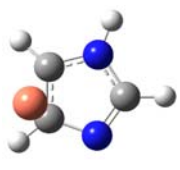
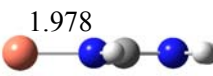
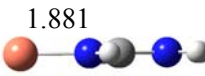
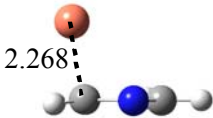
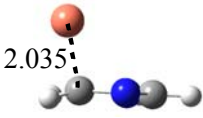
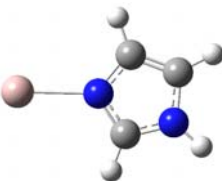
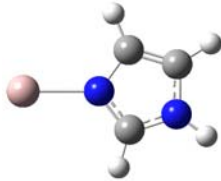
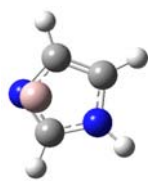
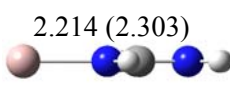
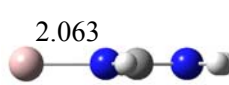
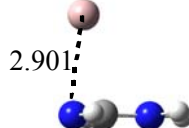
	σ complexes		π complexes	
(a) Cu-imidazole	Neutral	Ion	Neutral	Ion
Top view				
Side view				
state	${}^2A'$	${}^1A'$	2A	1A
E_e (kJ mol $^{-1}$)	0	465.8	39.5	559.7
AIE (cm $^{-1}$)	39147		43535	
D_0 (kJ mol $^{-1}$)	52.9	284.2	13.7	192.5
(b) Al-imidazole				
Top view				
Side view				
state	${}^2A'$ (${}^2A''$)	${}^1A'$	2A	
E_e (kJ mol $^{-1}$)	0 (17.9)	397.7	36.4	
AIE (cm $^{-1}$)	33399 (31663)			
D_0 (kJ mol $^{-1}$)	62.7 (42.0)	208.5	27.0	

Figure 7.2. σ and π structures of Cu-imidazole (a) and Al-imidazole (b) from MP2/6-311+G(*d,p*) calculations. Bond distances are in angstrom. AIE, adiabatic ionization energy; D_0 , metal-ligand bond dissociation energy.

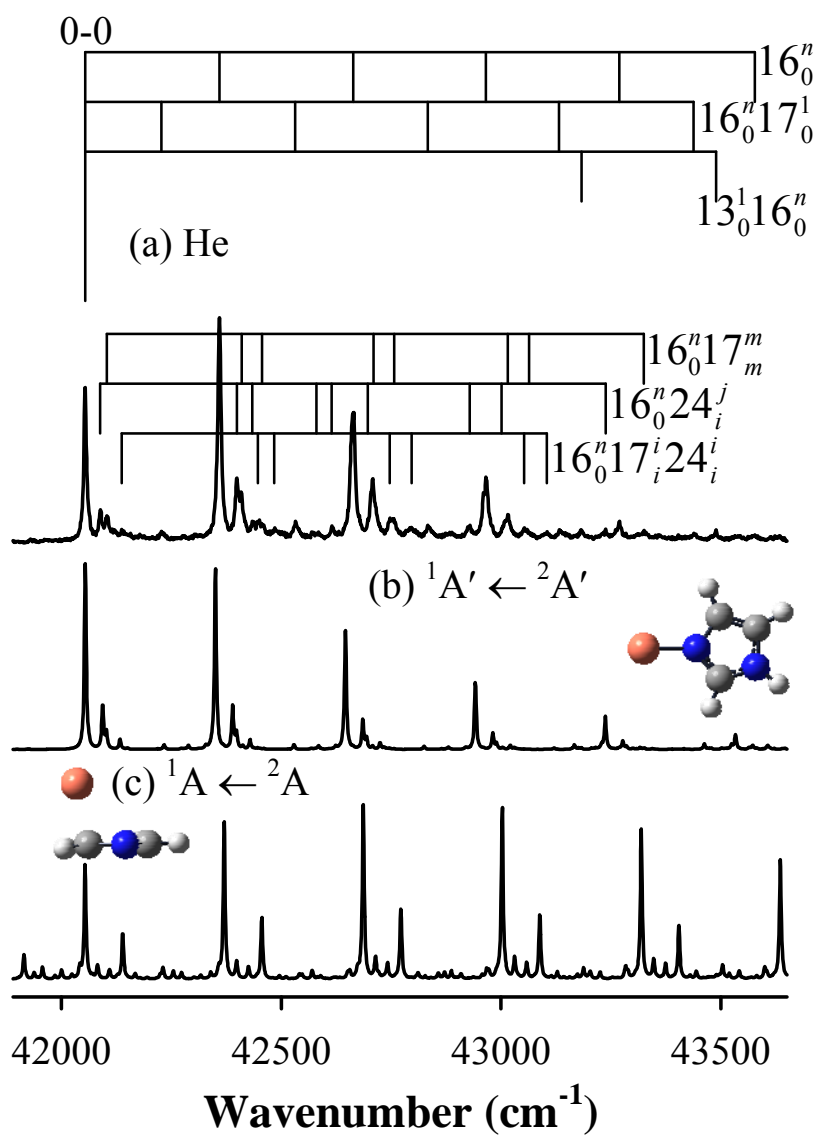


Figure 7.3. ZEKE spectrum of Cu-imidazole seeded in helium (a) and simulations of the ${}^1A' \leftarrow {}^2A'$ transition of the σ structure (b) and the ${}^1A \leftarrow {}^2A$ transition of the π structure (c) at 80 K.

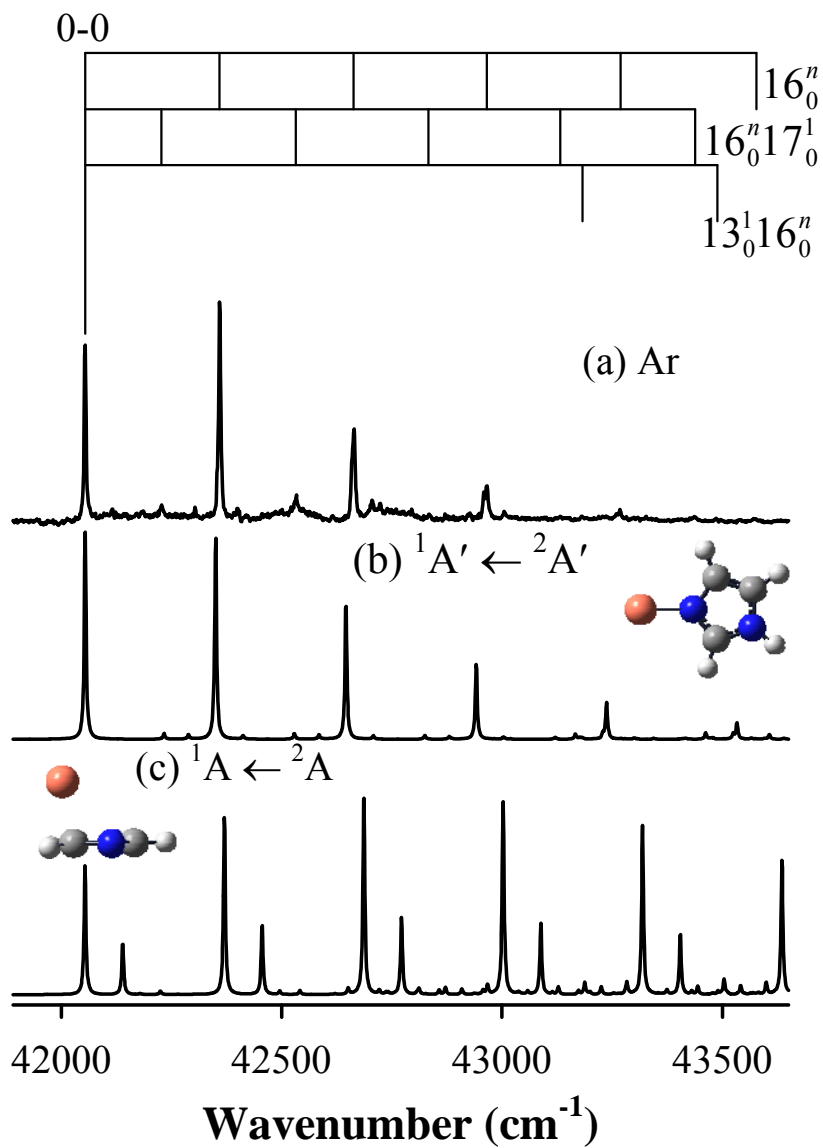


Figure 7.4. ZEKE spectrum of Cu-imidazole seeded in argon (a) and simulations of the ${}^1A' \leftarrow {}^2A'$ transition of the σ structure (b) and the ${}^1A \leftarrow {}^2A$ transition of the π structure (c) at 10 K.

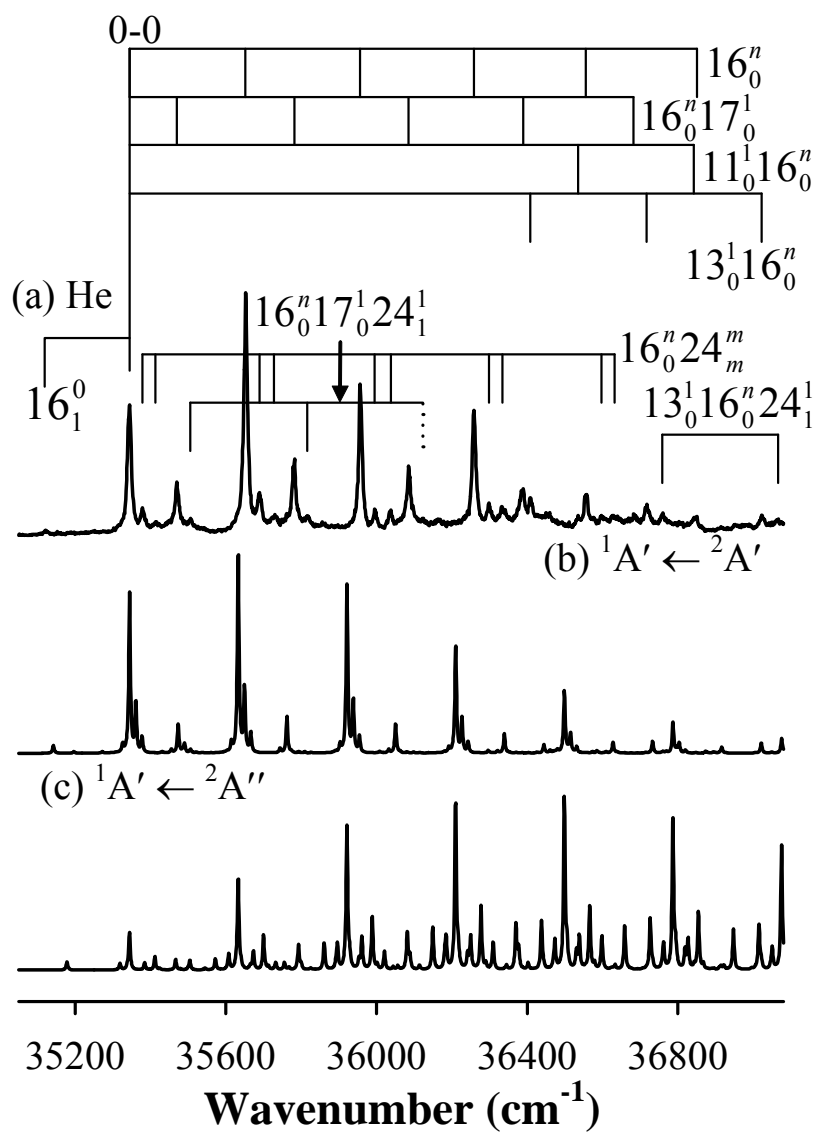


Figure 7.5. ZEKE spectrum of Al-imidazole seeded in helium (a) and simulations of the ${}^1A' \leftarrow {}^2A'$ (b) and ${}^1A' \leftarrow {}^2A''$ (c) transitions of the σ structure at 80 K.

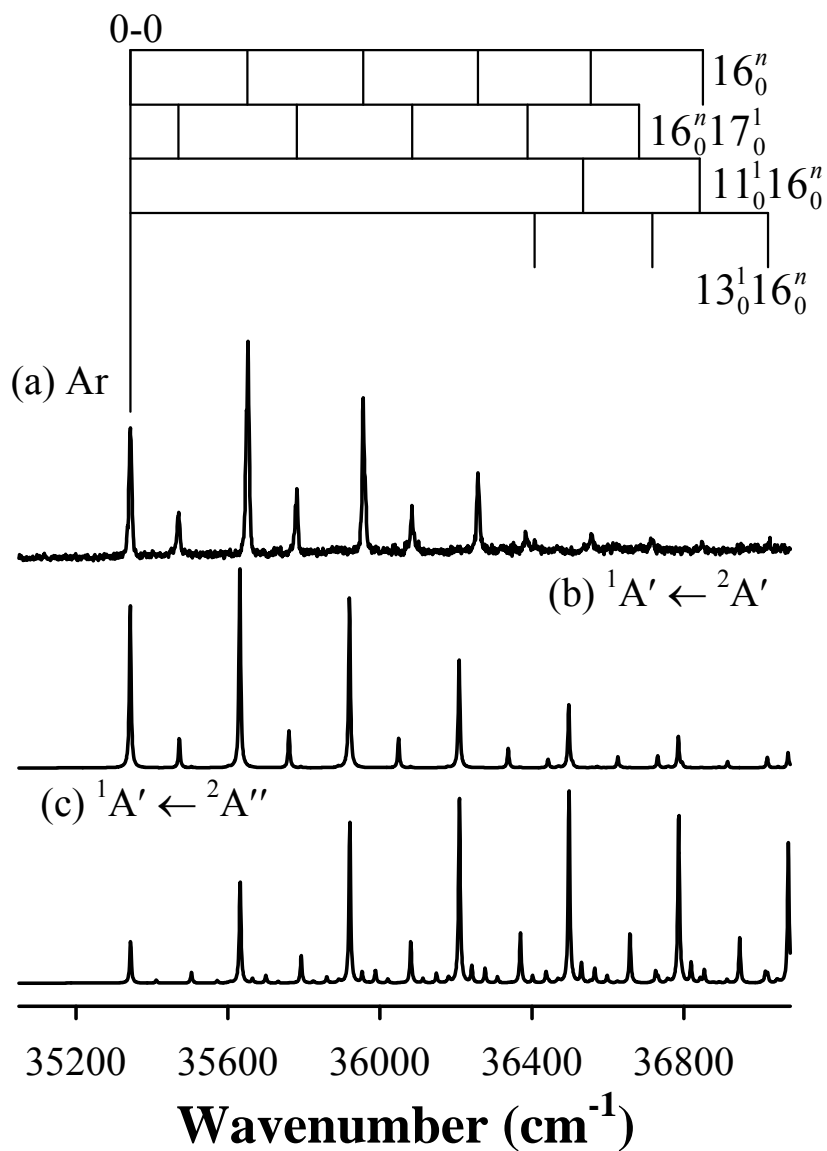


Figure 7.6. ZEKE spectrum of Al-imidazole seeded in argon (a) and simulations of the ${}^1A' \leftarrow {}^2A'$ (b) and ${}^1A' \leftarrow {}^2A''$ (c) transitions of the σ structure at 10 K.

Chapter 8 Summary

In this dissertation, I reported spectroscopic and theoretical studies of the Cu-organonitrogen complexes containing alkyl and aromatic amines (s). A number of minimum energy structures were predicted for each of the Cu complexes by quantum chemical calculations. These structures involve the mono-, bi- or tri-dentate Cu σ binding to one, two, or three nitrogens in the alkyl or aromatic amine (s) and the Cu π binding to the heterocyclic aromatic ring. The Cu-ethylenediamine, -(1,3-propanediamine), and -(1,4-butanediamine) complexes were determined to have hydrogen-bond stabilized monodentate bonding structures. However, Cu binds to both nitrogens of the methyl-substituted ethylenediamines. The six-membered and five-membered heterocyclic aromatic amines were determined to be σ bonding to Cu atoms via the nitrogen lone pair. For the ligands that contain both amino groups and an aromatic ring, the Cu atom was determined to exclusively bind to the nitrogen atom in the aromatic ring. Moreover, for those ligands containing two or more aromatic rings, the Cu atom will σ bind to the nitrogen (s). Such a metal-ligand σ bonding interaction is so strong that in the bipyridine and terpyridine complexes the pyridine rings are rotated about the C-C bond (s) to form bi- and tri-dentate structures. Thus, the σ -bond energy must be larger than the rotational energy barrier.

Table 8.1 summarizes the experimental AIEs and Cu⁺-ligand stretching vibrations (with Cu displacement) of the Cu-complexes studied in this work. The measured AIEs can be divided to three groups based on the energy ranges of 41200 to 46100 cm⁻¹, 36000 to 37700 cm⁻¹, and 29900 to 35200 cm⁻¹. These three groups corresponds to the monodentate, bidentate, and tridentate σ bonding modes, respectively, except for the Cu-(N,N,N',N'-tetramethylethylenediamine) and Cu-(pyridine)₂ complexes which are

bidentate and di-ligand complexes, respectively. This trend of the AIEs shows that the AIE shift from the metal atom to the metal complex increases with increasing the number of σ bonding sites.

Similarly, the Cu^+ -ligand stretching vibrations can also be divided into three groups based on the frequency ranges of 520 to 450 cm^{-1} , 310 to 250 cm^{-1} and 210 to 190 cm^{-1} . These three groups corresponds to the monodentate Cu bonding to the alkyl amine, the monodentate Cu binding to the aromatic amine, and the bidentate Cu binding two nitrogen atoms, respectively, except for the monodentate Cu-(4,4'-bipyridine) complex (200 cm^{-1}). This trend suggests that the measurement of the Cu^+ -ligand stretching frequency can be used to distinguish different binding modes.

By comparing the theoretical calculations to our experimental measurements in this work, the MP2 method provides better predictions for the monodentate Cu complexes, while the B3LYP method yields better results for the multidentate Cu complexes. More data sets may be required to evaluate the quality of these two methods, but that is beyond the current work.

Table 8.1. Adiabatic ionization energies (AIE, cm^{-1}) and Cu^+ -ligand stretching frequencies of the Cu-complexes from ZEKE measurements. The experimental AIEs have an uncertainty of $\sim 5 \text{ cm}^{-1}$. The Cu^+ -ligand stretching vibrations are largely characterized by Cu displacements.

Complexes	AIE	Cu^+ -L stretch
Cu-ethylenediamine	43491	474
Cu-(1,3-propanediamine), H-bond I	42376	Not available
Cu-(1,3-propanediamine), H-bond II	42578	487
Cu-(1,4-butanediamine), H-bond I	41638	512
Cu-(1,4-butanediamine), H-bond II	41207	593
Cu-(N-monomethylethylenediamine)	36020	449
Cu-(N, N-dimethylethylenediamine)	36284	469
Cu-(N,N,N'-trimethylethylenediamine)	36250 ^a	Not available
Cu-(N,N,N',N'-tetramethylethylenediamine)	34950 ^a	Not available
Cu-pyridine	43703	272
Cu-pyrazine	46038	265
Cu-pyrimidine	45332	270
Cu-pyridazine	43054	273
Cu-imidazole	42054	303
Cu-4-aminopyridine	41377	261
Cu-3-aminopyridine	42541	271
Cu-2-aminopyridine	43742	256
Cu-4,4'-dipyridine	43705	200
Cu-2,2-dipyridine	37641	192
Cu-1,10-phenanthroline	37333	201
Cu-(2,2':6':2''-terpyridine)	35190	Not available
Cu-(pyridine) ₂	29920	Not available

^a:These values are from photoionization efficiency measurements and have an uncertainty of $\sim 300 \text{ cm}^{-1}$.

References:

- (1) Borovik, A. S. *Comments Inorg. Chem.* **2002**, 23, 45.
- (2) Burrows, A. D. *Science Progress (St. Albans, United Kingdom)* **2002**, 85, 199.
- (3) Constable, E. *Chemistry & Industry (London, United Kingdom)* **1994**, 56.
- (4) Cronin, L. *Annu. Rep. Prog. Chem., Sect. A, Inorg. Chem.* **2005**, 101, 348.
- (5) Gianneschi, N. C.; Masar, M. S., III; Mirkin, C. A. *Acc. Chem. Res.* **2005**, 38, 825.
- (6) Hofmeier, H.; Schubert, U. S. *Chem. Soc. Rev.* **2004**, 33, 373.
- (7) Vlcek, A., Jr. *Electron Transfer in Chemistry* **2001**, 2, 804.
- (8) Wilkinson, M. J.; van Leeuwen, P. W. N. M.; Reek, J. N. H. *Organic & Biomolecular Chemistry* **2005**, 3, 2371.
- (9) Tyler, G. *Soil Biochem.* **1981**, 5, 371.
- (10) Cowan, J. A. *Chem. Rev.* **1998**, 98, 1067.
- (11) Thomson, A. J.; Gray, H. B. *Curr. Opin. Chem. Biol.* **1998**, 2, 155.
- (12) Feig, A. L.; Uhlenbeck, O. C. *Cold Spring Harbor Monograph Series* **1999**, 37, 287.
- (13) Siegbahn, P. E. M.; Blomberg, M. R. A. *Chem. Rev.* **2000**, 100, 421.
- (14) Sigel, H.; Sigel, A. *J. Indian Chem. Soc.* **2000**, 77, 501.
- (15) Davis, T. A.; Volesky, B.; Mucci, A. *Water Res.* **2003**, 37, 4311.
- (16) Rosen, B. P. *Topics in Current Genetics* **2006**, 14, 485.
- (17) Zamaraev, K. *Pure Appl. Chem.* **1997**, 69, 865.
- (18) Cundari, T. R.; Deng, J.; Fu, W.; Klinckman, T. R.; Yoshikawa, A. *J. Chem. Inf. Comput. Sci.* **1998**, 38, 941.
- (19) Francis, M. B.; Jamison, T. F.; Jacobsen, E. N. *Curr. Opin. Chem. Biol.* **1998**, 2, 422.
- (20) Psaro, R.; Recchia, S. *Catal. Today* **1998**, 41, 139.
- (21) Yamamoto, A. *J. Organomet. Chem.* **2000**, 600, 159.

- (22) Skoda-Foeldes, R.; Kollar, L. *Chemical Reviews (Washington, DC, United States)* **2003**, *103*, 4095.
- (23) Fairlamb, I. *Chemistry Review (Deddington, United Kingdom)* **2004**, *13*, 31.
- (24) O'Hair, R. A. J.; Khairallah, G. N. *Journal of Cluster Science* **2004**, *15*, 331.
- (25) Hultzsch, K. C. *Advanced Synthesis & Catalysis* **2005**, *347*, 367.
- (26) Sekhar, K. C.; Chary, N. S.; Kamala, C. T.; Anjaneyulu, Y. *Proceedings of the Indian National Science Academy, Part B: Biological Sciences* **2004**, *70*, 13.
- (27) Zubay, G. *Biochemistry*; Wm. C. Brown: Dubuque, IA, 1998.
- (28) Holm, R. H.; Kennepohl, P.; Solomon, E. I. *Chem. Rev.* **1996**, *96*, 2239.
- (29) Cotton, F. A.; Wilkinson, G.; Murillo, C. A.; Bochmann, M. *Advanced Inorganic Chemistry*, 6th ed.; Wiley: New York, 1999.
- (30) Baird, C.; Cann, M. *Environmental Chemistry*, 3RD ed.; W.H. Freeman & Company: New York, 2004.
- (31) Minisci, F. *Acc. Chem. Res.* **1975**, *8*, 165.
- (32) Boffa, L. S.; Novak, B. M. *Transition Metal Catalysis in Macromolecular Design*; American Chemical Society: Washington, DC, 2000.
- (33) Hotop, H.; Bennett, R. A.; Lineberger, W. C. *J. Chem. Phys.* **1973**, *58*, 2373.
- (34) Ying, Z. C.; Ho, W. *J. Chem. Phys.* **1990**, *93*, 9077.
- (35) Iino, T.; Ohashi, K.; Mune, Y.; Inokuchi, Y.; Judai, K.; Nishi, N.; Sekiya, H. *Chem. Phys. Lett.* **2006**, *427*, 24.
- (36) Jaeger, J. B.; Jaeger, T. D.; Duncan, M. A. *J. Phys. Chem. A* **2006**, *110*, 9310.
- (37) Koizumi, H.; Armentrout, P. B. *J. Am. Soc. Mass Spectrom.* **2001**, *12*, 480.
- (38) Koizumi, H.; Zhang, X.-G.; Armentrout, P. B. *J. Phys. Chem. A* **2001**, *105*, 2444.
- (39) Blitz, M. A.; Mitchell, S. A.; Hackett, P. A. *J. Phys. Chem.* **1993**, *97*, 5305.
- (40) Blitz, M. A.; Mitchell, S. A.; Hackett, P. A. *J. Phys. Chem.* **1993**, *97*, 5298.
- (41) Blitz, M. A.; Mitchell, S. A.; Hackett, P. A. *J. Phys. Chem.* **1991**, *95*, 8719.
- (42) Fang, C. C.; Parson, J. M. *J. Chem. Phys.* **1991**, *95*, 6413.

- (43) McCaffrey, J. G.; Bennett, R. R.; Morse, M. D.; Breckenridge, W. H. *J. Chem. Phys.* **1989**, *91*, 92.
- (44) Page, R. H.; Gudeman, C. S. *J. Chem. Phys.* **1991**, *94*, 39.
- (45) Zerkle, D. K.; Sappey, A. D. *IEEE Transactions on Plasma Science* **1996**, *24*, 37.
- (46) Amunugama, R.; Rodgers, M. T. *J. Phys. Chem. A* **2001**, *105*, 9883.
- (47) Vitale, G.; Valina, A. B.; Huang, H.; Amunugama, R.; Rodgers, M. T. *J. Phys. Chem. A* **2001**, *105*, 11351.
- (48) Rannulu, N. S.; Rodgers, M. T. *Phys. Chem. Chem. Phys.* **2005**, *7*, 1014.
- (49) Schroder, D.; Schwarz, H.; Wu, J.; Wesdemiotis, C. *Chem. Phys. Lett.* **2001**, *343*, 258.
- (50) Cerda, B. A.; Cornett, L.; Wesdemiotis, C. *Int. J. Mass spectrom.* **1999**, *193*, 205.
- (51) Cerda, B. A.; Wesdemiotis, C. *Int. J. Mass spectrom.* **1999**, *185/186/187*, 107.
- (52) Wu, J.; Wesdemiotis, C. *Chem. Phys. Lett.* **1999**, *303*, 243.
- (53) Cerda, B. A.; Wesdemiotis, C. *J. Am. Chem. Soc.* **1995**, *117*, 9734.
- (54) Doan, V.; Kasai, P. H. *J. Phys. Chem. A* **1997**, *101*, 8115.
- (55) Kasai, P. H.; Jones, P. M. *J. Phys. Chem.* **1986**, *90*, 4239.
- (56) Kasai, P. H.; Jones, P. M. *J. Am. Chem. Soc.* **1985**, *107*, 813.
- (57) Kasai, P. H. *J. Am. Chem. Soc.* **1984**, *106*, 3069.
- (58) Kasai, P. H.; McLeod, D., Jr. *Faraday Symp. R. Soc. Chem.* **1980**, *14*, 65.
- (59) Kasai, P. H.; McLeod, D., Jr.; Watanabe, T. *J. Am. Chem. Soc.* **1980**, *102*, 179.
- (60) Kasai, P. H.; McLeod, D., Jr. *J. Am. Chem. Soc.* **1978**, *100*, 625.
- (61) Kasai, P. H.; Bishop, R. J., Jr.; McLeod, D., Jr. *J. Phys. Chem.* **1978**, *82*, 279.
- (62) Kasai, P. H.; McLeod, D., Jr. *J. Chem. Phys.* **1971**, *55*, 1566.
- (63) Kasai, P. H.; Whipple, E. B.; Weltner, W., Jr. *J. Chem. Phys.* **1966**, *44*, 2581.
- (64) Norton, P. R.; Tapping, R. L. *Chem. Phys. Lett.* **1976**, *38*, 207.
- (65) Rupp, H.; Weser, U. *Bioinorganic Chemistry* **1976**, *6*, 45.
- (66) Leopold, D. G.; Ho, J.; Lineberger, W. C. *J. Chem. Phys.* **1987**, *86*, 1715.

- (67) Pettiette, C. L.; Yang, S. H.; Craycraft, M. J.; Conceicao, J.; Laaksonen, R. T.; Cheshnovsky, O.; Smalley, R. E. *J. Chem. Phys.* **1988**, *88*, 5377.
- (68) Cha, C. Y.; Gantefoer, G.; Eberhardt, W. *Rev. Sci. Instrum.* **1992**, *63*, 5661.
- (69) Gantefoer, G.; Cha, C.-Y.; Handschuh, H.; Icking-Konert, G. S.; Kessler, B.; Gunnarsson, O.; Eberhardt, W. *J. Electron Spectrosc. Relat. Phenom.* **1995**, *76*, 37.
- (70) Misaizu, F.; Tsukamoto, K.; Sanekata, M.; Fuke, K. *Laser Chem.* **1995**, *15*, 195.
- (71) Nakajima, A.; Taguwa, T.; Nakao, K.; Hoshino, K.; Iwata, S.; Kaya, K. *Surface Review and Letters* **1996**, *3*, 417.
- (72) Brock, L. R.; Duncan, M. A. *Chem. Phys. Lett.* **1995**, *247*, 18.
- (73) Brock, L. R.; Knight, A. M.; Reddic, J. E.; Pilgrim, J. S.; Duncan, M. A. *J. Chem. Phys.* **1997**, *106*, 6268.
- (74) Cockett, M. C. R. *Chem. Soc. Rev.* **2005**, *34*, 935.
- (75) Rothschof, G. K.; Perkins, J. S.; Li, S.; Yang, D.-S. *J. Phys. Chem. A* **2000**, *104*, 8178.
- (76) Li, S.; Rothschof, G. K.; Pillai, D.; Sohnlein, B. R.; Wilson, B. M.; Yang, D.-S. *J. Chem. Phys.* **2001**, *115*, 7968.
- (77) Rothschof, G. K.; Li, S.; Shannon Perkins, J.; Yang, D.-S. *J. Chem. Phys.* **2001**, *115*, 4565.
- (78) Fuller, J. F.; Li, S.; Sohnlein, B. R.; Rothschof, G. K.; Yang, D.-S. *Chem. Phys. Lett.* **2002**, *366*, 141.
- (79) Li, S.; Rothschof, G. K.; Sohnlein, B. R.; Yang, D.-S. *J. Phys. Chem. A* **2002**, *106*, 6941.
- (80) Li, S.; Rothschof, G. K.; Yang, D.-S. *J. Chem. Phys.* **2002**, *116*, 6589.
- (81) Rothschof, G. K.; Li, S.; Yang, D.-S. *J. Chem. Phys.* **2002**, *117*, 8800.
- (82) Li, S.; Fuller, J. F.; Sohnlein, B. R.; Yang, D.-S. *J. Chem. Phys.* **2003**, *119*, 8882.
- (83) Li, S.; Rothschof, G. K.; Fuller, J. F.; Yang, D.-S. *J. Chem. Phys.* **2003**, *118*, 8636.
- (84) Li, S.; Sohnlein, B. R.; Rothschof, G. K.; Fuller, J. F.; Yang, D.-S. *J. Chem. Phys.*

2003, *119*, 5406.

(85) Li, S.; Fuller, J. F.; Wang, X.; Sohnlein, B. R.; Bhowmik, P.; Yang, D.-S. *J. Chem. Phys.* **2004**, *121*, 7692.

(86) Li, S.; Rothschof, G. K.; Sohnlein, B. R.; Fuller, J. F.; Yang, D.-S. *Can. J. Chem.* **2004**, *82*, 1067.

(87) Wang, X.; Yang, D.-S. *J. Phys. Chem. A* **2004**, *108*, 6449.

(88) Li, S.; Sohnlein, B. R.; Yang, D.-S.; Miyawaki, J.; Sugawara, K.-I. *J. Chem. Phys.* **2005**, *122*, 214316/1.

(89) Miyawaki, J.; Sugawara, K.; Li, S.; Yang, D.-S. *J. Phys. Chem. A* **2005**, *109*, 6697.

(90) Sohnlein, B. R.; Li, S.; Yang, D.-S. *J. Chem. Phys.* **2005**, *123*, 214306/1.

(91) Sohnlein Bradford, R.; Li, S.; Fuller Jason, F.; Yang, D.-S. *J. Chem. Phys.* **2005**, *123*, 014318.

(92) Sohnlein, B. R.; Yang, D.-S. *J. Chem. Phys.* **2006**, *124*, 134305/1.

(93) Wang, X.; Lee, J. S.; Yang, D.-S. *J. Chem. Phys.* **2006**, *125*, 014309/1.

(94) Wang, X.; Yang, D.-S. *J. Phys. Chem. A* **2006**, *110*, 7568.

(95) Turner, D. W.; Baker, C.; Baker, A. D.; C. R. Brundle *Molecular Photoelectron Spectroscopy*; Wiley: New York, 1970.

(96) Richards, W. G. *International Journal of Mass Spectrometry and Ion Physics* **1969**, *2*, 419.

(97) Schlag, E. W. *Adv. Chem. Phys.* **1997**, *101*, 607.

(98) Yang, D. S. *Coord. Chem. Rev.* **2001**, *214*, 187.

(99) Gantefor, G. F.; Cox, D. M.; Kaldor, A. *J. Chem. Phys.* **1992**, *96*, 4102.

(100) Drechsler, G.; Boesl, U.; Bassmann, C.; Schlag, E. W. *J. Chem. Phys.* **1997**, *107*, 2284.

(101) Held, A.; Schlag, E. W. *Acc. Chem. Res.* **1998**, *31*, 467.

(102) Baranov, L. Y.; Held, A.; Selzle, H. L.; Schlag, E. W. *Chem. Phys. Lett.* **1998**, *291*, 311.

- (103) Wiley, W. C.; McLaren, I. H. *Rev. Sci. Instr.* **1955**, *26*, 1150.
- (104) Levine, I. N. *Quantum Chemistry, Fifth Edition*, 1999.
- (105) Bartlett, R. J. *Annu. Rev. Phys. Chem.* **1981**, *32*, 359.
- (106) Ziegler, T. *Chemical Reviews (Washington, DC, United States)* **1991**, *91*, 651.
- (107) Balbuena, P. B.; Seminario, J. M. *Theoretical and Computational Chemistry* **1995**, *2*, 383.
- (108) Barone, V.; Fliszar, S. *THEOCHEM* **1996**, *369*, 29.
- (109) Wesolowski, T. A.; Weber, J. *Molecular Orbital Calculations for Biological Systems* **1998**, 85.
- (110) Bromley, S. T.; French, S. A.; Sokol, A. A.; Sushko, P. V.; Richard, C.; Catlow, A. *Recent Advances in Computational Chemistry* **2002**, *1*, 45.
- (111) Cavalli, A.; Folkers, G.; Recanatini, M.; Scapozza, L. *Methods and Principles in Medicinal Chemistry* **2003**, *17*, 41.
- (112) Meier, R. J. *Faraday Discuss.* **2003**, *124*, 405.
- (113) M. J. Frisch, G. W. T., H. B. Schlegel, G. E. Scuseria, M. A. Robb, J. R. Cheeseman, J. A. Montgomery, Jr., T. Vreven, K. N. Kudin, J. C. Burant, J. M. Millam, S. S. Iyengar, J. Tomasi, V. Barone, B. Mennucci, M. Cossi, G. Scalmani, N. Rega, G. A. Petersson, H. Nakatsuji, M. Hada, M. Ehara, K. Toyota, R. Fukuda, J. Hasegawa, M. Ishida, T. Nakajima, Y. Honda, O. Kitao, H. Nakai, M. Klene, X. Li, J. E. Knox, H. P. Hratchian, J. B. Cross, V. Bakken, C. Adamo, J. Jaramillo, R. Gomperts, R. E. Stratmann, O. Yazyev, A. J. Austin, R. Cammi, C. Pomelli, J. W. Ochterski, P. Y. Ayala, K. Morokuma, G. A. Voth, P. Salvador, J. J. Dannenberg, V. G. Zakrzewski, S. Dapprich, A. D. Daniels, M. C. Strain, O. Farkas, D. K. Malick, A. D. Rabuck, K. Raghavachari, J. B. Foresman, J. V. Ortiz, Q. Cui, A. G. Baboul, S. Clifford, J. Cioslowski, B. B. Stefanov, G. Liu, A. Liashenko, P. Piskorz, I. Komaromi, R. L. Martin, D. J. Fox, T. Keith, M. A. Al-Laham, C. Y. Peng, A. Nanayakkara, M. Challacombe, P. M. W. Gill, B. Johnson, W. Chen, M. W. Wong, C. Gonzalez, and J. A. Pople. GAUSSIAN 03, Revision C.02;

Gaussian, Inc: Wallingford, CT, 2004.

(114) Becke, A. D. *J. Chem. Phys.* **1993**, *98*, 5648.

(115) Perdew, J. P. *Phys. Rev. B* **1986**, *33*, 8822.

(116) Perdew, J. P.; Wang, Y. **1986**.

(117) Lee, C.; Yang, W.; Parr, R. G. *Phys. Rev. B* **1988**, *37*, 785.

(118) Roy Dennington II, T. K., John Millam, Ken Eppinnett, W. Lee Hovell, and Ray Gilliland. GaussView, Version 3.09; Semichem, Inc.: Shawnee Mission, KS, 2003.

(119) Yang, D.-S.; Zgierski, M. Z.; Rayner, D. M.; Hackett, P. A.; Martinez, A.; Salahub, D. R.; Roy, P.-N.; Carrington, T., Jr. *J. Chem. Phys.* **1995**, *103*, 5335.

(120) Sharp, T. E.; Rosenstock, H. M. *J. Chem. Phys.* **1964**, *41*, 3453.

(121) Duschinsky, F. *Acta Physicochim URSS* **1937**, *7*, 551.

(122) Zgierski, M. Z.; Zerbetto, F. *J. Chem. Phys.* **1993**, *99*, 3721.

(123) Luna, A.; Amekraz, B.; Tortajada, J. *Chem. Phys. Lett.* **1997**, *266*, 31.

(124) Ma, J. C.; Dougherty, D. A. *Chem. Rev.* **1997**, *97*, 1303.

(125) House, D. A. Ammonia and Amine. In *Comprehensive Coordination Chemistry*; Wilkinson, G., Gillard, T. D., McCleverty, J. A., Eds.; Pergamon: Oxford, 1987; Vol. 2; pp 23.

(126) Jamet-Delcroix, S. *Acta Crystallogr., Sect. B* **1973**, *29*, 977.

(127) Marques, M. P. M.; Batista de Carvalho, L. A. E.; Tomkinson, J. *J. Phys. Chem. A* **2002**, *106*, 2473.

(128) Righini, R.; Califano, S. *Chem. Phys.* **1976**, *17*, 45.

(129) Batista de Carvalho, L. A. E.; Lourenco, L. E.; Marques, M. P. M. *J. Mol. Struct.* **1999**, *482*, 639.

(130) Radom, L.; Hariharan, P. C.; Pople, J. A.; Schleyer, P. V. R. *J. Am. Chem. Soc.* **1973**, *95*, 6531.

(131) Van Alsenoy, C.; Siam, K.; Ewbank, J. D.; Schaefer, L. *THEOCHEM* **1986**, *29*, 77.

- (132) Kazerouni, M. R.; Hedberg, L.; Hedberg, K. *J. Am. Chem. Soc.* **1994**, *116*, 5279.
- (133) Lee, S. J.; Mhin, B. J.; Cho, S. J.; Lee, J. Y.; Kim, K. S. *J. Phys. Chem.* **1994**, *98*, 1129.
- (134) Chang, Y. P.; Su, T. M.; Li, T. W.; Chao, I. *J. Phys. Chem. A* **1997**, *101*, 6107.
- (135) Kudoha, S.; Takayanagia, M.; Nakataa, M.; Ishibashib, T.; Tasumic, M. *J. Mol. Struct.* **1999**, *479*, 41.
- (136) Ikuta, S. *Chem. Phys.* **1986**, *108*, 441.
- (137) Ikuta, S. *Chem. Phys. Lett.* **1985**, *116*, 482.
- (138) Liau, Y. H.; Su, T. M. *J. Am. Chem. Soc.* **1992**, *114*, 9169.
- (139) Liu, H.; Sun, J.; Yang, S. *J. Phys. Chem. A* **2003**, *107*, 5681.
- (140) Alcami, M.; Luna, A.; Mo, O.; Yanez, M.; Tortajada, J.; Amekraz, B. *Chem. Eur. J.* **2004**, *10*, 2927.
- (141) Alcami, M.; Luna, A.; Mo, O.; Yanez, M.; Tortajada, J. *J. Phys. Chem. A* **2004**, *108*, 8367.
- (142) Moore, C. E. *Atomic Energy Levels*; National Bureau Standards: Washington, D.C., 1971.
- (143) Yang, D.-S.; Zgierski, M. Z.; Rayner, D. M.; Hackett, P. A.; Martinez, A.; Salahub, D. R.; Roy, P.-N.; Carrington, T., Jr. *J. Chem. Phys.* **1995**, *103*, 5335.
- (144) Berces, A.; Zgierski, M. Z.; Yang, D.-S. *Computational Molecular Spectroscopy*; Wiley: New York, 2000.
- (145) Bondi, A. *J. Phys. Chem.* **1964**, *68*, 441.
- (146) Boses, A. D.; Chandra, A.; Martin, J. M. L.; Marx, D. *J. Chem. Phys.* **2003**, *119*, 5965.
- (147) Perez, P.; Simon-Manso, Y.; Aizman, A.; Fuentealba, P.; Contreras, R. *J. Am. Chem. Soc.* **2000**, *122*, 4756.
- (148) Lakard, B.; Herlem, G.; Fahys, B. *J. Mol. Struct. THEOCHEM* **2002**, *584*, 15.
- (149) Maksic, Z. B.; Vianello, R. *J. Phys. Chem. A* **2002**, *106*, 419.

- (150) Allen, L. C. *J. Am. Chem. Soc.* **1975**, *97*, 6921.
- (151) Del Bene, J. E. *J. Chem. Phys.* **1972**, *57*, 1899.
- (152) Kollman, P. A.; Allen, L. C. *Chem. Rev.* **1972**, *72*, 283.
- (153) Calhorda, M. J. *Chem. Commun.* **2000**, 801.
- (154) Cotton, F. A.; Daniels, L. M.; Jordan, G. T. I. V.; Murillo, C. A. *Chem. Commun.* **1997**, 1673.
- (155) Desiraju, G. R. *Chem. Commun.* **2005**, 2995.
- (156) Mascal, M. *Chem. Commun.* **1998**, 303.
- (157) Miyawaki, J.; Sugawara, K.; Li, S.; Yang, D.-S. *J. Phys. Chem. A* **2005**, *109*, 6697.
- (158) Miyawaki, J.; Sugawara, K. *J. Chem. Phys.* **2003**, *119*, 6539.
- (159) Bennett, A., M. A.; Foulds, G. A.; Thornton, D. A. *Spectrochimica Acta* **1989**, *45A*, 219.
- (160) Yang, Y.-S.; Hsu, W.-Y.; Lee, H.-F.; Huang, Y.-C.; Yeh, C.-S.; Hu, C.-H. *J. Phys. Chem. A* **1999**, *103*, 11287.
- (161) Yang, Y.-S.; Yeh, C.-S. *Chem. Phys. Lett.* **1999**, *305*, 395.
- (162) Hsu, H.-C.; Lin, F.-W.; Lai, C.-C.; Su, P.-H.; Yeh, C.-S. *New J. Chem.* **2002**, *26*, 481.
- (163) Wu, D.-Y.; Ren, B.; Jiang, Y.-X.; Xu, X.; Tian, Z.-Q. *J. Phys. Chem. A* **2002**, *106*, 9042.
- (164) Guo, W.; Liu, H.; Yang, S. *Int. J. Mass. Spectrom* **2003**, *226*, 291.
- (165) Puskar, L.; Cox, H.; Goren, A.; Aitken, G. D. C.; Stace, A. J. *Faraday Discussions* **2003**, *124*, 259.
- (166) Wu, D. Y.; Hayashi, M.; Chang, C. H.; Liang, K. K.; Lin, S. H. *J. Chem. Phys.* **2003**, *118*, 4073.
- (167) Wu, D. Y.; Hayashi, M.; Shiu, Y. J.; Liang, K. K.; Chang, C. H.; Yeh, Y. L.; Lin, S. H. *J. Phys. Chem. A* **2003**, *107*, 9658.

- (168) Guo, C.; Cao, Z.; Zhang, Q. *Chem. Phys. Lett.* **2004**, *386*, 448.
- (169) Rodgers, M. T.; Stanley, J. R.; Amunugama, R. *J. Am. Chem. Soc.* **2000**, *122*, 10969.
- (170) Deng, H.; Kebarle, P. *J. Am. Chem. Soc.* **1998**, *120*, 2925.
- (171) Haq, S.; King, D. A. *J. Phys. Chem.* **1996**, *100*, 16957.
- (172) Giessel, T.; Schaff, O.; Lindsay, R.; Baumgartel, P.; Polcik, M.; Bradshaw, A. M.; Koebbel, A.; McCabe, T.; Bridge, M.; Lloyd, D. R.; Woodruff, D. P. *J. Chem. Phys.* **1999**, *110*, 9666.
- (173) Lee, J. G.; Ahner, J.; Yates, J. T., Jr. *J. Chem. Phys.* **2001**, *114*, 8722.
- (174) Douglas Edmonds, B.; Kandalam, A. K.; Khanna, S. N.; Li, X.; Grubisic, A.; Khanna, I.; Bowen, K. H. *J. Chem. Phys.* **2006**, *124*, 074316/1.
- (175) Miyawaki, J.; Sugawara, K.-i. *Chem. Phys. Lett.* **2004**, *386*, 196.
- (176) C.E. Moore *Atomic Energy Levels*; National Bureau Standards: Washington, DC, 1971.
- (177) A. Berces, M. Z. Z., and D. S. Yang; Wiley: New York, 2000.
- (178) Sohnlein Bradford, R.; Yang, D.-S. *J. Chem. Phys.* **2006**, *124*, 134305.
- (179) Wang, X.; Yang, D.-S. *J. Chem. Phys.* **2006**.
- (180) Amunugama, R.; Rodgers, M. T. *J. Phys. Chem. A* **2001**, *105*, 9883.
- (181) Wiberg, K. B.; Walters, V. A.; Wong, K. N.; Colson, S. D. *J. Phys. Chem.* **1984**, *88*, 6067.
- (182) Mizutani, G.; Ushioda, S. *J. Chem. Phys.* **1989**, *91*, 598.
- (183) Wiberg, K. B.; Nakaji, D.; Breneman, C. M. *J. Am. Chem. Soc.* **1989**, *111*, 4178.
- (184) Wu, D.-Y.; Ren, B.; Xu, X.; Liu, G.-K.; Yang, Z.-L.; Tian, Z.-Q. *J. Chem. Phys.* **2003**, *119*, 1701.
- (185) Brown, D. J. *The Chemistry of Heterocyclic Compounds, The pyrimidines*; John Wiley & Sons, Inc: New York, 1962; Vol. 16.
- (186) M. Tisler, B. S. *Advances in Heterocyclic Chemistry, Pyridazines*; Academic: New

York, 1968; Vol. 9.

(187) Castle, R. N. *The Chemistry of Heterocyclic Compounds, Pyridazines*; John Wiley & Sons, Inc: New York, 1973; Vol. 28.

(188) Barlin, G. B. *The Chemistry of Heterocyclic Compounds, The pyrazines*; John Wiley & Sons, Inc: New York, 1982; Vol. 41.

(189) George R. Newkome; Paudler, W. W. *Contemporary Heterocyclic Chemistry*; John Wiley & Sons: New York, 1982.

(190) Katritzky, A. R.; Pozharskii, A. F. *Handbook of Heterocyclic Chemistry*, 2nd ed.; Pergamon: Amsterdam, 2000.

(191) Dudde, R.; Frank, K. H.; Rocco, M. L. M.; Koch, E. E. *Surf. Sci.* **1988**, *201*, 469.

(192) Bader, M.; Haase, J.; Frank, K. H.; Ocal, C.; Puschmann, A. *J. Phys. (Paris) C* **1986**, *8*, 491.

(193) Rodriguez, J. A. *Surf. Sci.* **1990**, *234*, 421.

(194) Egelhoff, W. F. In *Chemical Physics of Solid Surfaces and Heterogeneous Catalysts*; King, D. A., Woodruff, D. P., Eds.; Elsevier: Amsterdam, 1984; Vol. 4.

(195) Baiker, A.; Kijenski, J. *Catalysis Rev. -Sci. Eng.* **1985**, *27*, 653.

(196) Iannelli, A.; Brolo, A. G.; Irish, D. E.; Lipkowski, J. *Can. J. Chem.* **1997**, *75*, 1694.

(197) Dudde, R.; Frank, K. H.; Koch, E. E. *J. Electron Spectrosc. Relat. Phenom.* **1988**, *47*, 245.

(198) Child, M. D.; Foulds, G. A.; Percy, G. C.; Thornton, D. A. *J. Mol. Struct.* **1981**, *75*, 191.

(199) Bahat, M.; Yurdakul, S. *Spectrochimica Acta, Part A: Molecular and Biomolecular Spectroscopy* **2002**, *58*, 933.

(200) GAUSSIAN 03, Revision C.02; Gaussian, Inc: Pittsburgh, PA, 2004.

(201) Duschinsky, F. *Acta Physicochim. URSS* **1937**, *7*, 551.

(202) Haynes, J. S.; Retting, S. J.; Sams, J. R.; Trotter, J.; Thompson, R. C. *Inorg. Chem.*

1988, 27, 1237.

(203) Darriet, J.; Haddad, M. S.; Duesler, E. N.; Hendrickson, D. N. *Inorg. Chem.* **1979**, 18, 2679.

(204) Lewin, A. H.; Michl, R. J.; Ganis, P.; Lepote, U.; Avitable, G. *Chem. Commun.* **1971**, 21, 1400.

(205) Wu, D.-Y.; Ren, B.; Jiang, Y.-X.; Xu, X.; Tian, Z.-Q. *J. Phys. Chem. A* **2002**, 106, 9042.

(206) Bondi, A. *J. Phys. Chem.* **1964**, 68, 441.

(207) Lide, D. R.; Frederikse, H. P. R. *CRC Handbook of Chemistry and Physics*, 78 ed.; CRC: New York, 1997.

(208) Miyawaki, J.; Sugawara, K.-I. *Chem. Phys. Lett.* **2004**, 386, 196.

(209) Billes, F.; Mikosch, H.; Holly, S. *J. Mol. Struct. (THEOCHEM)* **1998**, 423, 225.

(210) Zhu, L.; Johnson, P. *J. Chem. Phys.* **1993**, 99, 2322.

(211) Amunugama, R.; Rodgers, M. T. *Int. J. Mass Spectrom.* **2000**, 195/196, 439.

(212) Rodgers, M. T. *Journal of Physical Chemistry A* **2001**, 105, 8145.

(213) Akyuz, S. *Journal of Molecular Structure* **1998**, 449, 23.

(214) Akyuz, S. *Journal of Molecular Structure* **1999**, 482-483, 171.

(215) Topaçli, A.; Bayari, S. *Spectrochimica Acta, Part A: Molecular and Biomolecular Spectroscopy* **2001**, 57A, 1385.

(216) Akyuz, S. *Journal of Supramolecular Chemistry* **2003**, 2, 401.

(217) Baek, S. J.; Choi, K.-W.; Choi, Y. S.; Kim, S. K. *Journal of Physical Chemistry A* **2003**, 107, 4826.

(218) Belcher, D. E.; Cockett, M. C. R. *Chemical Physics Letters* **2004**, 398, 539.

(219) Proch, D.; Trickl, T. *Rev. Sci. Instrum.* **1989**, 60, 713.

(220) Wang, X.; Yang, D.-S.

(221) Moore, C. E. *Atomic Energy Levels*; National Bureau Standards: Washington, D.C., 1971.

- (222) Wang, X.; Yang, D.-S.; (unpublished).
- (223) Miyawaki, J.; Sugawara, K.-i. *Journal of Chemical Physics* **2003**, *119*, 6539.
- (224) Wang, X.; Lee, J. S.; Yang, D.-S. *J. Chem. Phys.* **2006**, *125*, 014309.
- (225) Kaes, C.; Katz, A.; Hosseini, M. W. *Chemical Reviews (Washington, D. C.)* **2000**, *100*, 3553.
- (226) Sammes, P. G.; Yahioğlu, G. *Chemical Society Reviews* **1994**, *23*, 327.
- (227) Luman, C. R.; Castellano, F. N. *Comprehensive Coordination Chemistry II* **2004**, *1*, 25.
- (228) Kalyanasundaram, K. *Coordination Chemistry Reviews* **1982**, *46*, 159.
- (229) Meyer, T. J. *Accounts of Chemical Research* **1978**, *11*, 94.
- (230) DeArmond, M. K.; Carlin, C. M. *Coordination Chemistry Reviews* **1981**, *36*, 325.
- (231) Calabrese, J. C.; Tam, W. *Chem. Phys. Lett.* **1987**, *133*, 244.
- (232) Andres, P. R.; Schubert, U. S. *Advanced Materials (Weinheim, Germany)* **2004**, *16*, 1043.
- (233) Dwyer, F.; Reid, I. K.; Shulman, A.; Laycock, G. M.; Dixon, S. *Australian Journal of Experimental Biology and Medical Science* **1969**, *47*, 203.
- (234) Meyer, T. J. *Accounts of Chemical Research* **1989**, *22*, 163.
- (235) Yamauchi, O. *Pure and Applied Chemistry* **1995**, *67*, 297.
- (236) Kramer, R. *Bioinorganic Chemistry* **1997**, 606.
- (237) Patel, R. N.; Singh, N.; Shukla, K. K.; Niclos-Gutierrez, J.; Castineiras, A.; Vaidyanathan, V. G.; Nair, B. U. *Spectrochimica Acta, Part A: Molecular and Biomolecular Spectroscopy* **2005**, *62A*, 261.
- (238) Sha, K.; Li, D.; Wang, S.; Qin, L.; Wang, J. *Polymer Bulletin (Heidelberg, Germany)* **2005**, *55*, 349.
- (239) Sigman, D. S.; Thederahn, T.; Kuwabara, M. D.; Bruice, T. C.; Spassky, A. *Molecular Structure and Energetics* **1988**, *10*, 281.
- (240) Hermann, T.; Heumann, H. *Methods in Enzymology* **2000**, *318*, 33.

- (241) Papavassiliou, A. G. *Methods in Molecular Biology (Totowa, NJ, United States)* **2001**, 148, 77.
- (242) Benedix, R.; Birner, P.; Birnstock, F.; Hennig, H.; Hofmann, H. J. *Journal of Molecular Structure* **1979**, 51, 99.
- (243) Almenningen, A.; Bastiansen, O. *K. Nor. Vidensk. Selsk. Skr.* **1958**, 1.
- (244) Merritt, L. L., Jr.; Schroeder, E. D. *Acta Cryst.* **1956**, 9, 801.
- (245) Castellano, S.; Gunther, H.; Ebersole, S. *Journal of Physical Chemistry* **1965**, 69, 4166.
- (246) Sone, K.; Krumholz, P.; Stammreich, H. *Journal of the American Chemical Society* **1955**, 77, 777.
- (247) Nakamoto, K. *Journal of Physical Chemistry* **1960**, 64, 1420.
- (248) Galasso, V.; De Alti, G.; Bigotto, A. *Tetrahedron* **1971**, 27, 991.
- (249) Barone, V.; Lelj, F.; Cauletti, C.; Piancastelli, M. N.; Russo, N. *Molecular Physics* **1983**, 49, 599.
- (250) Jaime, C.; Font, J. *Journal of Organic Chemistry* **1990**, 55, 2637.
- (251) Goller, A.; Grummt, U. W. *Chem. Phys. Lett.* **2000**, 321, 399.
- (252) Ould-Moussa, L.; Castella-Ventura, M.; Kassab, E.; Poizat, O.; Strommen, D. P.; Kincaid, J. R. *Journal of Raman Spectroscopy* **2000**, 31, 377.
- (253) Goller, A. H.; Grummt, U.-W. *Chem. Phys. Lett.* **2002**, 354, 233.
- (254) Boag, N. M.; Coward, K. M.; Jones, A. C.; Pemble, M. E.; Thompson, J. R. *Acta Crystallographica, Section C: Crystal Structure Communications* **1999**, C55, 672.
- (255) Candan, M. M.; Eroglu, S.; Ozbey, S.; Kendi, E.; Kantarcl, Z. *Spectrosc. Lett.* **1999**, 32, 35.
- (256) Nather, C.; Riedel, J.; Jess, I. *Acta Crystallographica, Section C: Crystal Structure Communications* **2001**, C57, 111.
- (257) Perez-Jimenez, A. J.; Sancho-Garcia, J. C.; Perez-Jorda, J. M. *Journal of Chemical Physics* **2005**, 123, 134309/1.

- (258) Drew, M. G. B.; Hudson, M. J.; Iveson, P. B.; Russell, M. L.; Liljenzin, J.-O.; Sklberg, M.; Spjuth, L.; Madic, C. *Journal of the Chemical Society, Dalton Transactions: Inorganic Chemistry* **1998**, 2973.
- (259) Bessel, C. A.; See, R. F.; Jameson, D. L.; Churchill, M. R.; Takeuchi, K. J. *Journal of the Chemical Society, Dalton Transactions: Inorganic Chemistry (1972-1999)* **1992**, 3223.
- (260) Nakamura, K. *Bulletin of the Chemical Society of Japan* **1972**, 45, 1943.
- (261) Berka, L. H.; Edwards, W. T.; Christian, P. A. *Inorganic and Nuclear Chemistry Letters* **1971**, 7, 265.
- (262) McKenzie, E. D. *Coordination Chemistry Reviews* **1971**, 6, 187.
- (263) Strukl, J. S.; Walter, J. L. *Spectrochimica Acta, Part A: Molecular and Biomolecular Spectroscopy* **1971**, 27, 223.
- (264) Wu, H.-F.; Brodbelt, J. S. *Inorganic Chemistry* **1995**, 34, 615.
- (265) Haeffner, F.; Brinck, T.; Haerberlein, M.; Moberg, C. *Theochem* **1997**, 397, 39.
- (266) Corongiu, G.; Nava, P. *International Journal of Quantum Chemistry* **2003**, 93, 395.
- (267) Knuehl, B.; Pintauer, T.; Kajiwara, A.; Fischer, H.; Matyjaszewski, K. *Macromolecules* **2003**, 36, 8291.
- (268) Pintauer, T.; Reinoehl, U.; Feth, M.; Bertagnolli, H.; Matyjaszewski, K. *European Journal of Inorganic Chemistry* **2003**, 2082.
- (269) Burke, P. J.; McMillin, D. R.; Robinson, W. R. *Inorganic Chemistry* **1980**, 19, 1211.
- (270) Burke, P. J.; Henrick, K.; McMillin, D. R. *Inorganic Chemistry* **1982**, 21, 1881.
- (271) Goodwin, K. V.; McMillin, D. R.; Robinson, W. R. *Inorganic Chemistry* **1986**, 25, 2033.
- (272) Hazell, A. *Polyhedron* **2004**, 23, 2081.
- (273) Smith, C. I.; Dolan, G. J.; Farrell, T.; Maunder, A. J.; Fernig, D. G.; Edwards, C.;

- Weightman, P. J. *Phys.: Condens. Matter* **2004**, *16*, S4385.
- (274) Li, Q.; Wu, X.; Huang, J.; Yang, J. *Ultramicroscopy* **2005**, *105*, 293.
- (275) Velez, P.; Dassie, S. A.; Leiva, E. P. M. *Phys. Rev. Lett.* **2005**, *95*, 045503/1.
- (276) Wu, X.; Li, Q.; Huang, J.; Yang, J. *The Journal of chemical physics* **2005**, *123*, 184712.
- (277) Xu, B.; Tao Nongjian, J. *Science* **2003**, *301*, 1221.
- (278) Constable, E. C. *Advances in Inorganic Chemistry and Radiochemistry* **1986**, *30*, 69.
- (279) Liantonio, R.; Logothetis, T. A.; Messina, M. T.; Mentrangolo, P.; De Santis, A.; Pilati, T.; Resnati, G. *Collection of Czechoslovak Chemical Communications* **2002**, *67*, 1373.
- (280) Deacon, G. B.; Patrick, J. M.; Skelton, B. W.; Thomas, N. C.; White, A. H. *Australian Journal of Chemistry* **1984**, *37*, 929.
- (281) Pruchnik, F. P.; Robert, F.; Jeannin, Y.; Jeannin, S. *Inorganic Chemistry* **1996**, *35*, 4261.
- (282) Ramdeehul, S.; Barloy, L.; Osborn, J. A.; De Cian, A.; Fischer, J. *Organometallics* **1996**, *15*, 5442.
- (283) Holyer, R. H.; Hubbard, C. D.; Kettle, S. F. A.; Wilkins, R. G. *Inorg. Chem.* **1966**, *5*, 622.
- (284) Lytle, F. E.; Petrosky, L. M.; Carlson, L. R. *Analytica Chimica Acta* **1971**, *57*, 239.
- (285) Allmann, R.; Henke, W.; Reinen, D. *Inorganic Chemistry* **1978**, *17*, 378.
- (286) Novak, I.; Klasinc, L. *Zeitschrift fuer Naturforschung, Teil A: Astrophysik, Physik und Physikalische Chemie* **1978**, *33A*, 247.
- (287) Kremer, S.; Henke, W.; Reinen, D. *Inorganic Chemistry* **1982**, *21*, 3013.
- (288) Henke, W.; Kremer, S.; Reinen, D. *Inorganic Chemistry* **1983**, *22*, 2858.
- (289) Kwik, W. L.; Ang, K. P. *Transition Metal Chemistry (Dordrecht, Netherlands)*

1985, 10, 50.

(290) Folgado, J. V.; Henke, W.; Allmann, R.; Stratemeier, H.; Beltran-Porter, D.; Rojo, T.; Reinen, D. *Inorganic Chemistry* **1990**, 29, 2035.

(291) Rabbe, C.; Mikhalko, V.; Dognon, J. P. *Theoretical Chemistry Accounts* **2000**, 104, 280.

(292) Beauchamp, D. A.; Loeb, S. J. *Supramolecular Chemistry* **2005**, 17, 617.

(293) Leroy-Lhez, S.; Fages, F. *Comptes Rendus Chimie* **2005**, 8, 1204.

(294) Holyer, R. H.; Hubbard, C. D.; Kettle, S. F. A.; Wilkins, R. G. *Inorg. Chem.* **1965**, 4, 929.

(295) Yoshida, T.; Sawada, S. *Bulletin of the Chemical Society of Japan* **1975**, 48, 3379.

(296) Kaim, W. *Journal of the American Chemical Society* **1982**, 104, 3833.

(297) Scaltrito, D. V.; Thompson, D. W.; O'Callaghan, J. A.; Meyer, G. J. *Coordination Chemistry Reviews* **2000**, 208, 243.

(298) Furuhashi, A.; Takano, K.; Ogawa, S.; Tsuchiya, S. *Theochem* **2003**, 620, 49.

(299) De Luca, L. *Curr. Med. Chem.* **2006**, 13, 1.

(300) Lee, W.-J. *Mater. Sci. Eng., A* **2003**, 348, 217.

(301) Otmacic, H.; Stupnisek-Lisac, E. *Electrochim. Acta* **2003**, 48, 985.

(302) Zhao, G.; Lin, H. *Curr Med. Chem. -Anti-Cancer Agents* **2005**, 5, 137.

(303) Sundberg, R. J.; Martin, R. B. *Chem. Rev.* **1974**, 74, 471.

(304) Caminati, W.; Melandri, S.; Millemaggi, A.; Favero, P. G. *Chem. Phys. Lett.* **1998**, 294, 377.

(305) Andrei, B.-S.; Solca, N.; Dopfer, O. *J. Phys. Chem. A* **2005**, 109, 3598.

(306) Van Bael, M. K.; Smets, J.; Schoone, K.; Houben, L.; McCarthy, W.; Adamowicz, L.; Nowak, M. J.; Maes, G. *J. Phys. Chem. A* **1997**, 101, 2397.

(307) Carles, S.; Lecomte, F.; Schermann, J. P.; Desfrancois, C. *J. Phys. Chem. A* **2000**, 104, 10662.

(308) Rodgers, M. T.; Armentrout, P. B. *Int. J. Mass Spectrom.* **1999**, 185/186/187, 359.

- (309) Huang, H.; Rodgers, M. T. *J. Phys. Chem. A* **2002**, *106*, 4277.
- (310) Rannulu, N. S.; Amunugama, R.; Yang, Z.; Rodgers, M. T. *J. Phys. Chem. A* **2004**, *108*, 6385.
- (311) Rannulu, N. S.; Rodgers, M. T. *Phys. Chem. Chem. Phys.* **2005**, *7*, 1014.
- (312) Sletten, E.; Stogard, A. *Theochem* **1987**, *38*, 289.
- (313) Alcamí, M.; Mo, O.; Yanez, M. *J. Phys. Chem.* **1989**, *93*, 3929.
- (314) Alcamí, M.; Mo, O.; Yanez, M. *J. Phys. Chem.* **1992**, *96*, 3022.
- (315) Cornilsen, B. C.; Nakamoto, K. *J. Inorg. Nucl. Chem.* **1974**, *36*, 2467.
- (316) King, S. T. *J. Phys. Chem.* **1970**, *74*, 2133.
- (317) Perchard, C.; Bellocq, A.; Novak, A. *J. Chim. Phys.* **1965**, *62*, 1344.
- (318) Loeffen, P. W.; Pettifer, R. F.; Fillaux, F.; Kearley, G. J. *J. Chem. Phys.* **1995**, *103*, 8444.
- (319) Yang, D.-S.; Miyawaki, J. *Chem. Phys. Lett.* **1999**, *313*, 514.
- (320) Houriet, R.; Schwarz, H.; Zummack, W.; Andrade, J. G.; Schleyer, P. V. R. *Nouv. J. Chim.* **1981**, *5*, 505.
- (321) Taft, R. W.; Anvia, F.; Taagepera, M.; Catalan, J.; Elguero, J. *J. Am. Chem. Soc.* **1986**, *108*, 3237.

VITA

Xu Wang

Date of Birth: May 3, 1974

Place of Birth: Yinchuan, Ningxia, China

Education:

B.S., Chemical Engineering, Tianjin University, 1995

M.S., Chemistry, Institute of Chemistry, Chinese Academy of Science, 2001

Publications:

1. Wang, X.; Yang, D.-S., "Bonding structures in copper-aminopyridine complexes studied by pulsed-field ionization electron spectroscopy and ab initio calculations," *in preparation*.
2. Wang, X.; Sohnlein, B. R.; Yang, D.-S., "Molecular structures and vibrations of copper-(pyridine)_n (n=1,2) complexes," *in preparation*.
3. Wang, X.; Yang, D.-S., "Pulsed-field ionization electron ZEKE spectroscopy of Cu-(2,2'-bipyridine) and -(4,4'-bipyridine) complexes," *in preparation*.
4. Wang, X.; Yang, D.-S., "Photoelectron spectroscopy and density functional theory of multidentate binding structures of Cu-2,2':6',2"-terpyridine and -1,10-phenanthroline complexes." *in preparation*.

5. Wang, X.; Yang, D.-S., "Electronic states and molecular structures of group VIII metal (Ni, Co and Fe) 2,2'-bipyridine complexes," *in preparation*.
6. Wang, X.; Lee, J. S.; Yang, D.-S., "Electron spectroscopy, molecular structures, and binding energies of Al- and Cu-imidazole," *J. Phys. Chem. A* **2006**, 10(47), 12777.
7. Wang, X.; Lee, J. S.; Yang, D.-S., "Pulsed-field ionization electron spectroscopy and ab initio calculations of copper-diazine complexes," *J. Chem. Phys.* **2006**, 125, 014309.
8. Wang, X.; Yang, D.-S., "Spectroscopy and structures of copper complexes with ethylenediamine and methyl-substituted derivatives," *J. Phys. Chem. A* **2006**, 110, 7568.
9. Wang, X.; Yang, Dong-Sheng. A Hydrogen-Bond Stabilized Copper Complex: Cu-Ethylenediamine. *J. Phys. Chem. A* **2004**, 108(31), 6449.
10. Li, S.; Fuller, J. F.; Wang, X; Sohnlein, B. R.; Bhowmik, P.; Yang, D.-S. "Photoelectron spectroscopy and density functional theory of puckered ring structures of Group 13 metal-ethylenediamine," *J. Chem. Phys.*, **2004**, 121(16), 7692.

Xu Wang